PROCEEDINGS
Of The
ELECTRON BEAM SYMPOSIUM

SIXTH ANNUAL MEETING

APRIL 1964

EDITOR – J. R. MORLEY

alloyd general corporation
MEDFORD, MASSACHUSETTS

PROCEEDINGS

of the

ELECTRON BEAM SYMPOSIUM

SIXTH ANNUAL MEETING

Somerset Hotel

Boston, Massachusetts

J. R. Morley
Editor

Sponsored

by

ALLOYD GENERAL CORPORATION

Published

by

NUCLIDE CORPORATION

Alloyd General Vacuum Division

81 Hicks Avenue

Medford, Massachusetts

Copies of the Proceedings of the Electron Beam Symposia are available from Nuclide Corporation, Alloyd General Vacuum Division, 81 Hicks Avenue, Medford, Massachusetts, USA.

The year and price are as follows:

1959 - $ 5.00	1962 - $20.00
1960 - $10.00	1963 - $20.00
1961 - $15.00	1964 - $20.00

The complete set of six volumes is available for $80.00.

PREFACE

This volume is the account of the papers presented at the sixth annual meeting of the Electron Beam Symposium held at Boston in the Somerset Hotel April 27-28, 1964, under the sponsorship of the Alloyd General Corporation.

The technical content of the program followed the established pattern of previous meetings by reporting on both the theoretical aspects and the experimental techniques and equipment associated with the development of electron beam technology.

Any meeting concerned with the rapidly expanding technology of energy beams must be selective in its content. In a meeting of this nature, which has industrial sponsorship and which draws attendance from both laboratories and manufacturing organizations, it is our policy to provide a program concerned with three main topics. These are: the physics of electron beams; the application of electron beams to materials; and new energy beam equipment and processes.

A special feature of this conference was the section devoted to the two types of hollow cathode discharge. In addition, the panel discussion of this topic is also recorded in the proceedings in question and answer format.

Although somewhat out of place at an electron beam meeting, four papers on lasers were included under the energy beam section mainly to provide a comparison with electron beam applications.

It is a great pleasure to acknowledge with sincere thanks the efforts of all of the authors and speakers and members of the panel for their contributions, the committee members, Drs. L. McD. Schetky and S. S. White, for their assistance and encouragement in establishing the program, to the moderators of the sessions for conducting the meeting, and to Jane Caldow for typing the manuscript for photographic reproduction.

Cambridge, Mass. May, 1964 John R. Morley

CONTRIBUTORS

Adams, C. M., Massachusetts Institute of Technology, Cambridge, Massachusetts

Adair, H. L., Union Carbide Corporation, Oak Ridge, Tennessee

Argon, R., Alloyd General Corporation, Cambridge, Massachusetts

Bloomsburgh, R. A., Philco Corporation, Philadelphia, Pennsylvania

Buritz, R. S., Alloyd General Corporation, Cambridge, Massachusetts

Caldarella, C. J., U. S. Army Laboratories, Natick, Massachusetts

Degering, E. F., U. S. Army Laboratories, Natick, Massachusetts

Drangel, I., Materials Research Corporation, Orangeburg, New York

Edmonds, D. S., Nuclide Corporation, Allston, Massachusetts

El-Kareh, A. B., Pennsylvania State University, University Park, Pennsylvania

Ellman, R. P., Aerovac Corporation, Troy, New York

Goel, T. R. S., Delco Radio, Kokomo, Indiana

Haines, G. H., U. S. Army Laboratories, Natick, Massachusetts

King, J., Philco Corporation, Philadelphia, Pennsylvania

Kirk, N., General Electric Company, Pittsfield, Massachusetts

Kobisk, E. H., Union Carbide Corporation, Oak Ridge, Tennessee

Kusko, A., Alexander Kusko, Cambridge, Massachusetts

Lidsky, L. M., Massachusetts Institute of Technology, Cambridge, Massachusetts

McMahon, P., Materials Research Corporation, Orangeburg, New York

McManaman, D. W., Delco Radio, Kokomo, Indiana

Miller, A., Autonetics, Anaheim, California

Moll, S., Advanced Metals Research, Somerville, Massachusetts

CONTRIBUTORS

Morley, J. R., Alloyd General Corporation, Cambridge, Massachusetts

Morritz, F. L., Autonetics, Anaheim, California

Muly, E. C., Martin Company, Baltimore, Maryland

Meyers, J. D., Cornell Aeronautical Laboratories, Inc., Buffalo, New York

Namba, S., Institute of Physical and Chemical Research, Tokyo, Japan

Nyenhuis, H. A., Electron Beam Techniques, Inc., Plainville, Connecticut

Parker, D., Massachusetts Institute of Technology, Cambridge, Massachusetts

Payne, P. R., Alloyd General Corporation, Cambridge, Massachusetts

Reyner, E. M., Pennsylvania State University, University Park, Pennsylvania

Roos, J. P., Alloyd General Corporation, Cambridge, Massachusetts

Shima, R., Autonetics, Anaheim, California

Smullin, L. D., Massachusetts Institute of Technology, Cambridge, Massachusetts

Stauffer, L. H., General Electric Company, Schenectady, New York

Terhune, J. H., General Electric Company, Schenectady, New York

Tulisiak, G., NASA, Lewis Research Center, Cleveland, Ohio

Vibrans, G. E., Massachusetts Institute of Technology, Lincoln Laboratory, Lexington, Massachusetts

Voorhes, W. G., Pratt & Whitney Company, West Hartford, Connecticut

Weinig, S., Materials Research Corporation, Orangeburg, New York

Weiss, S., Massachusetts Institute of Technology, Cambridge, Massachusetts

Whitaker, E. G., Delco Radio, Kokomo, Indiana

TABLE OF CONTENTS

TABLE OF CONTENTS

INTRODUCTORY REMARKS

J. R. Morley

Gentlemen, I wish to welcome you to Boston and to the 1964 Electron Beam Symposium.

Since this is the sixth annual meeting in this series it is perhaps pertinent to open these proceedings by taking a few moments to find out how the meeting originated and why in fact we come to be here at all.

It was back in 1958 that James Hetherington, a member of the Alloyd Research Corporation, originated the idea of holding an Electron Beam Symposium. This came about for two reasons - First, he realized that there was a growing potential and interest in the application and use of electron beams, and second, since the available technical information on this subject was perhaps even more widely scattered than some of the beams of that time, there was a need to provide a proceedings of the meeting.

In 1959 he conducted the first Electron Beam Symposium here in Boston, and the support which it and succeeding Symposia have received confirmed Hetherington's belief in the need for a technical meeting to discuss current problems and ideas, to exchange information, and to commit the proceedings to print.

Between 1959 and 1963 the amount of time devoted at meetings concerning the generation of electron beams and their applications has increased from two to approximately five days per year.

Even more remarkable this year - in fact in the spring of 1964 alone there will be a total of more than fourteen full days of such papers at meetings throughout the world, or a total of almost three working weeks, and there are probably more sessions about which I have not heard.

We should perhaps remember that five years ago it was a considerable achievement to build an electron gun that worked at all, let alone one which could weld a quarter inch of steel, and during this same period, electron

beam technology has made the very big step from the laboratory to the production shop.

In this same interval new energy beam sources have also come along in the form of lasers and the hollow cathode discharge to supplement the classical electron beam, and the new applications have multiplied correspondingly.

In keeping with the founder's original concepts, we have compiled a program for this meeting which is principally directed towards these two main aspects of electron beam technology - Physics and Applications, together with papers and discussions on hollow cathode discharges and lasers.

Before turning the meeting over to Don Hay who is the moderator for the first morning session, I wish to acknowledge the assistance from L. McD. Schetky and S. S. White, the symposium committee members, who have been most active in compiling this program and I wish to express my sincere appreciation for their efforts and co-operation.

Thank you for being here today and I hope you enjoy the program.

COMPUTATION OF THE SPACE CHARGE SPREADING OF AN ELECTRON BEAM UNDER ACCELERATION

Gerwig E. Vibrans
Lincoln Laboratory*, Massachusetts Institute of Technology
Lexington, Massachusetts

ABSTRACT

The known differential equation, which describes the spreading of a circular electron beam in an accelerating field under space-charge repulsion, is derived in a simplified form so that the general solution can be precomputed. The solution is given in the form of a diagram.

*Operated with support from the U. S. Advanced Research Projects Agency.

COMPUTATION OF THE SPACE CHARGE SPREADING OF AN ELECTRON BEAM UNDER ACCELERATION

In electron optical devices in which there is a high electron current density, as in cathode-ray tubes, the space charge field due to the electrons themselves, is an important factor in the determination of the shape of the electron beam. The diverging effect of space charge upon the electron beam in a drift region which is field free is a standard presentation in many books on electron optics. The equation of motion usually being attributed to Watson.

The space charge effect during acceleration of an electron beam is also important but does not appear to have been treated extensively in the literature. This paper will investigate a circular electron beam in an accelerating field. The electrons have a certain initial velocity, and enter an axial electrical field--for example, through a hole in a plane electrode. The electrons are now subjected to a constant accelerating electric field and also experience mutual repulsion. The equation of motion has been derived and solved by H. Moss[1] who gives several examples for the conditions found in cathode-ray tubes. Such an example is defined by a set of six independent parameters.

By Moss' method, every example is solved by computing a function numerically and then integrating it. For a given beam length, the limit of integration must be found by trial and error. The mathematical difficulties have apparently prevented any wider application of this solution.

In the course of voltage breakdown studies, we became interested in field emission as an initiating mechanism. The high current density of field emission makes the space-charge effect especially important, and in this connection it was desirable to compute many cases which would have been very laborious by Moss' method. A simplified method has been found for computing the shape of an accelerated circular electron beam with

space charge. This method is presented here in detail.

Imagine a thin slice (thickness Δz) of a circular electron beam (Fig. 1) and assume that in any plane perpendicular to the beam axis the electrons are monoenergetic. Assume that the field strength and the flux are constant in the axial direction, so that all the flux from the charge in the slice goes through the outer surface and nothing through the end discs.

The radial electrical field is then:

$$E_{rad} = \frac{D}{\varepsilon_o} = \frac{1}{\varepsilon_o} \frac{I}{2\pi r \dot{z}}$$

The equations of motion of the electrons with an external axial field E, are:

$$z = \frac{e\,E}{m\ 2} t^2 + \dot{z}_o t \qquad (1)$$

$$\frac{d^2 r}{dt^2} = \frac{eI}{\varepsilon_o 2\pi r m \left(\frac{e}{m} Et + \dot{z}_o\right)} \qquad (2)$$

This is Eq. (6) of H. Moss[1] except for a factor $1/4\ \pi\varepsilon_o$ due to the use of different units. In order to simplify the differential equation, the following abbreviations are introduced:

$$K = \frac{eI}{\varepsilon_o 2\pi m} \quad , \left(\frac{m^3}{sec^3}\right)$$

$$A = \frac{e}{m} E \quad , \left(\frac{m}{sec^2}\right)$$

$$B = \dot{z}_o \quad , \left(\frac{m}{sec}\right).$$

and the dimensionless variables:

$$R = r \frac{A}{\sqrt{BK}}$$

$$T = t \frac{A}{B}$$

$$Z = z \frac{A}{B^2}$$

The dimensionless equations of motion become:

$$Z = \frac{1}{2} T^2 + T \tag{3}$$

$$R \frac{d^2R}{dT^2} = \frac{1}{T + 1} \tag{4}$$

The solution of this equation is given in the literature, for example, by Kamke[2]. This solution may be called a formal one since it is given in terms that have no direct physical meaning. Introducing a new variable:

$$W = \frac{R}{\sqrt{T + 1}} \tag{5}$$

and after one integration, the variables can be separated and written:

$$\int_{W_o}^{W} \pm \frac{dW}{\sqrt{\frac{1}{4} W^2 + 2 \ln |W| + C}} = F(W) - F(W_o) = \ln(T + 1) + C_1 \tag{6}$$

The initial conditions (T = 0) giving:

$$W_o = R_o$$

$$C = \dot{R}_o^2 - \dot{R}_o R_o - 2 \ln R_o \qquad (7)$$

$$\dot{R}_o = \left(\frac{dR}{dT}\right) T = 0$$

$$C_1 = 0$$

F is computed numerically[3] as:

$$F(W) = \int_{W_n}^{W} \frac{dW}{\sqrt{\frac{1}{4} W^2 + 2 \ln |W| + C}}$$

where W_n is arbitrary; for convenience it is chosen so that:

$$\frac{1}{4} W_n^2 + 2 \ln |W_n| + C = 0 \quad . \qquad (8)$$

The function F(W) is plotted in Figs. 2 and 3 for the values of C which are of practical interest. The time T is found from the other equation of motion, Eq. (3), where:

$$T + 1 = + \sqrt{1 + 2Z} \quad . \qquad (9)$$

Inserting Eq. (9) into Eq. (6):

$$F(W,C) = \ln \sqrt{1 + 2Z} + F(W_o,C).$$

COMPUTATION OF THE SPACE CHARGE SPREADING OF AN

ELECTRON BEAM UNDER ACCELERATION

Since W_o, C and Z are defined by the initial conditions, F is found by this equation, and Fig. 2 or 3 gives W, which in turn yields:

$$R = W\sqrt{T + 1} = W\sqrt[4]{1 + 2Z}$$

or

$$\frac{r}{r_o} = \frac{R}{W_o} = \frac{W}{W_o} = \sqrt[4]{1 + 2Z} \quad .$$

The following sequence summarizes the steps in computing a beam diameter:

Input:

Beam current	I
Initial beam radius	r_o
Initial beam divergence	$r_o' = \left(\frac{dr}{dz}\right)_o$
Initial potential of electrons	U
Accelerating electric field	E_z
Beam length	Z

Intermediate steps:

$$\dot{z}_o = \sqrt{2U\,\frac{e}{m}}$$

$$W_o = r_o\,\frac{e}{m}\,E_z\sqrt{\frac{\epsilon_o 2\pi m}{\dot{z}_o e I}}$$

$$\dot{R}_o = r_o'\sqrt{\frac{\dot{z}_o^3\, 2\pi\epsilon_o m}{eI}}$$

$$C = \dot{R}_o^2 - W_o\dot{R}_o - 2\ln W_o$$

$$Z = z\,\frac{E_z\,\frac{e}{m}}{\dot{z}_o^2}$$

$|F(W_o,C)|$ is taken from Fig. 2 or Fig. 3. The sign is still indeterminate; the sign of W_o must be taken:

$$\dot{W}_o = \dot{R}_o - \frac{1}{2} W_o$$

$$F(W_o,C) = \frac{\dot{W}_o}{|\dot{W}_o|} \cdot |F(W_o,C)| ,$$

$$F(W,C) = F(W_o,C) + \ln \sqrt{1 + 2Z}$$

W(F) is taken from Fig. 2 or Fig. 3

Result:

$$\frac{r}{r_o} = \frac{W}{W_o} \sqrt[4]{1 + 2Z}$$

Thus the problem is reduced to some slide rule work. It is difficult to precompute a ready-made solution because there are too many parameters. But under certain conditions one solution can be applied to a variety of cases. Looking again at the equation of motion, Eq. (2). The following transformations leave the equation unchanged:

$$r^* = Kr;\ I^* = K^2 I;\ \dot{r}^* = K\dot{r} \tag{10}$$

$$E^* = KE;\ \dot{z}_o^* = \dot{z}_o \sqrt{K};\ I^* = K^{3/2} I;\ t^* = \frac{t}{\sqrt{K}};\ \dot{r}_o^* = \dot{r}_o \sqrt{K} \tag{11}$$

$$t^* = Kt;\ r^* = Kr;\ Z^* = KZ;\ E^* = \frac{E}{K} \tag{12}$$

The author is indebted to Mr. F. M. Charbonnier of Field Emission Corporation for Eqs. (10) and (11).

COMPUTATION OF THE SPACE CHARGE SPREADING OF AN

ELECTRON BEAM UNDER ACCELERATION

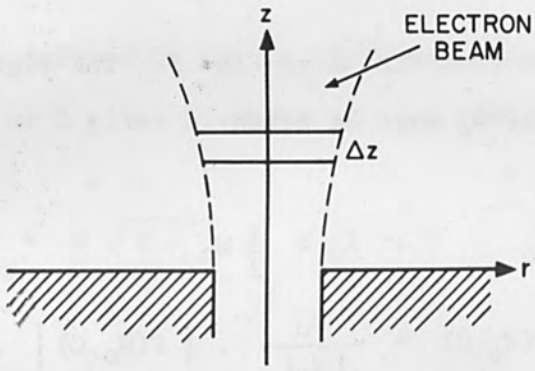

FIGURE 1 Geometry for Space-Charge
Spreading of a Beam in an Electric Field

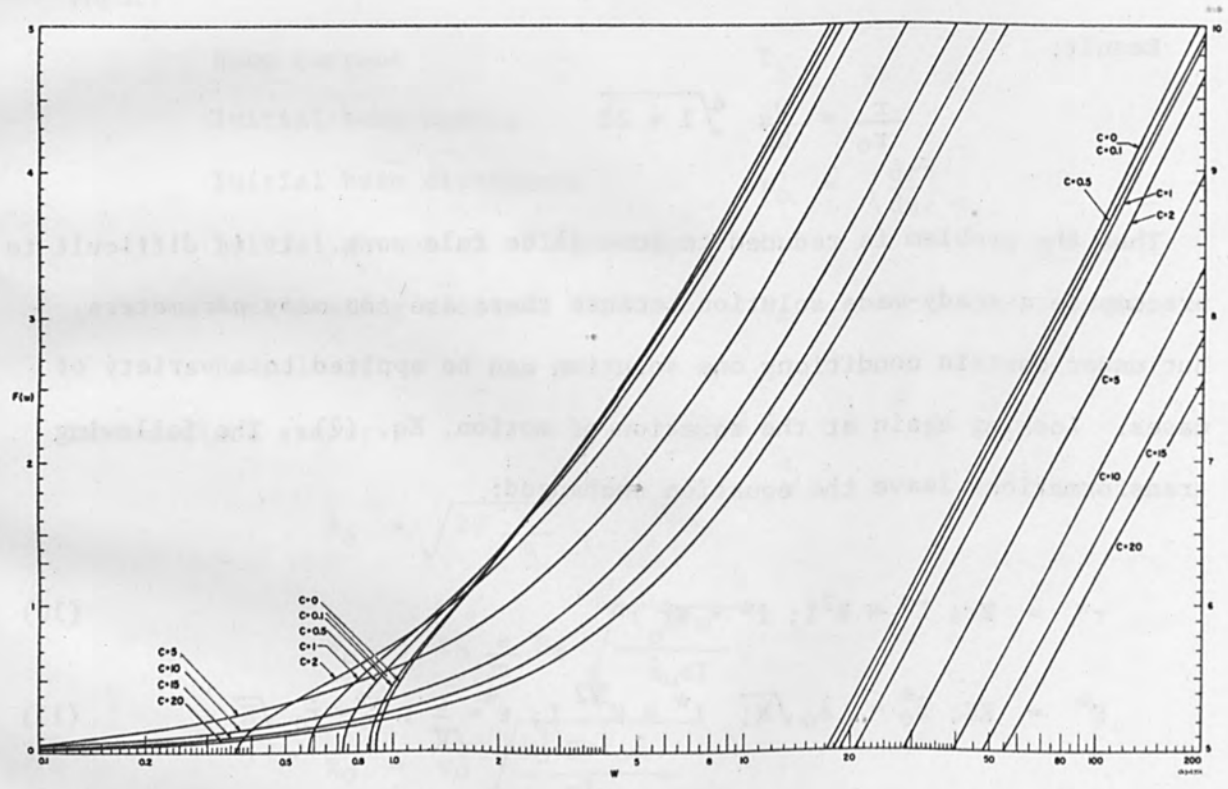

FIGURE 2

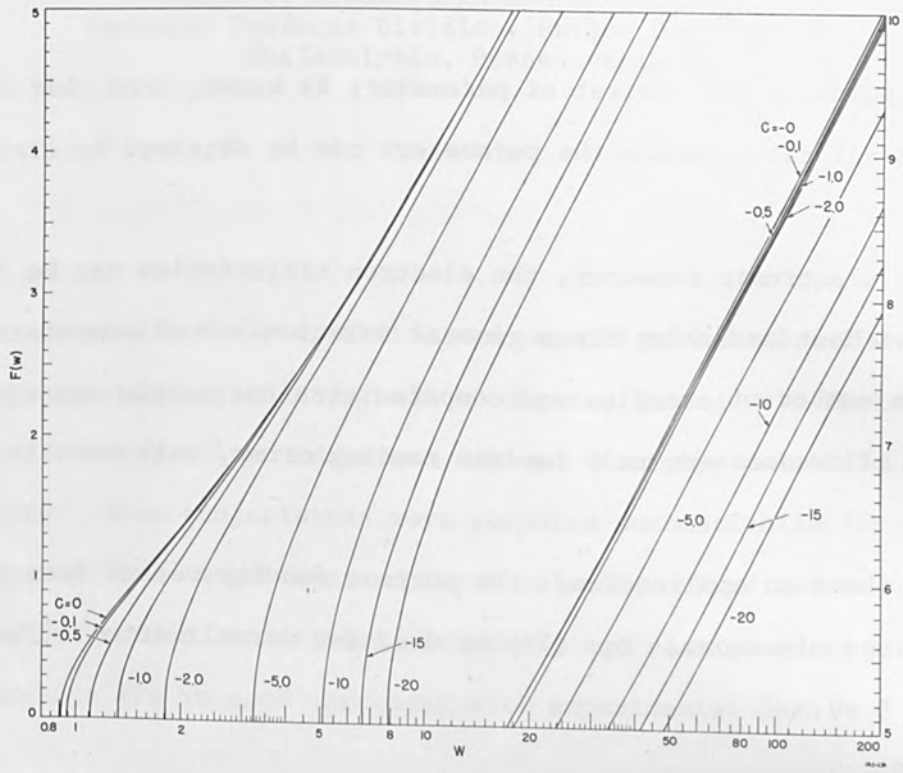

FIGURE 3

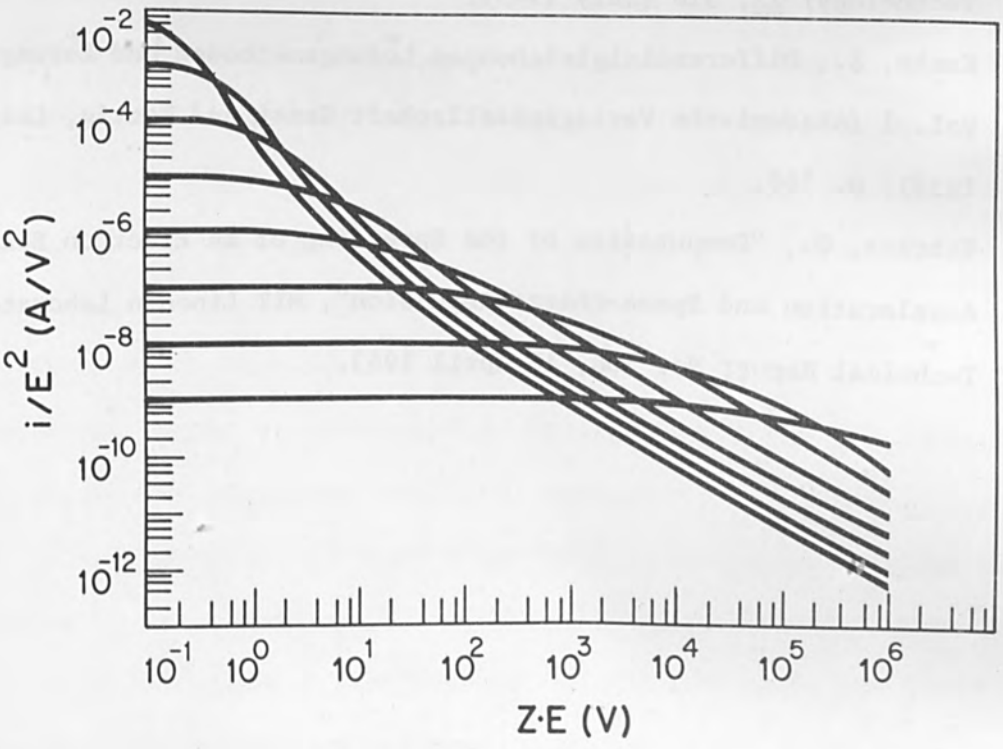

FIGURE 4 Current Density vs Beam Length for Field Emitted Electrons

If the solution for one set of parameters is known, then this solution applies to all cases, where the parameters can be obtained by transformation.

With an electronic computer, the electron trajectories can be determined directly without searching for a general solution. Such computations were made for a number of examples and compared with the method described here. If allowances are made for the reading error, both results are equal.

Fig. 4 shows an application: the current density versus beam length for field emitted electrons. Eq. (12) is used for normalization. The initial energy is 5 eV.

REFERENCES

1. Moss, H., "A Space Charge Problem," Wireless Engineer (Electronic Technology) 22, 316 (July 1945).
2. Kamke, E., Differentialgleichungen Lösungsmethoden und Lösungen, Vol. 1 (Akademische Verlagsgesellschaft Geest and Portig, Leipzig, 1959), p. 568.
3. Vibrans, G., "Computation of the Spreading of an Electron Beam Under Acceleration and Space-Charge Repulsion", MIT Lincoln Laboratory Technical Report No. 308, 18 April 1963.

COMPUTER DETERMINATION OF ELECTRON PATHS IN MAGNETIC DEFLECTION FIELDS

Ralph A. Bloomsburgh and James King
Consumer Products Division, Philco Corporation
Philadelphia, Pennsylvania

ABSTRACT

This paper describes the preparation and results of a Philco 2000 digital computer program for calculating electron paths in magnetic fields of two-dimensional symetry. Input data was derived from physical field plotting measurements. Beam trajectories were computed automatically for selected repetitions of field magnitude and input velocity. Predictions of beam clearance, deflection sensitivity, linearity and scan geometry in television displays are in good agreement with experimental data.

COMPUTER DETERMINATION OF ELECTRON PATHS IN MAGNETIC DEFLECTION FIELDS

INTRODUCTION

A method for determining the path of an electron beam which is subjected to the non-uniform magnetic deflection field of a given physical device is described. Such information is useful for understanding and predicting the behavior of electron beam systems especially when wide deflection angles are involved, as for example, in television displays.

There are two main questions to be answered. First, what is the magnetic field produced by the device at all points in the space to be traversed? Second, given the input direction and velocity of the electron, what are the coordinates of its path? Should accurate trajectories be required, the field determination can become quite awkward theoretically, but is less difficult experimentally. Finding the path once the field is known is straightforward theoretically involving only a large number of calculations. Direct experimental measurements of complete electron beam paths are usually impractical and consequently an approach was taken combining an experimental probe technique with a digital computer program for calculating the beam path coordinates.

The beam deflection problem in a television cathode ray tube is illustrated in Fig. 1. The electron beam emitted by the gun enters the magnetic yoke field along the Z-axis with a velocity determined by the accelerating voltage. It follows a curving path through the yoke region and eventually strikes a point P on the tube face. It is of practical interest to know how the location of P depends on the magnetic field strength and shape, and whether or not the beam clears the neck of the evacuated envelope at maximum deflection. This data can be used to predict deflection sensitivity and scanning geometry errors such as non-linearity and pincushion

distortions. The nature of a typical yoke magnetic field is shown in Fig. 2. The magnetic flux pattern is non-uniform as indicated in the view of the X-Y plane taken near yoke center. Furthermore the shapes of the X-Y patterns vary continuously along the Z-axis as shown by the flux distribution curve.

These field shapes are functions of the yoke winding and core geometry. The vertical deflection coils show similar effects and deflection fields for oblique planes are, of course, vector superimpositions of the horizontal and vertical patterns.

The procedure set up to solve this complex problem is illustrated in the block diagram of Fig. 3. The experimental phase consists of measuring the field at all points of interest. The computer phase comprised setting up the equations in algebraic form, transcribing the data to punched cards, and preparing a set of exact instructions to tell the computer how to operate on the data, print out the results, etc. The program deck and data cards are fed to the computer and, if all goes well, the correct path coordinates are printed out. The procedure for these two phases will be described.

EXPERIMENTAL MEASUREMENTS

The equipment for making point-by-point measurements of the magnetic field is shown in Fig. 4. The yoke and probe are mounted via non-magnetic supports to the adjustable carriages of an optical bench. The probe is of the Hall effect type. The indium arsenide sensing element is about 2mm by 4mm with a thickness of 0.5mm. The voltage generated by the probe is proportional to the magnetic field component perpendicular to the blade, and reads directly in gauss. A precision milliammeter measures the current in the yoke windings. The limits of precision attainable with the present

apparatus are estimated to be 0.2mm for probe position, 0.5% for yoke current and about 1% for the magnetic field. A close-up view of the probe is shown in Fig. 5. No attempt was made to compensate for the earth's field since it was desired to include this background contribution in the problem under investigation.

The experimental procedure comprised first aligning the yoke and probe axes for coincidence and then traversing horizontal, vertical and diagonal planes with the appropriate yoke windings energised. Typical data for a standard television yoke is shown in Fig 6 where the flux variation along the Z-axis is plotted for the horizontal, vertical and diagonal cases. The asymmetry of these curves is due to the flared exit end of the 114° yoke. This axial data while indicative of the field is not used in the proposed method since the beam obviously departs from the axis on passing through the yoke. The off-axis data for the horizontal case is given in Fig. 7. This shows the field produced by a yoke current of 300 ma. as a two-dimensional array in the X-Z plane. Values are entered at 2mm intervals in each direction. Although only a few are shown in this figure the actual number of data boxes tabulated is typically 800 for one plane. As will be discussed later the computer must be instructed how to select the right boxes during its calculations. The nature of the off-axis field for the horizontal and vertical windings is illustrated more clearly by Fig. 8. The curves of flux density are shown for planes near the rear, middle and front cross-sections of the yoke. Similar arrays are compiled for the vertical and diagonal cases. The experimental magnetic field data thus acquired is used in conjunction with the set of equations discussed in the next section.

COMPUTER DETERMINATION OF ELECTRON PATHS IN MAGNETIC DEFLECTION FIELDS

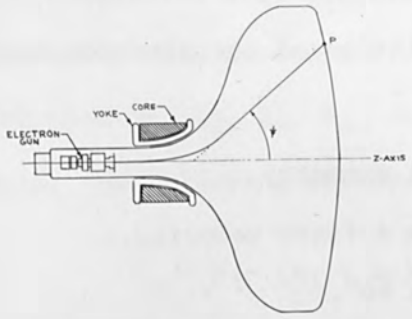

FIGURE 1 Electron Beam Deflection Problem

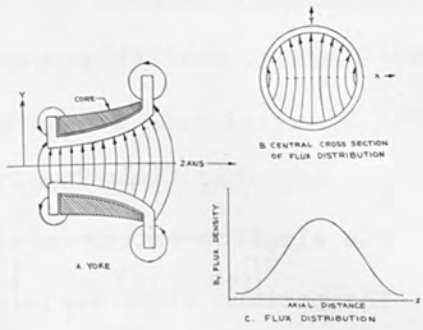

FIGURE 2 Nature of Yoke Fields

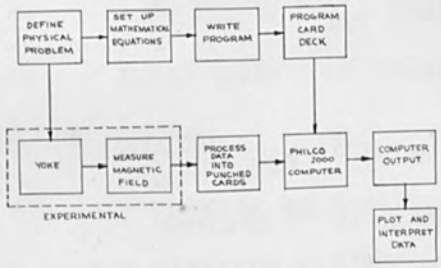

FIGURE 3 Block Diagram of Procedure

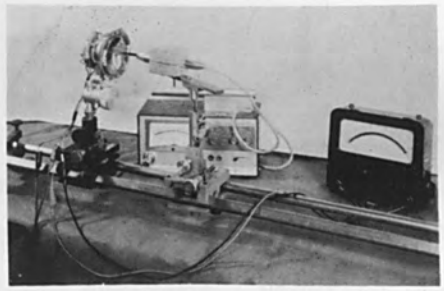

FIGURE 4 Set Up for Mapping Magnetic Flux Distribution

FIGURE 5 Close Up of Probe and Yoke

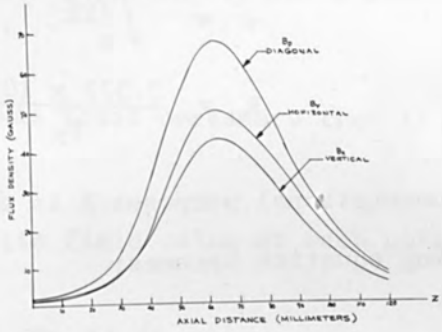

FIGURE 6 Axial Flux Distribution

COMPUTER DETERMINATION OF ELECTRON PATHS IN MAGNETIC DEFLECTION FIELDS

BEAM TRAJECTORY EQUATIONS

The following conditions govern the calculation of the electron trajectory:

1. The magnetic field has two-dimensional symmetry.
2. The electron enters on the Z-axis with a fixed velocity.
3. The maximum slope angle of the path is 90^{o}.

The method used to calculate the path was to divide the yoke field into a large number of incremental strips along the Z-axis. Within any given strip the field was assumed to be constant, and hence the electron would travel a circular arc of radius R given by Eq. (1).

$$R_n = \frac{mv}{eB_n} \tag{1}$$

m = Electron mass 9.108×10^{-31} kg.

e = Electron charge 1.602×10^{-19} coulomb

v = Electron velocity in meters/sec.

B = Magnetic flux density in weber/m^2

n = Strip index no. (1,2,3,.....k)

For an accelerating voltage E:

$$v = \sqrt{\frac{2eE}{m}} \quad \text{, so that}$$

$$R_n = \frac{3.372 \times 10^{-6} \sqrt{E}}{B_n} \text{ meters} \tag{1a}$$

For computational purposes R is expressed millimeters and B is in gauss. The working equation becomes:

$$R_n = \frac{33.72 \sqrt{E}}{B_n} \text{ millimeters} \tag{2}$$

The successive arcs calculated by Eq. (2) are blended together by trigonometry (See appendix A) as indicated in Fig. 9. The lateral displacements, X_1, X_2, X_3, X_n, are then calculated for each interval. For example, the following expression holds for the third interval:

$$X_3 = R_1 - (x_1 + x_2) - \sqrt{(R_3)^2 + \left[Z_3 - (z_1 + z_2)\right]^2}$$

where X_3 and Z_3 are the path coordinates, R_1 and R_3 are the radii for the first and third intervals and the lower case x and z quantities account for the shifting centers of curvature of the arc segments.

The nth term is given by:

$$X_n = R_1 - \sum_{n=1}^{k} x_{n-1} - \sqrt{R_n^2 - \left[Z_n - \sum_{n=1}^{k} z_{n-1}\right]^2}$$

where k = total number of intervals.

COMPUTER PROGRAM

The main purpose in developing the computer program was to obtain a plot of the electron trajectory with speed and accuracy. Previous work with a desk calculator took 16 hours for one ray. By contrast, the same experimental field data can be prepared for the computer in less than two hours and a ray computed in a matter of seconds. Furthermore the initial conditions and yoke currents can be varied artificially and a number of rays computed in a few minutes.

In planning the computer program it was found necessary that it perform the following specific functions:

1. Select the proper magnetic field value at each point of the array.
2. Compute each path radius from the selected field and the given input velocity.

COMPUTER DETERMINATION OF ELECTRON PATHS IN

MAGNETIC DEFLECTION FIELDS

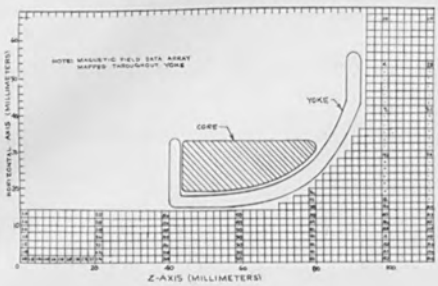

FIGURE 7 Horizontal Field Data Array

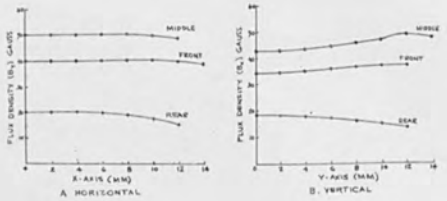

FIGURE 8 Off-Axis Field

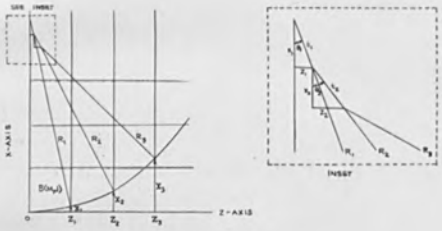

FIGURE 9 Electron Path Through Three Incremental Areas

Z (MM)	B (GAUSS)	RADIUS (MM)	X (MM)	XIN (INCHES)
2.	1.0000	0.246833340+004	0.810269541-003	0.319002161-004
4.	1.1000	0.225815260+004	0.331614402-002	0.130557638-003
6.	1.3000	0.205861544+004	0.768268108-002	0.302467759-003
8.	1.4400	0.185125005+004	0.141046047-001	0.555299398-003
10.	1.6000	0.166612504+004	0.228075981-001	0.897036934-003
12.	1.7800	0.149764049+004	0.340464115-001	0.134040990-002
14.	2.0400	0.135676474+004	0.481513739-001	0.189572338-002
16.	2.3800	0.112004846+004	0.655727386-001	0.258160388-002
18.	2.7400	0.972919733-003	0.868358612-001	0.341873469-002
20.	3.2500	0.820246175+003	0.112594088+000	0.443283498-002
22.	3.7400	0.708869380+003	0.142612842+000	0.561424467-002
24.	4.5000	0.592400015+003	0.190831432+000	0.751034773-002
26.	5.4300	0.489137627+003	0.229519776+000	0.887873139-002
28.	6.5800	0.405136788+003	0.279241880+000	0.109937717-001
30.	7.9000	0.337443046+003	0.343841910+000	0.135370831-001
32.	9.5000	0.280610533+003	0.421521187+000	0.165953233-001
34.	11.6000	0.229915260+003	0.519229291+000	0.202844603-001
36.	14.2000	0.187732399+003	0.628515009+000	0.247446852-001
38.	17.2000	0.154988376+003	0.765502572+000	0.301378965-001
40.	20.4000	0.130674674+003	0.930944324+000	0.366513913-001
42.	24.0000	0.111075003+003	0.113011718+001	0.444928033-001
44.	28.0000	0.952871453+002	0.136901391+001	0.538981853-001
46.	32.2000	0.827888220+002	0.165425420+001	0.651281180-001
48.	36.0000	0.740900019+002	0.199025024+001	0.783469308-001
50.	39.5000	0.674886093+002	0.239041471+001	0.941181155-001
52.	42.5000	0.627247075+002	0.285415184+001	0.112368183+000
54.	45.5000	0.585890125+002	0.339022338+001	0.133473362+000
56.	47.5000	0.561221067+002	0.400493979+001	0.157674795+000
58.	49.5000	0.538854868+002	0.472456666+001	0.185219171+000
60.	50.5000	0.527681202+002	0.549541235+001	0.216354817+000
62.	51.0000	0.522705896+002	0.638342953+001	0.251316133+000
64.	50.5000	0.527681202+002	0.737416816+001	0.290321581+000
66.	50.0000	0.533160013+002	0.847322819+001	0.333591582+000
68.	49.0000	0.544240832+002	0.968617864+001	0.381339159+000
70.	48.5000	0.549640498+002	0.110022316+002	0.433949551+000
72.	47.0000	0.567191584+002	0.124882405+002	0.491663011+000
74.	45.0000	0.592400015+002	0.140924042+002	0.554819065+000
76.	41.5000	0.650179138+002	0.159397388+002	0.627511766+000
78.	41.5000	0.642361462+002	0.177405567+002	0.698647115+000
80.	37.0000	0.720486505+002	0.198056438+002	0.779749756+000
82.	35.0000	0.761657162+002	0.220416493+002	0.867781470+000
84.	33.0000	0.808600023+002	0.244930046+002	0.964216716+000
86.	27.0000	0.987333358+002	0.272394081+002	0.107245436+001
88.	24.0000	0.111075003+003	0.298038104+002	0.117337836+001
90.	21.5000	0.123990781+003	0.327486479+002	0.128931685+001
92.	17.5000	0.152331432+003	0.358683834+002	0.141214108+001
94.	14.0000	0.190414291+003	0.391463991+002	0.154139568+001
96.	11.0000	0.242345461+003	0.429631359+002	0.169171401+001
98.	8.0000	0.333225008+003	0.460944134+002	0.181474088+001
100.	5.0000	0.533110013+003	0.497092162+002	0.195705967+001
102.	4.0000	0.666455017+003	0.533446334+002	0.210179722+001
104.	3.3000	0.807818202+003	0.571109958+002	0.224844627+001
106.	1.0000	0.226580007+004	0.606868919+002	0.239638157+001
108.	1.0000	0.466580007+004	0.644397204+002	0.254487088+001
110.	1.0000	0.466580007+004	0.684260068+002	0.269393736+001
112.	1.0000	0.466580007+004	0.722278913+002	0.284358627+001

SCALE(K)	EA	ZOIN	TOAPSI	ENDMT
1.600	16000.	6.00000	1.98054	14.24683

FIGURE 10 Computer Print Out

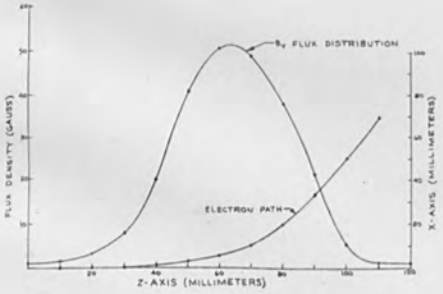

FIGURE 11 Electron Path in Horizontal Plane and Magnetic Field

3. Blend successive radii for common tangents.

4. Compute the lateral displacement from the Z-axis at each point.

5. Determine the final slope of the ray and its intercept with a plane located at the tube face.

6. Repeat all of the above for different specified yoke currents.

7. Repeat all of the above for different specified anode voltages.

8. Provide safeguards if an electron jumps out of the array because the field is too strong or the anode voltage too low.

9. Print out for each Z-axis coordinate the field selected, the path radius and the lateral displacement.

10. Print out for each trajectory the yoke current scale factor, anode voltage, final ray angle and final intercept at the tube face plane.

The final print-out form of Fig. 10 shows a sample tabulation of the results. From this, the trajectory is readily plotted as in Fig. 11.

The major steps in digital computer programming are selecting the computer, devising a flow chart of the mathematical and logical operations required to solve the problem, converting the flow chart operations into a formal computer language and running the computation. The computer used for this problem was the Philco 2000 which has a core memory capacity of 32,768 locations and an access time of one microsecond. The native language of this computer is called ALTAC.

The flow chart of Fig. 12 represents all of the operations needed to implement the required program functions previously discussed. The input

data contains values for the axis position (Z), the magnetic field (B), anode voltage (E), yoke current (I) and tube face position (ZDIS). The yoke current enters as a multiplying scale factor on all B values since the field was found to be linear with current for the yoke tested, i.e., core saturation was negligible because of the large air gap. The first blocks of the chart advise the computer of the input and its form. It sets up subscripts on each variable for indexing purposes so that every item of data can be identified later. The next block selects the first anode voltage and sets up a loop to permit repetition for all other input voltages specified. The next block operates similarly for the yoke input current scale factors. The third loop is started for the first Z interval and assigns the first B value in the array. From here on the first values of R and X are computed from the equations and then printed out. A test is then made for the electron position to determine if the trajectory is finished and, if not, then which B value should be selected from the array for the next calculation. The third loop is repeated over and over through all the Z intervals, usually about 60 times, until the last given Z value signals the end of the trajectory. At this point the final slope and ray height are calculated and printed out. The computer then takes the next current value and the entire operation is repeated until all the current values are used. Control is then returned to the anode loop which then repeats the entire sequence until all voltages have been selected. At this stage all calculations are complete and the requested quantities printed out, thus ending the program.

There are, however, certain contingencies which must be provided for. For example, if the electron leaves the array before the terminal Z value, corresponding to over deflection, the program senses this, resets the

indexing counters and jumps to the next trajectory calculation. A second contingency can occur if the path angle exceeds 90^{o}, in which case some of the square root functions can go negative. The program tests for this and bypasses such a result.

After the flow chart appears to be functionally completed and free of any errors which the computer may find, the next step is to prepare a full program in the ALTAC language. This comprises a set of detailed coded statements written to a precise format. The YOKEPLOT program contains about 70 statements which cover the functions of the data input, the mathematical operations, the logical decisions and the data output. These statements are shown in Figs. 13a, b and c. The first 22 statements start the computer, reserve memory space, define the input data quantities, specify the exact format for the input numbers on the punched cards and also the exact print-out instructions. The three statements headed by the instruction "DO" represent the loop starting points. The three CONTINUE statements near the end of the program are the loop ending points. The other portions of the program are concerned with the mathematical operations and tests. The latter appear as IF statements that switch control to various program statements depending on the outcome of a comparison between two variables. The quantities I, J, K, L, and M are either subscripts or counters which serve to index the repetitive operations.

The program statements, one per punched card, form a program deck which is first tested on the computer along with data from a known case. If the computer rejects it because of disallowed statements, logical fallacies or other reasons a period of program checking may follow. Once the program operates successfully it is then combined with real data cards and is run for actual results. In the YOKEPLOT program the computer run time for one

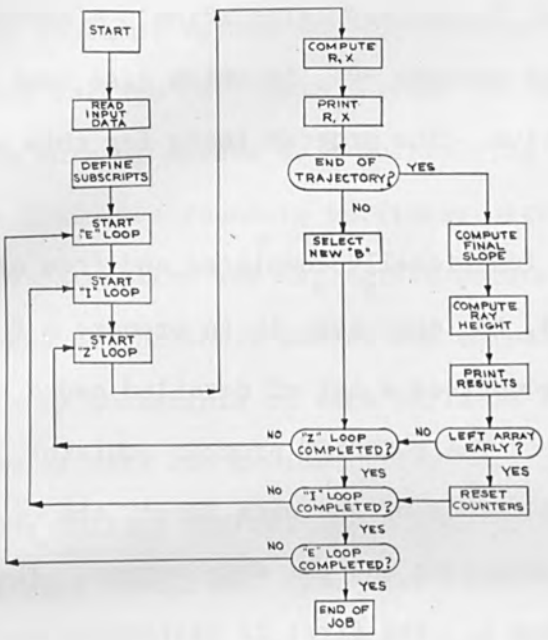

FIGURE 12 "Yokeplot" Flow Chart

```
1          JOB
2   ABS    ALTAC MAGTAPE, LIB
3 I        YOKEPLOT
4          DIMENSION B(200, 50), Z(200), EA(5), X(200), XIN(200),
5                    R(200), SCALE(50) $
6          READ INPUT TAPE 11, FMT1, N1, N2, N3, N4, N5, N6 $
7          READ INPUT TAPE 11, FMT2, ((B(I, J), I=1, N1), J=1, N2) $
8          READ INPUT TAPE 11, FMT3, (Z(I), I=1, N3) $
9          READ INPUT TAPE 11, FMT4, (EA(I), I=1, N4) $
10         READ INPUT TAPE 11, FMT5, ZDIS $
11         READ INPUT TAPE 11, FMT2, (SCALE(K), K=1, N6) $
12  FMT1   FORMAT (6I8) $
13  FMT2   FORMAT (10F8.3) $
14  FMT3   FORMAT (20F4.0) $
15  FMT4   FORMAT (5F8.0) $
16  FMT5   FORMAT (1F8.4) $
17  FMT6   FORMAT (1H1, 6X6HZ(MM), 4X9HB(GAUSS), 5X11HRADIUS(MM),
18                 12X6HX (MM), 10X12HXIN (INCHES)) $
19  FMT7   FORMAT (1H , F10.0, F12.4, 3E20.9) $
20  FMT8   FORMAT (1H0, 5X8HSCALE(K), 5X2HEA, 18X4HZDIS,
21                 14X6HTOAPSI, 15X5HENDPT) $
22  FMT9   FORMAT (1H , F13.3, F9.0, 3F20.5) $
23         SUMEXX = 0.0 $
24         SUMZEE = 0.0 $
25         J = 1          $ ROW NUMBER
26         S = 2.0        $ MILLIMETERS OFF AXIS
27         MRFR = 1       $ REFERENCE VALUE FOR TEST
```

FIGURE 13a Computer Program in ALTAC Language

```
28         DO (ADVA) L=1, N4          $ START LOOP A
29         VOLT = SQRTF(EA(L))        $
30         DO (ADVB) K=1, N6          $ START LOOP B
31         PRINT (FMT6)               $ PRINT TITLES
32         DO (ADVC) M=1, N1          $ START LOOP C
33         ZAXIS = Z(M)               $
34         FLUX = SCALE(K) * B(M, J)  $
35         R(M) = 33.72 * VOLT / FLUX $
36         IF (M) E (MRFR), GO TO ALPHA  $
37         THYPO = R(M-1) - R(M)      $
38         SOHPHI = (Z(M-1) - SUMZEE / R(M-1)$ CALCULATE SINE
39         CAHPHI = SQRTF(1.0 - SOHPHI**2)  $ CALCULATE COSINE
40         EXX = THYPO * CAHPHI       $
41         SUMEXX = SUMEXX + EXX      $
42         ZEE = THYPO * SOHPHI       $
43         SUMZEE = SUMZEE + ZEE      $
44 ALPHA   ZS = ZAXIS - SUMZEE        $
45         RMZS = R(M) * R(M) - ZS * ZS  $
46         IF (RMZS) 70, 5, 5         $
47  5      X(M) = R(1) - SUMEXX - SQRTF(RMZS)  $
48         XIN(M) = X(M) / 25.4       $
49         PRINT (FMT7), Z(M), B(M, J), R(M), X(M), XIN(M) $
50         IF (M-N1) 10, 20, 70       $ TEST FOR LAST CALCULATION
51  10     IF (X(M) - S) 40, 50, 50   $ TEST POSITION OF ELECTRON
52  50     S = S + 2.0                $ ADVANCE OFF-AXIS SUBSCRIPT
53         J = J + 1                  $ ADVANCE ARRAY SUBSCRIPT
```

FIGURE 13b Computer Program in ALTAC Language

```
54         IF (J - N2) 60, 60, 20     $ TEST FOR J INSIDE DATA ARRAY
55  60     IF (X(M) -S) 40, 50, 50    $ TEST FOR ELECTRON POSITION
56  40     GO TO ADVC                 $
57  20     TOAPSI = (X(M) - X(M-1))/(Z(M) - Z(M-1))  $
58         ENDPT = ZDIS * TOAPSI + XIN(M)  $
59         PRINT (FMT8)               $ PRINT TITLES
60         PRINT (FMT9), SCALE(K), EA(L), ZDIS, TOAPSI, ENDPT  $
61         IF (M - N1) 70, 40, 70     $
62  ADVC   CONTINUE                   $ CONTINUE LOOP C
63         GO TO 90                   $
64  70     M = 1                      $ RETURN J TO INITIAL VALUE
65  90     S = 2.0                    $ RETURN S TO INITIAL VALUE
66         SUMEXX = 0.0               $ RETURN SUMEXX TO INITIAL VALUE
67         SUMZEE = 0.0               $ RETURN SUMZEE TO INITIAL VALUE
68  ADVB   CONTINUE                   $ CONTINUE LOOP B
69  ADVA   CONTINUE                   $ CONTINUE LOOP A
70         STOP                       $
71         END                        $
```

FIGURE 13c Computer Program in ALTAC Language

field array with 10 current values and 3 anode voltages took 1.2 minutes.

RESULTS

The electron path found by the computer is shown in Fig. 14. The boxes marked in the field array are those selected by the computer during its run. In Fig. 15 the final ray angles and end points for several currents are superimposed on a tube drawing. Projection of the rays back to the Z-axis show there is no common "center of deflection" as indicated by the ray pattern in the yoke region. Close inspection of the data indicates that the shift in the apparent center of deflection with field strength is not monotonic but tends to oscillate. The enlargement of the projected ray pattern in Fig. 16 reveals this more clearly. The total spread of the axial intercepts is about 12mm which represents 15% of the yoke length. This oscillation effect with increasing deflection is believed due to the non-uniform off-axis field. It is believed that this effect has not been previously reported in the literature.

The intercepts with the actual tube face are located graphically and from these the desired information about the deflection properties of the system can be found. For example, Fig. 17 shows a comparison between the computed and experimentally determined spot positions for a 19" television display operating at 16kv. The horizontal deflection measured (along the tube face arc) is plotted versus d c horizontal yoke current. The upward non-linearity is characteristic of wide-angle displays. Agreement between computed and measured spot positions is within 3%. The vertical and diagonal runs agreed within 4%. At extreme deflection angles measurements of shadowing by the neck contour showed similar agreement with the computed data. For a known neck contour this permits a check on the actual beam path inside the yoke.

Fig. 18 shows the pincushion shape of the raster. The computed spot positions fell within 1/8" of the measured values and predicted slightly more horizontal and less vertical pincushion than the actual distortions. The pincushion correction magnets had been removed from the yoke prior to the field measurements in order to evaluate the coil fields alone. The removal of auxiliary permanent magnets however is not an essential requirement of the method. Combined permanent magnet and electro-magnetic systems which have symmetry with respect to the deflection plane can be mapped and computed provided that the total field array is measured for each yoke current.

CONCLUSIONS

A method for determining the electron path in non uniform magnetic deflection fields by a combined field plotting and computer technique has been described. Application of the method to a standard television yoke yielded data on beam deflection angle and position as a function of yoke current and anode voltage. Experimental tests of beam position with the same yoke on a 19" cathode ray tube indicated agreement with the computer results to within 4%. Since this approaches the experimental error of normal display tests it was concluded that the method is useful for predicting the deflection properties of yokes independently of the display environment. It also appears feasible to evaluate rapidly the effects of changing system parameters by modifying the computer input data. In addition the computer program itself offers the possibility of testing the electron behavior in postulated deflection fields and this assists in the prediction of design performance for systems using magnetic deflection. The computer program is available from the authors through the courtesy of Philco Corporation.

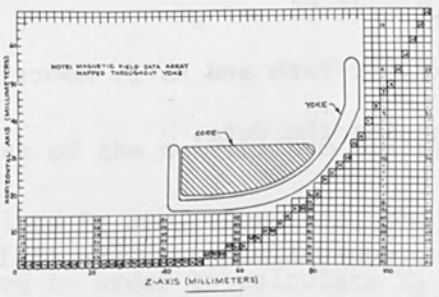

FIGURE 14 Horizontal Field Data Array with Computer Selected Values

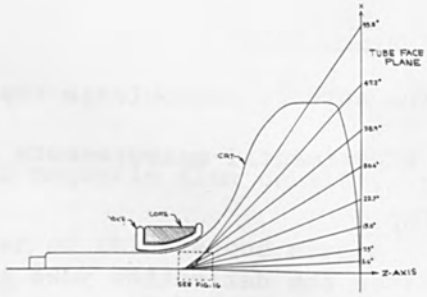

FIGURE 15 19" CRT with Final Electron Slopes in Horizontal Plane

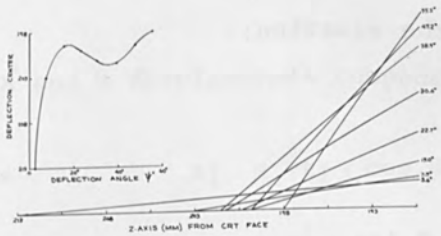

FIGURE 16 Expanded View of Deflection Centers for Various Electron Trajectories for Increasing Deflection Angles

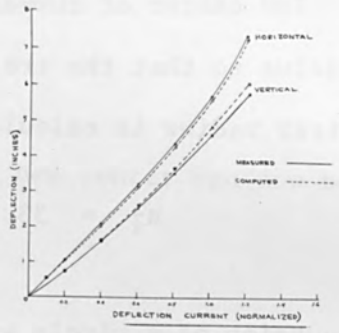

FIGURE 17 Scan Linearity

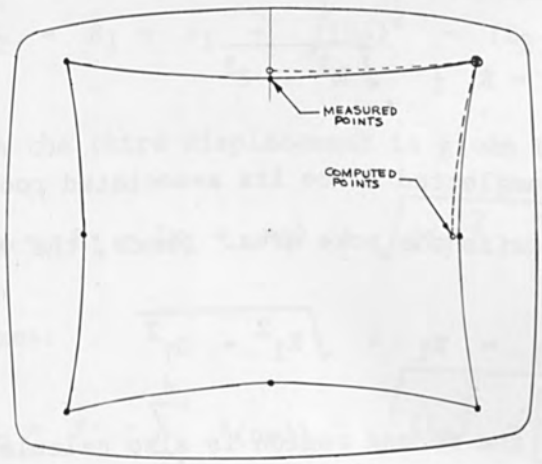

FIGURE 18 Raster Scan Geometry

ACKNOWLEDGEMENTS

The authors acknowledge the work of R. F. Fath and R. F. Moors in making the experimental measurements and processing the data.

APPENDIX

Since the deflection yoke generates a non-uniform magnetic field, the Z-axis is divided into incremental regions of approximately uniform flux density. Thus, the electron trajectory is found by computing the successive radii of the path of the electron as it progresses through these regions. The center of curvature of each arc is made to lie on the preceding radius so that the trajectory is smooth as shown in Fig. 9.

The first radius is calculated from the equation:

$$R_1 = 33.72 \frac{\sqrt{E_a}}{B_1} \tag{1}$$

The equation of a circle with radius R is:

$$(X-h)^2 + (Z-k)^2 = R^2 \tag{2}$$

Since h = R and k = 0, then

$$X = R \pm \sqrt{R^2 - Z^2} \tag{3}$$

The plus sign is neglected since its associated root would cause the value of X to lie outside the yoke area. Hence, the value of X_1 is:

$$X_1 = R_1 - \sqrt{R_1^2 - Z_1^2} \tag{4}$$

The radius R_2 for the second region is also calculated with the measured value of flux density in this region:

$$R_2 = 33.72 \frac{\sqrt{E_a}}{B_2} \tag{5}$$

Because of the non-uniform distribution of magnetic flux density, R_2 is not equal to R_1 and, therefore, the new center of this second circle must be located in order to calculate X_2. This is accomplished in the following steps.

$$t_1 = R_1 - R_2 \tag{6}$$

$$\sin \theta_1 = \frac{Z_1}{R_1} \tag{7}$$

The x and z displacement components of the new center can now be found:

$$x_1 = t_1 \cdot \cos \theta_1 \tag{8}$$

$$z_1 = t_1 \cdot \sin \theta_1 \tag{9}$$

Therefore, the value of X_2 may now be calculated:

$$X_2 = R_1 - x_1 - \sqrt{(R_2)^2 - (Z_2 - z_1)^2} \tag{10}$$

In similar fashion the third displacement is given by:

$$X_3 = R_1 - (x_1 + x_2) - \sqrt{(R_3)^2 - \left[Z_3 - (z_1 + z_2)\right]^2} \tag{11}$$

The nth term becomes:

$$X_n = R_1 - \sum_{n=1}^{k} x_{(n-1)} - \sqrt{(R_n)^2 - \left[Z_n - \sum_{n=1}^{k} z_{(n-1)}\right]^2} \tag{12}$$

where:

n = 1, 2, 3, ...k

k = total no. of incremental regions

The above expressions are subject to the following conditions:

1. The electron enters on the Z-axis
2. The field is symmetrical about the X-Z plane, for example, it must be orthogonal to the deflection plane.
3. The maximum slope angle must not exceed 90^{o}.
4. The magnetic field must not become zero.

These conditions are usually satisfied by practical yoke fields.

ANALYSIS OF A COLLIMATED HOLLOW CATHODE DISCHARGE

J. H. Terhune and L. H. Stauffer
Advanced Technology Laboratories, General Electric Company
Schenectady, New York

ABSTRACT

The physical mechanisms of the hollow cathode electron beam source are discussed using a steady-state, one-dimensional theoretical treatment. A mathematical model is developed which relates phenomena internal to the cathode to phenomena in the external cathode fall. Numerical solution of the resulting system of equations is required in order to obtain expressions for the beam current dependence on cathode voltage and gas pressure. The general nature of the solution is indicated for several gases by experimental data on cathode characteristics.

ANALYSIS OF A COLLIMATED HOLLOW CATHODE DISCHARGE

INTRODUCTION

The high voltage cold hollow cathode electron beam source and some of its applications have been reported elsewhere[1-3]. The cathode used for this study is shown in Fig. 1, operating in the steady state beam mode. The cathode has operated at voltages between 10 kv and 50 kv. Gases used have been H_2, H_e, N_2, A_r, and air. Typical gas pressures have been between 3 microns and 200 microns of mercury.

The beam mode exhibits both voltage and pressure thresholds which are a function of the gas, cathode material, and geometry. The ground potential shield enclosing the cathode assists in stabilizing the beam mode of operation and improving its efficiency. At a sufficiently high pressure and voltage the beam mode is unstable, culminating in a negative-impedance arc.

Inside the cathode there exists a plasma which supplies the electrons for the beam. Electrons escaping through the beam aperture are accelerated across the cathode dark space and into the positive column in essentially a rectilinear flow. Nearly all the potential drop occurs across the dark space, and the discharge surrounding the cathode behaves in a similar manner to an abnormal glow.

The cathode face is heated by bombardment with fast ions and energetic neutrals created in charge-transfer collisions. The temperature of the cathode surface is well below that for thermionic emission to occur, and, the electric field is probably low enough such that Schottky and field emission from the cathode surface are negligible. Relatively large beam currents can be obtained from these hollow cathodes, the electrons being supplied from the internal plasma.

The objective of this paper is to shed some light on the mechanisms

sustaining the beam mode of operation, including the origin of the electrons, their trapping in the internal plasma, and the role of fast ions and neutrals in maintaining the plasma source. An expression is developed coupling the internal plasma to the external dark space, which can be analyzed by existing theories of the cathode fall and positive column for high voltage glow discharges. The resulting system of integro-differential equations can be solved iteratively to obtain expressions for the cathode characteristics.

PHYSICAL MECHANISMS

It is convenient to discuss the system in terms of three separate, but interdependent, parts: a) the internal plasma; b) the cathode fall; c) the external glow discharge. This discussion will be restricted to the internal plasma, since the cathode fall and external glow are treated extensively in the literature[4,5,6].

The plasma internal to the cathode may be thought of an an electron trap, or a potential-well populated by electrons and ions in thermal equilibrium. This plasma is relatively weakly ionized, with a plasma potential of typically a few hundred volts positive with respect to the cathode. The plasma is sustained by ionization of the gas caused by electrons originating at the cathode surface and fast ions and neutrals entering the cathode aperture from the dark space. The fast neutrals originate from charge-exchange collisions between fast ions and thermal atoms or molecules. Many such collisions may occur as an ion traverses the cathode fall and the internal plasma, leading to avalanches of fast neutrals.

The fast ions and neutrals enter the cathode aperture and carry the energy necessary to sustain the internal plasma. These particles possess energies in the kilovolt range and ionize and excite the gas as they

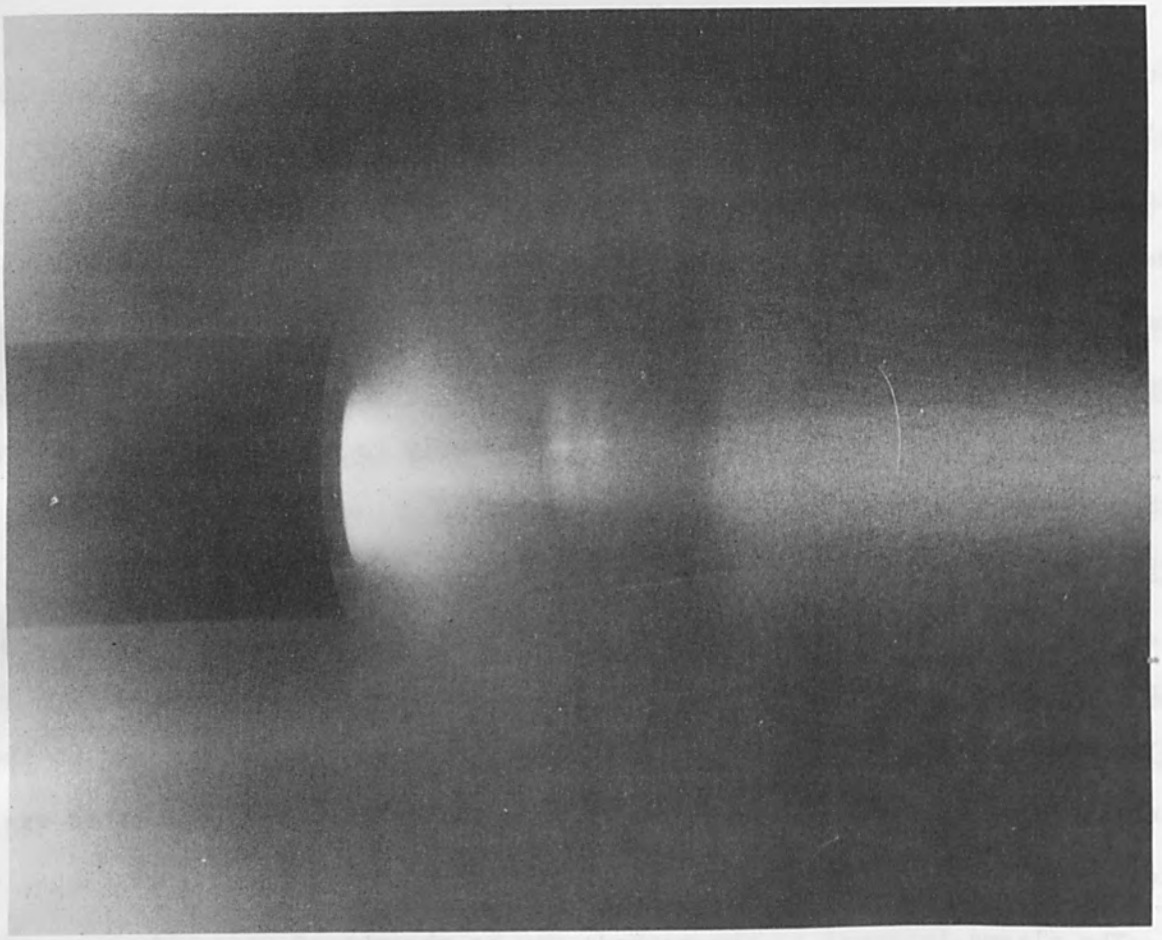

FIGURE 1 Shielded Hollow Cathode Operating in Beam Mode

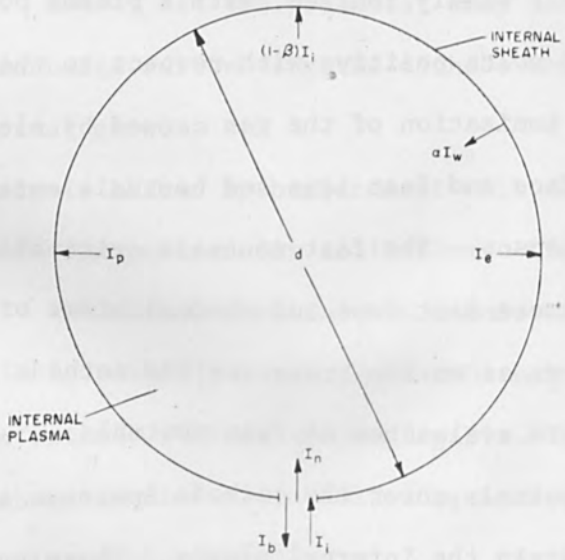

FIGURE 2 Schematic Representation of Internal Plasma

traverse the interior of the cathode. Furthermore, the fast ions continue to undergo charge-transfer collisions inside the cathode creating more fast neutrals and thermal ions. These thermal ions diffuse inside in the cathode and form the positive potential-well for the electrons. Thus, thermal ions are continually being pumped into the interior of the cathode from the external dark space.

The fast neutrals and some of the fast ions entering the cathode collide with its surface resulting in secondary electron emission. Thermal ions also diffuse to the plasma boundary, are accelerated across the internal sheath and continuously bombard the cathode surface with energies of a few hundred volts. Some secondary emission also occurs from these plasma ions. Furthermore, photo-emission at the cathode surface occurs due to the decay of some excited atoms and molecules in the plasma. Thus, an electron current emanates from the inside of the cathode walls as a result of photo-electric and secondary emission.

The electrons entering the plasma from the cathode have an initial energy distribution and are emitted nearly isotropically. However, they are immediately accelerated across the internal sheath toward the center of the plasma with the result that they enter the plasma with almost the energy corresponding to the sheath potential drop. This is very much greater than the initial emission energy. These fast electrons will traverse the plasma and strike the opposite cathode surface, where they re-combine with ions, unless some elastic or inelastic collision occurs in transit. If such an interaction takes place, there is an energy exchange in which the electron loses some of its kinetic energy, with the result that it is trapped within the plasma. It then loses more of its energy of formation and also that which it acquired in traversing the sheath

primarily by inelastic collisions with the gas. In this process the fast electrons ionize and excite the gas and quickly dissipate their excess energy to form an electron gas.

The probability that an electron emitted at the cathode surface will be trapped in the plasma is determined by the cathode geometry and the total inter-action mean-free-path for electrons in the gas. The latter quantity being function of the gas density and the electron energy as it enters the plasma (or the internal sheath drop). Actually, the trapping efficiency must be fairly high because of the rapid increase of the total cross section as the electron is slowed down in the sheath opposite to its point of origin. Of course, in an electron gas obeying Maxwell-Boltzmann statistics (which diffuse plasmas do) there is a statistical chance that some electrons will eventually acquire enough energy in collisions that they can escape from the potential-well. Such leakage is usually negligible for sheath-drops large compared to the mean electron energy in the plasma.

If the mean time between collisions of gas atoms is long compared to the excited state mean lifetime, each excited atom or molecule gives up its excitation energy in the form of a photon. Providing the gas is relatively transparent to such radiation, these photons release some electrons at the cathode surface by photo-emission. This photo-electric current is appreciable if the gas pressure is low (in the micron range) and if the quantum yield is appreciable. Ordinarily the quantum yield does not exceed five per cent or so, implying that a rather high density of excited states must exist in the plasma region for the photo-electric current to be a major contributor to the total cathode current. It is conceivable, however, that a fraction of the energy carried into the cathode by fast neutrals and ions can be trapped in the cathode through this mechanism of energy storage in

the excited states of the gas.

Plasma ions, or thermal ions, are created by ionization and charge transfer. Ion-electron recombination at these low pressures is negligible compared to diffusion losses of ions to the cathode walls, at least for cathodes with dimensions of a few centimeters. Therefore, the ion density in the plasma is maintained by these mechanisms.

The small amount of cathode heating is due to the absorption of radiation which does not produce photo-electrons, and also to the energy dissipated by internal and external ion bombardment. Some heating is also due to fast neutrals giving up a fraction of their kinetic energy as heat rather than in ejection of electrons. This heating effect is small for efficient cathodes, except at the cathode face.

At the cathode aperture there exists a relatively high concentration of ions due to the influx of ions from the dark space. The resulting space-charge fields extract electrons from the internal plasma by essentially lowering the height of the potential barrier an electron experiences in the vicinity of the aperture. Thus, electrons with sufficient energy to surmount this reduced barrier and with velocities directed such that they can emerge through the aperture are able to escape from the cathode to form the beam. The divergence of the beam and its stability are very sensitive to the space-charge fields near the aperture. Therefore, the size of the aperture, the thickness and shape of the face plate, and proximity of the shield are important factors in the beam collimation, stability and efficiency. The beam current is very sensitive to the height of the potential barrier and to the electron temperature. The aperture potential is determined by the local ion density, which is also a function of the gas density, temperature, cathode potential and ion current entering the dark

space from the positive column. The exact height of the aperture potential barrier may be found by an extension and modification of the theory of McClure and Kranzow[5].

ANALYSIS

The internal plasma will be treated as a spherically symmetric potential well for electrons. The height of the potential barrier is taken to be uniform except near the aperture, where it is lowered due to the influx of ions from the dark space. Macroscopically, the internal plasma remains electrically neutral; the conservation laws may be applied considering the plasma as an isolated system.

Referring to Fig. 2, current continuity requires:

$$I_b + I_e + \beta I_i = \alpha I_w + I_p \qquad (1)$$

where

I_b = electron beam current leaving plasma (amp)

I_i = fast ion current (amp)

I_w = cathode electron current (amp)

I_p = cathode ion current (amp)

I_e = electron diffusion current to cathode (amp)

The factor β accounts for injection of thermal ions by charge transfer and is given by:

$$\beta = 1 - \exp(-p.P_{ce}.d) \qquad (2)$$

where:

p = gas pressure (mm-Hg at $20^{o}C$)

P_{ce} = charge-exchange probability (cm^{-1} $mm\text{-}Hg^{-1}$)

d = effective plasma diameter (cm).

The factor α gives the fraction of electrons entering the plasma which are trapped.

$$\alpha = 1 - \exp(-p.P_t.d) \tag{3}$$

where:

P_t = total electron interaction probability (cm^{-1} $mm\text{-}Hg^{-1}$).

No net effect due to fast neutrals occurs in (1), since creation of ion-pairs by these particles leaves the plasma neutral.

The thermal ion diffusion current to the cathode is given by the kinetic theory:

$$I_p = n_o .e.A. \sqrt{\frac{kT/2\pi M}{p}} \tag{4}$$

where:

n_o = plasma density (cm^{-3})

A = plasma surface area (cm^2)

e = electronic charge (coul)

k = Boltzmann's constant ($erg/^{o}K$)

M = ionic mass (gm)

T_p = ion temperature (^{o}K).

Likewise, the electron leakage across the sheath is:

$$I_e = I_p \sqrt{MT_e / mT_p} \exp(-eV_s / kT_e) \quad (5)$$

where:

V_s = sheath drop relative to cathode (volts)

T_e = electron temperature (^oK)

m = electron mass (gm)

These expressions presume Maxwellian distributions for ions and electrons in the plasma. By defining:

$$\eta(V_s) = \sqrt{MT_e / mT_p} \exp(-eV_s / kT_e) \quad (6)$$

eq. (5) can be written as:

$$I_e = \eta I_p. \quad (7)$$

For ordinary operating conditions $\eta << 1$ since $eV_s / kT_e >> 1$.

The electron current from the cathode walls is composed of electrons liberated by fast ions, fast neutrals, thermal ions, and photons. All these particles possess energy distributions, so their respective electron yields depend on the cathode potential in a complicated way. For simplicity, the average secondary emission and photo-electric coefficients can be defined [4], if the dependence of the yield on energy is known. In this treatment it is assumed that the appropriate average emission coefficients are known.

Electrons liberated at the cathode surface due to fast neutral and fast ion bombardment give a contribution to the wall current of $\gamma_i(I_i + I_n)$. Plasma ions bombard the cathode and give a contribution to the wall current of $\gamma_p I_p$. All electrons coming from the cathode are accelerated across the sheath and those trapped give up their energy to the plasma by either elastic or inelastic collisions. Here I_n represents the electronic charge

times the current of fast neutrals.

The probability of electrons causing excitation of gas atoms rather than ionization is P_{ex}/P_i, provided the sheath-drop is greater than the first excitation potential. The quantities P_{ex} and P_i are the excitation and ionization probabilities, respectively, (cm^{-1} mm-Hg^{-1}). The number of excited atoms formed per electron is given by:

$$\frac{eV_s}{w} \frac{P_{ex}}{P_i} \tag{8}$$

where w is the energy required to create an ion pair. Fast ions and neutrals also excite the gas as they traverse the interior of the cathode. Assuming an excitation probability P_f(cm^{-1} mm-Hg^{-1}) to be the same for both fast species, there are $(I_i + I_n)$ $PP_f d$ excited atoms or molecules created by fast particles.

Each state gives up a photon by radiative decay which occasionally yields a photo-electron, thereby giving a contribution to the wall current of $I_w \gamma_{ph}(P_{ex}/P_i) \frac{eV_s}{w} + pP_f d\gamma_{ph} (I_i + I_n)$. The sum of all these constributions is

$$I_w = (\gamma_i + pP_f d\gamma_{ph}) (I_i + I_n) + \gamma_p I_p + \frac{\gamma_{ph} P_{ex} eV_s}{P_i w} I_w \tag{9}$$

Solving for I_w gives:

$$I_w = a (I_i + I_n) + bI_p \tag{10}$$

where:

$$a = \left(\gamma_i + pP_f d\gamma_{ph}\right) \Big/ \left[1 - \gamma_{ph} P_{ex} eV_s/P_i w\right] \tag{11}$$

$$b = \gamma_p \Big/ \left[1 - \gamma_{ph} (P_{ex}/P_i) \frac{eV_s}{w}\right] \tag{12}$$

Thus, the effect of energy trapping by excitation of atoms or molecules inside the cathode is simply to increase the effective secondary emission coefficients for ions and neutrals.

The continuity equation for thermal ions can be written as:

$$\beta I_i + \alpha\delta I_w + \mu (I_i + I_n) = I_p \tag{13}$$

provided that the ionization probability of fast ions is roughly equal to that of fast neutrals, P_n (cm^{-1} $mm\text{-}Hg^{-1}$). The first term in eq. (13) gives the thermal ion creation by charge-exchange. The second term accounts for ionization by electrons coming from the cathode walls, with:

$$\delta = \frac{eV_s}{w} \tag{14}$$

and assuming all secondaries are retained by the plasma. The third term is the ionization by fast ions and neutrals, provided that only singly charged ions are created, and that:

$$\mu = pP_n d. \tag{15}$$

The sum of these is then equal to the ion losses by diffusion and volume recombination. The latter is negligible for plasma densities and volumes of interest here.

An equation for the continuity of electrons, similar to Eq. (13), can be obtained by subtracting Eq. (13) from Eq. (1). However, this expression yields no new information and need not be considered further in this

discussion.

Each thermal ion created by ionization and charge transfer carries its ionization potential, V_i , into the plasma. Each electron liberated at the cathode surface and subsequently trapped in the plasma carries into the system its original energy plus the energy gained crossing the sheath. Ordinarily, the sheath drop is much larger than the energy the electron has when formed, and hence, to a good approximation, the electrons from the walls carry energy equal to the sheath drop into the plasma. These are the only energy sources sustaining the internal plasma, and they can all be traced to the kinetic energy carried by fast ions and neutrals entering the plasma.

Energy lost from the system is primarily due to the thermal energy carried out of the plasma by electrons forming the beam and the ionization energy carried by thermal ions recombining at the cathode surface. Other energy losses of a secondary nature occur, such as volume recombination and thermal radiation losses; these will be neglected in this treatment. Electrons which have sufficient energy to cross over the potential barrier and reach the cathode surface are lost to the system by recombination, carrying their kinetic energy out of the plasma. This energy loss is a sensitive function of the sheath drop and the electron temperature and is ordinarily small. However, near the threshold of the beam mode it can become important.

Balancing the power input to the power lost, gives:

$$\left[\beta I_i + \mu (I_i + I_n)\right] V_i + \alpha I_w V_s = \frac{2kT_e}{e} I_b + I_p V_i + I_e V_e \qquad (16)$$

neglecting recombination and heating losses. The quantity V_e can be

derived by a straightforward application of the Maxwell-Boltzmann statistics to a classical electron gas in a spherical potential well of depth eV_s. This results in:

$$V_e = \frac{k\,T_e}{e}\left[\frac{3}{\sqrt{\pi}}\left(1 + \frac{2\,x_o^{\,2}}{3}\right) x_o\, e^{-x_o^{\,2}} + \frac{3}{2}\,\mathrm{erfc}\,(x_o)\right] \qquad (17)$$

where,

$$x_o = \sqrt{eV_s\,/kT_e}\ . \qquad (18)$$

For very small x_o the energy carried by the escaping electrons is just the electron average energy $3kT_e/2$. However, for a large potential barrier compared to the mean electron energy, eq. (17) reduced to:

$$V_e = \frac{2k\,T_e}{e}\left[\frac{x_o^{\,3}\, e^{-x_o^{\,2}}}{\sqrt{\pi}}\right] \quad ; \quad x_o >> 1 \qquad (19)$$

which is small compared to $2kT_e\,/e$.

By using eqs. (7) and (10), the electron currents to and from the cathode walls can be eliminated from the set of equations describing the system. The resulting set of equations may then be written compactly in the form:

$$I_b \sum_{j=1}^{3} C_{ij}\, B_j = D_i\, I_n \quad ; \quad i = 1,2,3 \qquad (20)$$

where the coefficients and reduced currents are defined as:

$$C_{11} = 1 \tag{21-a}$$

$$C_{12} = -(1 + \alpha b - \eta) \tag{21-b}$$

$$C_{13} = (B - \alpha a) \tag{21-c}$$

$$C_{21} = 0 \tag{21-d}$$

$$C_{22} = (1 - \alpha\delta b) \tag{21-e}$$

$$C_{23} = -(B + \alpha\delta a + \mu) \tag{21-f}$$

$$C_{31} = 2kT_e/e \tag{21-g}$$

$$C_{32} = (V_i + \eta V_e - \alpha b V_s) \tag{21-h}$$

$$C_{33} = -\left[(B + \mu) V_i + \alpha a V_s\right] \tag{21-i}$$

$$D_1 = \alpha a \tag{21-j}$$

$$D_2 = (\mu + \alpha a \delta) \tag{21-k}$$

$$D_3 = (\mu V_i + \alpha a V_s) \tag{21-l}$$

$$B_1 = 1 \tag{21-m}$$

$$B_2 = I_p/I_b \tag{21-n}$$

$$B_3 = I_i/I_b \tag{21-o}$$

This set of equations may be manipulated to obtain a single expression relating the beam current to the effective current of fast neutrals. This is equivalent to eliminating I_i and I_p from the set of three equations. The result may be expressed in the form:

$$I_b = \gamma_{eff} I_n \tag{22}$$

where γ_{eff} is a quantity analogous to a secondary emission coefficient, given by:

$$\gamma_{eff} = \left[\frac{(C_{22}D_1 - D_2C_{12})}{(C_{22}C_{13} - C_{23}C_{12})} - \frac{(C_{22}D_3 - D_2C_{32})}{(C_{22}C_{33} - C_{32}C_{23})} \right] \left[\frac{C_{22}C_{11}}{(C_{22}C_{13} - C_{23}C_{12})} - \frac{C_{22}C_{31}}{(C_{22}C_{33} - C_{32}C_{23})} \right]^{-1} \tag{23}$$

From eqs. (2), (3), (6), (11), (12), (14), (15), (17), and (21) it is possible to see that γ_{eff} is a function of the gas properties and pressure, the cathode material and geometry, the electron and ion temperatures, and the sheath-drop (hence the cathode potential). An explicit display of these dependences is possible but tedious and unnecessary.

DISCUSSION

The essential results of the analysis are contained in eqs. (22) and (23). These two expressions contain all the pertinent information concerning the phenomena inside the cathode and their analytical relationship to the exterior phenomena. Eq. (22) is the desired coupling equation, which is necessary for a discussion of the cathode fall.

The effective emission coefficient, γ_{eff}, expresses the approximate number of beam electrons coming from the cathode per fast neutral entering the aperture in the steady-state. Furthermore, an operational pressure and voltage regime for the beam mode is implied by the form of eq. (23). The beam thresholds are indicated by the vanishing of the numerator in (23). Beam instability occurs when the denominator vanishes. Therefore, there exists a certain minimum voltage at a given pressure above which the beam mode can exist for each gas, cathode, and temperature. In principle, this threshold voltage could be estimated by setting the numerator equal to zero in (23) and numerically solving the resulting transcendental equation. However, this requires knowledge of the electron temperature, ion

temperature, secondary emission coefficients, photo-electric yields, and several interaction cross-sections. Since many of these quantities are not known accurately, the threshold calculation would be approximate. Similarly, for a given cathode potential there exists a pressure threshold for the beam mode, which could be determined in the same way.

As the operating potential is increased in the beam mode at constant pressure and temperature, the denominator in eq. (23) approaches zero. The beam becomes unstable and gives the impression of having a negative impedance. A similar behavior occurs when the pressure is increased at constant cathode voltage.

A complete description of the system requires the analysis of the cathode fall. Eq. (22) gives the relationship between the fast neutral current and the beam current at the cathode aperture only. The currents vary across the dark space and through the positive column in a complicated manner, which must be treated in a way similar to the McClure and Kranzow theory for planar cathodes[5]. The resulting equations describing the various currents are coupled non-linear integro-differential equations. Their solution can be obtained numerically using a digital computer by a self-consistent iterative scheme. Even so, this approach is one-dimensional and requires a number of simplifying approximations in order to describe the situation at all. A discussion of the cathode fall will be the subject of a future publication.

The general nature of the solution for the pressure and voltage characteristics is indicated by the data shown in Figs. 3 and 4. Note that the characteristics do not follow the simple power-law formulae, as do planar[4] or screen[7] type cathodes. For a given gas, both the voltage and pressure characteristics are monotonically increasing functions in the

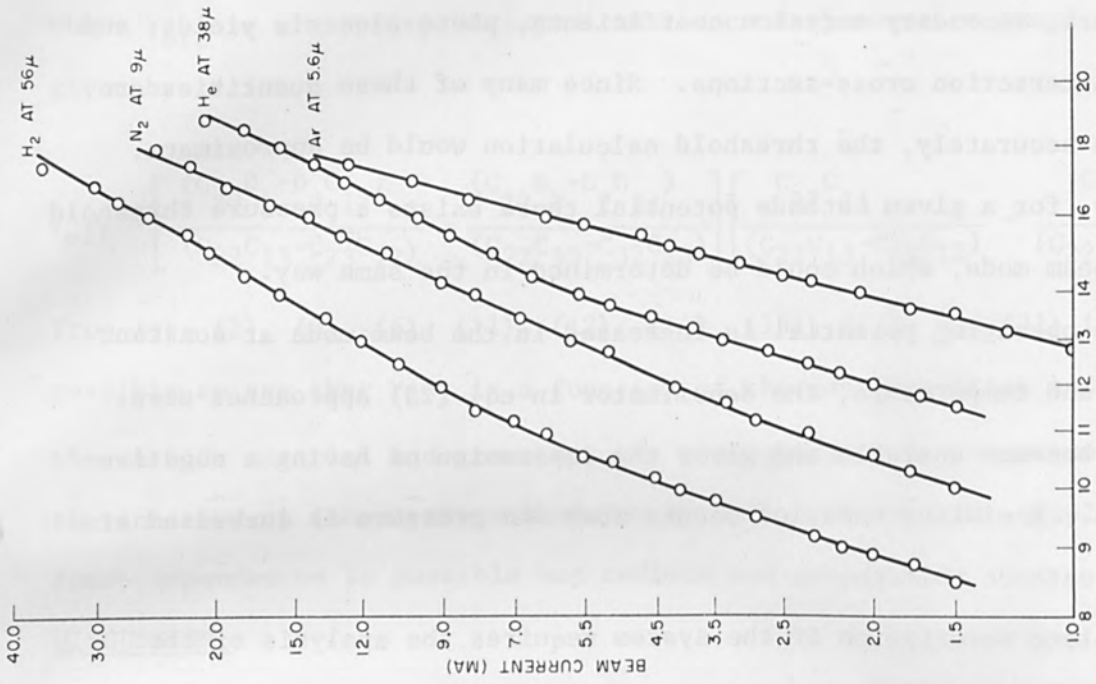

FIGURE 3 Plasma Electron Beam Characteristics for H_2, N_2, Ar, He at Various Pressures

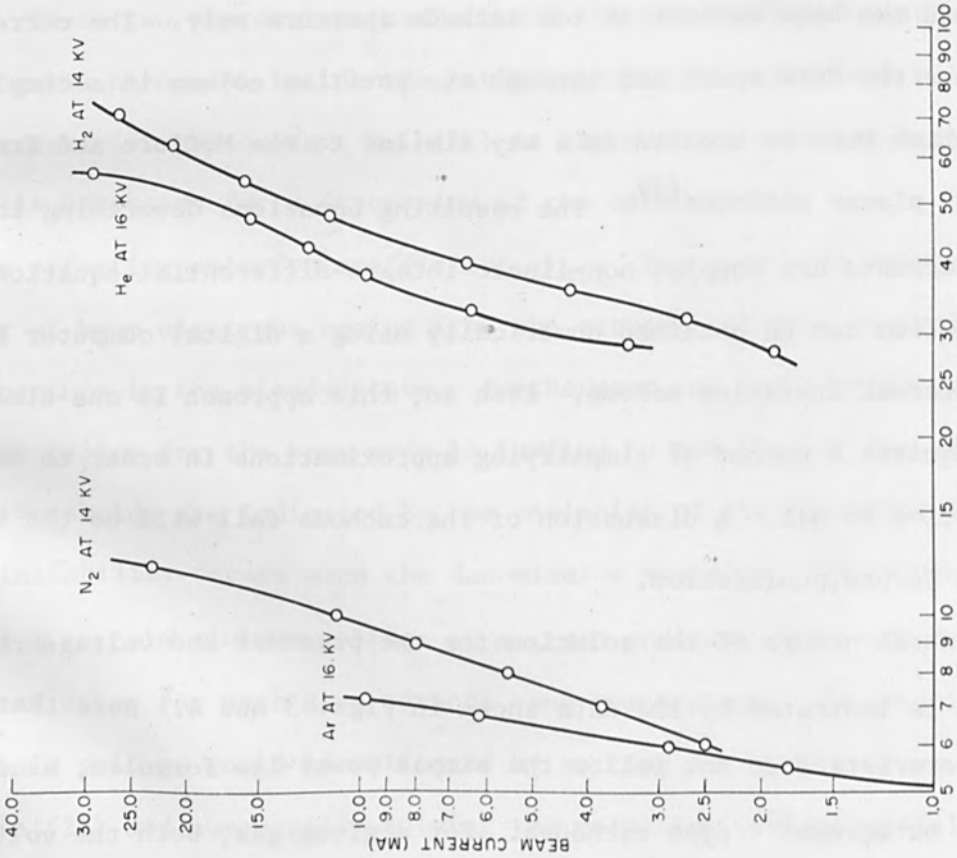

FIGURE 4 Typical Beam Current Dependence on Pressure in H_2, He, Ar and N_2

regime of stable beam mode operation. The dependence of the characteristics on the cathode material was found to be of secondary importance by experiment and is born out by Eq. (23). The material properties enter only weakly into γ_{eff} because the secondary emission and photo-electric yields are not too different from one metal to another. The cathode size and shape are somewhat more important, especially near the aperture. However, no simple similitude relationship is evident from examination Eq. (23).

The cathode efficiency appears to be a function of the pressure and voltage. Most of the energy losses in the system occur due to the bombardment of the cathode face by fast particles from the dark space. Most of this energy eventually leaves the system by radiation and some by gaseous conduction. The gas probably is not isothermal because of this heat transfer, with a higher temperature near the aperture.

Evidently space-charge near the aperture plays an important role in extracting the electrons from the internal plasma. The starting conditions for the beam mode are quite sensitive to the thickness of the cathode face plate, indicating that the depression of the potential barrier near the aperture by the incoming ions, is all important. Perforated face plates have been tried without success in achieving a stable beam mode. Presumably the high influx of fast particles so ionizes and excites the gas inside the cathode that breakdown occurs.

The beam appears to be quite well collimated as it traverses the positive column, even though there is a high current density. The beam divergence is primarily determined by aperture conditions rather than by space-charge spreading. This can be explained qualitatively by the Linder and Hernquist theory of space-charge-neutralization[8] in which thermal ions, created by ionizing collisions of electrons traversing the positive

column, are trapped in the beam and neutralize a large part of the electron space-charge. The degree of this neutralization depends on the gas properties, pressure, electron energy, ion energy, beam radius, and the radius of the positive column.

From these considerations it is evident that the characteristics of the cold-cathode electron beam discharge can be described fully only by analyzing the interactions of the internal plasma, the cathode dark space, and the positive column. Each part of the system accounts for certain of the observable properties of the beam. No simple linearized analytical model is capable of describing quantitatively the complex behavior of the system.

REFERENCES

1. Stauffer, L. H. and Boring, K. L., Electronics 35, 60 (1962).
2. Cocca, M. A. and Stauffer, L. H., Proc. Electron Beam Symposium, Fifth Annual Meeting, 342 (1963).
3. Boring, K. L. and Stauffer, L. H., Proc. Nat. Elec. Conf. 19, 535 (1963).
4. McClure, G. W., Phys. Rev. 124, 969 (1961).
5. McClure, G. W. and Kranzow, K. D., Phys. Rev. 125, 3 (1962).
6. Cobine, J. D., Gaseous Conductors, Dover, New York, 1958, p. 236.
7. Van Passen, H. L. L. and Muly, E. C., Proc. IEEE 52, 316 (1964).
8. Linder, E. G. and Hernquist, K. G., J.A.P. 21, 1088 (1950).

ACKNOWLEDGEMENTS

Experimental equipment and data were provided by K. L. Boring and W. R. Giard. Fruitful discussions were held with G. C. Baldwin, Lewi Tonks, and L. B. Loeb on various aspects of this work.

PLASMA GENERATION IN THE HOLLOW CATHODE DISCHARGE*

L. M. Lidsky
Nuclear Engineering Department and
Research Laboratory of Electronics
Massachusetts Institute of Technology
Cambridge, Massachusetts

ABSTRACT

The Hollow Cathode Discharge was developed as a convenient source of highly ionized high density plasmas. The plasma originates in the interior of the cathode tube (typically 3 mm ID, 0.04 mm wall thickness) and flows, along a collimating magnetic field, into a high vacuum observation region. These devices are generally operated at about 50 A when used as a plasma source but will run for long periods of time (several hours) at from 3 to 350 A. The plasma in the cathode interior has a density of about $3 \times 10^{16}/cm^3$ and is traversed by an electron current of more than 3500 A/cm^2. The mechanisms important in the operation of the hollow cathode will be discussed with particular attention given to those that might explain the anomalously high electron emission at measured operating temperatures.

*This work was supported in part by the U. S. Army, Navy, and Air Force under Contract DA36-039-AMC-03200 (E); and in part by the National Science Foundation (Grant G-24073).

PLASMA GENERATION IN THE HOLLOW CATHODE*

INTRODUCTION

The hollow cathode discharge was originally developed as a source of high density, highly ionized plasmas for studies of plasma physics. As such, the properties of the external plasma were of more interest than those of the plasma in the cathode interior. Today, I will concentrate primarily on the less well understood cathode properties. The remarks to follow will be a rather speculative abstract of previously published material[1].

DISCUSSION

Fig. 1 shows the general arrangement of the hollow cathode discharge. An evacuated chamber contains both the cathode and anode axially aligned. An inert gas, typically Argon, enters the system through the hollow cathode and is pumped off by the diffusion pump. The inert gas plasma generated within the hollow cathode supplies electrons which are drawn to the anode, and are collimated by an axial magnetic field generated by a pair of coils. Typical electron currents range from a few amperes up to three hundred or so for a 1/8" dia. cathode at voltages from 30 to 100 v.

A selection of cathodes is shown in Fig. 2. One of these, a 1/8" dia. tantalum tube, has been finned in an attempt to cool it by radiation, thus increasing the amount of current that can be drawn from it. A volt-ampere curve for a simple unfinned cathode is shown in Fig. 3. The current is plotted up to only 70 amperes but currents of from two to somewhere upwards of three hundred amperes are possible in the steady state. A steady state here means times like six to twelve hours, and they will operate in this range at voltages from 30 to 100 v or so. Now, before discussing the major

---

*Note: This contribution is an edited transcript of an oral presentation.

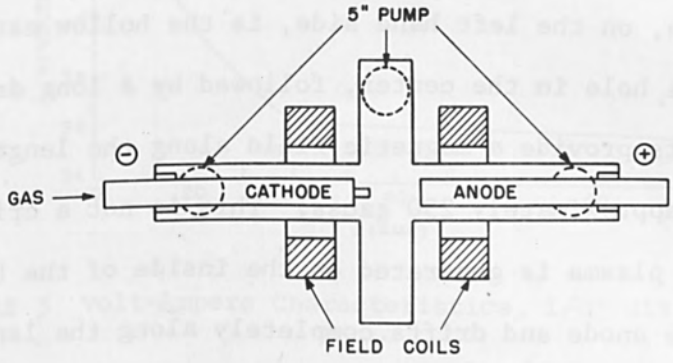

FIGURE 1 Schematic of the Hollow Cathode Discharge (Apparatus)

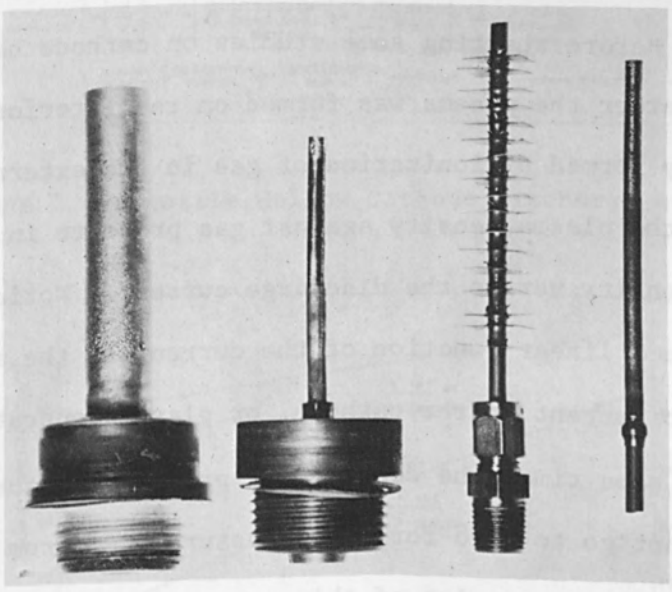

FIGURE 2 Various Cathodes

features of operation of the cathode, an examination of Fig. 4 will show a rather more versatile hollow cathode discharge apparatus. In the upper part of the figure, on the left hand side, is the hollow cathode, then a fixed anode with a hole in the center, followed by a long drift space. Containment magnets provide a magnetic field along the length of the device at a strength of approximately 250 gauss. This is not a critical number. In operation, the plasma is generated on the inside of the hollow cathode, passes through the anode and drifts completely along the length of the device. The gas that escapes from the cathode without becoming ionized, and the gas that returns and is neutralized at the cathode are both pumped preferentially in the plasma generation zone. The plasma is constrained to follow the field lines into the drift region and here it is at almost the same density as in the cathode region, but with background gas at a much lower density. Before starting some studies on cathode behavior, the first question was whether the plasma was formed on the interior of the cathode, or was it simply formed by ionization of gas in the external region? Fig. 5 shows plots of the plasma density against gas pressure in the drift region, and of plasma density versus the discharge current. Notice that the density of the plasma is a linear function of the current to the anode, and projects to zero for zero current in the cathode, or plasma generation, region. Whereas, at the same time, the density vs. pressure in the external region certainly does not go to zero for zero pressure. So from the very simplest considerations, a plot of this nature shows that the plasma is formed in the cathode and is certainly not dependent on pressure in the drift region. There are other results that show similar behavior. Fig. 6 shows a plot taken spectrographically of light from the plasma column in the drift region. There are two distinct families of curves. The curves for

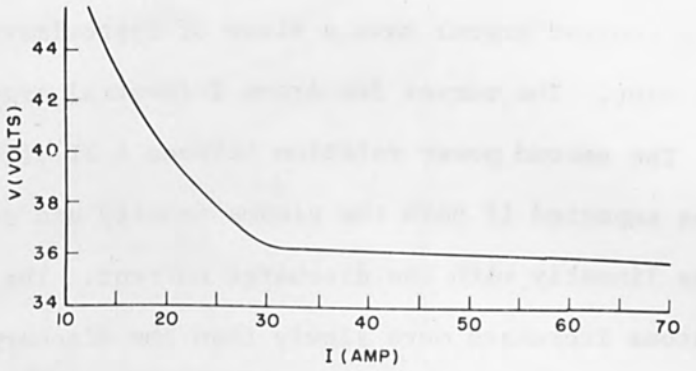

FIGURE 3 Volt-Ampere Characteristics, 1/8" dia. Ta. Cathode

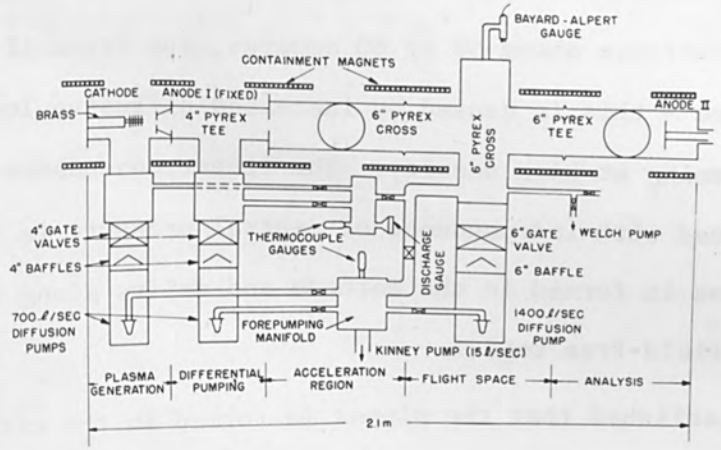

FIGURE 4 Versatile Hollow Cathode Discharge Apparatus

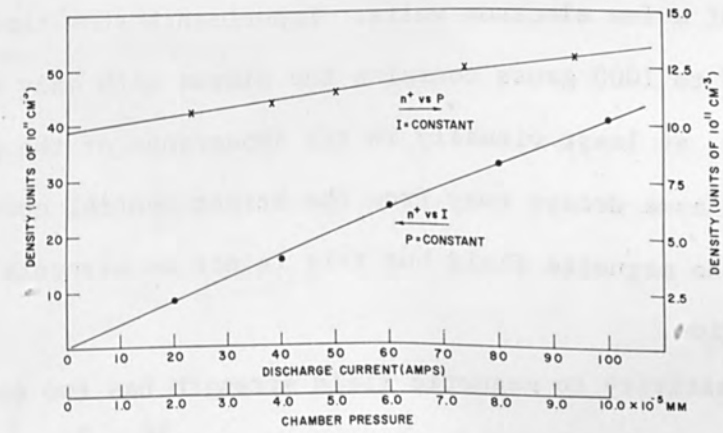

FIGURE 5 Plasma Density vs. Gas Pressure, External Region

Argon II (singly ionized Argon) have a slope of approximately two on the semilogarithmic plot. The curves for Argon I (neutral Argon) have a much smaller slope. The second power relation between A II light and discharge current is to be expected if both the plasma density and streaming electron current increase linearly with the discharge current. The light from excited neutral atoms increases more slowly than the discharge current indicating that the neutral atoms are being burned out in the drift region. This has been observed to make a small contribution to the total plasma density. At currents above 50 or 60 amperes, the Argon II curves take on a smaller slope - this is caused by increased diffusive loss and reduced electron streaming at high density. The linear dependence of density on current combined with independence of neutral pressure is further evidence that the plasma is formed in the cathode and drifts along field lines in the external field-free region.

Having established that the plasma is formed in the cathode, the next question was: How is a dense plasma maintained in a rather weak magnetic field? The plasma densities are on the order of a few times 10^{13}/cc with temperatues of a few electron volts. Experiments show that any magnetic field from 50 to 1000 gauss contains the plasma with only slight second order effects, at least visually in the appearance of the plasma column. The way the plasma decays away from the bright central core is a strong function of the magnetic field but this is not an essential feature of discharge operation.

This insensitivity to magnetic field strength has two causes. In the cathode interior, the plasma density is about $10^{16}/cm^3$ and the temperature is close to the cathode wall temperature of approximately $2500^{o}K$. Under these conditions, the collision time is very much shorter than the cyclotron

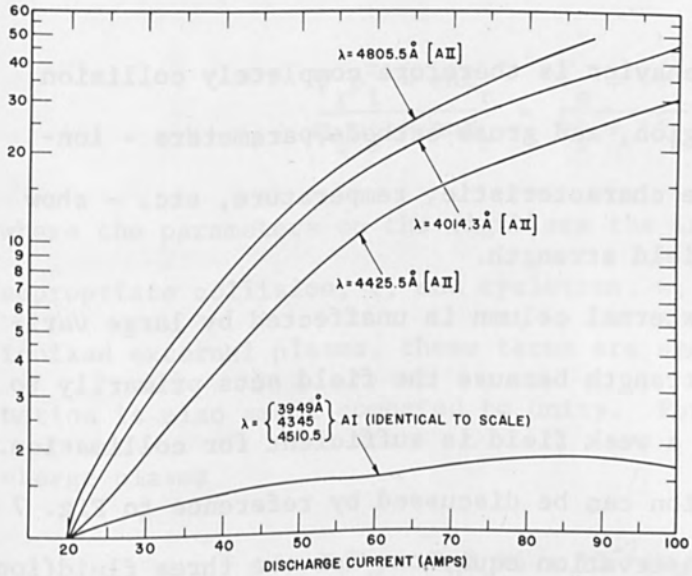

FIGURE 6

$$\vec{\nabla} p_i - en\vec{E} = -m_i \nu_{ie}(\vec{\Gamma}_i - \vec{\Gamma}_e) - m_i \nu_{io}\vec{\Gamma}_i + e(\vec{\Gamma}_i \times \vec{B})$$

$$\vec{\nabla} p_e + en\vec{E} = -m_e \nu_{ei}(\vec{\Gamma}_e - \vec{\Gamma}_i) - m_e \nu_{eo}\vec{\Gamma} - e(\vec{\Gamma}_e \times \vec{B})$$

FIGURE 7

$$\frac{\nabla_r p_i - enE_r}{\nabla_r p_e + enE_r} = \frac{\delta_e + \epsilon\delta_i}{\delta_i + \epsilon\delta_e}$$

$$\delta_i = \nu_{io}/\nu_{ie}\,,\ \delta_e = \nu_{eo}/\nu_{ei}$$

$$\epsilon = (\nu_{eo}\nu_{io} + \nu_{ie}\nu_{eo} + \nu_{ei}\nu_{io})/\omega_e\omega_i$$

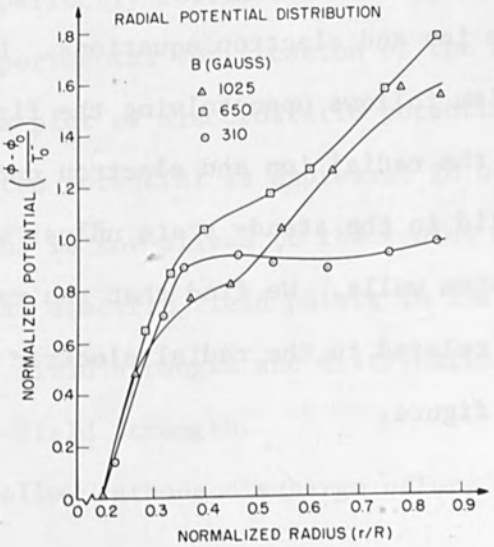

FIGURE 8

rotation period. The plasma behavior is therefore completely collision dominated in the generation region, and gross cathode parameters - ionization efficiency, volt-ampere characteristic, temperature, etc. - show no change with variations of field strength.

The gross behavior of the external column is unaffected by large variations of the magnetic field strength because the field acts primarily to confine the electrons and even a weak field is sufficient for collimation. The details of plasma collimation can be discussed by reference to Fig. 7 which presents the momentum conservation equations for the three fluid(ion, electron, neutral atom) plasma in the external region. In these expressions, the deriving terms (pressure gradient and electric field) are related to the "frictional" terms. For example, $M_i O_{ie}\left[\Gamma_i - \Gamma_e\right]$ represents the rate of destruction of momentum to the difference of ion and electron particle currents, Γ_i and Γ_e. This is the "resistance" due to counterflowing ion and electron streams. In this expression ν_{ie} refers to the ion-electron collision rate and M_i the ion mass. The rest of the notation is equally obvious with subscripts (i,e) and (o) referring to ions, electrons, and neutrals. The effect of the magnetic field, B, is represented by the last term on the right hand sides of the ion and electron equations. Understanding of the confinement mechanism follows upon solving the first two equations with the constraint that the radial ion and electron currents are equal. This constraint must be valid in the steady state unless we are drawing current from the vacuum system walls. We find that the radial pressure gradients, P_i and P_e, are related to the radial electric field, E_r, by the third expression of the figure,

$$\frac{\nabla_r p_i - enE_r}{\nabla_r p_e + enE_r} = \frac{\delta_e + \epsilon\delta_i}{\delta_i + \epsilon\delta_e}$$

where the parameters on the right are the indicated functions of the appropriate collision, V, and cyclotron, w, frequencies. For the highly ionized external plasma, these terms are small and furthermore, their combination is also small compared to unity. For a typical hollow cathode discharge plasma

$$\nabla_r P_e - R_n E_r \approx 5 \times 10^{-2} (\nabla_r P_e + e_n E_r)$$

which, since $p_i \approx p_e$, implies that

$$\frac{dp_i}{dr} \approx e_n E_r$$

or that the radial gradient of ion pressure is balanced by the electric field. Thus there is magnetic field confinement of the electrons, and electrostatic confinement of the ions. This so-called "hybrid confinement" is little affected by the magnetic field because the electrons are, in effect, perfectly collimated even by very weak fields.

An experimental verification of the confinement mechanism is shown in Fig. 8, a plot of electrostatic potential as a function of radius. In this figure, the potential is expressed in units of the electron temperature and the radius is normalized to the radius of the vacuum system. Notice that the radial electric field points in the direction of the axis and that the electric field strength and distribution is relatively independent of magnetic field strength.

The hollow cathode discharge offers very high ionization efficiency at

very low voltages. What peculiarities of the cathode make this possible? Because of the very high gas density inside the cathode, it is possible to postulate a simple explanation of the operation of the discharge. In any situation where a plasma is in contact with a surface, and the plasma is dense enough, it is well known that there are very small voltage gradients in the plasma itself, and that any voltage difference between plasma and the surface must be made up in the sheath at the surface. The sheath thickness is on the order of the Debye length. Inserting numerical values for known cathode parameters (10^{16}/cc, fractional electron volt temperature), we find that this distance is in the order of 10^{-5} cm. The cathode diameter is approximately three millimeters or more, so the sheath thickness is a very small fraction of the cathode diameter. There appears to be an equipotential, well inside the cathode, with very sharp boundaries near the cathode surface; this leads to the model shown in Fig. 9. The plasma near the axis of the cathode will be at some voltage nearly that of the anode. The sidewalls of the cavity will, by definition, be at cathode potential. There will be a very thin sheath whose thickness can, for present purposes, be neglected. What in effect happens is that electrons are injected into the sheath, ionize or excite the gas somewhere in the interior of the cathode and can no longer return to the cathode surface.

On the other hand, the radiation arising from excitation and recombination inside the cathode returns, with very high probability, to the cathode walls. The ions formed in the cathode interior make many collisions with the interior walls before diffusing to the orifice and because they fall through the electrostatic sheath at the surface serve to heat the cathode surface. The high current density at the cathode orifice ensures that very few gas atoms escape without ionization.

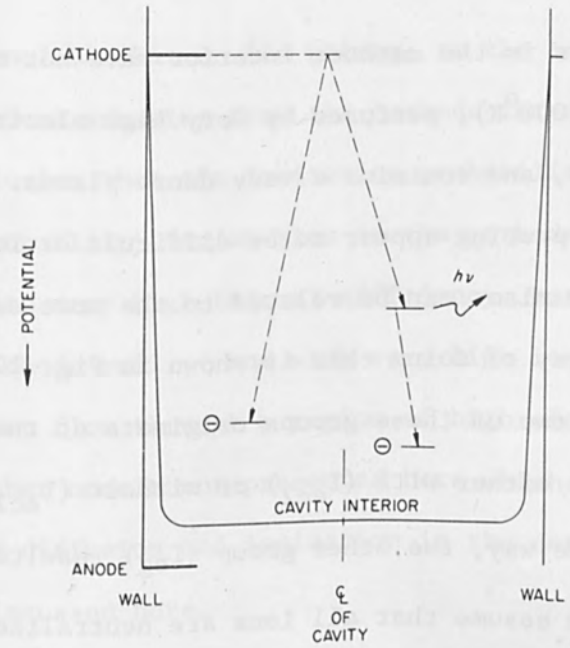

FIGURE 9

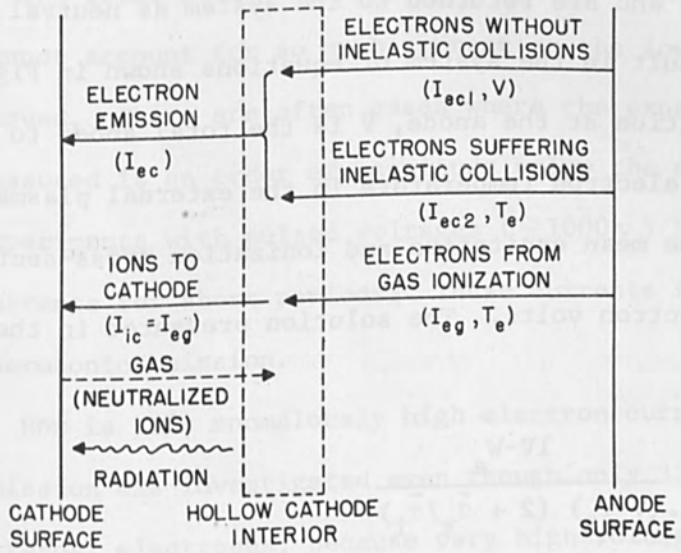

FIGURE 10

$$W_a = I_{ecl}\, V + (I_{ec2} + I_{eg})\, T_e$$

$$I = I_{ecl} + I_{ec2} + I_{eg}$$

$$I_{ic} = I_{eg} = I_{ec2} / (1 + \bar{\sigma}_x / \bar{\sigma}_i)$$

FIGURE 11

$$I_{ic} = \frac{IV - W_a}{(V - T_e)(2 + \bar{\sigma}_x / \bar{\sigma}_i)}$$

Detailed experimental measurements in the cathode interior have not been made - the interior region is hot ($2000^{o}K$), perfused by very high electron currents (several thousand amps/cm^2), and contains a very dense plasma. Probes, spectroscopy, and microwave probing appear to be difficult or impossible. However, the cathode mechanisms can be related to the more easily measured external parameters. One way of doing this is shown in Fig. 10. Consider three groups of electrons; two of these groups originate at the cathode wall and stream to the anode either with (I_{ec2}) or without (I_{ec1}) suffering inelastic collisions on the way, the other group (I_{eg}) results from ionization of the feed gas. We assume that all ions are neutralized at the cathode interior walls and are returned to the system as neutral gas atoms. These assumptions result in the system of equations shown in Fig. 11 where W_a is the power dissipation at the anode, V is the total anode to cathode potential, T_e is the electron temperature in the external plasma, and $\bar{\sigma}_x/\bar{\sigma}_i$ is the ratio of the mean excitation and ionization cross-sections for electrons of energy V electron volts. The solution presented in the last line of this figure is:

$$I_{ic} = \frac{IV-W_a}{(V-T_e)\ (2 + \bar{\sigma}_x/\bar{\sigma}_i)}$$

and expresses the ion current to the cathode wall in terms of easily measured quantities, and a reasonably well-known cross-section ratio. Because the anode is cold, W_a is easily determined calorimetrically. The resulting ion current, for a typical case of a 30 amp, 30 v discharge operating in Argon, is approximately 5 amps. The neutral gas input rate corresponds to only 0.7 amp if each gas atom was ionized only once. We

conclude that an ion returns to the cathode wall between 5 and 10 times before escaping from the cathode interior. This is equivalent to the conclusion that the ionization probability is much higher than the escape probability for an atom in the cathode interior. We have therefore a system with very high thermal efficiency, both ions and radiation returning to the cathode wall, - and with very high ionization efficiency for the gas atoms must flow through a region of high electron flux. It should be noted that other models not presented here which are based on the macroscopic physics of diffusion and ionization in the cathode interior, agree with the model discussed here.

The total electron current is another interesting number because we cannot account for so much current at the low operating temperatures observed. There are often cases where the expected current at the temperature measured is an order of magnitude below the observed current. Furthermore, experiments with pulsed voltages (~ 1000 v) have resulted in kiloampere currents for short periods. These currents far exceed those predicted for thermionic emission.

How is this anomalously high electron current accounted for? Field emission was investigated even though only 30-50 v was applied across the external electrodes, because very high voltage gradients can exist in the cathode sheath. With the 10^{-5} cm sheath previously mentioned, the electric field will be of a few times 10^{6} v/cm at the cathode surface. This would probably cause noticeable emission current enhancement if the cathode surface was rough enough but falls short of the field necessary with smooth surfaces. It is hard to believe that a rough cathode surface exists, because of the high current density which would tend to smooth any local high current zones. The combination of field and thermionic emission

(T-F permission) has been investigated by several workers but these also fall short of explaining the situation in the hollow cathode discharge. Other effects that are operative in the more usual high voltage devices - ion and photon secondary emission, for example, γ_i and γ_p processes - are completely negligable at the low voltages under discussion here. The ions and photons have typical energies at the cathode surface of 30 and 15 ev in contrast to the several hundred volts found in glow discharges. Thus we are at a loss to explain this high electron emission except for one further possibility. The combination of high surface fields with ionic bombardment may yield large increases in the secondary emission characteristic. If γ_i approaches unity, the HCD may be considered to be a very low voltage abnormal glow discharge. This γ_i-F effect has been noticed before in low-voltage mercury discharges[2].

REFERENCES

1. Lidsky, L. M., Rose, D. J., Rothleder, S. D. and Yoshikawa, S. Jour. Appl. Phys. 33, 2490 (1962).
2. Newton, R. R., Phys. Rev. 73, 1122 (1948).

PANEL DISCUSSION ON HOLLOW CATHODE DISCHARGES

PANEL MEMBERS

J. R. Morley, Moderator	Alloyd General Corporation Cambridge, Massachusetts
L. M. Lidsky	Massachusetts Institute of Technology Cambridge, Massachusetts
E. C. Muly	Martin Company Baltimore, Maryland
L. D. Smullin	Massachusetts Institute of Technology Cambridge, Massachusetts
L. H. Stauffer	General Electric Company Schenectady, New York
J. H. Terhune	General Electric Company Schenectady, New York

Question C. H. Banas, United Aircraft Corporation. Is the neutral density or the degree of ionization in the cathode itself known? Is the particle density of 10^{16} ions/cm^3 highly localized?

Answer Lidsky: The limits only are known; we know at one end of the cathode that there is complete neutralization. At the other end we see at least 95% ions coming out. We assume that things vary monotonically inside the cathode and it is localized in a region judged only by the size of the hot spot that appears externally on the cathode surface. The change from completely neutral to completely ionized plasma takes place in a space in the order of a centimeter long. Exactly how the degree of ionization varies, whether it is a linear function or is happening in a much more local spot we don't know; all we observe is the average effect somewhere on the outside of the cathode itself.

Morley: Following on from this Prof. Lidsky, what do you think would be the maximum current you could obtain from one of these

cathodes or perhaps it would be better to call it current density; what defines the upper limit of this?

Lidsky: We're not quite sure; we must have some limits, but in most cases since we are operating at a rather high current level, we have been limited by our power supplies. The 1/8" diameter cathode will operate at 300 amperes for several hours. Cathodes have also been pulsed to a kilovolt or so but only for short periods of time, hundreds of microseconds, in fact, with currents of up to 100 amperes. Current is not linear with voltage and there are places where the discharge prefers to operate. For example if we pulse it to a kilovolt, we find the current remains for a long time, (long in this regime is hundreds of microseconds), at roughly 500 amperes peak, in the case of the 20 ampere d.c. discharge I discussed earlier. The voltage varies from a kilovolt down to about 200 volts and the current then falls to the 20 amperes set by the external circuit. Currents do not seem to vary very quickly with voltage, and this seems to be some gas effect. Perhaps due to secondary emission as we change ionization states of the gas. An upper limit of approximately 500 amperes for the cathode with a total emitting surface of half a centimeter in area or so would be my best guess.

Morley: You say that during these pulse conditions the pulse voltage is in the kilovolt range, whereas in the d.c. mode it is typically 40 volts?

Lidsky: Yes, the discharge is pulsed to a kilovolt or a little more with a capacitor bank and the voltage then falls; the

object being to see what happens as a function of voltage. We find as the voltage falls, the current just goes through several plateaus that we can almost, but not quite, ascribe to different degrees of ionization of the gas being used.

Morley: We find under d.c. conditions that with 600 to 800 amperes there's a slight but continuous increase of voltage across the discharge, and we end up somewhere around 80 volts, so this must be a starting phenomena that you're talking about.

Lidsky: I'm sure it must be because it's hard to separate the voltage effects from those of time, and that's the reason why this isn't the world's best experiment, because both things are going on at the same time. The voltage falls with time and we don't know if we're burning out metastables that are giving us rather high secondary ionization or simply that the voltage has passed through a plateau value.

Morley: I noticed on your slide (Fig. 4) that you had two anodes in your system - you had a cathode, then a differential pumping section, an anode and a second anode further on beyond the drift space. Did you do anything here with your discharge in establishing different voltages on these anodes or did you run them at the same voltage?

Lidsky: This has more bearing I think, in the study of the external plasma than it does in the cathode itself. We've run them through both anodes and through one or the other of the anodes. The anodes were disposed one across magnetic field lines, and one along field lines, as nearly as we can tell with the reflex discharge. With the hole in the anode, and the

plasma following across field lines, the discharge operates at a higher voltage only because there's a larger voltage drop in the external plasma, since the electrons can no longer directly stream to the anode. In our case since we run both anodes at ground, when we run them at all, the way the current splits depends on the magnetic field, now ostensibly this could be related to the voltage also, but at high field strengths, naturally most of the current goes to the anode disposed along field lines. In lower strength fields it splits more equally.

Question From the same questioner, C. H. Banas. You stated that the larger cathodes must be cooled. Is this due to an increase in discharge power or a decrease in efficiency?

Answer Terhune: We have measured the efficiency of these cathodes using a calorimeter and we find that this increase of cathode heating is primarily due to an increase in the discharge power. The efficiency of course is a function of the current and I would like to have Lynn Stauffer comment further on this.

Stauffer: The beam currents that you saw in the curves today were for a small 1" cathode with no liquid cooling. It simply radiated the heat of bombardment from the face of the cathode. If one wants ampere beam currents, then you have to take care of the heat dissipated in the cathode or you'll crack the insulating bushing or damage something, so we took care of this by using a squirt tube. We run water down the hollow stem of the cathode into the top section and remove the heat caused by ion bombardment at the top of the cathode. In some of the larger cathodes we have water cooled the shield and obtained beam

currents as high as 1.3 amperes from a cathode which had an internal diameter of 3" and was about 4" long, and was made of copper. I should state that the efficiency is about 60 to 70% so that the remainder has to appear as heat, and a good deal of this is given up at the cathode itself.

Question H. Schwarz, Rensselaer Polytechnic. Please comment on the pressure change due to ion pumping. Does this give reason for the high secondary emission or the "runaway" effect?

Answer Terhune: When I mentioned ion pumping this was more graphical than actual. There is a very slight pressure effect due to the transfer of momentum between the ions and the gas molecules on the inside of the cathode but we have been unable to detect this even though we have tried to measure the pressure internal to the cathode independently of that in the external bell jar. However we feel that the current density of the ions is low enough that this is probably not an important effect. Certainly the ion pumping, or a better term would be ion injection, does give some effect, and provides the reason for the runaway of the current as the voltage of the cathode is increased. Obviously, as the cathode potential rises, there is a greater and greater drop across the cathode fall. The ions have higher energy, they can release more and more secondary electrons on the inside of the cathode and this creates a divergence in the beam.

Stauffer: I would like to add a word to that - there are two connotations of pumping in what Mr. Terhune says. Energy is pumped into the internal plasma by high energy ions entering the aperture. These are accelerated across the dark space and

this is where the energy of excitation comes from for the internal plasma body. The actual gas pumping is quite negligable as he mentioned.

Question — Smullin: John, I'd like to ask a question if I may. The cathode as I understand it is a cylinder which is an inch or two in diameter and it has a cap on its front face with a hole which is 1/4" or 3/8" dia. What is the relative importance of the size of the aperture to the size of the cathode dia. for peak current or peak power?

Answer — Stauffer: The cathode aperture you might say, determines the impedance of the beam. If you make it small you require a higher voltage to get the same beam current, but if you make it too large it can initiate a glow discharge and then go into the beam mode. We've found in general that for optimum results the cathode aperture should be about 1/4 to 1/5 of the diameter of the cathode. The thickness of the front plate is quite critical and should be in thickness, about equal to the radius of the aperture. Then you get the best beam collimation and stability.

Terhune: I might add that the shape of the face also is very important in the amount of beam current you can get out of the cathode as well as its collimation. This is something that we have observed empirically and it must concern the distribution of the space charge fields about the aperture.

Question — D. J. Vargo, NASA. Would you comment in more detail on the amount of secondary electrons emitted by combination of the high electric field and of the ions striking the surface?

Answer — Lidsky: The briefest answer is - no, I can't comment in much

more detail! We have a situation wherein we cannot explain the current we see on any basis. If our temperature measurements are accurate, and they've been repeated by several people, then the only thing we can say is that this other effect seems to be of major importance, although we cannot by any means put any numbers to it. What is needed is a secondary emission coefficient near 1. Whether the number we need is 0.2 or 0.9 depends very much on the particular pressures at which we are running in the cathode at the time and many other effects. We know there must be a larger effect than simple secondary emission or simple photoelectric emission at these low voltages. The reason I mentioned the combination of electric fields and ion bombardment is the fact that this physical model seems capable of giving a rather large secondary emission coefficient, even though no one has worked it out in any great detail. The numbers worked out by Newton, I believe, in some cases lead to secondary emission coefficients much larger than 1.

Question R. A. Denton, Denton Vacuum. To what extent have you observed cathode sputtering during operation and if so under what conditions does this occur?

Answer Stauffer: We ran one cathode which was 1 1/2" in dia. It had a molybdenum face with an aperture in it, and after 500 hours operation in air at about 10 microns there was a very pronounced dishing out of the face due to ion bombardment around the aperture. When this face becomes concave the beam tends to diverge due to the change in electrostatic field, and the ultimate life of the cathode I suppose, would be determined when

the face became so concave that the focussing disappeared.

Muly: We also have a cold hollow cathode discharge which we operate and it is of the screen mesh variety. The aperture section of the cathode face is of screen mesh, as distinct from a solid face. Any deterioration by sputtering will then be uniform over the screen mesh and its opening, so that you don't notice any destruction of the focussing properties due to the deterioration of the screen because the screen is just a support to maintain the potential in front of the beam. Sputtering is observed in these geometries but not to the point where it affects beam focussing as far as I know.

Lidsky: In the hot hollow cathode it's a harder question to answer because it is difficult to separate thermal and sputtering effects. There is some motion of the material, but I don't know what this is in grams per ampere hour. The total operating time for a 1/8" dia. cathode I would estimate to be 30 to 50 hours, at 20 amperes. Its failure is generally caused by the high pressure inside the cathode and this is measured in millimeters of mercury. Here we have a density of 10^{16} particles/cc, and a temperature near $2000^{o}K$ and if the gas is at all coupled to the walls blowing out of the hot spot on the side wall can occur. Now whether the thin spot is caused by local overheating, in other words the thin spot just being weak, or due to a thin spot made by sputtering, I really don't know. There's little sputtering showing up in the external plasma but there's a good reason for this. Any sputtered ions would, by the same argument that returns argon ions to the

side walls 8 or 10 times also makes the tantalum ions do the same thing. My feeling is there's very little sputtering at the low voltages we use, for example, 30 - 50 volts, and thermal effects seem to be predominant.

Question R. J. Schwinghamer, Marshall Space Flight Center. Do you think there's a difference of temperature existing on the electrodes? And, the second part is, is it possible that the Cline effects may be contributing to the generation of current? (The Frenchman Cline has observed high currents from electrodes in plasmas when such a temperature differential exists).

Answer Lidsky: The first part of the question - I know there's a difference of temperature existing between the electrodes, the cathode is running at just about white heat, the anode is a copper disc some meter or two away and it is at room temperature since it is cooled with water, so there's a 2000°C difference in temperature between the electrodes. The Cline effect may be contributing to the current for there is certainly something happening - we think it's the field that's more important than the thermal effects, but we're not sure.

Question E. Rainer, Pennsylvania State University. Did the aperture size have any dependence on the cathode to anode spacing and the field?

Answer Stauffer: The shield has the function of concentrating the electric field at the aperture and therefore affects the beam focus, it is rather critical. We operate with the end of the shield just slightly above the plane of the cathode face and for a one inch cathode that can be anywhere from 1/8" to 1/4". It

has also been operated in a plane below the aperture, and we find that this concentrates the discharge more into the aperture but it makes it more difficult to start. The importance of the spacing between the cathode and the shield is that it must be small enough to prevent an avalanche type discharge in the space. We make use of the well known relationship for breakdown and the gap due to Paschen. If the gap is small enough so that collisions between electrons and gas atoms are improbable, it will not break down and this is the consideration that primarily determines the gap between the shield and the cathode.

Terhune: One more thing on this particular question; the distance between the cathode and the anode per se has not been one of parameters which we can easily adjust in our apparatus. To my knowledge we have not done any concentrated study on the dependence of the aperture size to this particular spacing.

Question

Morley: At this point in the discussion, I'd like to call on Emil Muly to say a few words about the hollow cathode discharge work that's been done at the Martin Company, especially in respect to some of their findings on secondary emission work there.

Muly: As an introduction I'd like to say that we've been working for three years in this field and that we have been recently involved in the diagnostics of the interior cathode region, much like those discussed here by Dr. Stauffer. In particular we've taken a broader approach to the problem, and because of this, we may well have missed a few things, but

because of it, we may have found a few more. We've used microwave, Langmuir probe, spectroscopic, and Faraday cage techniques, on either the beam or the interior region of the cathode. One of the most interesting results we've had is quite recent and concerns screen mesh cathodes. We asked the question, "what are the properties of a screen mesh cathode"? To answer this, we've tried to determine what would be the equivalent secondary electron emission coefficient for a surface in which the screen mesh holes were so small that they represented only a small purtabation on the cathode's surface, either for a planar type, or any other geometry. If you select a hole size for a mesh opening which allows the returning ions to be essentially ballistic in nature when they reach this opening and go into the interior of the cathode, then they will produce a plasma and, some electrons will therefore be emitted. Using a model somewhat similar to that used for the ion bombardment of solid surfaces, we asked what would be the equivalent secondary emission of a hole in the mesh. By taking both solid ball and screen mesh cathodes and taking the ratio between their currents at fixed pressures, an empirical equation has been set up containing this number which is essentially a secondary emission coefficient. In addition, we've done experiments which have given data for balls and also allowed us to examine the properties of screen mesh surfaces and to evaluate their secondary emission properties, and to assign numerical values. To obtain these values we took two copper screen meshes 0.004" thick, etched from the same master, and then superimposed one

above the other in such a manner that one was movable with respect to the other along the diagonal of the square holes. The square holes were made so that on looking down from the top you see about 20% maximum transparency, and as one mesh is moved along the diagonal the transparency reduces linearly down to about 2%. Unfortunately, the corners of the holes are slightly rounded by the photo-etching process and hence zero transparency is not possible. We measured current at constant voltage across the discharge maintaining constant pressure. By puting a micro-wave cavity underneath the screen mesh we also monitored the electron density in the cavity region below the screen mesh. This, in the solid cathode, is the region on the other side of the aperture. We've taken this data for low transparencies and determined that you can disregard the increased ion current to the cathode between 2% to 10% transparency, and only consider the increase of electrons coming from these holes and going to the exterior discharge to account for the increase in current. With this kind of interpretation of data we were able to determine the equivalent secondary emission coefficient for the holes. It turns out for transparencies of 2% to 20% that the holes are approximately five to twenty times better secondary electron emitters than the solid portions surrounding them. The concept of giving a secondary emission coefficient to a hole can be interpreted for low transparencies very nicely because of a linearity in the current versus transparency characteristics. Another point that I'd like to comment on is the fact that there appears to be a

high sheath potential and I think that this is very much a function of what you might call optical transparency. Now in the particular case of the hollow cathode that the General Electric Co. is investigating, they have one large hole in a reasonably large surface surrounding it. I'm not sure whether you might call this a high optical or low optical transparency. How much coupling this hole does to the environment behind it I don't know. In our particular experiments we found that by using a cathode made from three great circles in a spherical type configuration, with transparency of about 99%, that the sheath potential rises to within 50 volts of the anode potential. At low transparencies, for example, less than 30%, but with the same diameter cathode, the sheath potential decreases to within 40 volts of the cathode potential. I think that there is something significant in that the lower the transparency, the closer one gets to cathode potential. You could look at this as a pertabation or bending in of the external fields into the interior of the cathode and more closely upon the idea of the plasma inside the cathode being generated by the back bombarding of the ions to the cathode surface. (Note - A more comprehensive treatment of this work will be published in the proceedings of the Electrochemical Society, 125th meeting.)

Question J. J. Difiglio, Continental Can Company. In the hot hollow cathode, what effect does gas pressure variation have on beam current and what magnitude of pressure are you operating at?

Answer Lidsky: Here again we need to separate the cathode interior from the exterior region. Outside the cathode itself after

passing through a stage of differential pumping the pressure is 10^{-4} mm-Hg, order of magnitude. There seems to be little effect on the beam at all unless you go to much higher pressures and that seems to be limited by the pumping capacity available. Once the beam is formed, once the electrons are released from the cathode, the beam isn't affected much by conditions outside the cathode. Inside the cathode the pressure seems to be in the order of mm-Hg. Here its more difficult to separate the pressure effects from anything else. The current-voltage characteristic is a function of the pressure, but again realize the pressure is not measured directly, but only the gas flow into the cathode so we only know the order of magnitude of the pressure. At higher gas flows into the cathode we find the same current at a lower voltage, for example, 30 amps - 30 volts instead of 30 amps at 35 volts if we have more gas feed.

Morley: Another interesting point here is the difference in the sensitivity of the two kinds of hollow cathode discharge to the operating pressure. With the hot cathode, the pressure in the chamber as distinct from that in cathode, can vary over quite a range of at least two orders of magnitude with only a few percent change in the beam current. I would like to ask Dr. Stauffer to comment on the cold hollow cathode discharge and say a few words about the current variations with pressure there.

Stauffer: In the cold hollow cathode we of course operate in the beam region and the pressure is considerably higher than it is in the low voltage mode. We can operate this way due to the

higher energy of the electrons which are therefore less susceptible to scattering. If we increase the pressure the beam current increases steeply to a point where instability sets in. A typical operating condition using argon, is a 20 kilovolt cathode potential, and a pressure of about 10 microns. The permissable pressure variation on this values is about ± two microns before the discharge is out of the beam mode. This is a distinct operating disadvantage and one has to use some sort of an automatic pressure servo regulating system, which we have, and in which we let the cathode current monitor the pressure.

Question Speaker from the floor - What is the operating pressure range for a hollow cathode discharge?

Answer Morley: For the hot hollow cathode, you can operate typically from 10^{-5} mm Hg through a hundred microns and higher, into the millimeter range if you desire. Of course at these pressures some loss of beam occurs by scattering, and you lose on efficiency somewhat. Any particular operating pressure is determined by the dynamic equilibrium between the gas load and the pumping speed.

Terhune: I would point out that in the operation of the cold cathode that we have very different pressure conditions for the different gases - for example with the heavier gases the pressure is a few microns at room temperature. With the light gases a few tens of microns pressure is necessary, and we have also operated in the range of one or two hundred microns with these lighter gases. The pressure not only depends upon the

type of gas and the sensitivity of the beam to the gas pressure but it is also very much a function of the particular gas being used.

Muly: We found in the screen mesch cathode electron beam that the range of operation before it arcs over into hollow cathode mode is a function of how sophisticated a focussing system is used on the outside. If simple geometries are used without focussing of the beam, then there is a wider range of pressure over which you can notice electron beams eminating from the dominant aperture. I'm speaking of the screen mesh balls in which there is one aperture which is say three times larger than the background hole size. With this kind of geometry, a sphere mounted on a very fine wire suspended in the center of a spherical chamber, you can operate over reasonably wide pressure ranges. With increase of beam power the operating pressure is reduced. It is limited by arcing over into the hollow cathode mode and will operate only over a small dynamic pressure range at high beam currents. If you want to obtain maximum power then the dynamic range of operation is decreased. For an increased dynamic range of operation the power is limited.

Question C. B. Montgomery, Union Carbide Corporation, and this has almost been answered, but we'll just round it off. What gases have been used with the hollow cathode discharge?

Answer Morley: You've already heard of argon, hydrogen, helium.

Muly: May I add another one? Water vapor!

Question J. Solomon, Sciaky Bros. and H. A. Steinherz, N.R.C. (Two very similar questions) Please comment on the practical applications

of hollow cathode devices.

Answer

Morley: Both types of hollow cathode are vacuum heat sources and hence there are a multitude of applications. In particular, the hot hollow cathode has been used for industrial vacuum melting and casting, strip annealing and brazing. It has also been used as an intense monochromatic light source, and also as the discharge within a duoplasmatron ion source for the production of heavy ions.

Stauffer: I would add that we have used the cold cathode for laboratory scale welding and button melting, but its prime use to us has been in attempting to understand the physics of its operation.

LASER INDUCED ELECTRON EMISSION

A. B. El-Kareh and E. Reyner
Electrical Engineering Department, Pennsylvania State University
University Park, Pennsylvania

ABSTRACT

The maximum thermionic emission obtainable from existing cathodes under pulsed conditions is on the order of 10 amp/cm^2. A theoretical analysis is made in which it is shown that the energy output of existing lasers should be able to raise the temperature of the surface of a tungsten rod 6.3 mm dia. to 3500^{o}K in less than 1 microsecond. The thermal decay time, to the point where the emission is reduced to 0.1 of its maximum value, is less than 1/2 microsecond. At 3500^{o}K the emission is 230 amp/cm^2. A system is described for the experimental verification of the theoretical conclusions. At the high temperatures involved, the tungsten vapor pressure is high enough to cause space charge neutralization. There is reason to believe that careful control of the laser input energy could result in an appreciably higher current density without initiating an arc.

LASER INDUCED ELECTRON EMISSION

Conventionally, pulsed electron beams are generated by either pulsing the grid voltage of a triode gun, or by pulsing the total accelerating voltage of the gun. In either case the cathode remains at a steady thermionically emitting temperature, and is typically limited to a current density 10 to 20 amp/cm^2. If a tungsten cathode is preheated to just below the level of substantial thermionic emission, and then pulsed with the energy from a laser beam, the resulting pulsed thermionic emission rises to values exceeding 200 amp/cm^2.

The first point to be considered is the rapidity with which the heat transmitted to the cathode will result into an acceptable emission value and the rate of the interruption of the emission thereafter. Namely the rise and decay times of the pulsed electron emission.

Consider an emitting area of 0.25" dia. or 0.316 cm^2 in area from a tungsten cathode 0.040" or 0.1 cm in thickness. This will be heated by a laser beam with a pulse length of 10^{-6} sec. with a pulse repetition rate of 1000/sec. Naturally other durations and rates might be chosen but this will not affect the derivations.

A laser beam is projected on the emitter area during the time $0 < t < t_o$ with an intensity such that the adsorbed power during this time is Q watts/cm^2. For the time $t_o < t < T$ the laser is turned off. Here $t_o = 1\ \mu$ sec. and $T = 10^{-3}$ sec.

The cathode configuration is shown in Fig. 1. Since the cathode diameter is large compared to the thickness, lateral effects can be neglected, the problem is considered unidimensionally, thus simplifying it considerably. Also, although the process is actually periodic, the periodic deviation $u(x,t)$ from the average temperature distribution can be computed adequately in aperiodic fashion, since $u(x,t)$ decays in the time of one cycle to about

1/200 of its peak value. The error, therefore, is negligible. The absolute temperature is given by:

$$T(x,t) = u(x,t) + \left[T_1 - (T_1 - T_2)\ \frac{X}{d}\right]$$

where:

d = cathode thickness

x = the distance along the thickness to the point considered

T_1 and T_2 = the temperatures at the cathode surfaces.

The average temperature is maintained by conductive heating, and the average energy of the laser beam is balanced by radiation from both surfaces of the cathode. u(x,t) obeys the well-known diffusion equation:

$$\frac{\partial^2 u}{\partial x^2} = \frac{1}{a^2}\ \frac{\partial u}{\partial t} = \frac{\rho c}{k}\ \frac{\partial u}{\partial t}$$

where:

ρ = density gm/cm^3

c = specific heat in cal/gm/deg

k = thermal conductivity in w/cm /deg

a^2 = diffusivity $/cm^2/sec$

We have the boundary conditions:

$$\left(\frac{\partial u}{\partial x}\right)_{x=o} = \frac{-Q}{k} + pu \qquad u(\infty,t) = o \qquad 0 < t < t_o$$

$$\left(\frac{\partial u}{\partial x}\right)_{x=o} = pu \qquad u(\infty,t) = o \qquad t_o < t < T$$

with:

$$p = \frac{4\sigma\epsilon T_1^3}{k}$$

where:

σ = Stefan-Boltzmann constant,

$\left(5.67 \times 10^{-12} \text{ watts/cm}^2/\text{deg}^4\right)$

ϵ = the surface emissivity of the surface

At this point this boundary condition should be explained. The interest here is in the dynamic case and not the static one, and the assumption is that the cathode is initially at a uniform temperature T_1 and that $T_1 > T_a$ where T_a is the ambient temperature. The temperature T_1 is maintained from the heat generated by a cathode heater and by the heat loss by conduction via the leads and by radiation from the surfaces of the cathode. This heat loss is of no concern to this analysis and attention is focussed on the heat gained or lost in excess of the T_1 equilibrium state, or mathematically, the heat loss due to $\left[\theta + T_1\right]^4 - T_1^4$ is to a first order of approximation, $4T_1^3\theta^{(1)}$.

For the case where $0 < t < t_o$, the solution is given by[2]

$$u(x,t) = \frac{Q}{kp}\left[\left(1\text{-erf } \frac{x}{2a\sqrt{t}}\right) - e^{-px+p^2a^2t}\left(1\text{-erf}\left(\frac{x}{2a\sqrt{t}} + pa\sqrt{t}\right)\right)\right]$$

For the case where $t_o < t < T$ the solution is[3]

$$u(x,t) = \frac{Q}{k}\frac{e}{2}^{px+a^2p^2(t-t_o)}\int_o^\infty \left(1-\text{erf}\frac{x'}{2a\sqrt{t_o}}\right)\left[e^{-px'}\left(1-\text{erf}\frac{x-x'+2a^2p(t-t_o)}{2a\sqrt{t-t_o}}\right)\right.$$

$$\left.-e^{px'}\left(1-\text{erf}\frac{x+x'+2a^2p(t-t_o)}{2a\sqrt{t-t_o}}\right)\right]dx'$$

For tungsten at 3000°K,

$a^2 = 0.5$ / cm^2 / sec

$k = 1.32$ watts/cm. degree.

$p = 0.05$/cm. (between 2000 to 2500° K)

Then for $0 < t < t_o$, remembering that

$$\text{erf}(x) = \frac{2}{\sqrt{\pi}}\int_o^x e^{-y^2}dy$$

and that for very small values

$$\text{erf}(x) \approx \frac{2x}{\sqrt{\pi}}$$

then,

$$u(o,t) \approx \frac{Q}{kp}\,\text{erf}(pa\sqrt{t}) \approx 0.61 \cdot Q\sqrt{t}$$

Now $Q = \dfrac{u(o,t_o)}{0.61\sqrt{t_o}}$ or for a variation of 1000°K and a time $t_o = 10^{-6}$ sec.

Q = 1.6 megawatts per square centimeter.

For a variation of 1500°K, this Q will be 2.4 megawatts/cm^2.

However, for tungsten the absorbtivity at the laser wavelength of 7000 Å is approximately 0.4. Therefore the power concentration will be

$$\frac{2.4 \times 10^6}{0.4} = 6 \text{ Mw/cm}^2$$

The emission density for tungsten is given by

$$j = 60T^2 e^{-52.4 \times 10^3 / T} \text{ amp/cm}^2$$

Table I shows the electron emission for tungsten for various temperatures:

TEMPERATURE, degK	ELECTRON EMISSION, amp/cm^2
2000	9.8×10^{-4}
2100	3.9×10^{-3}
2200	1.3×10^{-2}
2300	4.1×10^{-2}
2400	1.2×10^{-1}
2500	3.0×10^{-1}
2600	7.0×10^{-1}
2700	1.6
2800	3.5
2900	7.3
3000	14.0
3100	27
3200	49
3300	82
3400	140.
3500	230.

TABLE I

The life of the cathode is determined mainly by the rate of vaporization of the material at the cathode surface. It is generally accepted that the life of a cathode is determined by the length of time taken to vaporize 12% of its original weight. If v is the rate of evaporation of the material per second per cm^2, and if the circumference of the cathode (in the case of wire filaments) be S then the rate of loss of weight is $dm=v.S.dt$. If now ρ is the specific weight and r the radius of the cathode then $\rho dr=v.dt$ or

$$(r_1 - r_2) = \frac{v}{\rho} \cdot t$$

now we have $r_2 = r_1\sqrt{0.88}$ (this can be readily seen when the 12% reduction is considered).

Hence:

taking $\rho = 19.3$ for tungsten

$$\frac{1.16r_1}{v} = t \text{ seconds}$$

gives the life of the cathode as a function of the radius and rate of evaporation. The rate of evaporation is naturally a function of the emission.

The life plotted on the curves in Fig. 2 was computed from the published empirical results for circular filaments heated by direct currents passing through them. It should be borne in mind that while the life is given with these assumptions in mind they do not apply too well to this cathode, because the configuration is entirely different. Nevertheless these figures are given to an order of magnitude approximation of the life to be expected.

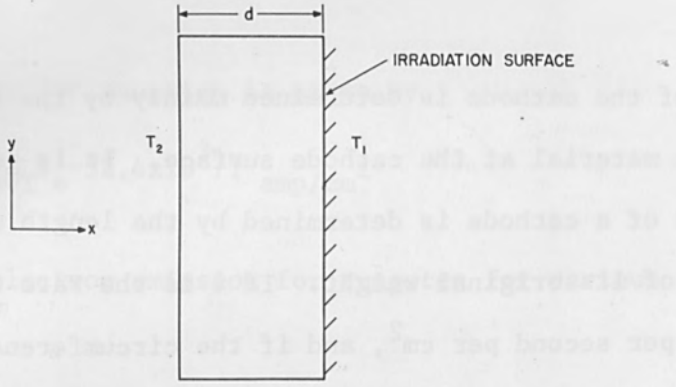

FIGURE 1 Cathode Configuration

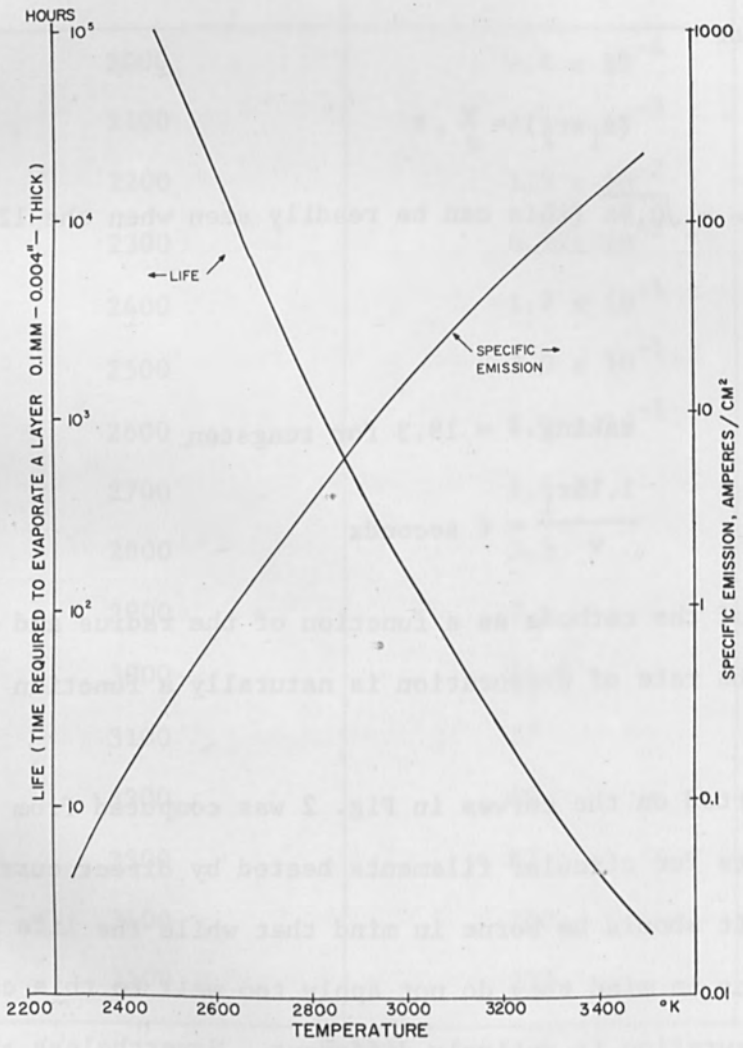

FIGURE 2 Specific Emission and Life of Tungsten Cathode as a Function of Temperature

After the interruption of the laser pulse, $t_o < t < T$, and this case will now be investigated:

$$u(o,t) \; \frac{Q}{k} \cdot \int_o^\infty \left(1-\text{erf}\frac{x'}{2a\sqrt{t_o}}\right)\left(\text{erf}\;\frac{x'}{2a\sqrt{t-t_o}}\right) dx'$$

If $t - t_o < t_o$

this can be written as:

$$u(o,t) \approx u(t_o) \left[1 - \frac{\sqrt{t-t_o}}{t_o} + \frac{1}{2}\frac{t-t_o}{t_o} - \frac{1}{8}\left(\frac{t-t_o}{t_o}\right)^2 + \frac{1}{16}\left(\frac{t-t_o}{t_o}\right)^3 - \frac{5}{128}\left(\frac{t-t_o}{t_o}\right)^4 \cdots\right]$$

and $t - t_o >> t_o$, $\therefore$

$$u(o,t) \approx \frac{Q}{k}\;\frac{4a}{\sqrt{\pi}}\;\frac{t_o}{\sqrt{t-t_o}} \int_o^\infty x(1-\text{erf}\;x)\;dx.$$

$$\approx \frac{Q}{k}\;\frac{at_o}{\sqrt{\pi(t-t_o)}}$$

Fig. 3 shows the temperature variation, with corresponding specific emission and life during the pulse.

Fig. 4 shows the temperature variation, with corresponding specific emission and life after termination of the laser pulse.

It is well known that the output from a laser can reach a power concentration of several megawatts per cm^2 in a very small finite area under pulsed conditions. The pulse repetition rate is very limited. With the presently known techniques, it is possible to obtain a small power concentration with c.w. operation. If the pulse repetition exceeds the permissible rate of the laser (which is very low) the power output drops

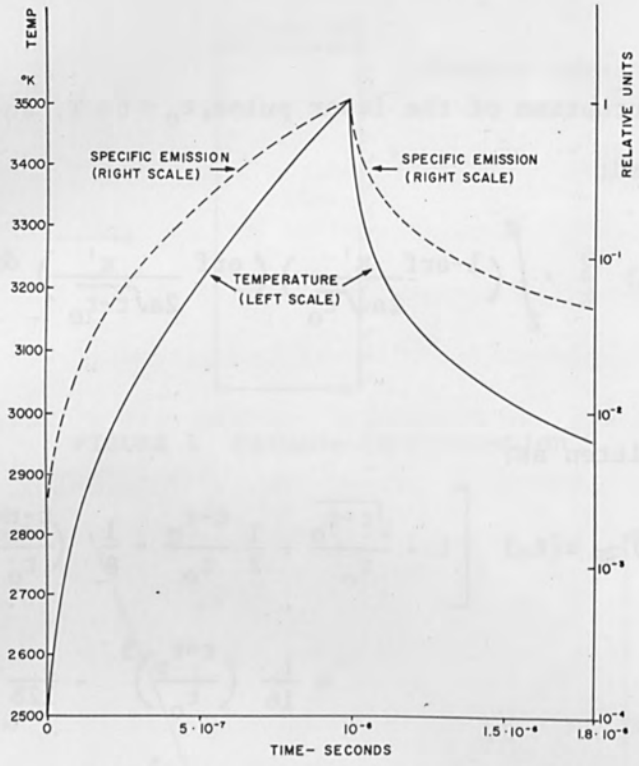

FIGURE 3 Variation of Temperature, and Specific Emission During Pulse

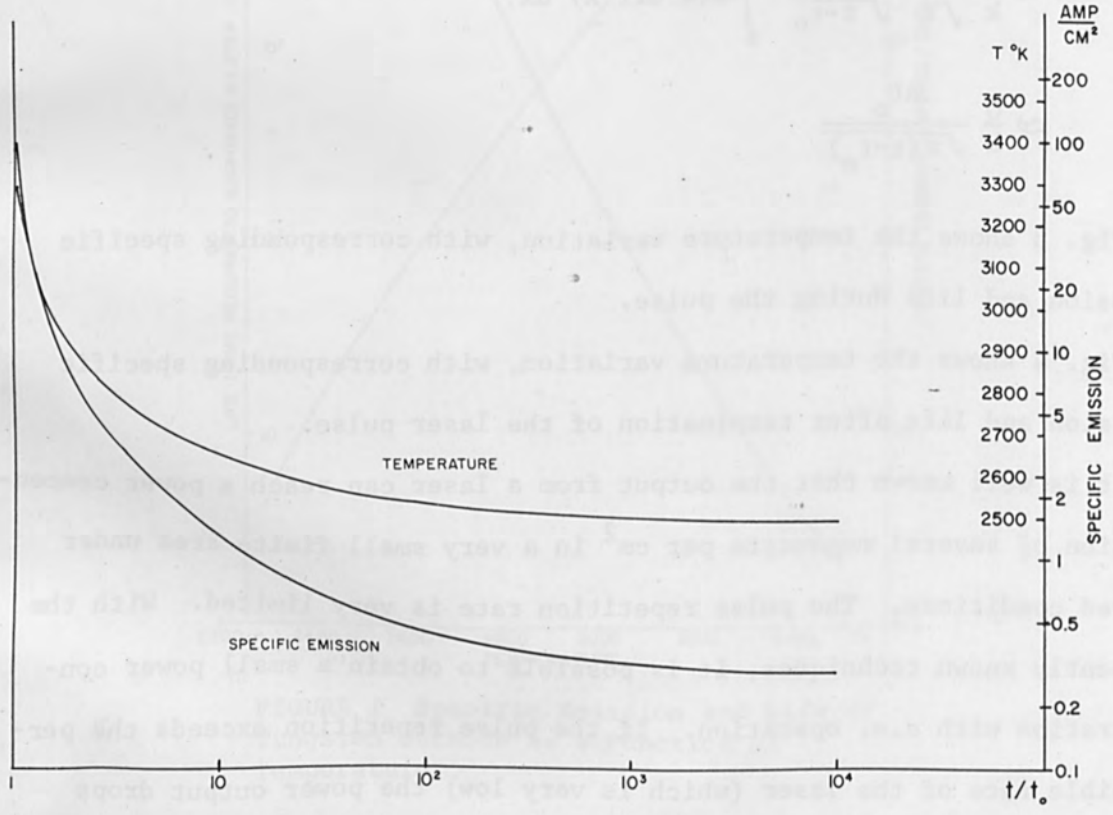

FIGURE 4 Decline of Temperature, Specific Emission After Termination of Laser Pulse

accordingly. In the limit one approaches the c.w. output. It should be said at this point that for a successful operation of a microwave tube, uniform concentration at each pulse is absolutely essential.

Laser induced thermionic emission has been investigated by many authors (4, 5, 6, 7, 8). While most of the workers agree that the enormous value of the emission (almost 10^8 times larger than the space-charge limit computed for a single diode) is not space-charge limited, no attempt has been made to explain the complex situation arising due to space-charge neutralization.

It was determined that field emission is not the mechanism, for at optical frequencies, the field does not act in one direction long enough to free electrons from the target material.

At the high temperature of nearly $3500^{o}K$, the vapor pressure of the cathode material becomes high enough to cause a dense vapor cloud which could lead to space-charge-neutralization and under such conditions it would be inappropriate to apply the Child-Langmuir law. It is clear that a plasma is formed from which enormous currents can be obtained.

By carefully adjusting the input power of the laser, or the power concentration at the cathode, it is possible to momentarily raise the temperature of the cathode high enough to generate a plasma, but not sufficiently high to initiate an arc. There is reason to believe that this difference has not been taken into account by many authors in this field.

In addition to providing an enormous cathode current, space-charge-neutralization offers the possibility of extracting currents from the cathode at a lower anode voltage. If these effects can be shown to be stable and controllable, they will be of primary importance in the design of a new generation of high perveance electron guns.

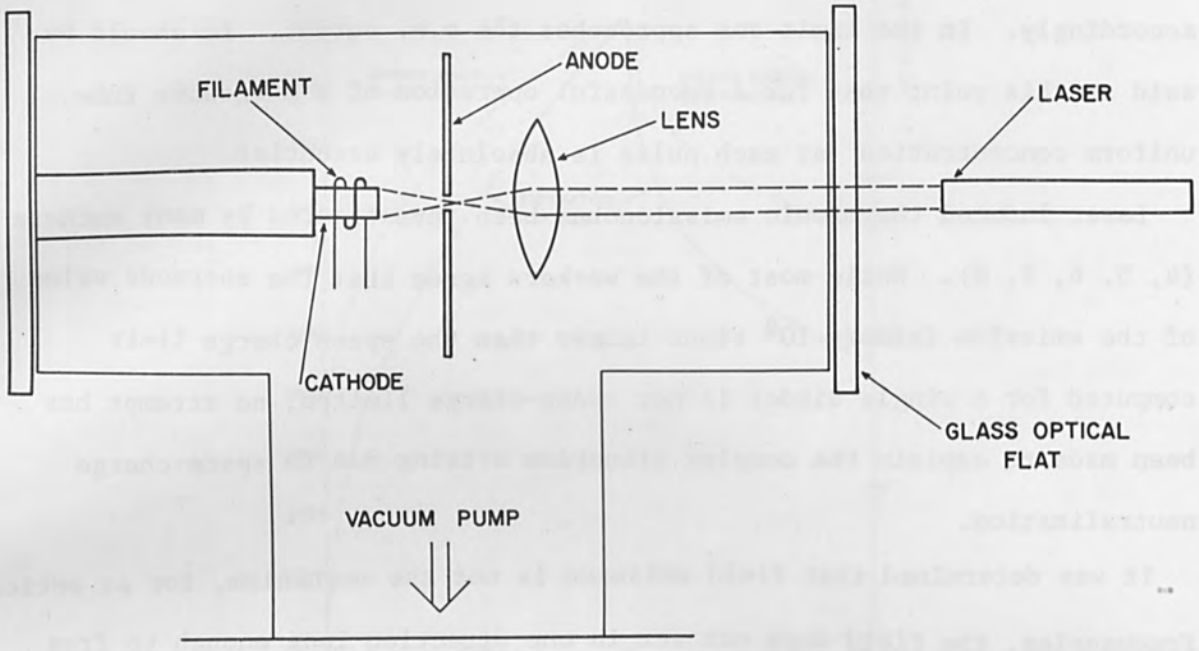

FIGURE 5 Experimental Arrangement

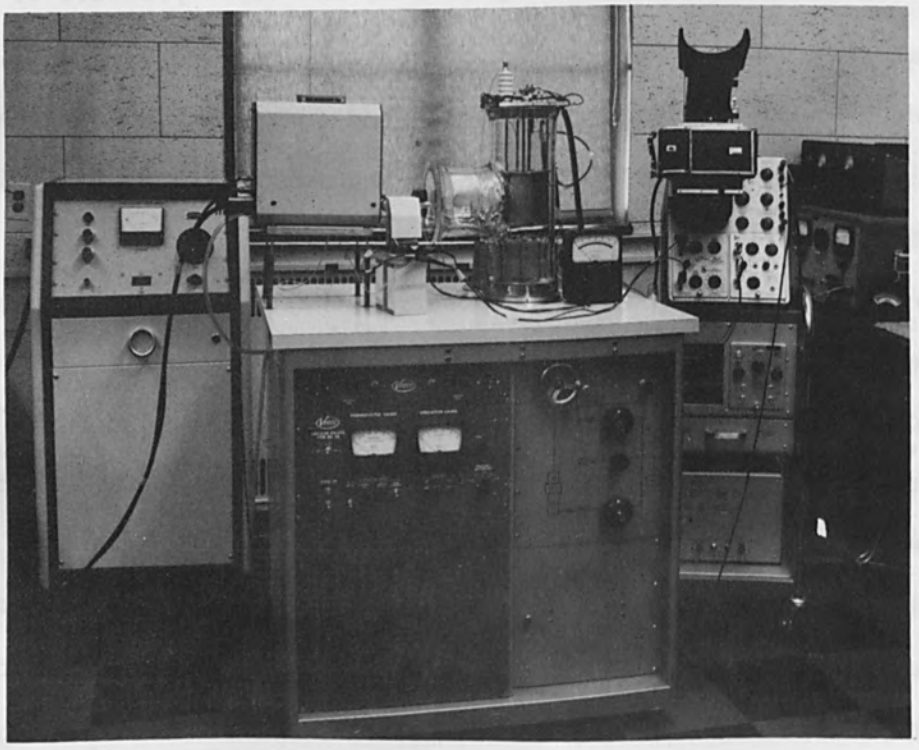

FIGURE 6 General View of Apparatus

Since intense laser beams of small cross section are currently available, this system of cathode heating would appear ideal for incorporation into millimeter-wave klystron (or T.W.T.) designs intended for the generation of high peak powers.

EXPERIMENTAL LAYOUT

Fig. 5 shows a schematic of the assembly. A tungsten rod of appropriate diameter is installed inside a large holder and is heated by electron bombardment emanating from a tantalum strip surrounding the rod. The anode is in the shape of a disc facing the cathode with an opening in the center to allow the passage of the laser beam. The tungsten rod diameter, the spacing between anode and cathode, the concentration of the laser power and the steady state temperature of the cathode can all be varied at will. A glass lens of appropriate focal length is mounted in front of the anode. The whole system is assembled inside a Pyrex T and evacuated by a vacuum system. A laser of 25 joules output is used to irradiate the surface of the cathode. Preliminary results have shown that electron pulses can be obtained. Quantitative as well as qualitative results will be reported at a later date.

Fig. 6 shows the actual assembly.

ACKNOWLEDGEMENT

The authors wish to thank W. Felling and K. Bowness of Raytheon for the use of the laser equipment. Thanks are also due to E. G. Ramberg for his assistance in the theoretical derivation.

REFERENCES

1. Carslow and Jaeger, Conduction of Heat Through Solids, Clarendon Press, Oxford 1947, Page 15.
2. Idem, Equation 5, Page 53.
3. Idem, Equation 1, Page 40.
4. Honig, R. E. and Woolston, J. R., Applied Physics Letters 2, 138 (1963).
5. Verber, C. M. and Adelman, A. H., Electrochem Soc. Meeting, Pittsburgh, Abstract 39 (1963).
6. Lichtman, D. and Ready, J. F., Phys. Rev. Letters 10, 342 (1963).
7. Honig, R. E., Applied Physics Letters 3, 8 (1963).
8. Giori, F., MacKenzie, L. A. and McKinney, E. J., Applied Physics Letters 3, 25 (1963).

ELECTRON BEAM APPLICATION TO WELDING SPACE PROPULSION COMPONENTS

George Tulisiak
NASA, Lewis Research Center
Cleveland, Ohio

ABSTRACT

Electron beam techniques for joining space engine components have been employed at the Lewis Research Center of NASA for more than three years. Fabrication methods developed include the production of porous tungsten ion emitters, thermionic diodes, and liquid metal heat transfer assemblies. Materials involved in these applications include solid and porous tungsten, molybdenum, tantalum, columbium 1% zirconium, columbium, titanium, and stainless steel. Some applications have involved the use of the electron beam for vaporizing metals onto nonmetals. Components produced for Zero G gravity testing required the vaporizing of tungsten and nichrome materials for deposition onto glass and ceramics.

The electron beam equipment employed includes both high and low voltage power sources.

ELECTRON BEAM APPLICATION TO WELDING SPACE PROPULSION COMPONENTS

The manufacture of space propulsion components has necessitated the use of very fine electron beam welding techniques. Many components of space engines required joints be made under extremely clean conditions due to the nature of the materials involved. Initial attempts at making some of these joints with normal heliarc techniques were unsuccessful. The joint either had too wide a weld band, and the large heated area caused cracking, or the joints became contaminated. In view of this, consideration was given to the possibility of solving these joining problems by the application of electron beam techniques.

Electron beam welding of space engine components at Lewis Research Center has been in use for more than three years. A high voltage welder was installed in December, 1960. Journeymen model-makers were selected to operate the equipment. Due to their thorough experience in fixturing and knowledge of metal movement and heat transfer, satisfactory welds were produced by them within a few weeks after the equipment was installed.

One of the first fabrication problems solved by the electron beam welder was the manufacture of emitters for ion engines. Propulsion engines for space travel require the use of an emitter that causes a metallic vapor, such as mercury or cesium, to ionize when it contacts the emitter surface. When a potential difference is impressed between the emitter surface and accelerator plates, the ionized metallic vapor is extracted from the emitter surface at a certain velocity. The kinetic energy of this ionized beam develops a thrust suitable for space propulsion. The emitter itself must have a good capacity, or a work function suitable for ionizing the vapors, and it must use its maximum surface area to obtain the greatest amount of ionization. A material that satisfies these requirements is porous tungsten. In an ion engine assembly, the porous tungsten emitter

must be joined to a supporting structure which is usually of wrought tungsten. The first design (Fig. 1) involved the installation of a porous tungsten plate 0.060" x 0.300" x 6" long, into a wrought tungsten window of overall dimensions 1 1/2" x 8". All attempts at making this weld resulted in cracking of the base material. These assemblies were finally made by dividing the wrought tungsten into four pieces and welding each piece to the porous tungsten individually. In this manner, the problem of welding in the center of a wrought tungsten mass with its shrinkage problem, was overcome.

The second joint to be made was the attachment of a tantalum housing to the wrought tungsten supporting plate. This was performed by the use of a titanium filler to fuse the tungsten to the tantalum housing. In this design the emitter and its housing required a large heat input before the porous tungsten would reach its operating temperature of 2350°F. A new design was suggested to reduce the necessary heat input. Instead of a tungsten window, it was suggested that a wrought tungsten channel be formed which would then be attached to the porous tungsten. (See Figs. 2 and 3.) Two 6" longitudinal seams were required. End pieces of wrought tungsten were then attached to the porous tungsten and wrought tungsten channel. A hole was then made in one end piece, and a tantalum tube attached. A columbium or titanium ring was first fitted over the tantalum tube, and the electron beam was focused on this filler ring. While the ring was melting, the adjacent areas of tungsten and tantalum got just hot enough with the use of the beam to cause fusion by a brazing action. This technique of brazing with the electron beam was used and gave a crack-free joint. In this particular instance, a weld of the tantalum tube to the tungsten end plate was unsatisfactory. The weld alloy formed was brittle and, in some

instances, showed cracks.

This design was used as a single emitter engine in most cases. In one assembly, an array of 10 emitters was constructed in one engine and connected to the cesium boilers by tantalum and stainless steel tubing.

The most recent emitter constructed with the electron beam welder has eliminated the need of a channel. The porous tungsten was purchased in the form of a tube. With the aid of beam deflection, most of the porous tungsten surface was scanned by the beam to give an impervious surface, (Fig. 4). Only a narrow strip of the surface was not scanned by the beam and remained porous. End pieces were then welded to the porous tungsten tube, and a tantalum feed tube was attached to the end piece using titanium or columbium as a braze material.

The fabrication of ion emitters with porous tungsten tubes provided an increased strength to the assembly, with the additional advantage of being able to heat it by resistive means rather than by reflective methods.

Electron beam methods have proven very satisfactory for the welding of thin tungsten reflector shields and cylinders down to 0.0015" in thickness. The methods used required welding speeds up to 100"/min. In some instances, the material was overlapped, and the beam was pulsed while welding the initial seam. Pulsation techniques minimized the shrinkage and lowered the tendency to crack of the recrystallized tungsten weld. Butt welds were also made on 0.002" tungsten sheet. In this case also, a high welding speed, up to 100"/min helped to obtain a crack-free weld.

Research efforts in extruding various materials have required the encapsulation of powders inside molybdenum and tungsten billets. A billet was installed in the vacuum chamber with the billet lid held open by a solenoid device. A heater around the billet raised its temperature to 400°F,

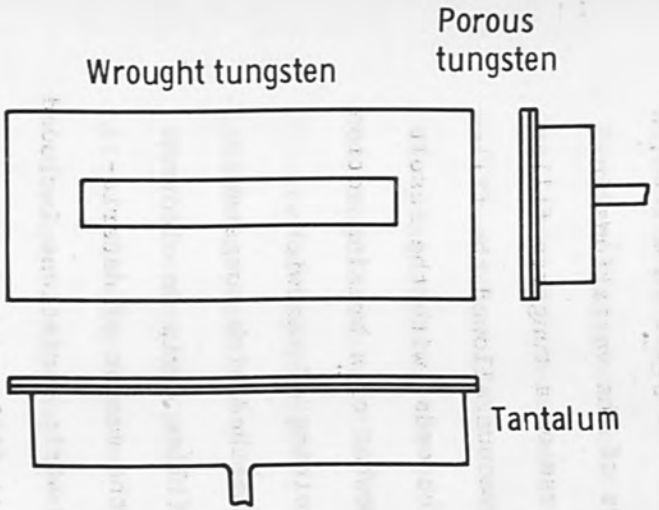

FIGURE 1 Plate and Box Ion Emitter

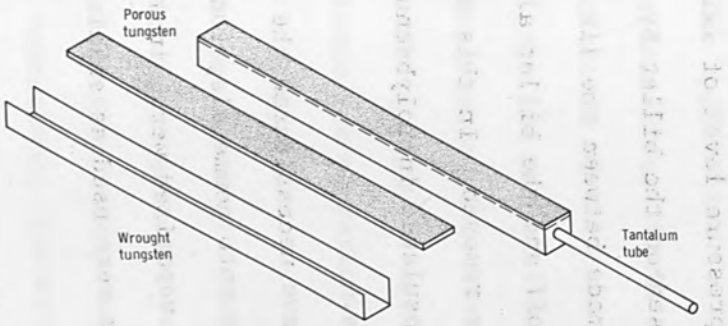

FIGURE 2 Ion Emitter Assembly

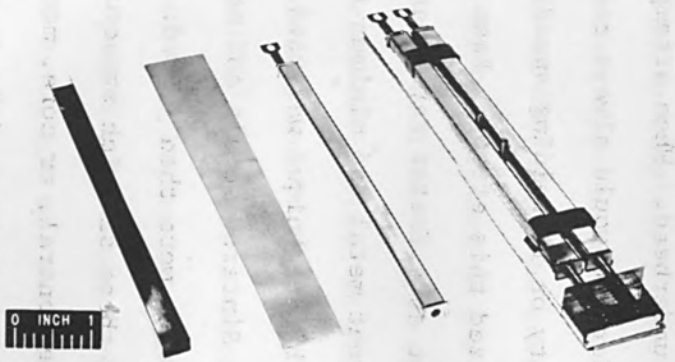

FIGURE 3 Ion Engine Emitter Assembly

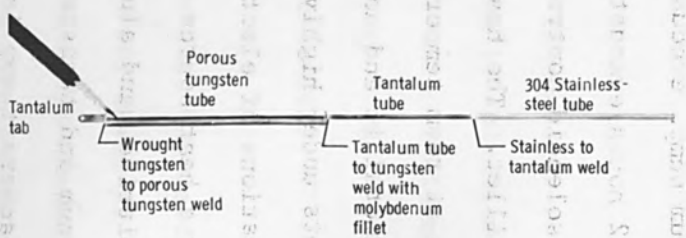

FIGURE 4 Porous Tungsten Ion Engine Emitter Assembly

while the vacuum pumps evacuated the system to a pressure level of $1x10^{-5}$ Torr. After 12 hours evacuation, the lid was closed on the billet by actuating the solenoid control. A weld was then made between the lid and the tungsten billet. The heater was then turned off and the billet allowed to cool. When at room temperature, the billet was removed. In this manner, powders, both metallic and nonmetallic, were encapsulated in molybdenum and tungsten billets under highly evacuated conditions.

Some applications of electron beam equipment have necessitated the use of the beam as a heat source for vaporizing metals onto nonmetals, such as pyrex, boron nitride, and alumina. The materials vaporized were, in most cases, molybdenum and tungsten. Films of tungsten were used as small heaters for spacecraft applications.

Tungsten tubes were also required which had a weld seam with essentially no crown or underbead. When attempting a straight butt joint on a tube, a crown or underbead would always result, regardless of the variations in beam intensity or in welding speed; however, the use of a tungsten filler strip minimized this effect. Beam welding under vacuum allowed the filler strip to heat at a faster rate than the butted tube ends, with the result that the parent metal had minimum fusion, and somewhat of a brazing action resulted. This technique was used also for the joining of sandwich structures. Sintered metals and nonmetals were sheathed with tungsten. These sandwiches were then joined. The use of a filler strip in electron beam welding these sandwich structures minimized the amount of deterioration of the central, or core, material. Filler strip variations included the use of "T" sections. "T" sections were used as filler strips to prevent blow-thru of the top tungsten sheath. The total mass of the "T" section filler was assimilated in the joint area.

ELECTRON BEAM APPLICATION TO WELDING SPACE PROPULSION COMPONENTS

One application for electron beam welding necessitated the construction of a heater for liquid metals from columbium-1% zirconium alloy. The manufacture of this heater posed a number of fabrication problems. (See Fig. 5) The material was 1" I.D. by 0.050" wall, columbium-1% zirconium tubing, selected because of its compatibility with liquid metals and its relatively high strength at elevated temperature. The heater coil was designed for operation at 500 kw and was approximately 6' long, 18" deep, and 4' high.

A requirement in producing the heaters was that the weld material impurity level must not be higher than the impurity level of the parent metal itself. Also, the parent material must not be contaminated by the processing operations. Incomplete penetration of the parent metal by welds was unacceptable. Underbead was to be held to a minimum, undercut was completely unacceptable, and the weld metal had to be completely free of inclusions. Previous research indicated the need to over-age the welds at 2200^{o}F. This was a precautionary measure against loss of ductility and corrosion resistance that might occur from precipitation of zirconium gas complexes at the grain boundaries of the weld metal. In addition to all of these welding requirements, the tubing had to be chemically clean at all times.

The tubing provided, as previously stated, was 1" I.D. and 0.050" wall thickness, and the lengths varied between 17' and 19.5'. After some initial consideration was given to the welding of this heater by inert arc methods, it was finally decided to perform this operation by electron beam welding techniques. The equipment used was a 30 k.v., 250 ma. machine. The chamber on this unit was approximately 84" long, 36" deep, and 66" high. The chamber was evacuated by two 20" diffusion pumps which were backed by two 300 C.F.M. mechanical roughing pumps. This vacuum pump system was

capable of evacuating the chamber down to 1×10^{-6} Torr in 1 hour. The outgassing rate was 1μ/hr, when clean procedures were observed in the chamber.

To fabricate the heater in this chamber, a decision had to be made about the method of welding. Obviously, since the heater would be completed as one single length of tubing over 200 feet long fabricated from 19-foot lengths, the tubing would have to protrude through both ends of the welding chamber. The question therefore was whether to rotate the tubing, or the welding apparatus. It was decided to attempt to obtain good welds by rotating the welding apparatus.

A table was available with the electron beam welding equipment, which allowed rotation of the electron gun in the horizontal plane. This table was modified to allow the gun to revolve in the vertical plane. The tubing would therefore pass through one port in the chamber, through the center of the welding table which was set vertically, and then through the port in the opposite end of the welding chamber. The necessary fixturing was provided at the welding area to allow close abutment of the tubes to be joined. In addition to slipping the tube through the welding fixture and chamber ports, a heater coil was also wrapped around the tubing in the far end of the chamber, away from the welding apparatus. The heater coil was to be used for over aging the welds at 2200°F.

Initial attempts at making a good weld with the gun rotating around the tube were very discouraging. The high voltage for the gun, had to pass from the power leads to stationary power rails on the welding table. (See Fig. 6) The power rails were mounted on nylon supports. Brass shoes sliding on the rails then picked up the high voltage power and fed it into the gun. Serious arcing was observed on the insulating supports on this apparatus.

The shoes had to be remachined and the supports cleaned. Finally, with adequate shielding from the products vaporized by the electron beam, the table remained clean, the arcing eliminated, and the welding commenced.

Short lengths of tubing were initially used in the chamber to evaluate the fixturing. When these welds showed good penetration and quality, full length tubes were inserted through the ports. It was decided that no attempt would be made to maintain a high vacuum on the inside of the heater tube as it grew in length, but to insert a baffle inside the tube about 3 feet from the weld area. In this manner, only one length of tubing required evacuation, regardless of the length of the tubing in the coil. On the side of the heater where the loops were formed, only a rough vacuum was maintained. (See Fig. 5.) On the side where the extra tube was to be added, a diffusion pump and roughing pump held the inside of the tube at a pressure 1×10^{-5} Torr and it had an outgassing rate of 1μ/hr. The outgassing rate was obtained by repeatedly flushing the system with high purity argon, with subsequent preheat of the tubing, and further pumpdown.

With this evacuation technique, the first weld was made, X-rayed, and cut out for analysis. The analysis indicated that there was no contamination in the weld. Subsequently, another weld was made, heat treated at $2200^{\circ}F$, cut out, and analyzed. Once again, no contamination of the weld metal was observed by the analytical techniques.

The next weld was then processed with X-ray inspection, heat treated, and the two tube length was bent to the loop dimensions. New lengths of tubing were then added until 14 welds were made and a coil, made from over 200 feet of the tube, was formed. In obtaining the 14 good welds, two bad welds were cut out and the tubing rewelded. The bad welds were rejected because arc-over of the welding apparatus caused blow-through on the

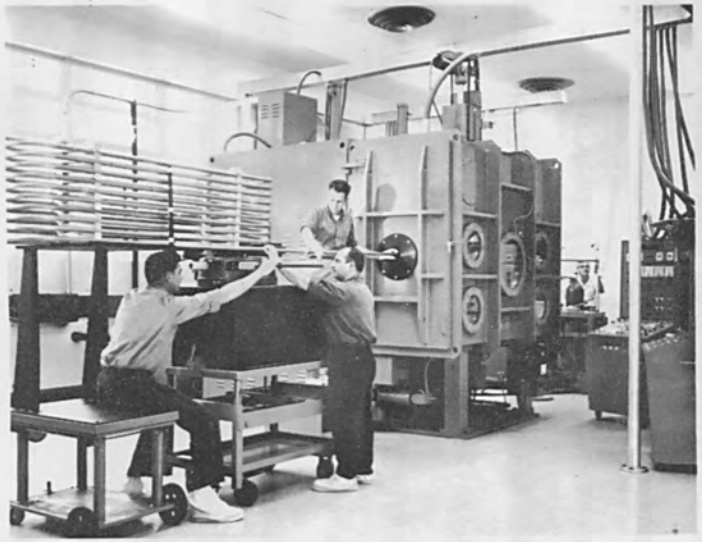

FIGURE 5 Columbium - 1% Zirconium Heater Manufacturing Operation

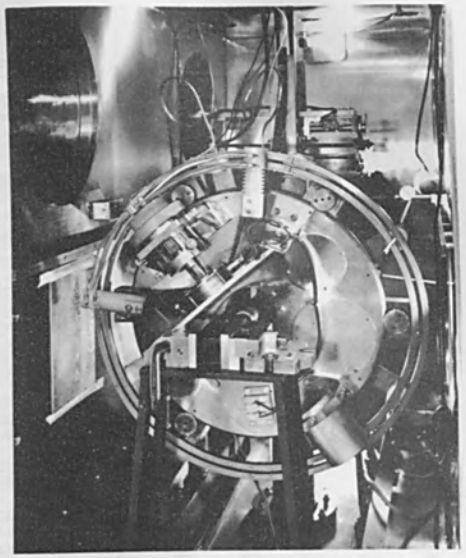

FIGURE 6 Fixture for Welding 1" I.D. Columbium - 1% Zirconium Tubing

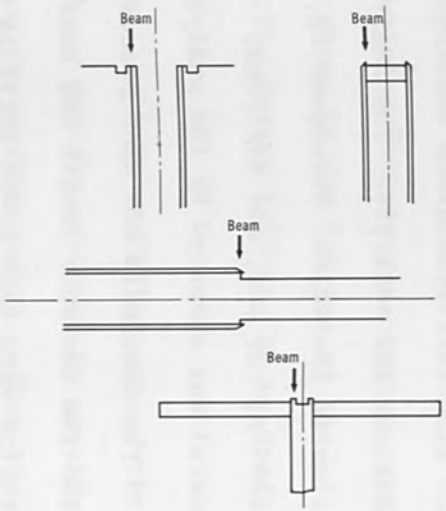

FIGURE 7 Joint Preparation for Welding

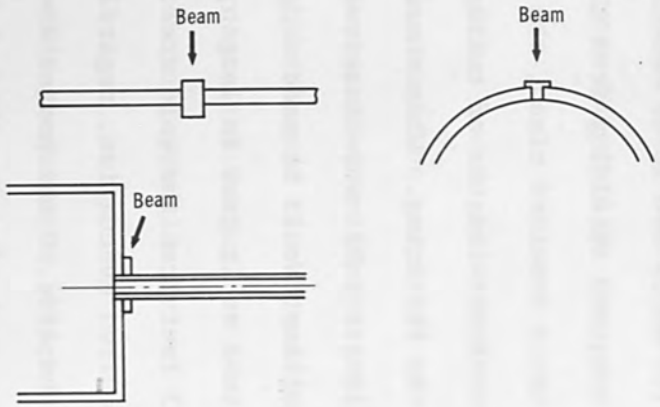

FIGURE 8 Welding with Fillers Preplaced

tubing. This condition was eliminated by cleaning the electron gun.

The applications discussed comprise essentially 90 percent of the work necessitating electron beam welding. In most instances, these applications involved the use of refractory metals. Occasionally, electron beam techniques are used involving other than refractory materials. The attachment of metallic auxiliary equipment to glass, metal, and ceramic-metal apparatus at times requires the use of the electron beam to keep the heat-affected area down to a minimum to prevent the fracture of glass components from thermal shock. Another application required beam penetration through a stainless-steel sheath into some strain gage apparatus supports. In this case, the requirement of high depth-to-width ratios in the weld bead was extremely important to prevent overheating of the fine wire circuits in the strain gage. The electron beam method was found to be most suitable for applications of this type.

Another area of interest was the attachment of metals to nonmetals such as alumina and zirconia refractories. Success in performing these operations have been limited to the joining of small diameter tubes and the attachment of wire to the ceramics. In all cases, poor results were obtained when the beam was directed on the ceramic-metal joint area. Best results were obtained when it was possible to direct all of the beam onto the metal and allow conduction of heat from the metal to the ceramic to cause fusion in the joint area.

Experience has indicated that fixturing, along with a knowledge of the material characteristics, account for 80% of the effort required to obtain a satisfactory product. The advantages gained by welding in a vacuum with a high energy density electron beam are counterbalanced by the high degree of accuracy required in setting up parts to be welded.

Generally, a part will be joined by normal heliarc methods, unless the need for cleanliness and small heat-affected areas requires the use of electron beam methods. Electron beam joining when necessary, is noted on prints, and then the machinists are aware that the part tolerances are much closer for such joints.

In preparing joints, usually an attempt is made to avoid focusing the beam in the center of a mass of metal. When the beam is focused in the center, the contraction that occurs upon solidification sets up very high stresses and in the case where the material has a brittle recrystallization, as tungsten does, then cracking occurs to relieve the stress. One way to eliminate this cracking is to design the joint so as to prevent any melting in the center of a mass. Trepanning the parts is one way to accomplish this. (See Figs. 7 and 8.)

Size consideration is also of the utmost importance. When attempting joints in dissimilar material, especially with the refractory materials, it is usually worthwhile to place the more highly expansive material on the I.D. and the less expansive material on the O.D. Less joint cracking will be observed with this technique. Some dissimilar combinations tend to form brittle intermetallics, even though the parent materials are basically ductile, for example, the welding of molybdenum to tantalum usually results in a brittle joint. The addition of titanium as a filler will improve the ductility and give a crack-free joint. The weld metal formed would have of course, a somewhat lower melting point and must be compatible with the application.

Many applications require a large number of tubes to enter into a header plate. One such application required 34 ceramic feed-thru connectors to be attached to a stainless-steel plate. Each connector had a 3/8" diameter

nickel-iron tube attached to the ceramic by metallizing. The other end of the nickel-iron tube was to be attached to the stainless-steel plates. Attempting to put 34 of these tubes into a 3-inch-diameter stainless-steel plate is an almost impossible task with normal electron beam techniques. Moving the electron beam in a circle, rather than rotating the part however, simplified this task. The 34 tubes were fitted to the stainless plate in a revolving chuck fixture with the stainless plate held horizontally. The tubes were then programmed and indexed over the electron beam generated circle. In this manner 34 tube to header welds were made with only one pumpdown of the chamber.

Many applications required extremely good chamber evacuation techniques prior to welding. In these cases, the part to be welded was fitted with a heater to preheat it to approximately $350^{\circ}F$. The chamber was baked out by radiation heating, and argon purges of the chamber were conducted to obtain a pressure of 1×10^{-6} Torr, and a rate of pressure rise in the chamber, after closing the vacuum valves, of less than 1μ/hr.

Generally, in electron beam welding, 80% of the task is considered accomplished prior to the part being inserted into the welding chamber. The close tolerances needed in joint preparation together with a good materials knowledge, has required the services of personnel who were well acquainted with fixturing, machining, and model making. When attempting joints for space engine components, the success or failure of the assembly depends to a great extent on how well the welding personnel understand the materials and also on the metal movement which occurs when the heat is applied. At the Lewis Research Center, the people who make electron beam welds are selected from instrument model-making personnel. These people understand the intricacies of jigging and fixturing, metal movement,

tolerances required, and the effect of heat when the beam is applied. Since these people are basically instrument men, they can handle equipment maintenance of the vacuum control system, and to a certain extent, trouble-shoot the electronic circuits.

Electron beam welding at Lewis has in the past solved many joining problems which we previously considered impossible. The future for electron beam techniques in joining space propulsion components is definitely showing signs of increased application.

ELECTRON BEAM AS A DIRECT OR AUXILIARY TOOL FOR BRAZING

Clyde M. Adams, Jr., David Parker and Stanley Weiss
Department of Metallurgy, Massachusetts Institute of Technology
Cambridge, Massachusetts

ABSTRACT

The brazing of beryllium and other metals or alloys which form stable and refractory oxides, can be greatly improved by surface treatments which promote wetting by liquid metals. The essential feature of the treatment is that wetting and solution of the oxide itself is accomplished by the use of wetting agents and has found application in the preparation of glass-to-metal or ceramic-to-metal seals. One such agent is metallic titanium. The technique of pre-coating the beryllium surface, in preparation for brazing, by the vacuum evaporation and deposition of titanium, has exhibited a profound influence on the wetting and spreading of a variety of filler alloys. These include silver-copper, gold-nickel, copper-beryllium, and pure aluminum. Although the primary objective of this work has been to develop improved techniques for brazing beryllium, the titanium pre-coating process has been found equally effective with other difficult-to-braze compositions, such as martensitic stainless steels and several high temperature alloys.

In this work both the titanium evaporation plating and the brazing processes were conducted in a vacuum environment at 10^{-4} Torr using a low voltage electron beam as a heat source. Since liquid titanium is almost a universal solvent, and the metal has quite a high melting point, an electron beam may be the only workable heat source for rapid evaporation of this metal, and this technique was used. Fortunately titanium has a high enough vapor pressure that treatment can be accomplished in a period of 5 minutes or less. Evaporation plating and brazing are accomplished in separate steps; the titanium plating treatment is in no way poisoned by intermediate contact with air, prior to brazing.

ELECTRON BEAM AS A DIRECT OR AUXILIARY TOOL FOR BRAZING

INTRODUCTION

A low voltage electron beam promises to be a very useful tool for brazing, and may be applied in either or both of two ways:

1. For pre-treatment of surfaces to be joined by brazing, and
2. As a vacuum heat source for the brazing operation itself.

Little is known about wetting agents in metallic or ceramic systems. The use of reagents which promote wetting has long been used in the joining by brazing of difficult-to-wet surfaces such as ceramic oxides, graphite, highly reactive metals, and in the production of glass-to-metal seals. Most of these reagents contain one or more of the following metals, either in pure form or as a hydride or halide: Mn, Mo, Ta, Ti, Zr, or B. In some cases the reagent is dissolved in the brazing alloy while in others it is pre-deposited on the solid surfaces. In all cases the objective is to promote wetting. Vacuum evaporation has been found extremely effective as a technique for activating a surface to promote wetting. The most effective reagent tested to date has been pure titanium, deposited by electron beam evaporation on the surface to be wet, and the results of this technique as applied to the joining of beryllium are outlined below.

In addition, certain of the unique features, advantages, and difficulties associated with low voltage electron beam brazing are outlined.

SURFACE TREATMENT TO PROMOTE WETTING

Vacuum deposition of extremely thin layers of titanium promotes the wetting of a large number of solid surfaces with a wide variety of liquid metals. No combination has been found for which the titanium vapor treatment did not promote wetting. Most of the tests have involved the use of liquid silver and gold base brazing alloys and also aluminum on the surfaces of various metals and metal oxides.

ELECTRON BEAM AS A DIRECT OR AUXILIARY TOOL FOR BRAZING

Titanium has long been recognized as a wetting promoter in the production of glass-to-metal seals; the titanium is often used in the form of the hydride, which partially reduces to the metal at brazing temperature. Alternatively, titanium may be incorporated in certain brazing alloys to promote wetting. The hydride treatment is not as effective as vacuum deposition, although the reasons for this are not clear. The incorporation of titanium in the brazing alloy itself can be effective, but only when relatively large concentrations of titanium are involved, which leads to brazing alloys which have limited applicability, principally because of their relatively high melting temperature. The exact nature of the titanium film which is produced by vacuum evaporation in a relatively low vacuum (10^{-4} Torr) is not clear except that it is known that the oxygen and nitrogen concentrations are fairly high. Further investigations of surface structure and chemistry of these films is under way. It is certain there is a substantial difference between a vacuum deposited surface and other kinds of titanium surfaces; in this connection, it should be noted that solid titanium is not easily wet by brazing alloys.

Other reagents deposited by vacuum evaporation have not proved as effective as titanium for the combinations which have been tested. Zirconium acts in the same way as titanium, but to a lesser degree. Vacuum deposits of tantalum almost completely inhibit wetting.

The effect of the vacuum deposited titanium as a wetting agent in brazing beryllium is shown in Figs. 1 through 13. The brazing alloys used in this investigation were:

72% Silver, 0.2% Lithium, 27.8% copper.

82% Gold, 18% Nickel.

99.995% Aluminum.

When the silver alloy was melted in a vacuum environment on the surface of untreated beryllium, there was very slight wetting, not nearly enough to accomplish the capillary flow essential to successful brazing. In Fig. 1 is shown a plan view at low magnification of the limited spreading obtained with this combination. Fig. 2 at 500 magnifications shows the character of the interface between the silver alloy and the beryllium, which reflects almost a complete absence of bonding.

The picture was dramatically changed when the beryllium surface was treated with titanium.

The effect of vacuum deposited titanium on spreading is shown in Figs. 3 and 4. In Fig. 3, titanium evaporation and melting of the silver alloy were accomplished simultaneously by the use of a titanium susceptor interposed between the electron beam and the specimen. The spreading shown in Fig. 4 was accomplished by a two-step process, in which the titanium was deposited on the beryllium surface, the vacuum chamber opened, the brazing alloy positioned on the specimen, and, after pumpdown, spreading was accomplished by direct heating with the electron beam. Exposure of the titanium deposit to the atmosphere, even for long periods of time, prior to brazing, in no way inhibited the wetting action. The titanium pre-treatment consists of evaporation by the direct electron bombardment of a relatively large piece of commercially pure titanium plate, using just enough beam power to sustain a small molten puddle in the titanium, and exposing the surface to be brazed to the titanium vapor for a period of 3 to 5 minutes. This will result in a titanium deposit less than two microns thick. This thickness is not critical except that, in an excessively thick deposit, titanium compounds are likely to be formed either with the base material or with the brazing alloys, dependant of course, on their compositions. As

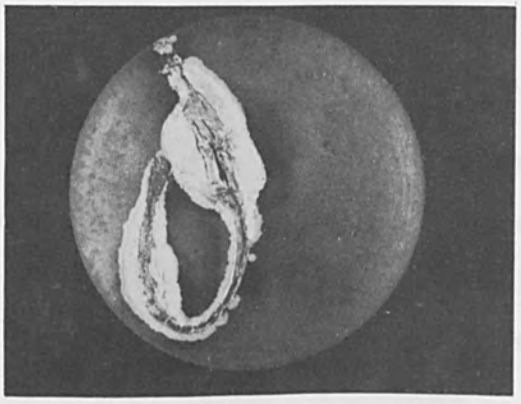

FIGURE 1 Spreading of Ag-Cu-Li Alloy on Be - No Surface Treatment

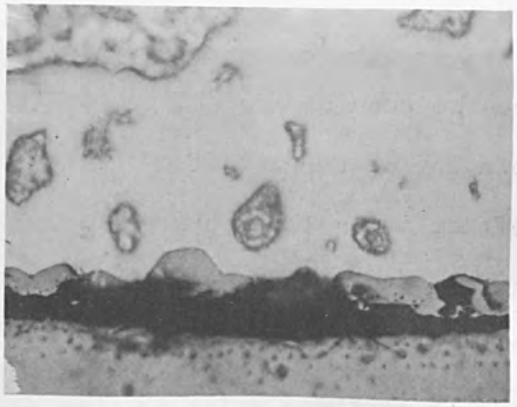

FIGURE 2 Contact Interface from the Sample of Fig. 1 (500X)

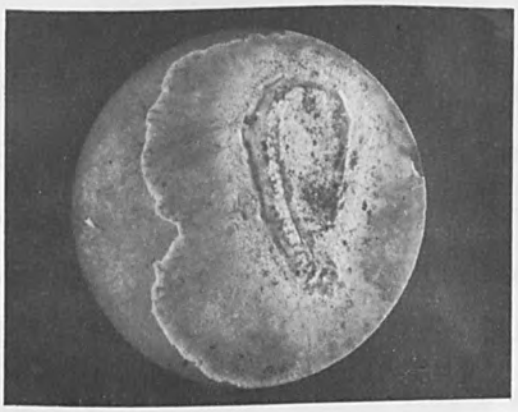

FIGURE 3 Spreading of Ag-Cu-Li Alloy on Be - Indirect Heating with a Ti Shield.

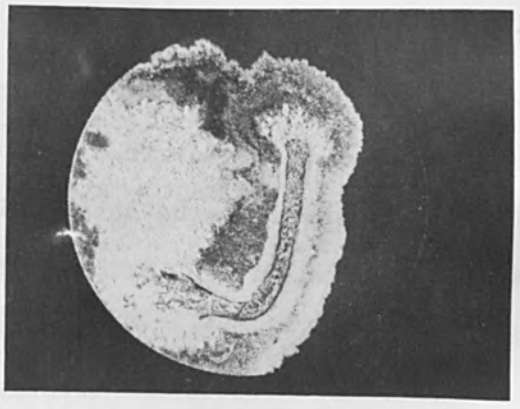

FIGURE 4 Spreading of Ag-Cu-Li Alloy on Be - Surface Pre-treated with Ti

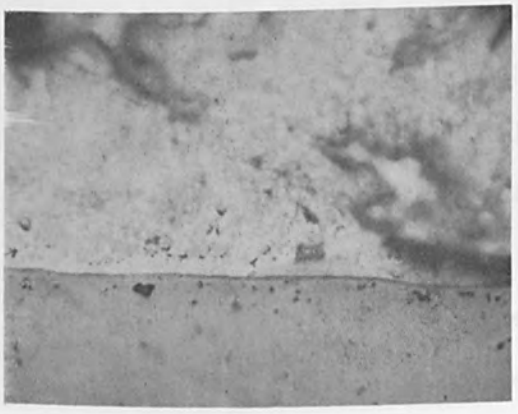

FIGURE 5 Contact Interface from the Sample of Fig. 4 (500X)

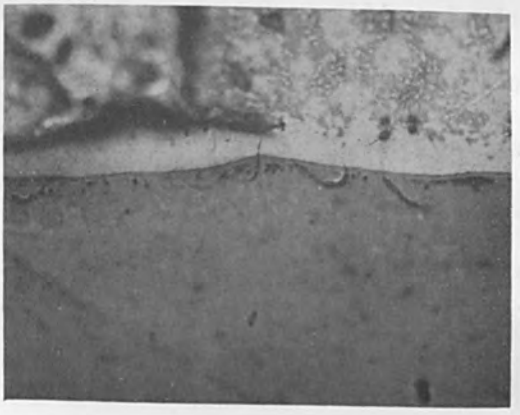

FIGURE 6 Same as Fig. 5 Except for Longer Time at Elevated Temperature (500X)

can be seen by comparison of Fig. 5 with Fig. 2 the titanium has promoted bonding at the interface between the silver alloy and the beryllium. One effect which is observed when precious metal alloys are used with beryllium is the generation of voids in the beryllium, and these are somewhat removed from the interface between the braze alloy and the beryllium. The growth of these voids is time dependent, so that longer exposures have a more serious effect (Fig. 6).

The behavior pattern of gold-nickel brazing alloys closely parallels that of the silver alloys. In Fig. 7 is shown the limited spreading developed when no surface treatment is used. Fig. 8 shows the nature of the bond between the gold-nickel alloy and the beryllium. Even when spreading is limited there can be substantial interaction between the liquid and the solid as shown in Fig. 8; often in combinations where spreading is limited, intergranular penetration takes place fairly rapidly.

The effect of titanium treatment using a gold-nickel alloy is shown in Figs. 9 and 10. Spreading is definitely promoted and the nature of the bond is entirely different. In this case, instead of the braze alloy penetrating the beryllium grain boundaries, the beryllium has dissolved in the gold-nickel. The development of porosity in the beryllium is so pronounced, that a continuous void develops in the beryllium on a plane which parallels the original liquid-solid interface. Gold-nickel alloy obviously is not an attractive filler for joining beryllium.

Most metals or alloys which might otherwise be entirely suitable as fillers for brazing, unfortunately form brittle intermetallic compounds with beryllium. Exceptions are aluminum and the alkaline earth metals. Aluminum is a very attractive candidate, because of its good mechanical and corrosion properties. In fact, aluminum silicon alloys have enjoyed

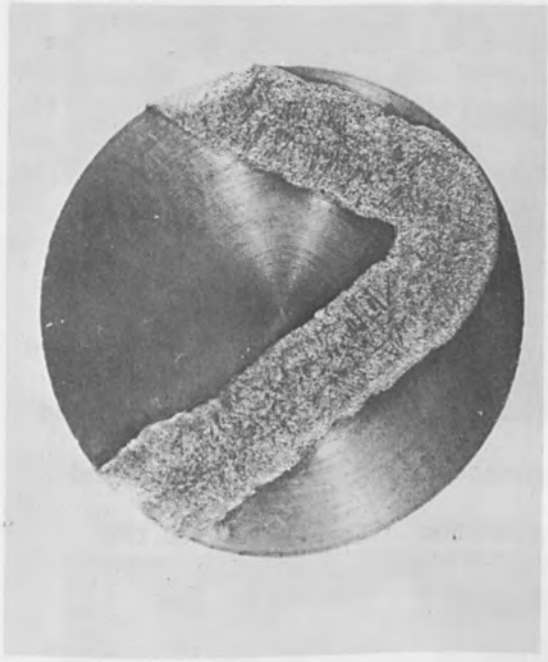

FIGURE 7 Spreading of Au-Ni Alloy on Be - No Treatment

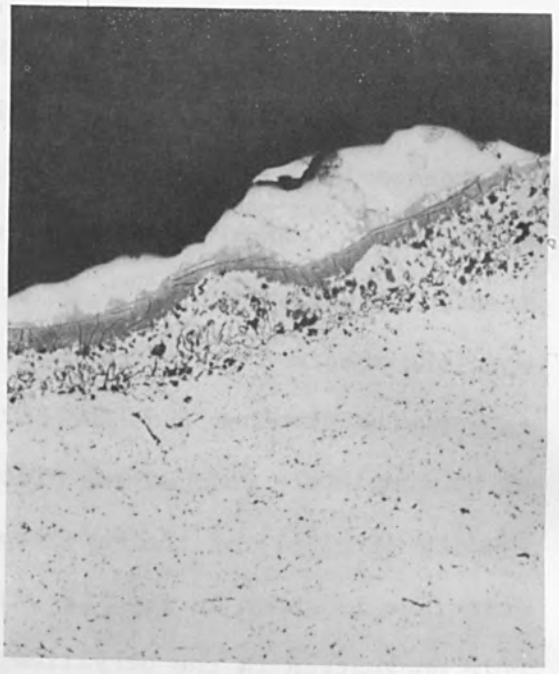

FIGURE 8 Contact Interface from the Sample Shown in Fig. 7 (100X)

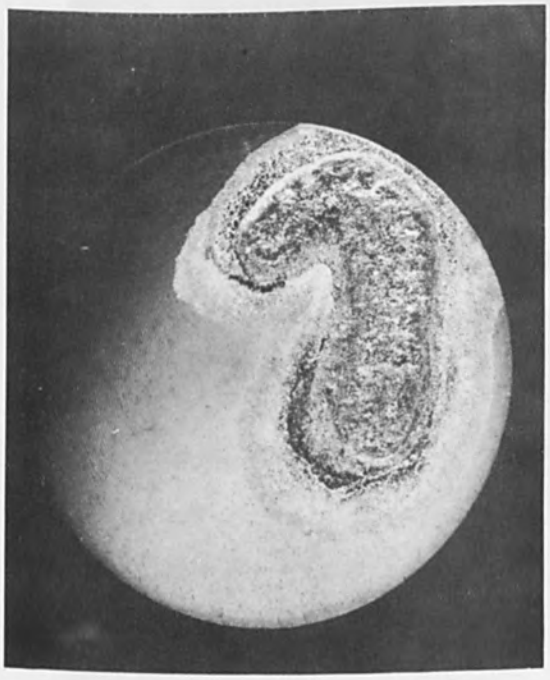

FIGURE 9 Spreading of Au-Ni Alloy on Be - Surface Pre-treated with Ti

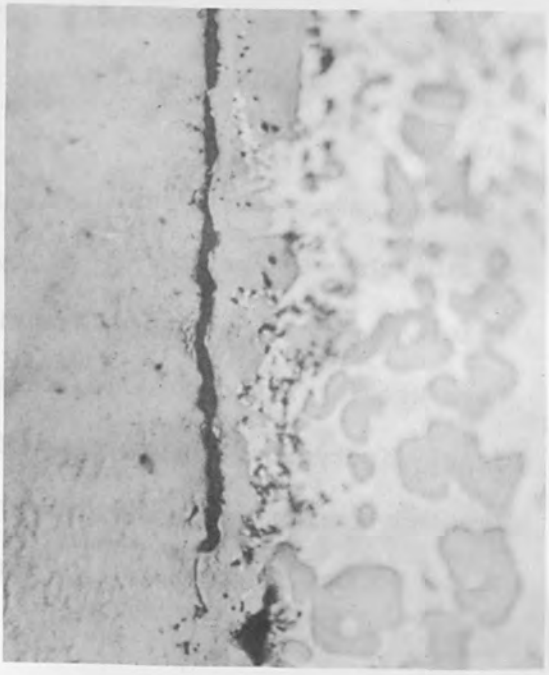

FIGURE 10 Contact Interface from the Sample Shown in Fig. 9 (500X)

limited use in the brazing of beryllium. The great difficulty has been to accomplish wetting with this combination. Liquid aluminum was reluctant to wet most solid surfaces and solid beryllium was difficult to wet with any liquid metal. When liquid aluminum was brought into contact with an untreated beryllium surface, almost complete non-wetting was observed, and when the specimen cooled to room temperature very little force was required to part the aluminum from the beryllium. The titanium treatment described above completely changed the picture and promoted both the spreading and wetting (Fig. 11) of the beryllium by the aluminum. The nature of the interface is shown in Fig. 12. Again there is a pronounced tendency for void nucleation in the beryllium, but this can be offset by use of rapid heating and short times at elevated temperature. When a relatively thick layer of titanium (in excess of 30 microns) was used, the aluminum beryllium interface changed markedly. The excess titanium promoting intergranular penetration of the beryllium and the precipitation of $TiAl_3$ needles in the aluminum.

These same effects have been observed with other systems, notably in brazing chromium containing alloys, including high temperature alloys and stainless steels, and with graphite and aluminum oxide. Even in systems where wetting would normally take place without treatment, the titanium greatly increases the velocity of spreading. Present investigations are directed to improved understanding of the surface mechanisms involved in the use of wetting agents such as titanium.

ELECTRON BEAM BRAZING

A low voltage electron beam is a remarkably convenient device for vacuum brazing. The mechanisms and procedures are entirely different from those used in electron beam welding and some of these are still being developed.

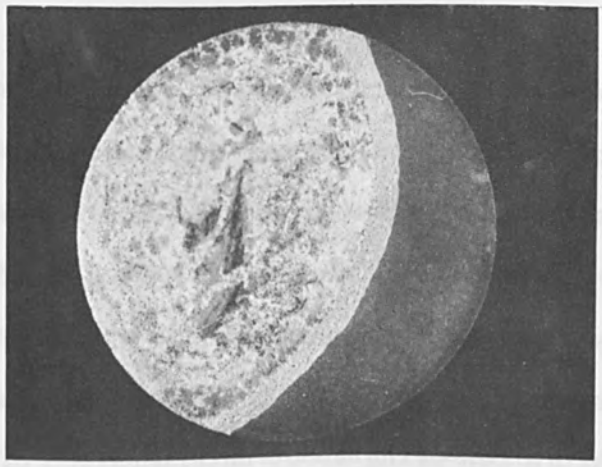

FIGURE 11 Spreading of Al on Be - Pre-treated with Ti

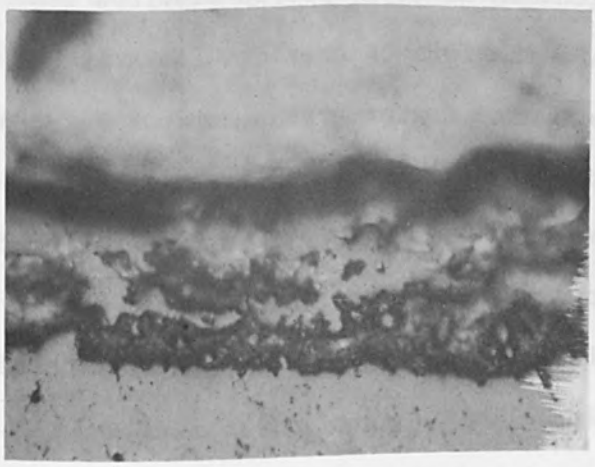

FIGURE 12 Contact Interface from the Sample of Fig. 11 (500X)

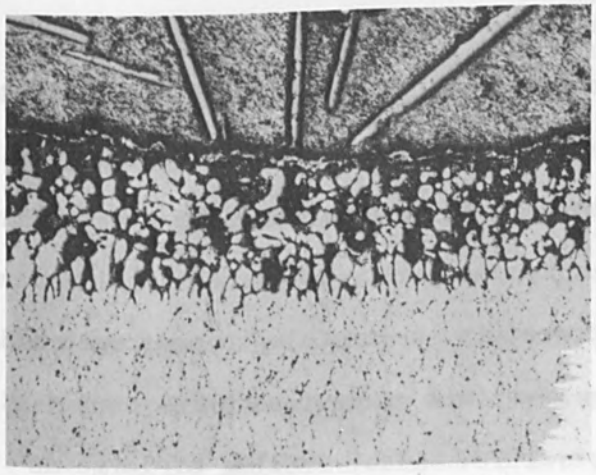

FIGURE 13 Contact Interface from a Sample in Which Al has Spread on a Be Surface Covered by a Thick Layer of Ti (100X)

With electron beam heating, visual control of the brazing process is made possible, a feature difficult to realize in a conventional vacuum brazing furnace. The operator knows by direct observation the moment the brazing alloy melts and proceeds to flow, and this marks the end point of any brazing process. Once capillary flow has been accomplished, nothing more is gained by maintaining the assembly at the brazing temperature; in fact, a long time at brazing temperature can bring about deterioration of the joint.

The heating and cooling rates which can be developed in electron beam brazing are substantially higher than with furnace brazing. This is a material advantage, because the opportunity for adverse reactions between liquid and solid is minimized by reducing the time at elevated temperature. This is of particular importance in brazing beryllium because of the tendency for nucleation and growth of voids, as described above. Also, with many brazing alloys, slow heating rates effect partial separation of the constituent elements of the filler alloys (liquation).

An obvious practical advantage associated with the rapid heating, visual control, and rapid cooling, is the shortening of the time cycle required to accomplish a brazed joint.

The use of an electron beam makes possible the combination of local heating with a vacuum environment which cannot easily be accomplished in any other way. In conventional vacuum brazing it is necessary for the entire assembly to be brought to the brazing temperature. Local heating has many useful consequences. In the first place, it is possible to perform brazing on parts of assemblies which contain materials or devices which cannot withstand excursions to the brazing temperature. Also, brazing of large assemblies can be accomplished incrementally, rather than all at once, which

helps in the maintenance of dimensions and in some cases reduces the tendency for the brazing alloy to migrate over relatively long distances in the assembly. For example, in the furnace brazing of honeycomb structures there is sometimes a difficulty with downhill flow and local accumulation of excess brazing alloy; a consequence of the fact that all the brazing alloy is liquid at one time.

Of course there is no temperature limitation with the electron beam heat source. Vacuum brazing with visual control can be done at whatever temperature the melting point of the filler metal dictates. Thus nickel and nickel-chromium alloys, which melt above 2500°F, can be, and have been used to braze molybdenum and tungsten much more easily, quickly, and with less expensive equipment than would be the case with resistance heating apparatus.

There is some difficulty in accomplishing the proper distribution of heat for brazing by the use of an electron beam. It is essential that the solid surfaces to be wetted attain a temperature above the melting point of the brazing alloy, and best results are associated with schemes in which direct heating of the brazing alloy itself is avoided. For this reason, it is sometimes necessary to use partial shielding to intercept that part of the electron beam which would otherwise bombard the brazing alloy, so that the brazing alloy becomes heated by radiation and mechanical contact with the solid surfaces of the intended joint. Since mechanical contact does not constitute very good thermal contact in a vacuum environment, it is sometimes useful to tack weld the brazing alloy to the substrate during the assembly operation, just to develop improved thermal contact.

The shields which were used to avoid direct heating of the filler metal performed the additional function of promoting wetting. Thus titanium

shields or susceptors have been used quite successfully in certain types of brazing operations where surface treatment and the brazing itself are accomplished in a single step.

Several procedures have been tested in attempting to use the electron beam as a heat source for brazing. The best appeared to be a beam which was not sharply focussed and which was subjected to a low frequency electromagnetic oscillation. Using a beam power of about 3 kw at 10 kv, the beam was focussed to a spot between 1/4" and 1/2" in dia. then electromagnetically deflected at 60 cycle frequency with a sweep distance of 2" or more. Generally, it has not been found possible to accomplish a sufficiently uniform heat distribution through the use of a static, defocussed beam, and the oscillation appears vital to the process.

CONCLUSION

Because of dual capability for surface treatment and heat transfer, there is every prospect the electron beam will find a prominent place in the brazing field.

ACKNOWLEDGEMENT

The authors express their sincere appreciation to the Manned Spacecraft Center of the National Aeronautics and Space Administration, which, through the M.I.T. Instrumentation Laboratory, provided the support for this investigation, and specifically to R. Gras and P. Bowditch of the Instrumentation Laboratory for their administration, guidance, and encouragement of this study.

PRACTICAL APPLICATION OF ELECTRON BEAM WELDING AND MILLING

Hans A. Nyenhuis
Electron Beam Techniques, Inc.
Plainville, Connecticut

ABSTRACT

A report on a variety of applications of the electron beam drilling and welding processes will be presented. Pictures of drilled holes and of holes being drilled will be shown. A new triode electron beam gun which delivers over 20 times the energy of commercially available drilling machines at very high energy densities permits holes to be drilled with depth to diameter ratios in the neighborhood of 100 to 1. Drilling speeds are very high and straightness is assured since the "drill" does not drift. Development work is continuing but applications will be discussed which are routine, economical and practical on a production basis.

Many unique applications of electron beam welding will be illustrated and discussed.

Specimens selected from various research programs will be presented to illustrate the joining of dissimilar materials.

Several illustrations will be presented of complex tooling developed for production welding.

PRACTICAL APPLICATION OF ELECTRON BEAM WELDING AND MILLING

INTRODUCTION

Electron beam welding, milling, and drilling are increasingly in demand as a manufacturing technique because of increased use of exotic materials and the close tolerances that are now required. Electron beam welding has from the beginning been more in demand than electron beam milling and drilling. The demand has resulted in welding equipment development with the result that for many applications the process has become quite economical. On the other hand, electron beam drilling was not very practical because the process was limited to drilling small holes through thin sheets of material by a maximum power output of 150 watts. This equipment limitation, together with a lack of demand caused its development to come almost to a complete stop. Furthermore, the holes drilled with these machines could frequently be made by conventional methods and on machines costing much less than an electron beam drilling apparatus.

An electron beam gun and its controls have been developed which can adapt the Hamilton-Zeiss welding machine making it a combination welding-drilling machine. This machine can weld thicknesses varying from 0.0005" up to 1" plate and can drill small holes with a depth to diameter ratio in excess of 100 to 1. A 0.005" diameter hole can be drilled through 0.500" of stainless steel in 8 seconds. This cannot be done mechanically with EDM, with ECM or with a laser apparatus, and thus, electron beam drilling becomes practical and economical. In thinner material the drilling speed has been increased to 300 holes per second.

Because of the elaborate and sophisticated electron optics incorporated in this equipment it is possible to manipulate large quantities of energy with optical precision.

Instead of presenting charts and diagrams and saying what things could

be done with this equipment, photographs of parts which have been processed and which are more or less routine will be presented. Unfortunately many interesting applications must be omitted because they are either classified or considered to be proprietary.

EQUIPMENT DESCRIPTION

Fig. 1 shows an electron beam welder which has a 21' long vacuum chamber which is used for the welding of nuclear fuel elements about 10' long. On top of the vacuum chamber is the electron optical column housing the electron beam gun. The binoculars of the built-in stereo-microscope can be seen near the bottom of the column. The magnetic lens and the electromagnetic beam deflection system are at the bottom of the column in the evacuated area. A cross section of the electron optical column will be shown later and explained in detail. To the right is the control cabinet, housing the necessary controls for the magnetic lens, filament heating, bias voltage for the control of beam current, the electromagnetic deflection system and the vacuum system. On top of this cabinet is the control synchronous stepping motor which is used to obtain motion of the work in various planes within the vacuum chamber. This control provides for both manual and automatic modes of operation. The maximum voltage of the electron gun is 150,000 volts at 20 milliamperes of current. Further to the left is the gun supply unit where the filament and bias voltages are added to the high voltage. It has been found necessary to have an assortment of vacuum chambers available and these vary from 20" x 20" x 5' long to 36" in diameter by 3' long. The vacuum chambers are connected to a standard pumping system consisting of a 120 C.F.M. mechanical pump and a 1700 L/sec diffusion pump. This system will evacuate most of the chambers from atmospheric pressure down to 1×10^{-4} mm Hg, within 5 minutes.

At the top of the electron optical column of the welder, the tungsten hairpin cathode, the bias cup and the anode are located. The cathode and the bias cup are charged negative with respect to ground. The potential difference is variable from 0 to 150,000 volts. The anode is positive and at ground potential. By making the bias cup more negative with respect to the electron emitter, an electrostatic prefocus is created and a beam is established. The electrons are accelerated and then travel through a hole in the anode. If the bias cup is made strongly negative with respect to the emitter, electron flow is inhibited, and hence a means for beam current control is established. Below the anode are two electromagnetic adjustments, which are used to align the beam to the axis of a magnetic lens. This also can be done by moving the cathode and the bias cup as a unit in relation to the axis of the anode and the magnetic lens. Below the electromagnetic adjusting system is a built-in stereo microscope which enables the operator to observe the welding or drilling processes at magnifications up to 40 times. Below the stereomicroscope is the magnetic lens which focuses the electron beam to an extremely high energy density on the workpiece surface. Below the magnetic lens is the electromagnetic deflection system with which the focused or defocused electron beam can be deflected in the X or Y direction or in a circular path as required. The workpiece is located below the column and is placed on an X or Y table or, in the case of a circular weld, a rotary fixture may be mounted with the axis of rotation in either the horizontal or vertical plane.

APPLICATIONS

Fig. 2 shows an aluminum wave guide assembly made from 0.032" thick, 6061 aluminum alloy in the T-6 condition. The wave guide assembly has a top and bottom skin, with very precisely spaced vertical ribs in between.

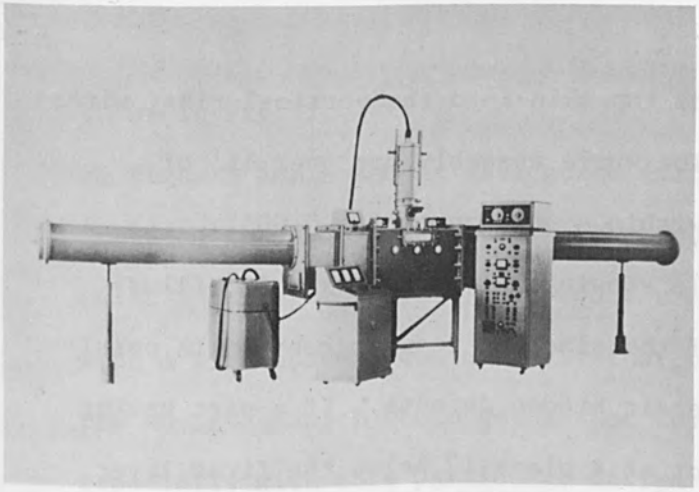

FIGURE 1

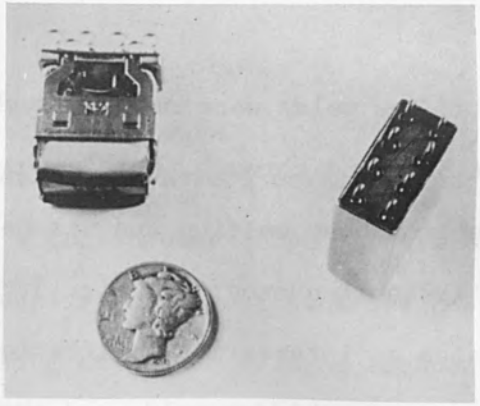

FIGURE 4

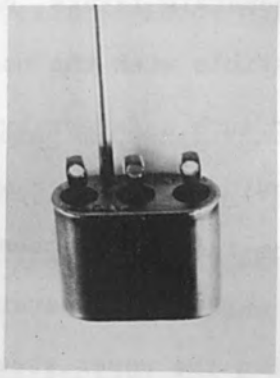

FIGURE 5

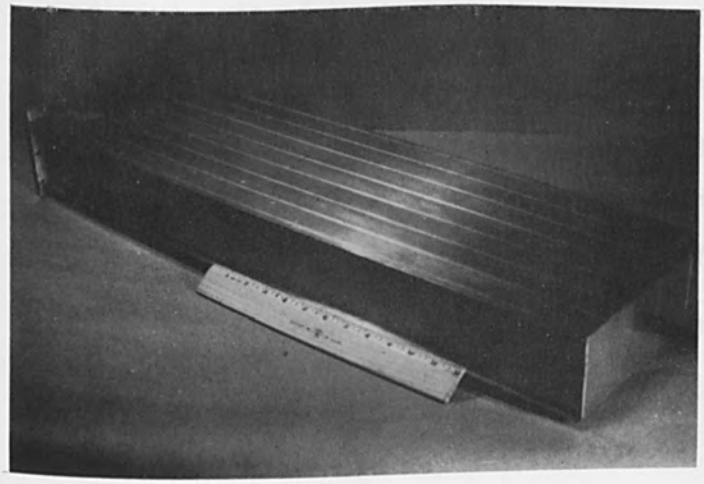

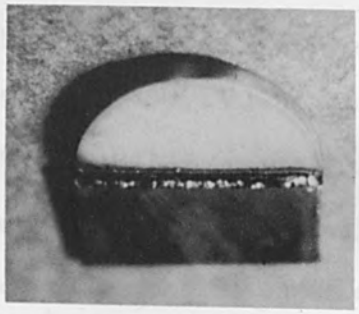

FIGURE 6

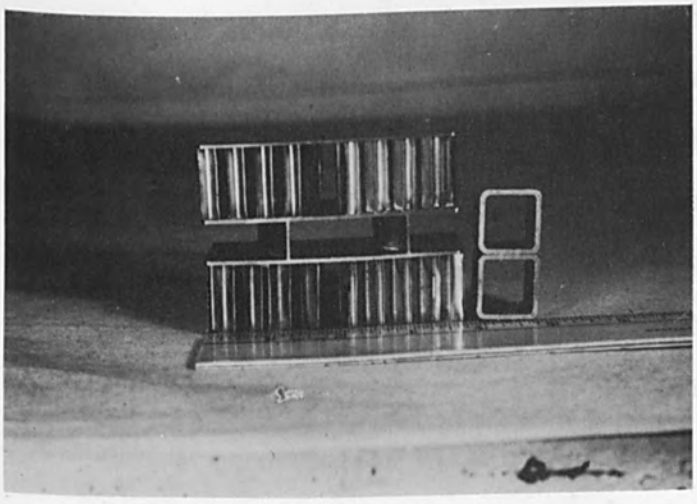

FIGURE 3

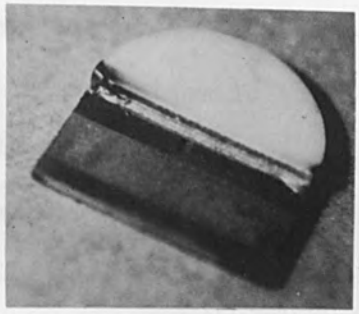

FIGURE 7

Blind tee welds were made through the top skin into the vertical ribs, without breaking through their sides. The whole assembly has over 45' of electron beam welding and was held within a tolerance of $\pm$ 0.005".

The next photograph, Fig. 3, while showing only a test sample, illustrates an interesting application of the electron beam whereby it is possible to make hidden welds and even repair hidden defects. If a part having several separate layers, has a defect at a place 1" below the first layer, it is possible with the use of a high energy density electron beam welder to repair such a defect by simply penetrating through the top skin and welding or fusing the defect without mechanically providing access. It is obvious from the picture that the electron beam has penetrated 4 layers of material which are separated by as much as 1 3/4" without actually cutting or damaging the upper sheets. The high energy density electron beam process offers the possibility of making such welds where the welds are almost equal in width; where the top weld is wider than the bottom; or where the bottom weld is wider than the top. These variations are accomplished by changing the position of the beam focus relative to the workpiece surface.

Fig. 4 shows a relay assembly in which it was necessary to weld a can to the base of the relay which contained a number of glass to metal seals. A leak tight assembly was made without cracking the glass to metal seals. The components which are mounted to the base of the relay can be seen. The difficulty of making such a joint with other joining methods can be imagined when one considers the precise control of heat that is required so as not to impair the function of the relay.

Fig. 5 shows a switch which has been hermetically sealed.

Figs. 6 and 7 show joints made between alumina and molybdenum. Note the very uniform fillet in the corner between the ceramic and the molybdenum

shown in Fig. 7.

Figs. 8 and 9 show a wave guide filter assembly where a ceramic window imbedded in kovar was welded to the end of a rectangular copper tube with walls about 1/4" thick. The copper represents a large heat sink and has such a high thermal conductivity that by using any other welding technique, the kovar sandwich would get so hot that the ceramic window would crack, especially with this particular design with the ceramic window 0.1" from the joint.

Fig. 10 shows a turbine wheel with the blade ring material Inco 713, the hub Inco 718, the downstream shaft is nitralloy and the upstream is PH17-4. Three separate welds were needed for this assembly and each is between dissimilar materials.

Fig. 11 shows a turbine wheel where it was necessary to add a shroud ring to the O.D. of the blades. A shroud ring was made in the form of a short cone with a ground I.D. so that thermal contact was made with every blade when the cone was assembled with the blade ring. The weld was made through the shroud ring into each individual blade, interrupting the beam between each blade segment so welds were not made where there was no blade below the ring. When the shroud had been welded to the blades on the O.D. the turbine wheel was turned so that its axis was in the horizontal position and, a fillet weld was made between the trailing edge of each blade and the shroud ring as shown in Fig. 12.

Fig. 13 shows the finished turbine wheel after the O.D. had been ground to the proper diameters, and slots had been cut through the shroud ring to provide space for expansion.

Fig. 14 shows 2 thermocouples. One thermocouple was welded with a tungsten inert gas (TIG) welder and the other thermocouple was welded with

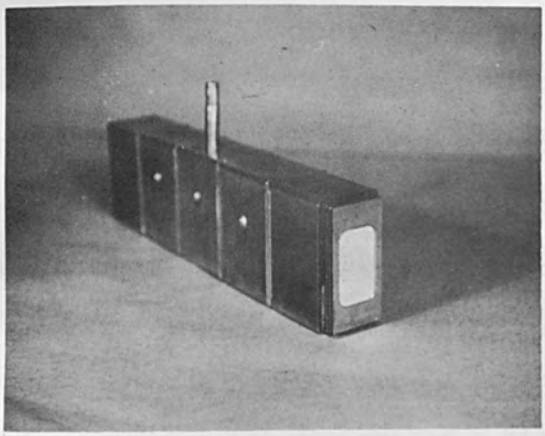

FIGURE 8

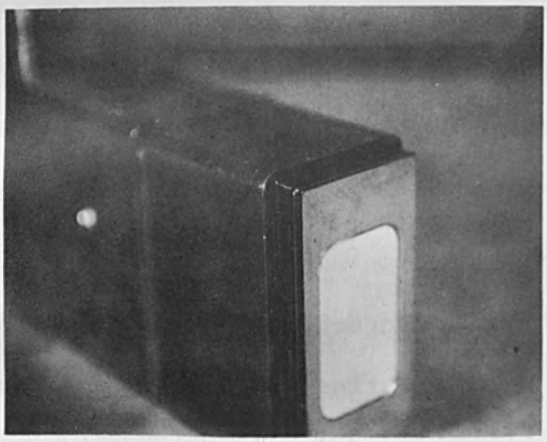

FIGURE 9

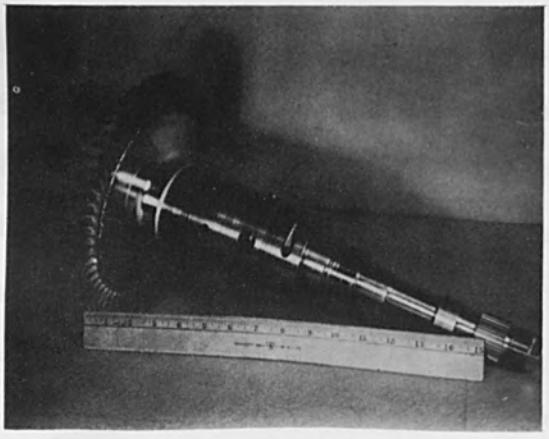

FIGURE 10

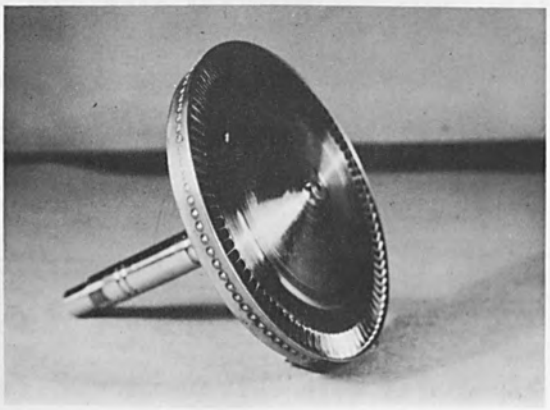

FIGURE 11

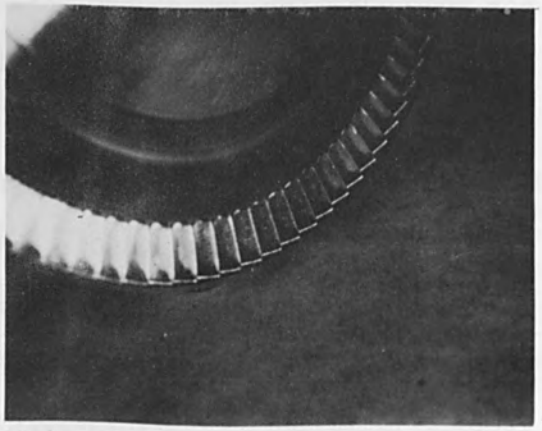

FIGURE 12

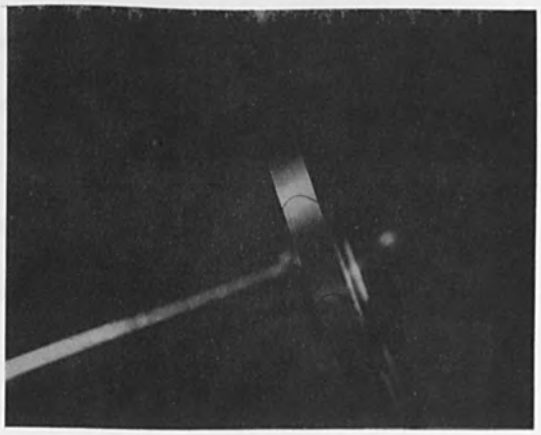

FIGURE 13

the electron beam equipment. The thermocouple which was TIG welded was badly deformed and the ceramic inside the thermocouple tube had been molten with the result that the thermocouple wires were shorted. The electron beam welded thermocouple was not shorted and the ceramic was not fused inside the tube.

Fig. 15 shows the repair of a machine gun where a 3/4" thick insert was welded into the side of the gun.

Fig. 16 shows an igniter for a rocket engine. All of the electrical connectors to the housing, and around all the screw heads were welded as also were the conductor tube fitting to the housing and the spark plug to the tube.

Fig. 17 shows a titanium pressure vessel where the wall thickness is 1/2". The welding speed was 75" per minute and no filler material was used.

Fig. 18 shows an aluminum pressure vessel with a 1/8" wall thickness welded at 120" per minute. Again no filler material was used.

Fig. 19 shows part of a thermionic converter which had a funnel welded to the top cover from the inside. A .010" thick molybdenum sheet was rolled to form a tube, and joined with a butt weld. Two circumferential welds on either end of the tube joined the top to the bottom of the assembly. The material in this case was molybdenum.

Fig. 20 shows one end of a long nuclear fuel element. The material was a zirconium alloy commonly known as Zircaloy 2. The welding operations were performed as follows: Two tubes were welded together at the tangent point and then additional tubes were added until the cluster shown was complete. The tube cluster was placed into the inner large tube and welded through the side wall. The six fins were welded to the O.D. of the inner tube, with a 100% penetration across these joints without affecting the I.D. of the large

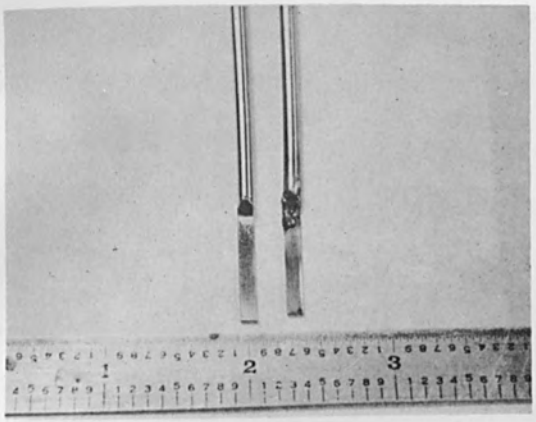

FIGURE 14

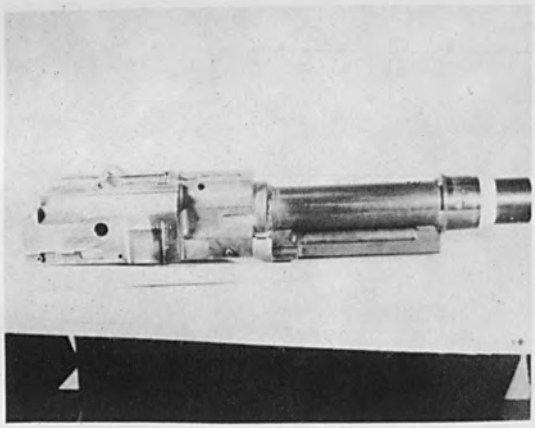

FIGURE 15

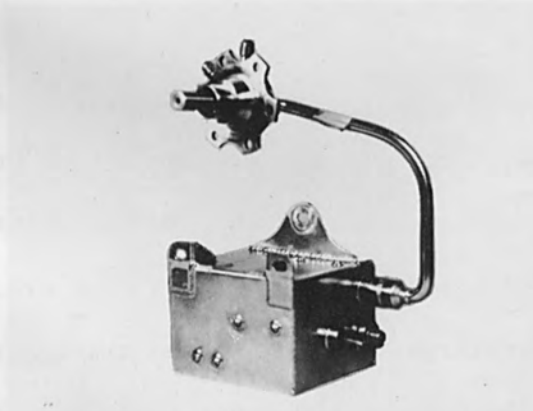

FIGURE 16

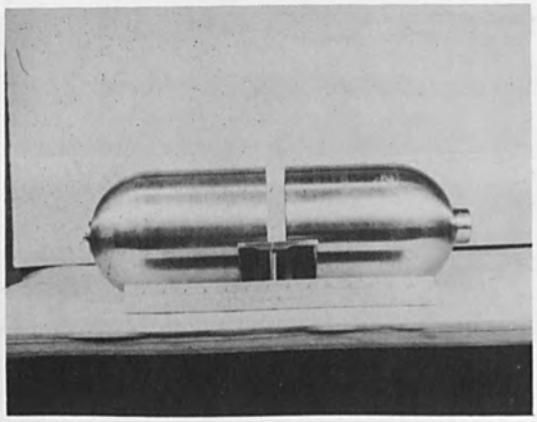

FIGURE 17

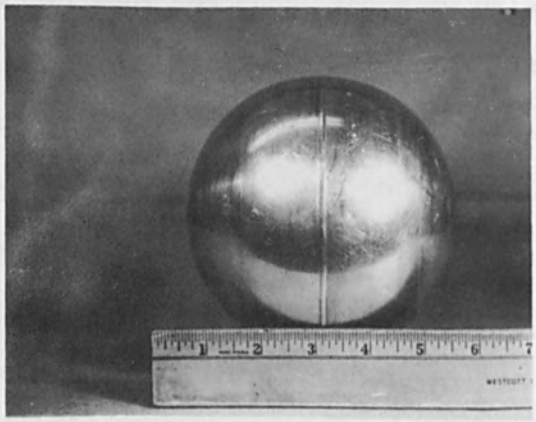

FIGURE 18

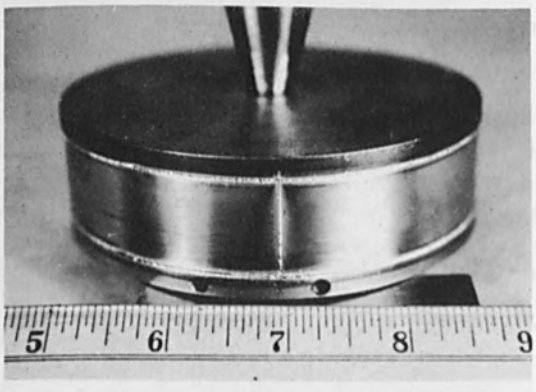

FIGURE 19

tube. The assembly was then inserted into the outer tube and 10' long blind tee welds were made through the tube wall into the fins. An interesting problem existed here in making the weld seam follow the approximate center of a .060" wide fin. Since there were no seam tracking devices available for electron beam equipment we were forced to develop one and with its help were able to track the center of the fins within .003". The welding speed used on this assembly was about 70" per minute.

Fig. 21 shows a cross section of the weld between a fin and the tube. The weld was made from both sides and did not affect the I.D. of the tube, the fusion zone penetrated only about 25% of the tube wall thickness.

Fig. 22 shows a cross section of a weld made between two of the tubes at the tangent point.

Fig. 23 shows a cross section of a weld made between one of the small tubes of the cluster and the outer tube. Penetration through the outer tube into the inner tube occurred without distorting the inner tube or without having any drop through on the I.D. of the small tube.

An ion bombardment cleaning technique is used in conjunction with the vapor deposition of various materials.

To obtain vapor deposits of various materials, the workpieces to be coated are positioned around the vapor source at appropriate angles. When using electron beam equipment for vapor deposition, it is extremely important to have very clean surfaces where the vapor is to be deposited. A procedure of chemically cleaning the substrates and then cleaning them in the vacuum chamber by ion bombardement just prior to the vapor deposition process gives good results.

Fig. 24 shows the apparatus used for electron beam drilling and cutting. The setup is quite similar to that of the welder. The electron

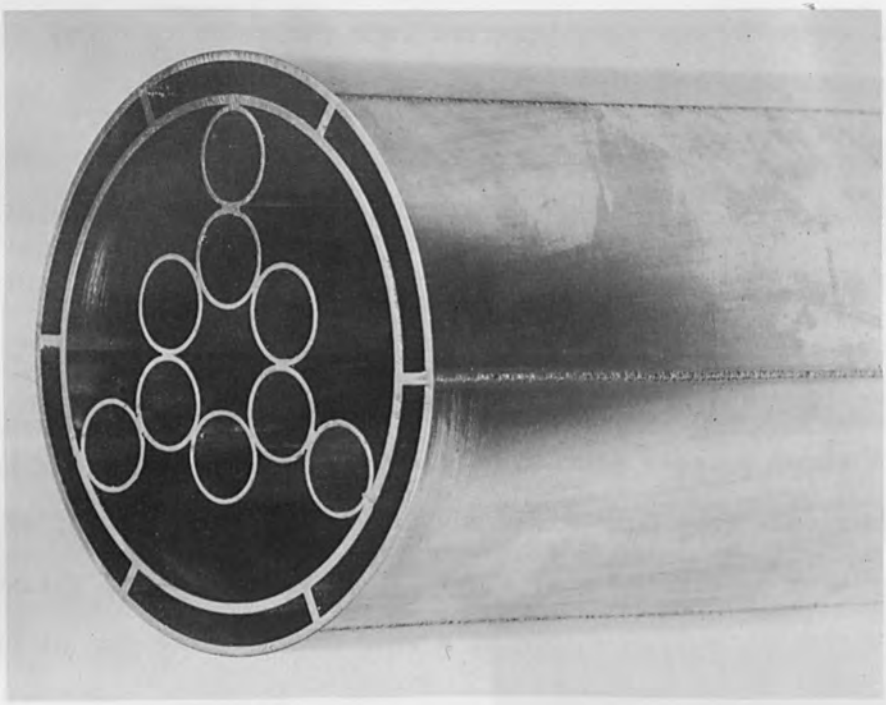

FIGURE 20

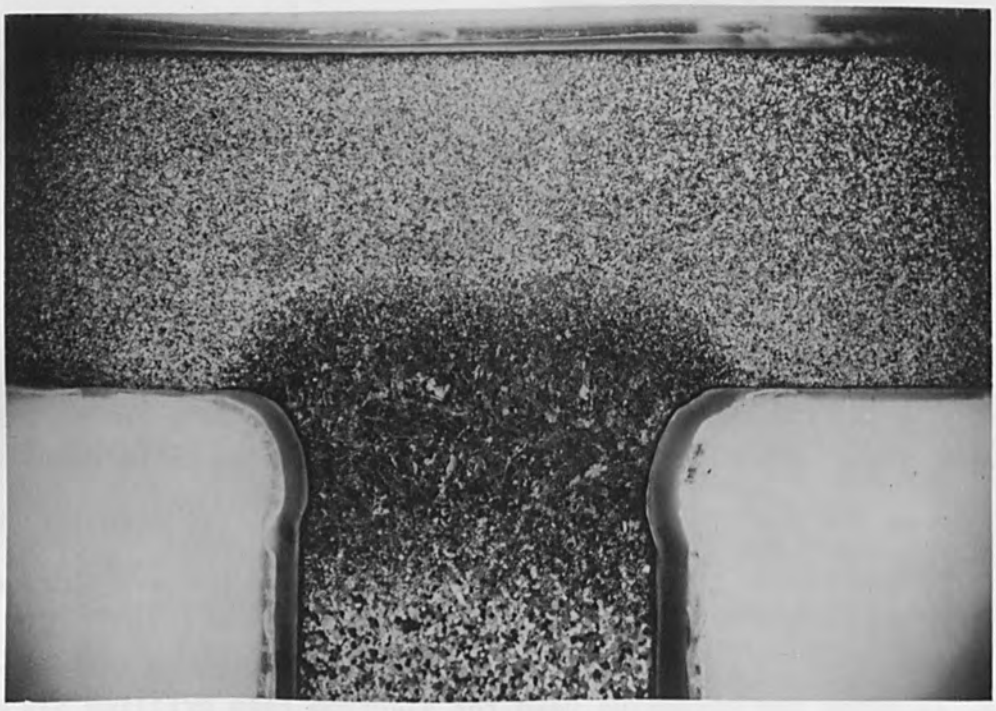

FIGURE 21

FIGURE 22

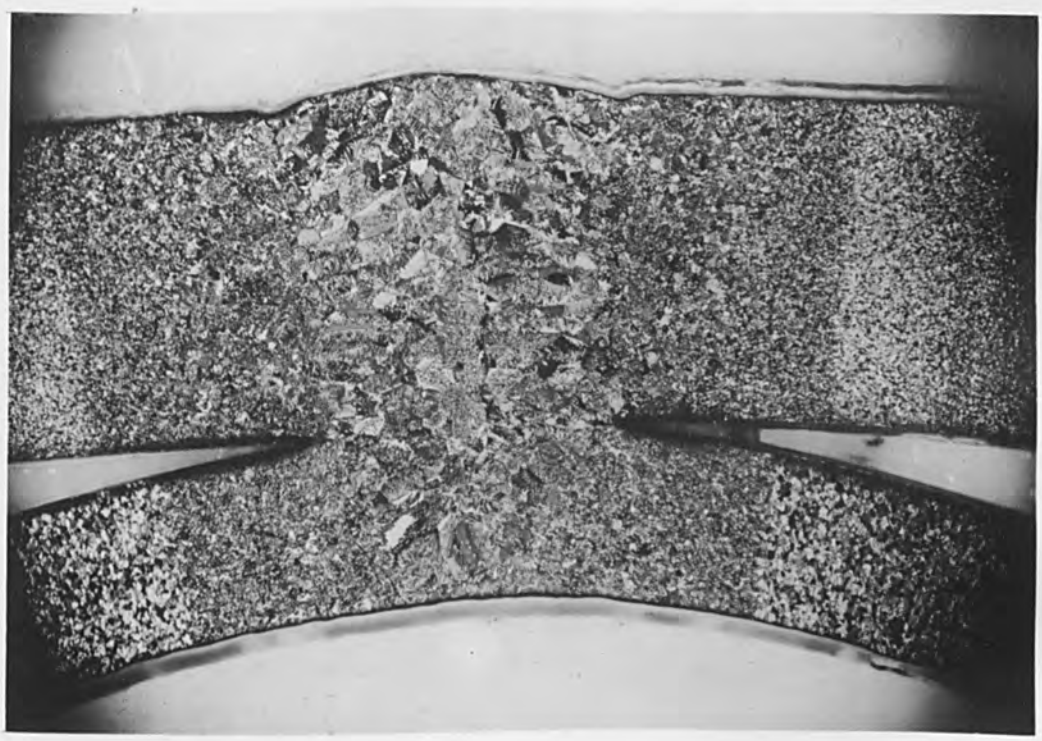

FIGURE 23

optical column, the vacuum chamber with the X or Y table, the high voltage control cabinet, the high voltage transformer and the control cabinet housing the controls for the magnetic lens, beam current, filament heating, etc.

Fig. 25 shows the electron beam milling machine being loaded with a workpiece. The door on the end of the chamber has been removed and the workpiece is being placed on top of the X and Y table. The bottom section of the electron optical column, especially the binoculars of the stereo microscope which play an extremely important role in positioning parts to be drilled may be seen clearly. With aid of this optical system it is possible to position the workpiece relative to the beam within $\pm$ .0005" and this is extremely important when very small holes are to be drilled or where very close spacing is required.

Fig. 26 shows a rectangular shaped tube with a wall thickness of approximately 0.060" where holes varying from .010" in diameter on the leading edge to .003" in diameter on the flat surfaces were drilled. All of the holes had to be drilled in specific locations and perpendicular to the surface which due to the radii of the edge and end made the fixturing rather complex. This workpiece had approximately 3,800 holes drilled in it. After drilling all of the holes in the tube, the rectangular shaped tube was then welded to the mounting flange, as can be seen more clearly in Fig. 27.

Fig. 28 shows a piece of stainless steel mounted in a slide frame with rows of holes drilled at the rate of 100 holes per second. The only difference between the holes is the spacing. The drilling time per hole was precisely the same. The holes are not precisely round, but this was unnecessary on this particular application because the holes were used in a pressure differential detecting device where only area of the hole was important.

FIGURE 24

FIGURE 25

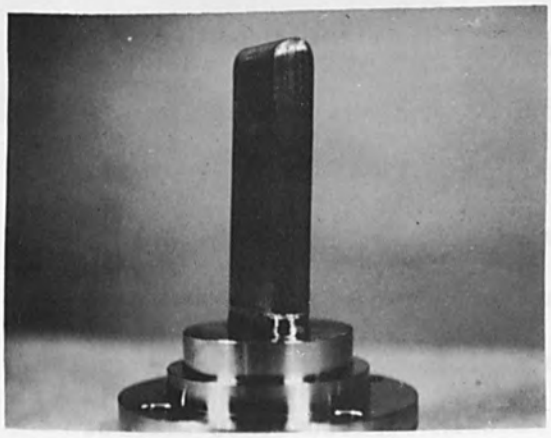

FIGURE 26

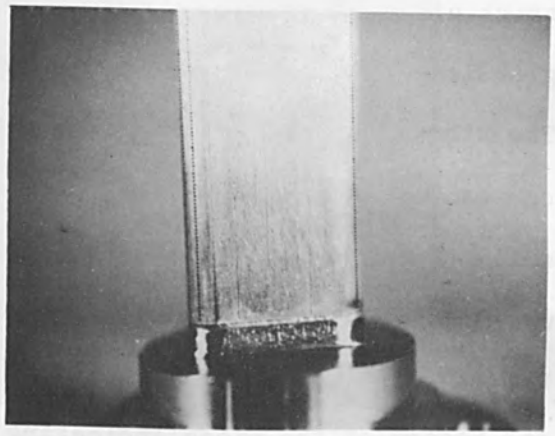

FIGURE 27

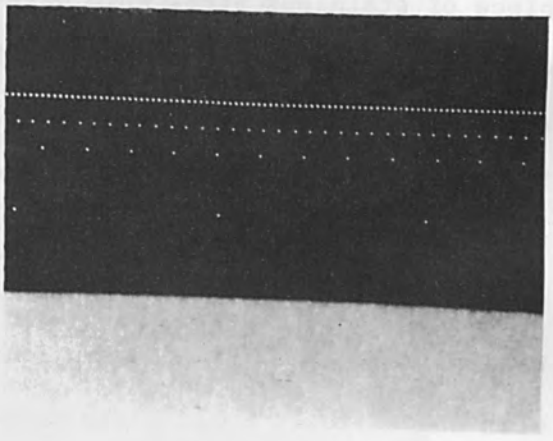

FIGURE 28

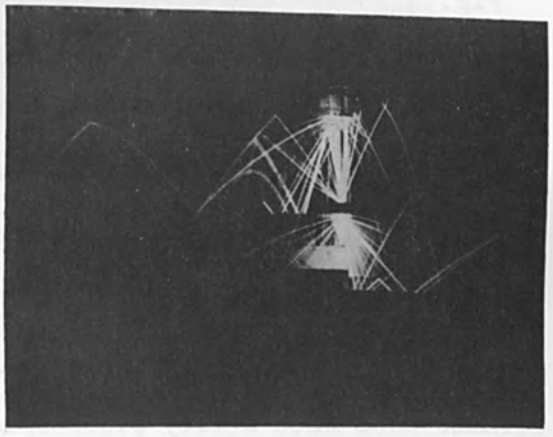

FIGURE 29

Fig. 29 shows a photograph of the beam drilling a hole through a 1/2" thick piece of stainless steel. The white streaks seen are sparks or globules of molten metal being ejected from the point of beam impingement. The tremendous energy density applied at the point of beam impingement causes instantaneous melting and vaporization of material in an area so small that the base material, for all practical purposes, remains cold. The workpiece is approximately in the center of this picture, which covers a time interval of several seconds. Sparks can be seen emanating from the top and bottom of the piece indicating that the hole was completed during the few seconds of exposure. It takes 2 to 3 seconds to penetrate a 1/2" thick piece of stainless steel when drilling a hole .005" in diameter, and approximately 5 seconds more to finish drill or ream the hole. Holes 1/2" deep are quite routine, and holes have been drilled through 1" thick stainless steel, but this is considered to be a laboratory project at the present time. Holes of this sort are made possible with the new electron beam gun which has been developed. This gun can deliver energy densities in the neighborhood of $10^{10} W/in^2$. It has a maximum power output of 3,500 watts compared with commercially available electron beam drilling machines with a maximum power output of 150 watts.

Fig. 30 shows a diametral section of a hole .005" in diameter drilled through a 1/2" thick piece of stainless steel in 8 seconds. The included angle of the hole is only 55 seconds of arc. This is due to an extreme depth of focus of the electron beam.

Fig. 31 shows a flat ceramic wafer with a chrome-nickel deposit. The scribed lines are very close together and this picture shows the precise heat control which is possible. The metal film was removed down to the ceramic base with a very close spacing between scribed lines without

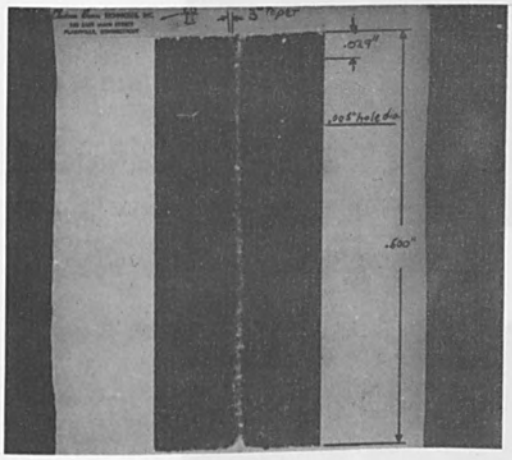

FIGURE 30

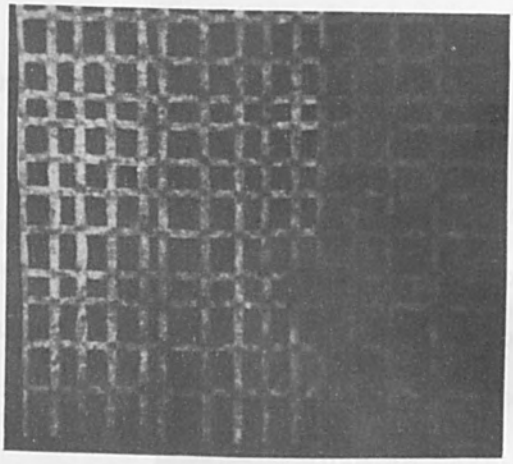

FIGURE 31

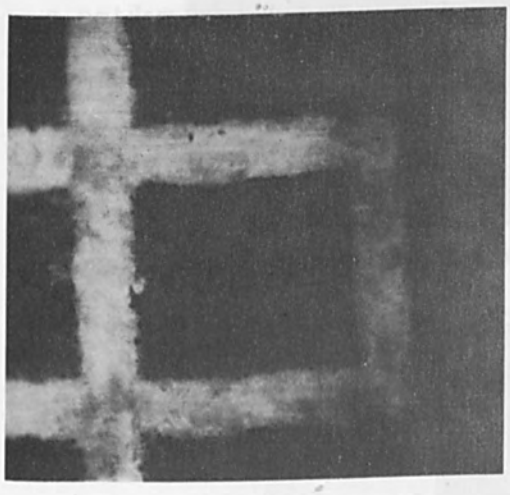

FIGURE 32

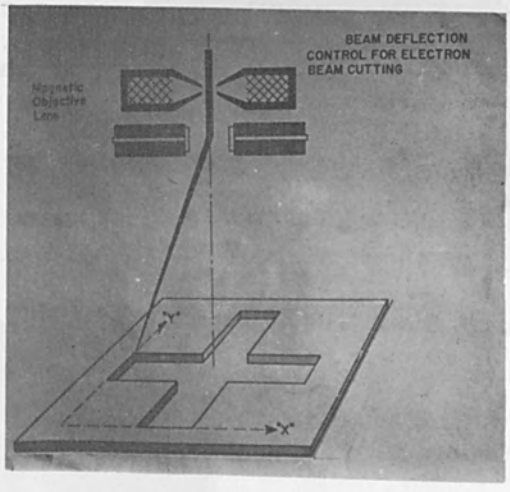

FIGURE 33

cracking the ceramic or without melting the small metal film islands which remain on the ceramic surface.

Fig. 32 is a very high magnification of one of the line patterns scribed on the flat resistor from Fig. 31. It can be seen that the ceramic is quite free from metal. The remaining metal islands are found to be completely insulated from each other. It is evident that cutting and drilling is not limited to round holes, and with an electromagnetic deflection system the beam may be moved in almost any direction to produce scribes or cuts in almost any pattern.

Fig. 33 shows one application of the beam control system. The beam is focused by the magnetic lens and directed straight down toward the workpiece from the electron gun. As soon as it enters the electromagnetic deflection system it is deflected in the X or Y direction by programming the electrical signals to the deflection coils. In this way patterns can be cut quite precisely. In this case a cross-shaped hole was cut by making a combination of X and Y movements of the electron beam.

Fig. 34 shows a star-shaped hole with spokes converging toward the center drilled by this technique.

Fig. 35 shows a star-shaped hole with parallel spokes. The star-shaped holes are about .040" in diameter and the spokes are about .003" wide.

Fig. 36 is a Y-shaped hole. Each leg is about .020" long and about .003" wide.

Fig. 37 is a cross-shaped hole. The legs are about .040" long; the width is about .005". All of the illustrated profile shaped holes were drilled through .025" or .030" thick stainless steel.

Fig. 38 shows cross-shaped holes drilled through white sapphire. The sapphire is about .040" thick and the legs of the crosses about .003"

FIGURE 34

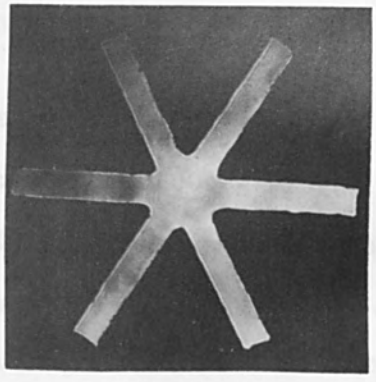

FIGURE 35

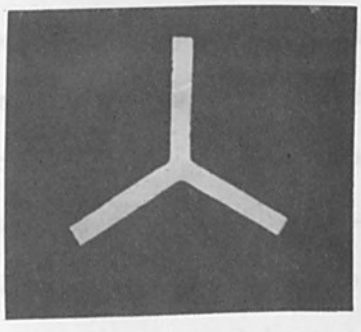

FIGURE 36

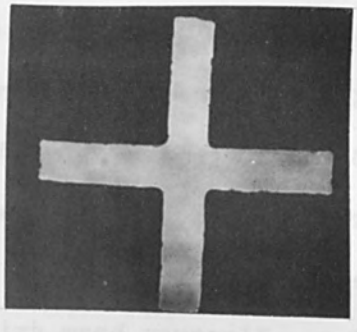

FIGURE 37

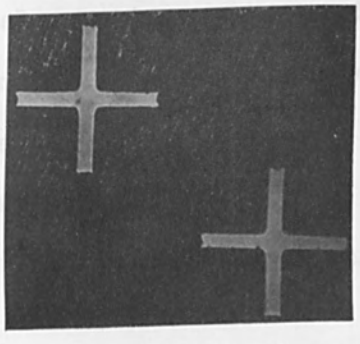

FIGURE 38

FIGURE 39

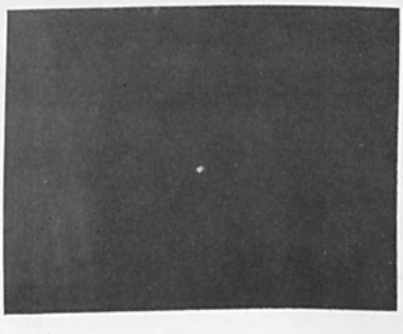

FIGURE 40

wide. The drilling time for each cross was about 4 minutes.

Fig. 39 is a .003" diameter hole drilled through a piece of stainless steel at 200 times magnification.

Fig. 40 shows a hole drilled through a piece of steel. The diameter is .00024".

CONCLUSION

Electron beam welding and drilling are in their infancy but are rapidly gaining acceptance by industry, and many new applications are found every day. Both electron beam welding and electron beam drilling have their limitations. They do not replace tungsten -inert gas, or resistance welding; neither do they replace electrical discharge or electro-chemical machining. Electron beam drilling should be used in areas where very small and deep holes or slots are required, and where very precise surface scribing is required. Electron beam welding should be used in areas where materials have to be joined which cannot be joined by any other methods, where it is important to hold distortion or shrinkage to a minimum, and where parts having appreciably different masses are to be joined.

ELECTRON AND LASER BEAM PROCESSING

Susumu Namba and Pil Hyon Kim
The Institute of Physical and Chemical Research
Tokyo, Japan

ABSTRACT

An apparatus for laser beam processing has been made. As a result of drilling holes in various materials by laser and electron beams, advantages, disadvantages and applicable limits of these processes are discussed. For the perforation of materials, the electron beam produces a smaller hole than the laser beam, but the latter is better in power efficiency. The reasons for this are explained by the characteristics of the two beams.

ELECTRON AND LASER BEAM PROCESSING

INTRODUCTION

Progress in micro-electronics has brought about the micro-processing method, and in this context, the subject of electron beam processing and its applications has been widely studied. Now that the laser beam has appeared as a new processing tool with a high energy output and pulsed behavior, it is well worth investigating its properties and making a comparison between the two types of beam.

The working spot size and energy density of laser beam on a workpiece have often been over estimated because a perfect coherency of the laser output beam has been assured. The true nature of the laser beam has now been revealed by many experiments and shows clear limits in its applications.

As both laser and electron beam processing are essentially thermal in nature, they will be discussed together. Based on experimental evidence, and taking into account the effect of pulsation of the beam, the spot size, the energy density and the power efficiency will be discussed, and the applicable limits, advantages and disadvantages of the two processes will be deduced.

APPARATUS

(a) Electron beam micro-machining apparatus

The electron beam machine shown in Fig. 1 is in two parts, an electron beam chamber and a machining chamber. Both chambers can be evacuated to 1×10^{-5} mm Hg. The electron beam chamber contains the electron gun, the first focusing magnetic lens, the stigmator, the electrostatic deflection plates and the second focusing magnetic lens. The electron beam is generated from a tungsten hair pin filament of 0.2 mm diamteter, and is accelerated by a potential of 50 kv.

The beam current is controlled by the negative bias potential of the

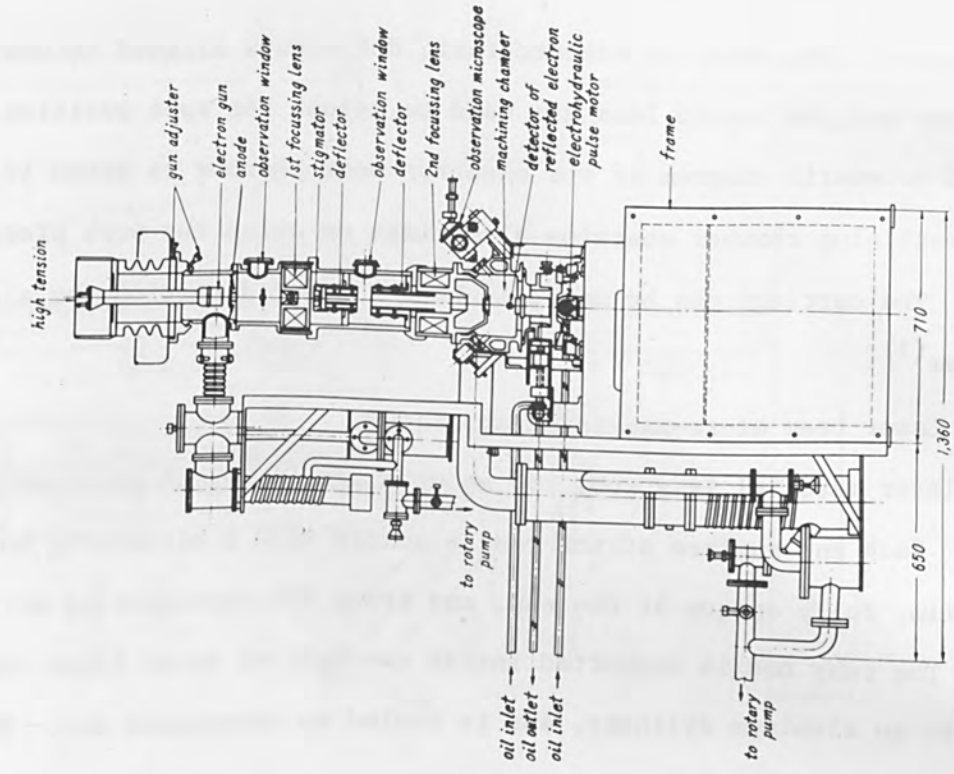

FIGURE 2 Schematic of Electron Beam Micro-Machining Unit.

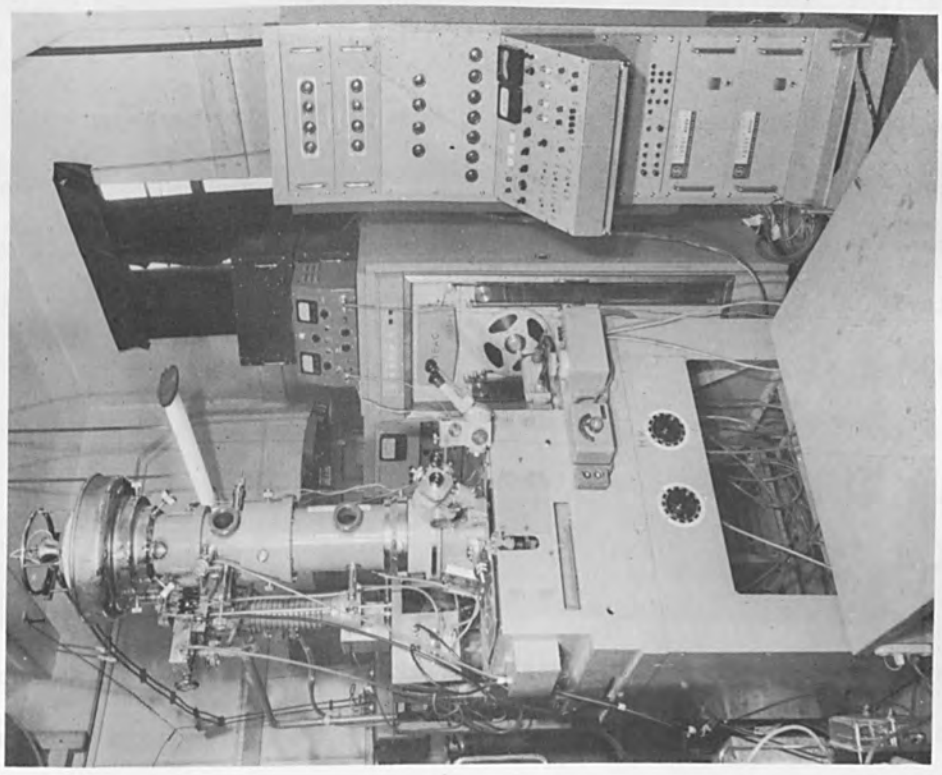

FIGURE 1 Electron Beam Micro-Machining Apparatus

control grid. Two pairs of electrostatic deflectors aligned between the first lens and the second lens are used to adjust the spot position. A detailed schematic diagram of the electron beam chamber is shown in Fig. 2.

The machining chamber contains a carriage on which the work piece is placed. The carriage can be moved in both X and Y directions by a drive mechanism[1].

(b) Laser beam micro-machining apparatus

The laser material is a ruby rod about 15 cm in length and 8 mm in diameter. Each end surface of the rod is coated with a dielectric multilayer film, fully opaque at one end, and about 40% transmitting at the other. The ruby rod is supported inside two helical xenon flash tubes enclosed in an aluminum cylinder, and is cooled by compressed air. The laser head is shown in Fig. 3.

A capacitor consisting of two 500 μF units supplies enough energy to the xenon tubes to flash them simultaneously, while the duration of the flash is controlled by varying the time constant of the discharge network. The generation of the trigger pulse that starts the discharge of the capacitor is suppressed whenever the reflector is used to view the work-piece through the built-in microscope. (Fig. 4) The maximum input energy is 12500 joules (5 kv, 500 μF x 2). The laser beam is focused onto the work-piece by a lens of either 30 mm or 15 mm focal length. The work-piece carriage can be moved in X, Y and Z directions independently.

EXAMPLES OF PROCESSING

Fig. 5 shows etched cross sections of drilled holes made in various metals by a dc. electron beam operating at 50 kv and 300 μA. The processing time was 5 seconds. The tungsten or copper samples were hardly drilled at all owing to their high melting temperature and high thermal conductivity

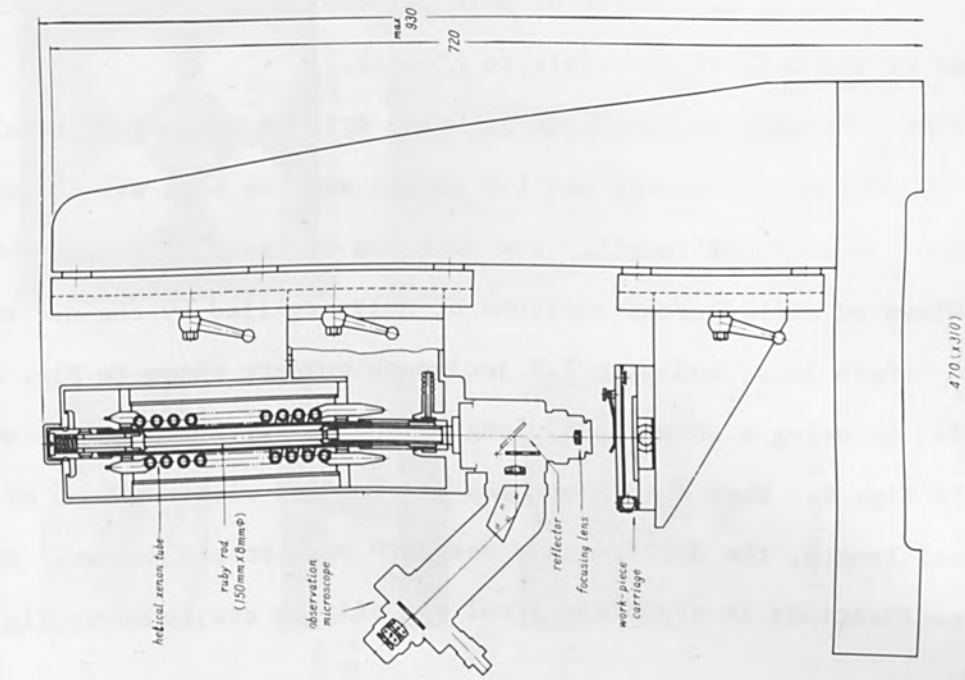

FIGURE 4 Construction Diagram of Laser Beam Micro-Machining Apparatus

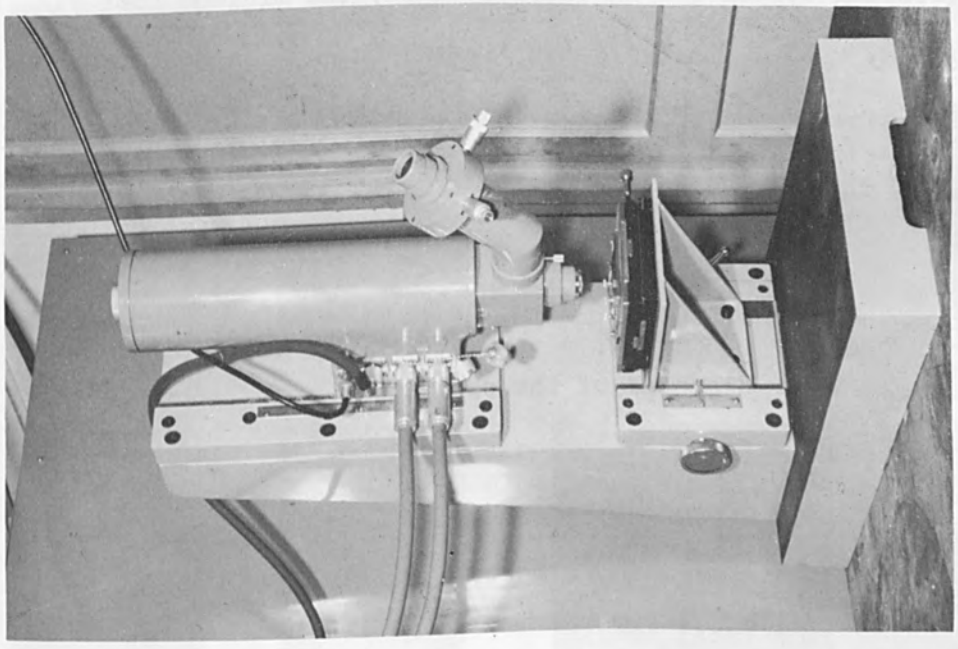

FIGURE 3 Laser Beam Micro-Machining Apparatus

respectively. Fig 6 is an example of hole perforation in stainless steel which is one of the easiest materials to process.

Fig. 7 shows etched cross sections of holes drilled in various metals by a laser beam. The output energy was 1.2 joules and the beam was focused with a lens of 30 mm focal length. The duration of laser pulse was about 2 m.sec. Views of etched cross sections of holes drilled by the use of a 15 mm focal length lens, and with 1.2 joules output are shown in Fig. 8. Those drilled by using a 30 mm focal length lens and with 2.2 joules output are shown in Fig. 9. When the laser beam was focused with the lens of shorter focal length, the drilled hole was both smaller and deeper. Examples of perforations in stainless steel and silicon are shown in Fig. 10.

DISCUSSION

(a) Minimum spot size

In the focusing system for an electron beam, the minimum spot size is usually ruled by the thermal velocity limitation and can be calculated by the following equation under optimum conditions[2];

$$d = 2\left(\frac{4}{3}\right)^{3/4} \left(\frac{K}{\pi e}\right)^{3/8} (cf)^{1/4} \left(\frac{T}{j_o}\right)^{3/8} \left(\frac{i}{V}\right)^{3/8} \quad (1)$$

where:

d = diameter of the spot,

K = Boltzmann's const.,

e = elementary charge,

c = aberration const.,

f = focal length,

T = absolute temperature of the source,

j_o = emission density,

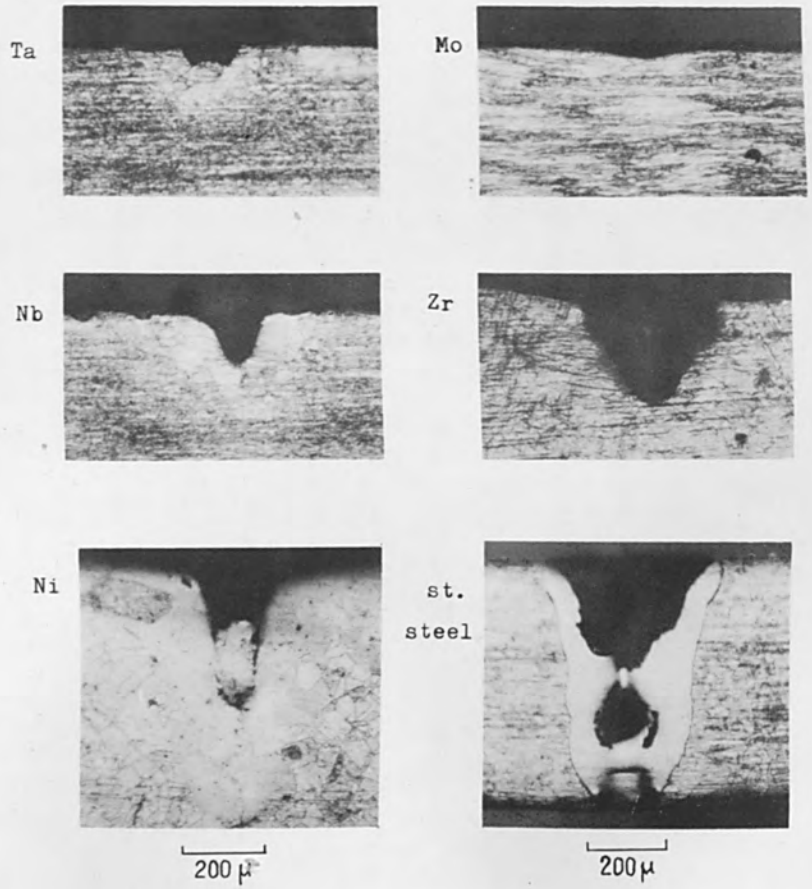

FIGURE 5 Etched Cross Sections of Drilled Holes in Various Metals by Electron Beam. Beam Intensity: 50 kv, 300 μA, d.c.

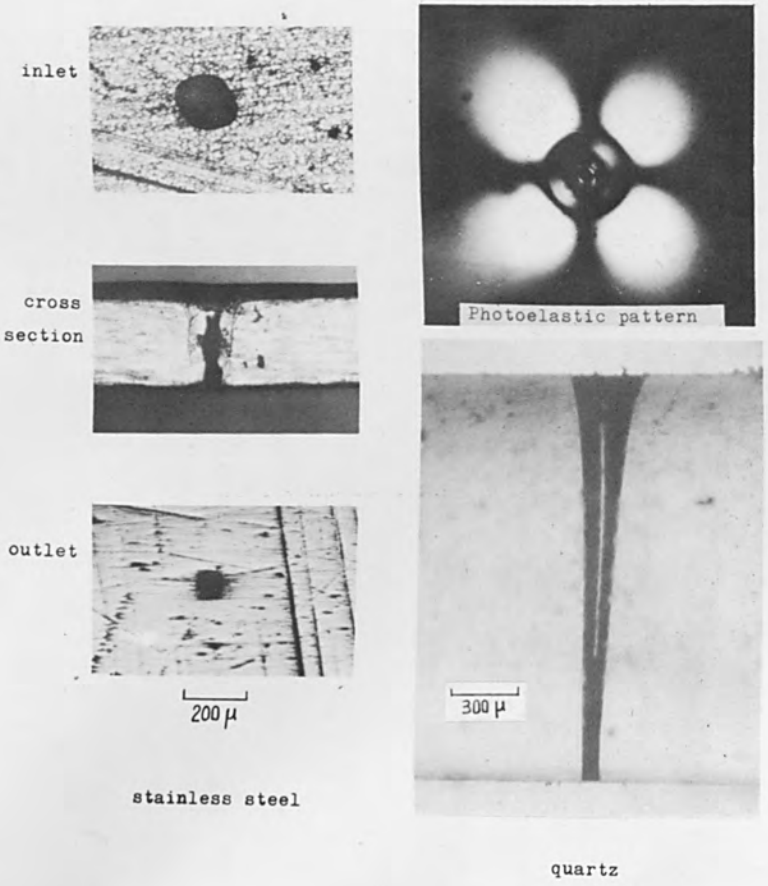

FIGURE 6 Electron Beam Perforation in Stainless Steel and Quartz

i = beam current and,

V = acceleration voltage.

In our case, the calculated spot diameter was several tens of microns.

As is well known, the spot diameter of a light beam at the focal plane of a lens of f mm focal length is given by

$$d = 2 f \theta \tag{2}$$

where d and θ are the diameter of the spot and the beam angle respectively, the aberration of the lens not being considered.

In the case of a perfectly parallel beam, the beam angle is given by the diffraction theory as

$$\theta \approx \frac{1.2\lambda}{d_s} \tag{3}$$

where d_s and λ are the diameter of the beam source and the wave length of the beam respectively.

Customarily, the parallelism of laser beam being taken for granted, Eq. (3) is used to obtain the beam angle, and in conjunction with Eq. (2), the spot diameter can be calculated. In our case, the calculated spot size was a few microns in diameter. This was very different from the observed value. The beam angle from Eq. (3) was about 10^{-4} rad., whereas the beam angle obtained with a ruby laser was about 10^{-2} rad. This extra spreading is caused by the off-axial modes of the laser oscillation, and this actual beam angle should be used to obtain the minimum spot diameter. If the laser beam is focused by a lens of 30 mm (or 15 mm) focal length, the diameter of the spot will become ~ 0.6 mm (or ~0.3 mm) by Eq. 2. In order to obtain a small size spot or a high energy density, it was necessary to

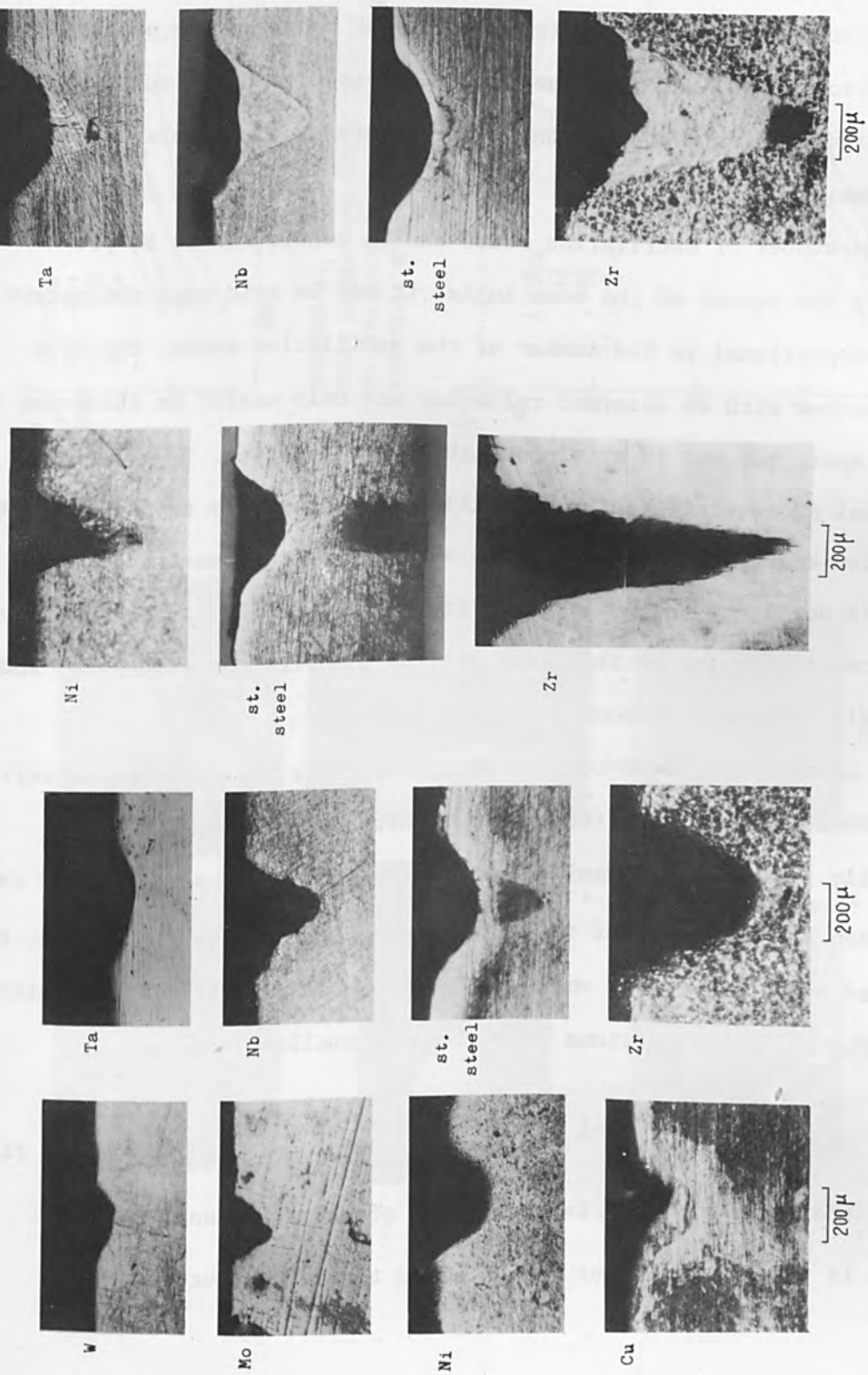

FIGURE 7 Etched Cross Sections of Holes Drilled in Metals by Laser Beam. Output 1.2 Joules. Focal length 30 mm.

FIGURE 8 Etched Cross Sections of Holes Drilled in Metals by Laser Beam. Output 1.2 Joules, Focal Length 15 mm.

FIGURE 9 Etched Cross Sections of Holes Drilled in Metals by Laser Beam. Output 2.2 Joules, Focal Length 30 mm.

reduce the beam angle as given by Eq.(2). The use of an external plane or convex mirror was a useful and simple method of mode selection.

As the distance between the output end of the ruby and the external plane reflector increased, the beam angle decreased, and the output energy also decreased nearly in proportion to the square of the beam angle as shown in Figs. 11 and 12[3].

Since the number of oscillation modes can be considered to be proportional to the square of the beam angle, it may be said that the output energy is proportional to the number of the oscillation modes. The mode selection method with an external reflector was only useful in obtaining a small size spot, but not to obtain a high energy density.

In thermal processing, the holes drilled were generally tapered for the reason of low energy density. When the absorbed energy density at the workpiece is not large enough to evaporate the material of the entire spot area at once, the center of this area will be the first to evaporate, and the hole will eventually become a tapered pit.

Since the action of a laser beam is pulsative, this was expected to influence the processing. This effect, with electron beam processing, was theoretically treated by N. Taniguchi and S. Maezawa[4]. According to their results, when the diameters of the pulsed and d.c. beams were the same, the hole drilled by pulsation was smaller than the hole drilled with no interruption. The optimum conditions that give the smallest hole are:

$$\tau/T \doteqdot 10^{-2}, \quad T/T_c \doteqdot 2 \times 10^{-2} \tag{4}$$

where τ is the pulse width, T is the period of pulsation and $T_c=\pi d^2/4k$ in which d is the beam diameter and k is the thermal conductivity.

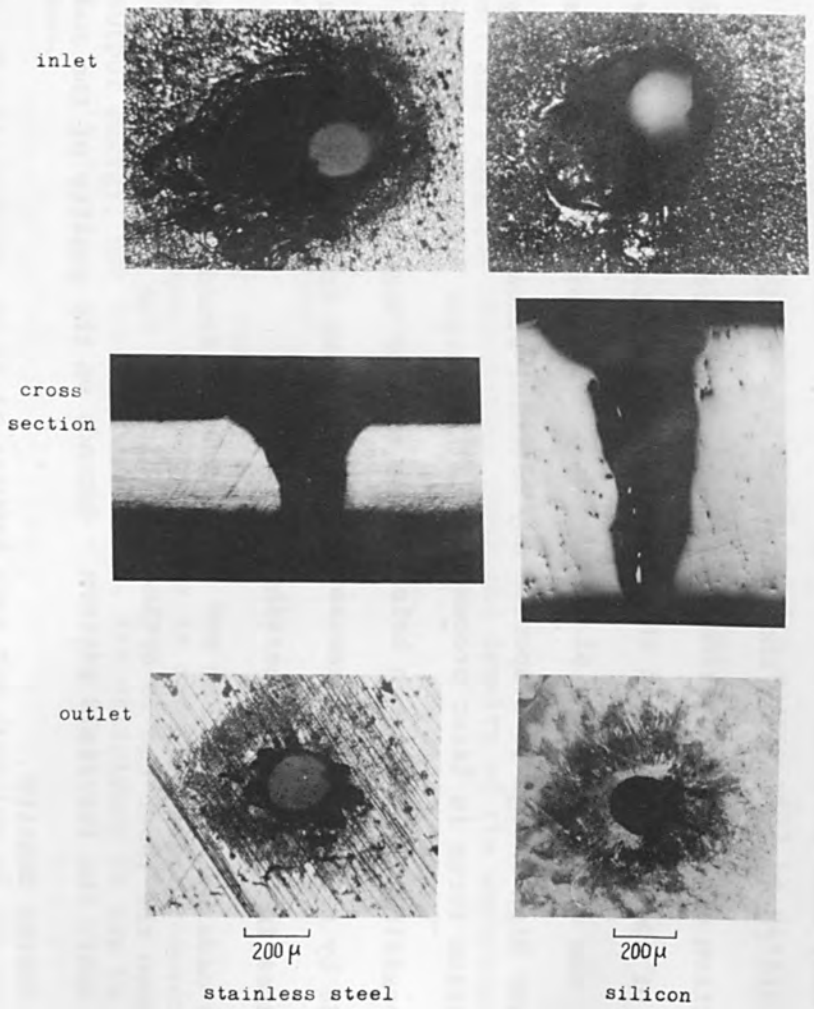

FIGURE 10 Laser Beam Perforation in Stainless Steel and Silicon. Output 1.2 Joules

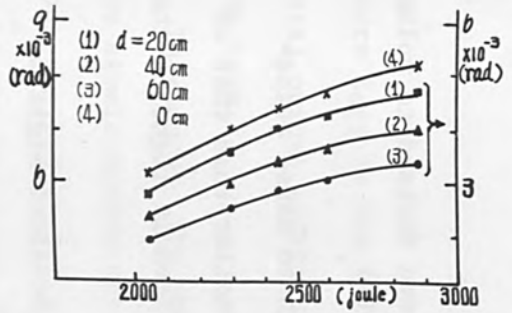

FIGURE 11 Relation between Beam Angle and Input Energy. d: Distance between Ruby and External Mirror

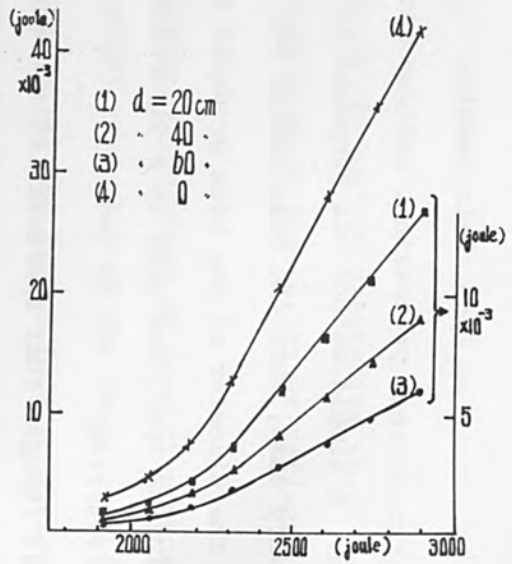

FIGURE 12 Relation between Output Energy and Input Energy. d: Distance between Ruby and External Mirror

The laser beam used satisfied the first of the above conditions with a T of about $10^{-5} \sim 10^{-6}$ sec., and the pulsation effect on various materials can be estimated from their result.

In electron beam processing, various methods have been devised to pulse the beam. A simple method was proposed by Namba et al[1].

In every case, when the beam energy was large enough to cause evaporation, the diameter of the hole produced was always smaller than that of the impinging spot, and this is a plausible result as seen in light of the above discussion.

It was thought that apertures of extremely small dimensions might be made by using the bottom of the tapered pit. But this expectation was not realized for around the pit bottom there is a zone of melting which gets carried away when perforated, leaving the outlet funnel-shaped.

The main forces acting on the pit bottom are the downward force due to the reaction of evaporating atoms, and the upward force due to the surface tension of the melt[5]. When the reaction force is larger than the surface tension, the melt around the pit bottom drops out. Since the laser has a peak power high enough to evaporate any material almost instantaneously, the reaction force in laser processing will be larger than that of electron beam processing. The through hole made by a laser beam will be larger than that made by electron beam because the melt will be carried away over a larger area in the laser processing.

Holes made by a laser beam are seldom round. Round holes are only obtained when the laser rod is optically faultless, for the form of the minimum spot- the far-field pattern - depends on the quality of the rod.

(b) Energy density

The surface energy density E_d can be obtained from the diameter of the

spot as:

$$Ed = \frac{4E_{eff}}{\pi d^2} \tag{5}$$

where E_{eff} is the effective energy to be used in processing which is the total output energy minus the energy loss by scattering or reflection of the beam.

In general, the energy loss of an electron beam by scatter depends upon the atomic number of the work material, and that of the laser beam depends upon the reflectivity of the work material and its surface condition.

If the two types of beam with the same energy content impinge upon a work-piece, the laser beam will realize a high volume density of energy near the surface, for it will be almost all absorbed there. The electron beam will penetrate into the material and its energy will be dissipated in a larger volume. The depth of penetration being given by:

$$t = 2.1 \times 10^{-12} \frac{V^2}{\rho} \tag{6}$$

where t and ρ are the penetration depth and density of the workpiece respectively.

(c) Power efficiency

(1) Output energy

For the electron beam, the input energy is almost entirely converted to the output energy, but for the laser beam, its efficiency is low by comparison.

For the laser beam, if it is assumed that the duration of the optical

pumping is shorter than the life time of the laser rod fluorescence, and that this is independent of the presence of any radiation, the excess energy over the threshold value will result in a laser output, due to R. H. Fairbanks[6], of:

$$E_o = \alpha (E_i - E_{th}) \tag{7}$$

where E_o, E_i and E_{th} are the output energy, the input energy and the threshold energy respectively and α is a constant. All of these values depend on the laser rod.

The experimental results, in which the output energy was measured by a calorimeter, agree with the functional form of Eq.(7) and α is about 3×10^{-4} which is nearly one order of magnitude smaller by comparison with the case where the straight xenon tube is used as the pumping source.

(2) Power efficiency in processing

The power efficiency in processing of various materials will be estimated from the drilled holes shown in Fig. 5 and Fig. 7, with the assumption that the hole was drilled by evaporation alone.

In the laser processing of stainless steel, for example, the reflection loss is smaller than that estimated from the reflection coefficient of the steel. A reduction in the loss by reflection would be expected under processing conditions because the laser beam is scattered by the vapor and also is reflected successively by the tapered surface.

The power efficiency cannot be estimated from a hole which is completely drilled through, for, as mentioned above, a part of the material at the outlet becomes molten and is carried away. If the through hole was formed by evaporation only, then the power efficiency would be more than 100% for the

laser processing of stainless steel.

In drilling with the laser beam, the power efficiency was found to be higher than that of an electron beam, and this is probably due to the pulsed nature of the former. When the beam is pulsed, the shorter the pulse width, the higher will be the power efficiency[4].

The advantages, disadvantages and applicable limits to be considered are as follows:

1. The apparatus for laser beam processing is simpler and more convenient than that for electron beam processing because the former requires no vacuum chamber.
2. In thermal processing, the use of a pulsed beam reduced the loss by thermal conduction and limited the zone of melt.
3. The depth of penetration is less for a laser beam than for electron beam, hence the former is better suited for surface processing.
4. The laser beam is applicable to the processing of insulators for it carries no electric charge.
5. The obtainable minimum spot size for processing purposes is larger for the laser beam than for the electron beam.
6. The laser beam is poor in power efficiency when used on materials highly transmissive or highly reflective for light.
7. With the laser beam, neither continuous processing nor a continuous output of high energy density is possible.
8. The difficulty in controlling the output intensity and the beam direction is the major disadvantage in laser processing.
9. The laser processing can be carried out under any desirable atmosphere.

10. With a laser beam drilling is easier than welding, for the output is of high peak energy and is pulsed.

SUMMARY

As both the electron and the laser beam processes are thermal, the results of experiments made with them were discussed together. In laser beam processing, continuous operation and control of output power were difficult, but the convenience of the apparatus and the speed of operation make laser beam processing readily applicable to micro-electronics. Both electron and laser beams with their useful characteristics will no doubt contribute to micro-processing.

ACKNOWLEDGEMENT

The authors wish to express their thanks to Y. Suge, chief of the laboratory, for his kind advice.

REFERENCES

1. Namba, S. et al., International Conference on Electron and Ion Beam Science and Technology, Toronto, 1964.
2. Schwarz, H. and DeMaria, A. J., Proc. National Electronics Conf. 18, 351, (1962).
3. Kim, P. H. and Namba, S., to be published in Japan J. Appl. Phys. 3, No. 5, (1964).
4. Taniguchi, N. and Maezawa, S., Proc. 5th Symposium on Electron Beam Technology, Alloyd Electronics Corporation, 1963, p. 135.
5. Bakish, R., Introduction to Electron Beam Technology, J. Wiley & Sons, N. Y., 1962, p. 340.
6. Fairbanks, R. H., Proc. 5th Symposium on Electron Beam Technology, Alloyd Electronics Corporation, 1963, p. 315.

ADVANTAGES AND DISADVANTAGES OF LASER MACHINING

William G. Voorhes
Pratt and Whitney Company
West Hartford, Connecticut

ABSTRACT

The concept of laser machining was evaluated for the case where a high average power laser would be used as a heat source to melt metal out of a workpiece. Since high average power lasers do not yet exist, a transferred arc plasma torch was used as the heat source for the experiments and the results were extrapolated to cover the case of a laser heat source. Equations were derived for the cross-sectional area of single grooves and the melting efficiency as functions of power, transfer efficiency, spot size, speed, and material constants. The theoretical values for the cross-sectional area were found to correlate reasonably well with test data. The maximum theoretical melting efficiency was found to be 0.66 for the plasma torch, although values approaching 1.00 would be attainable for lasers. An equation was derived showing the thickness of the heat affected zone to be inversely proportional to the energy density in the spot.

ADVANTAGES AND DISADVANTAGES OF LASER MACHINING

INTRODUCTION

In conventional machining there is a mechanical interaction between the cutting tool edge and the workpiece. This interaction causes the cutting tool to wear and the machine tool structural members to deflect. As the workpiece hardness increases, it is necessary to increase the cutting tool forces to maintain the metal removal rate at a desired level. This causes more rapid tool wear and increased structural deflection. In general, machine tool manufacturers cope with this problem by the evolutionary technique of developing both improved cutting tool materials, and more powerful and more rigid machine tools.

This problem can be sidestepped by utilizing a zero force machining process, one in which there is no mechanical interaction between the cutting head and the workpiece. Several zero force processes exist today; for example, electrolytic and electro-discharge machining. Such processes share a characteristic in common: the removal rate for a given material is independent of the material microstructure so that a workpiece can be fully hardened before being machined. Unfortunately, these processes share another characteristic: the material removal rate is low and consequently they cannot compete economically with conventional machine tools except in certain specific limited applications.

By utilizing a high energy density heat source to melt the material away, it may be possible to develop a zero force process having high material removal rate capability. Although existing lasers have average power outputs much too low (about 30 watts) to give high metal removal rates, lasers powerful enough for this purpose may be developed in the future. The Pratt and Whitney Company evaluated the concept of high power laser machining by using a transferred arc plasma torch as the heat source and extrapolating

the test results to cover the case of laser heat sources.

Molten Metal Removal

It is a relatively simple matter to melt metal with a high energy density heat source but removing the molten metal from the workpiece is not so simple. Although the metal could be removed by vaporization, this is not economic at high material removal rates because the energy required to vaporize metal is about ten times greater than that required for melting of the metal.

An analysis performed utilizing boundary layer theory explained the nature of metal flow in a groove generated by a high energy density jet such as a plasma arc torch and showed that the most effective way to remove the molten metal from the workpiece was to angle the torch and to blow the metal forward out of the groove (Fig. 1). The technique of having a simple forward angle on the torch is effective for removing molten metal only from single grooves; when grooves are overlapping and parallel, a simple forward angle causes the molten metal to blow over on the previously generated surfaces instead of being blown clear of the workpiece. However, a combination of both forward and side angles can minimize the blowback along the previously generated surfaces.

Since the laser is not a jet type device it may be necessary to incorporate some auxiliary removal device (such as an auxiliary jet) in a laser machining tool if metal is to be removed by melting rather than by vaporization.

Operating Parameters

Both plasma arc and laser systems will have at least three operating parameters in common: effective spot size, power level and speed. These parameters are discussed below:

FIGURE 1 Transferred Arc Plasma Torch

Effective Spot Size

The smaller the effective spot size across which a given amount of energy is being transferred from the heat source to the workpiece, the higher is the energy density: this will affect the operating efficiency.

Power Level

The cross-sectional area of a groove generated by a high energy density heat source traversing a workpiece at some constant speed increases as power is increased, all other conditions being equal. Furthermore, an increase in the power level increases the energy density of the spot and thus affects operating efficiency.

Speed

It is obvious that the width, depth and cross-sectional area of a groove will decrease as the traverse speed of the heat source is increased, all other conditions being equal. In addition, it will be shown that the operating efficiency of the system is a function of the speed, reaching a peak at some speed which is optimum for given operating conditions.

Effect of Operating Parameters upon the Generation of Single Grooves

In order to determine quantitatively the effect of power level, speed and spot size upon the characteristics of high energy density heat source systems, a series of tests was performed in which the three operating parameters were varied during the generation of single grooves with a plasma arc torch. The power level was varied between 15.7 and 22.5 kw, the speed between 50" and 400"/min, and the spot width between 0.295" and 0.437" The technique used for varying spot width was to tilt the torch to various combinations of forward (0^o, 15^o, 30^o) and side angles (0^o, 10^o, 15^o, 20^o); the spot width obtained for each combination was measured by the technique described in the following paragraph. Some 72 cuts were made. The

workpieces used were plates of ½" thick 1018 steel; the gas mixture used in the torch was a 65% argon-35% hydrogen mixture flowing at 115 CFH. After the tests were performed, the workpieces were sectioned and ground transverse to the grooves so that the width, depth and cross sectional area of each cut could be measured.

A relationship between the speed and width of cut for constant power input was established from the test data for each combination of forward and side angles; this is illustrated in Fig. 2. When the width was plotted against speed of the cut, the points fell more or less along a straight line. From this linear relationship, an empirical equation was derived relating width y and speed C:

$$\frac{y}{D} = \left(1 - \frac{C}{C_m}\right) \tag{1}$$

where, D is the groove width which would result during a cut made at an infinitely slow speed and can be considered to be the effective spot width. C_m is the critical speed above which no cutting takes place. Values for D and C_m were determined for each combination of forward and side angles by least squares regression analysis. The linear nature of the relationship is further illustrated in Fig. 3, where values of y/D are plotted against values of C/C_m for all cuts.

The following relationship relating y, D, C, and C_m was then established utilizing heat transfer theory (see Appendix I) and assuming a uniform energy density distribution across the spot:

$$\frac{y}{D} = \sqrt{1 - \left(\frac{C}{C_m}\right)^2} \tag{2}$$

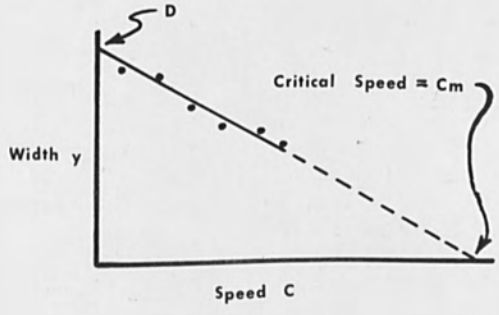

FIGURE 2 Relationship between Speed and Width for Constant Power

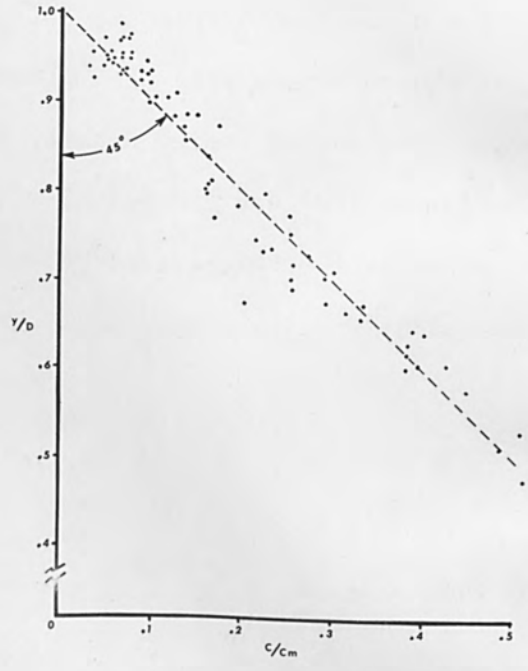

FIGURE 3 Scatter Diagram - Groove width/Spot width, vs Speed/Critical Speed

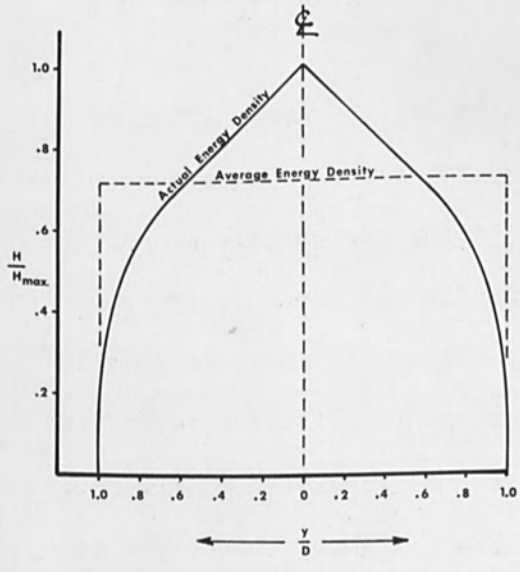

FIGURE 4 Energy Density Distribution across the Spot

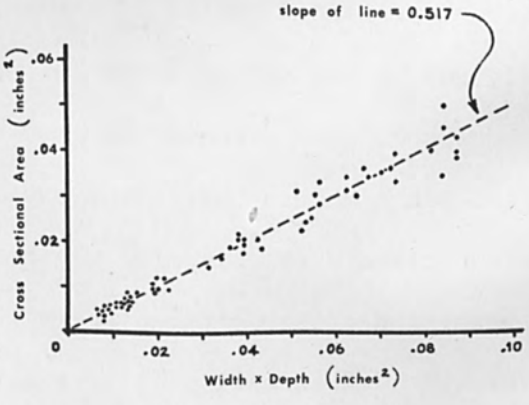

FIGURE 5 Scatter Diagram - Area vs. Width x Depth

The difference between Eq. (1) and (2) can be attributed to the fact that the energy density of a plasma arc torch is not uniform across the spot. The actual energy density distribution can be computed by comparing the theoretical and the actual width relationships. As shown in Eq. (3) of Appendix I, the critical velocity C_m is proportional to the square of the energy density H (kw/in^2). This leads to the relationship:

$$\frac{H^2 \text{ theory}}{H^2 \text{ test}} = \frac{C_m \text{ theory}}{C_m \text{ test}} \qquad (3)$$

By combining Eq. (1), (2) and (3), it can be shown that:

$$\frac{H^2 \text{ theory}}{H^2 \text{ test}} = \frac{(1 - y/D)}{\sqrt{1 - (y/D)^2}} \qquad (4)$$

the energy density distribution across the spot can be evaluated by using Eq. (4); the energy density distribution thus computed is presented in Fig. 4. This bell-shaped distribution is in agreement with the distribution shown by O'Brien[1].

It was desired to establish relationships between the melting efficiency (the theoretical amount of energy required to melt a given amount of metal divided by the actual amount of energy entering the workpiece) and the cross-sectional area of the groove as functions of power level, speed and spot width and the pertinent material constants. In order to do this, it was necessary to determine whether a relationship existed between the depth, width, and cross-sectional area for the grooves generated by the plasma arc torch. An examination of test data (see Fig. 5) shows that there is a single linear relationship between cross-sectional area and the width and

depth of the groove for all the combinations of forward and side angles tested:

$$A_m = .517\ y\ S \qquad (5)$$

where S is the depth of the groove. The value of the constant is dependent upon the geometry of the cut; for example, if the cross-section of the cut were a triangle, the constant would be 0.500; if the cross-section were a parabola, the constant would be 0.667.

By utilizing Eq. (1) and (5), an expression was derived (see Appendix II) relating melting efficiency η_m for a single groove to power P, transfer efficiency, η_t*, speed C, and spot size D for all torch angles:

$$\eta_m = .660\left[1-.616\ C_p\rho K(T_m-T_o)^2\ \frac{D^3C}{(P\eta_t)^2}\right]^2\left[1-.280\ \frac{P\eta_t}{D^2C}\ \frac{1}{\rho\left[C_p(T_m-T_o)+L\right]}\right] \qquad (6)$$

from which it was possible to derive a similar expression for the cross-sectional area A_m:

$$A_m = \frac{.660}{\rho\left[C_p(T_m-T_o)+L\right]}\cdot\frac{P\eta_t}{C}\left[1-(\text{ETC.})\right]^2\left[1-(\text{ETC.})\right] \qquad (7)$$

---

*Not all of the power developed in the heat source reaches the workpiece, since some power is lost in transfer. The concept of transfer efficiency is applicable to both plasma arc and laser operation. The plasma arc loses energy during transfer because of radiation -- the laser loses energy during transfer because of reflection from the workpiece.

where: 0.660 = maximum theoretical melting efficiency

ρ = density

T_m = melting temperature

T_o = ambient workpiece temperature

C_p = specific heat

K = thermal conductivity

L = heat of fusion

Eq. (6) is plotted in Fig. 6 for a typical case, and shows a peak melting efficiency η_m of 0.54; the form of equation (6) shows that the melting efficiency can be maximized by operating at the optimum speed for a given combination of power, transfer efficiency, and spot width.

The maximum theoretical melting efficiency is a function of the spot characteristics; if the distribution shown in Fig. 4 could be modified to give a uniform energy density distribution across the spot, the maximum theoretical melting efficiency would be increased from 0.66 to a value approaching 0.85 (see Appendix II). Furthermore, changing the shape of the spot from circular to square would increase the theoretical melting efficiency to a value approaching 1.00 (see Appendix II.)

An examination of Eq. (6) shows something about the type of material which can be adapted successfully to laser machining. The lower the thermal conductivity, all other things being equal, the higher the melting efficiency. This means that a laser machine tool should work well on carbon and low alloy steels, even better on stainless steels and the super alloys (which have lower K values than carbon steel) and not as well on aluminum and the refractory metals (which have much higher K values).

In order to utilize Eq. (6) and (7), it is necessary to know something about the transfer efficiency of the system. A subsequent series of

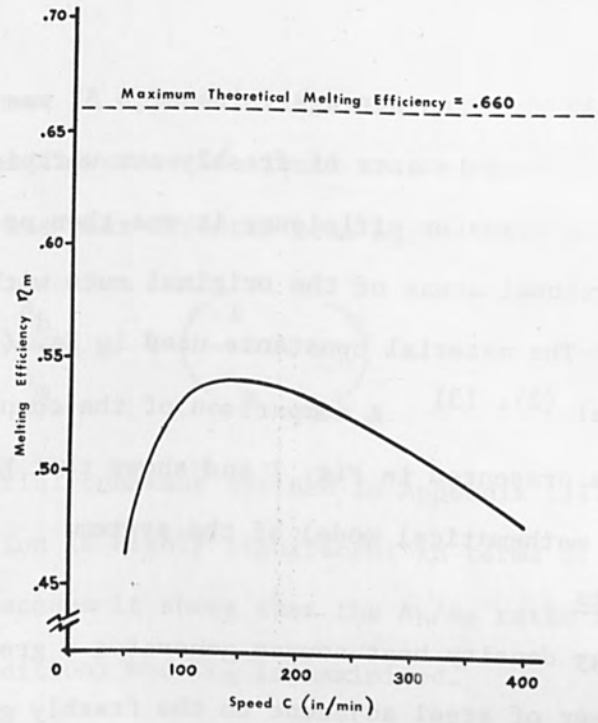

FIGURE 6 Plot of Computed Melting Efficiency η_m vs. Torch Speed C for a Power Level P of 20 KW, a Transfer Efficiency η_t of .62, and a Spot Width D of .300 in.

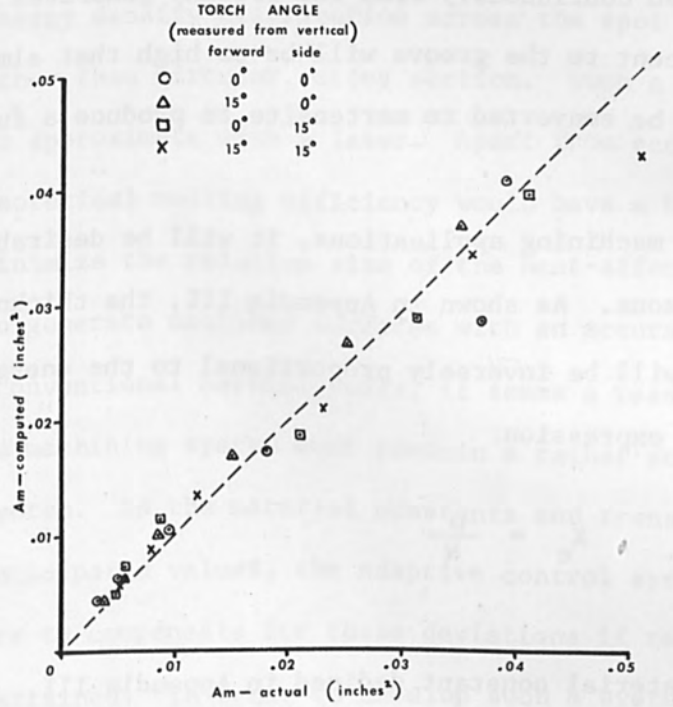

FIGURE 7 Comparison of the actual cross-sectional area A_m vs. the computed cross-section area A_m for several torch angles.

tests was performed in which an average value of 0.62 was obtained for η_t by making calorimetric measurements of freshly cut workpieces. Having obtained a value for the transfer efficiency it was then possible to compare the actual cross sectional areas of the original cuts with the values computed from Eq. (7). The material constants used in Eq. (7) were handbook values for mild steel.[2], [3] A comparison of the computed values versus the actual values is presented in Fig. 7 and shows that Eq. (7) is a reasonably accurate mathematical model of the system.

Metallurgical Effects

When a high energy density heat source generates a groove by traversing a steel plate, a layer of steel adjacent to the freshly generated surface is heated above its critical temperature, it is converted to austenite, and goes to make up a heat-affected zone upon cooling. If the freshly melted metal is removed continuously from the freshly generated surface, the cooling rates adjacent to the groove will be so high that almost all of this austenite will be converted to martensite to produce a full-hardened structure.

During most machining applications, it will be desirable to minimize this heat-affected zone. As shown in Appendix III, the thickness X_c of the heat-affected zone will be inversely proportional to the energy density H according to the expression:

$$X_c = \frac{\mu}{H} \tag{8}$$

where μ is a material constant defined in Appendix III. Since laser spots can be focused to extremely high energy densities, laser machining should be capable of producing a very minimal heat-affected zone thickness.

Moreover, as shown in Appendix III, the following relationship can be established between the cross sectional area of the groove A_m and the cross sectional area of the heat-affected zone A_h:

$$\frac{A_h}{A_m} = \gamma \left(\frac{1}{\eta_m} - 1 \right) \tag{9}$$

where γ is a material constant defined in Appendix III.

This last equation is highly significant in terms of establishing operating parameters because it shows that the A_h/A_m ratio is minimized (the most desirable condition) when η_m is maximized.

CONCLUSIONS

The maximum theoretical melting efficiency could be increased from 0.66 to a value approaching 1.00 by developing a high energy density heat source having a uniform energy density distribution across the spot and having a spot of square, rather than circular, cross section. Such a configuration should be simple to approximate with a laser. Apart from economy, increasing the maximum theoretical melting efficiency would have a beneficial side effect; it would minimize the relative size of the heat-affected zone.

If a laser is to generate machined surfaces with an accuracy approaching that available in conventional machine tools, it seems a reasonable assumption that the machining system must contain a rather sophisticated adaptive control system. As the material constants and transfer efficiencies deviate from the anticipated values, the adaptive control system must vary operating parameters to compensate for these deviations if reasonable accuracy is to be attained. In order to develop such a system, it will be necessary to define the process mathematically. Although the work presented here is only a first step to this goal, the fact that equations have

been developed relating single groove dimensions, heat-affected zone dimensions and melting efficiency to power, speed, spot width, material constants, and transfer efficiency, is encouraging and shows that it is well within reason to believe that an adaptive control system could be developed utilizing such mathematical relationships.

If a suitable control system could be developed, a laser machining tool would offer the following advantages over conventional machine tools:

1. Because hardened steels are difficult to machine, shops frequently machine steel in the softened condition, then heat treat to the desired hardness. Post-machining hardening may warp the machined surfaces, necessitating re-work. With a laser machine tool, the workpiece could be fully hardened before machining began.
2. Because laser machining develops such steep thermal transients immediately adjacent to the freshly generated surface, the heat-affected zone is almost completely martensitic, even in plain carbon and low alloy steels. Thus, it might be possible to make dies having extremely hard surface layers from inexpensive low alloy steels without having to use the more expensive die steels.
3. Because there would be no mechanical interaction between the cutting head and the workpiece, the laser machine tool could be much less rigidly constructed than a conventional machine tool, permitting a more flexible device.

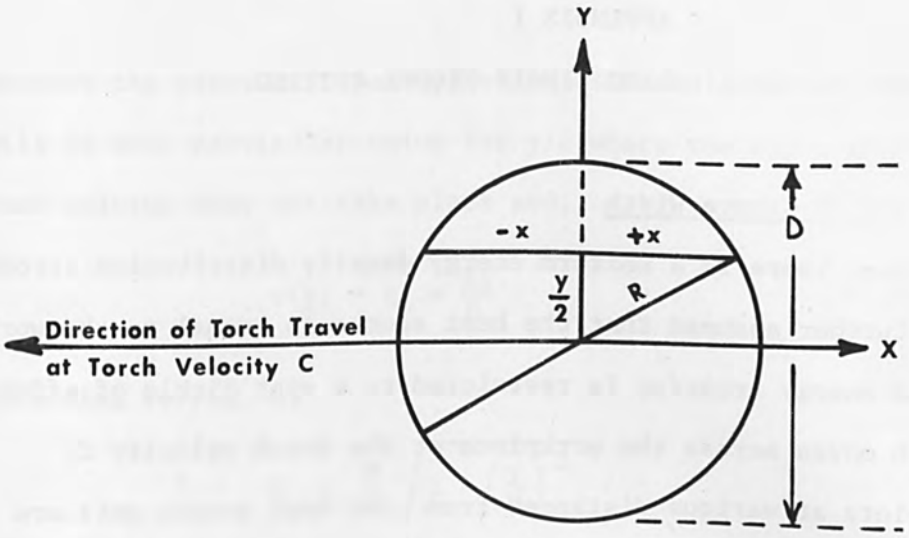

FIGURE 8
Circular Spot

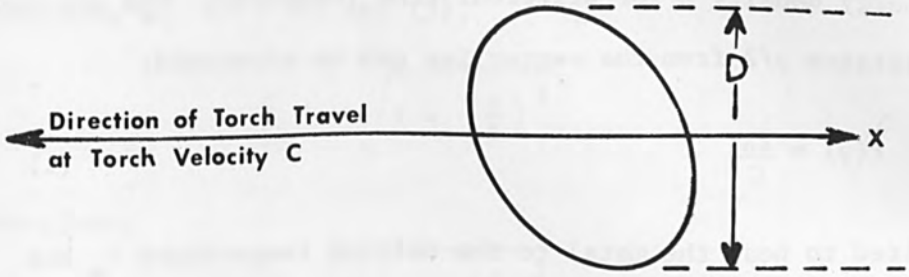

FIGURE 9
Elliptical Spot

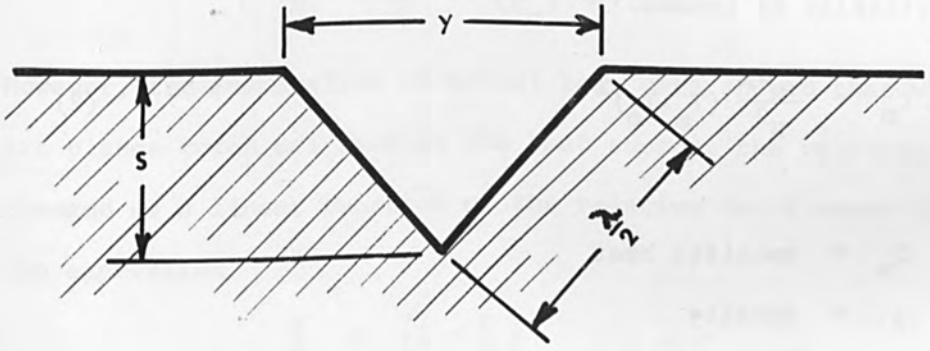

FIGURE 10
Groove Cross-Section

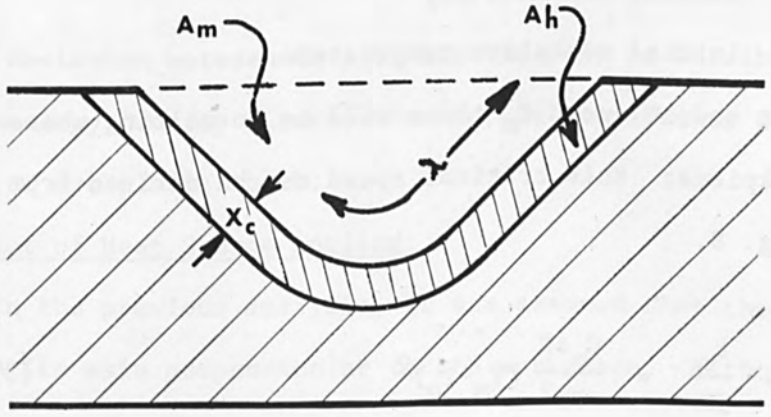

FIGURE 11
Heat Affected Zone

APPENDIX I

ENERGY TRANSFER DURING SINGLE GROOVE CUTTING

Theoretical Analysis of Groove Width

It is assumed that there is a uniform energy density distribution across the spot. It is further assumed that the heat source is normal to the workpiece and that the energy transfer is restricted to a spot circle of effective width D which moves across the workpiece at the torch velocity C. (See Fig. 8) Points at various distances from the heat source axis are exposed to the energy density H for different time intervals. The exposure time t(y) at a distance y/2 from the centerline can be expressed:

$$t(y) = \frac{2X}{C} \tag{1}$$

The time t_m required to heat the metal to the melting temperature T_m has been derived analytically by Landau.[4]

$$t_m = \frac{C_p \rho K}{H^2} (T_m - T_o)^2 \tag{2}$$

where:

C_p = specific heat

ρ = density

K = thermal conductivity

T_o = initial workpiece temperature

At some critical heat source speed C_m there will be no melting whatsoever taking place on the workpiece; this critical speed can be derived from Eq. (1) and (2), and Fig. 8.

$$\frac{1}{C_m} = \frac{t_m}{2R} = \frac{C_p \rho K}{DH^2} (T_m - T_o)^2 \tag{3}$$

Because the exposure time t(y) varies inversely with distance y/2, there will be some particular value for y/2 where the exposure time is so short that melting does not take place and,

$$t(y) = t_m = \frac{2X}{C} \tag{4}$$

According to Fig. 8,

$$X = \frac{D}{2}\sqrt{1 - \left(\frac{y}{D}\right)^2} \tag{5}$$

combining Eq. (3), (4) and (5),

$$\frac{C}{C_m} = \sqrt{1 - \left(\frac{y}{D}\right)^2}$$

Therefore,

$$\frac{y}{D} = \sqrt{1 - \left(\frac{C}{C_m}\right)^2} \tag{6}$$

However, the examination of actual test data showed that when a transferred arc plasma torch was used as the heat source, the relative cut width y/D changed as a linear function of the relative torch speed C/C_m according to the expression

$$\frac{y}{D} = \left(1 - \frac{C}{C_m}\right) \tag{6a}$$

The deviation between Eq. (6) and (6a) can be attributed to the fact that the energy density distribution across the spot is not uniform for a transferred arc plasma torch.

Effect of Heat Source Angling.

In the previous analysis, it was assumed that the heat source operated with its axis perpendicular to the workpiece. Although the proof is too

lengthy for inclusion here, it can be shown that upon tilting the heat source to various combinations of forward and side angles to form elliptical spots, the relationships shown in Eq. (6) and (6a) can be maintained simply by defining the spot width D to be as shown in Fig. 9.

APPENDIX II

DETERMINATION OF MELTING EFFICIENCY AND GROOVE CROSS SECTION

The melting velocity V of a rod experiencing a specific energy density H has also been derived by Landau[4] with the basic assumptions that the molten metal is removed continuously from the surface, and that the heat flow is unidirectional; according to Landau,

$$V = \frac{H}{\rho \left[C_p \left(T_m - T_o\right) + L\right]} \tag{7}$$

where L is the heat of fusion. Also, the depth, S, melted at velocity V, can be expressed:

$$S = (t - t_m)\, V \tag{8}$$

By definition, the melting efficiency η_m can be expressed as follows:

$$\eta_m = \frac{\text{Power required for melting}}{\text{Power received by workpiece}} \tag{9}$$

The power required for melting can be shown to be

$$P = \frac{A_m C \rho \left[C_p \left(T_m - T_o\right) + L\right]}{\eta_t \eta_m} \tag{10}$$

where A_m is the cross sectional area of the groove and η_t is the transfer

efficiency.

By assuming H to be the average energy density (as shown in Fig. 4), inspection of Fig. 8 shows that:

$$P\eta_t = \frac{\pi D^2}{4} \cdot H \tag{11}$$

Upon combining Eq. (9), (10) and (11), it can be shown that:

$$\eta_m = \frac{A_m C \rho \left[C_p (T_m - T_o) + L \right]}{\pi/4 \cdot D^2 H} \tag{12}$$

However, examination of actual test data showed that the cross sectional area of the groove can be expressed in terms of the width and depth of the groove:

$$A_m = .517\ yS \tag{13}$$

where S is the groove depth.

Combining Eq. (12) and (13) shows that:

$$\eta_m = \frac{.517}{\pi/4} \cdot \frac{y^2}{D^2} \cdot \frac{\rho \left[C_p(T_m - T_o) + L \right]}{H} \cdot \frac{CS}{y} \tag{14}$$

Therefore, by substituting Eq. (6a) in Eq. (14), the melting efficiency can be expressed:

$$\eta_m = .660 \left(1 - \frac{C}{C_m}\right)^2 \frac{\rho \left[C_p(T_m - T_o) + L \right]}{H} \cdot \frac{CS}{y} \tag{15}$$

However, this was not a useful expression because S and y vary with speed, and H varies with S. It was desirable to replace S and y with some function of H. In order to establish such a relationship, it was assumed that the cut has a triangular scross-section* as shown in Fig. 10. An exami-

*This was a realistic assumption because the actual cuts were very close

nation of Fig. 10 showed that the average energy density over the groove surface decreased from an initial value of H before cutting began, to a value of H_s, at depth S, such that

$$\frac{H_s}{H} = \frac{y}{\lambda} \tag{16}$$

or, upon combining Eq. (7) and (16),

$$\frac{V_s}{V} = \frac{y}{\lambda} \tag{17}$$

where V was the initial melting velocity and V_s was the melting velocity at depth S.

From Fig. 10, it can be shown that:

$$\frac{\lambda}{y} = \frac{1}{\sqrt{1 + 4\ (S/y)^2}}$$

and therefore,

$$\frac{V_s}{V} = \frac{1}{\sqrt{1 + 4\ (S/y)^2}} \tag{18}$$

From Eq. (8),

$$d(t-t_m) = \frac{1}{Vs}\, dS \tag{19}$$

Combining Eq. (18) and (19) shows that:

$$d(t-t_m) = \frac{1}{V_s}\sqrt{1 + 4(S/y)^2}\ .\ dS$$

---

to a triangular shape. If the cuts were exactly triangular, then A_m would have a value of 0.500 y.S, instead of the value 0.517 y.S as given in Eq. (13)

and therefore,

$$(t-t_m) = \frac{1}{V}\int_0^S \sqrt{1 + 4\ (S/y)^2}\ .\ dS \qquad (20)$$

Upon integrating Eq. (20) it can be shown that:

$$\frac{V(t-t_m)}{y} = \frac{1}{4}\left[\frac{2S}{y}\sqrt{1+\left(\frac{2S}{y}\right)^2} + \ln\left(\frac{2S}{y} + \sqrt{1+\left(\frac{2S}{y}\right)^2}\right)\right] \qquad (21)$$

Eq. (21) is very difficult to handle in this form. However, a simplifying approximation can be obtained by substituting numerical values for the quantity S/y over the closed interval $0 < S/y < 1.07$ (all of the test values fell within this interval), into Eq. (21), to obtain the corresponding values of $V(t-t_m)/y$. Upon plotting the values of S/y versus $V(t-t_m)/y$, it can be shown that S/y can be expressed in terms of $V(t-t_m)/y$ as follows:

$$\frac{S}{y} = \left[\frac{V(t-t_m)}{y}\right] - .220\left[\frac{V(t-t_m)}{y}\right]^2 \qquad (22)$$

where $0 < S/y < 1.07$. Upon substituting Eq. (22) into Eq. (15) it can be shown that: (23)

$$\eta_m = .660\left(1-\frac{C}{C_m}\right)^2 \frac{\rho\left[C_p(T_m-T_o) + L\right] C}{H} \cdot \frac{V(t-t_m)}{y}\left[1-.220\left(\frac{V(t-t_m)}{y}\right)\right]$$

From Eq. (3),

$$t = \frac{D}{C} \quad \text{and} \quad t_m = \frac{D}{C_m}$$

and therefore,

$$(t-t_m) = \frac{D}{C}\left(1 - \frac{C}{C_m}\right)$$

But from Eq. (6a),

$$D\left(1 - \frac{C}{C_m}\right) = y$$

Therefore,

$$\frac{(t-t_m)}{y} = \frac{1}{C} \tag{24}$$

Upon substituting Eq. (24) in Eq. (23),

$$\eta_m = .660 \left(1 - \frac{C}{C_m}\right)^2 \frac{\rho\left[C_p(T_m-T_o) + L\right]}{H} \cdot V\left(1 - .220\frac{V}{C}\right) \tag{25}$$

Substituting Eq. (7) into Eq. (25) yields the following:

$$\eta_m = .660 \left(1 - \frac{C}{C_m}\right)^2 \left[1 - .220 \frac{H}{\rho\left[C_p(T_m-T_o) + L\right] C}\right] \tag{26}$$

From Eq. (3), $\frac{1}{C_m} = \frac{C_p \rho K (T_m-T_o)^2}{DH^2}$; thus equation (26) can be rewritten:

$$\eta_m = .660 \left[1 - \frac{C_p \rho K (T_m-T_o)^2}{H^2} \cdot \frac{C}{D}\right]^2 \left[1 - .220 \frac{H}{\rho\left[C_p(T_m-T_o) + L\right] C}\right] \tag{27}$$

However, from Eq. (11), $H = \frac{4 P \eta_t}{\pi D^2}$; and upon substituting for H in Eq. (27), and simplifying, it can be shown that:

$$\eta_m = .660\left[1 - .616 C_p \rho K (T_m-T_o)^2 \frac{D^3 C}{(P\eta_t)^2}\right]^2 \left[1 - .280 \frac{P\eta_t}{D^2 C}\right] \frac{1}{\rho\left[C_p(T_m-T_o)+L\right]} \tag{28}$$

The cross-sectional area A_m of the cut can be expressed:

$$A_m = \frac{1}{\rho\left[C_p(T_m-T_o)+L\right]} \cdot \frac{P\eta_t}{C} \cdot \eta_m \tag{29}$$

Substituting Eq. (28) into Eq. (29),

$$A_m = \frac{.660}{\rho\left[C_p(T_m-T_o)+L\right]} \cdot \frac{P\eta_t}{C} \left[1 - ETC\right]^2 \left[1 - ETC.\right] \tag{30}$$

Maximizing the Melting Efficiency

As shown in Eq. (15) and again in Eq. (28), the maximum theoretical melting efficiency is 0.660. If the energy density distribution could be modified so as to be uniform across the spot, then a heat transfer analysis will show that the cross-sectional configuration of the cut would approach the shape of a parabola. Assuming a parabolic cross section, Eq. (13) would be modified from the form $A_m = 0.517\ y.S$ to the form $A_m = 0.667\ y.S$. As shown in Eq. (15), this would increase the maximum theoretical melting efficiency from $0.517/(\pi/4)$ to $0.667/(\pi/4)$ or from 0.660 to 0.850.

If the energy density were constant across a square spot, then a heat transfer analysis would show that the cross-sectional configuration of the cut would approach the shape of a rectangle. Assuming a rectangular cross-section, Eq. (13) would be modified to the form $A_m = 1.00\ y.S$. Furthermore, Eq. (11) would be modified from the form $P\eta_t = (\pi/4)D^2H$ to the form $P\eta_t = 1.0\ D^2H$. As shown in Eq. (15), this would increase the maximum theoretical melting efficiency from $0.517/(\pi/4)$ to 1.00/1.0 or from 0.660 to 1.00

APPENDIX III

DETERMINATION OF RELATIONSHIP BETWEEN HEAT-AFFECTED ZONE, WORKPIECE HEAT STORAGE, AND MELTING EFFICIENCY

Landau[4] has developed a relatively uncomplicated procedure for analyzing the heat conduction which accompanies and follows the ablative removal of metal by a high energy density heat source. This procedure is

based upon the same previous assumptions of constant energy density and unidirectional heat flow. According to Landau, once steady melting (and ablation) is established, the steady state temperature distribution in the solid can be expressed:

$$\frac{T - T_o}{T_m - T_o} = e^{-\left(\frac{VX\rho C_p}{K}\right)} \tag{31}$$

where X is the distance required for the temperature to drop from T_m to T.

As the high energy density heat source generates a groove when traveling along a steel plate, that portion of the groove immediately behind the moving heat source will cool down extremely rapidly from the temperature distribution defined by Eq. (31). Any steel which has been heated above the critical temperature T_c will be converted to martensite, because of this rapid cooling, and will go to make up the heat-affected zone. By proper substitution in Eq. (31) the thickness X_c of this heat-affected zone can be expressed by the relationship:

$$X_c = \frac{K}{\rho C_p V} \ln \left[\frac{T_m - T_o}{T_c - T_o}\right] \tag{32}$$

By combining Eq. (7) and (32), it can be shown that

$$X_c = \frac{K}{H} \cdot \left[(T_m - T_o) + \frac{L}{C_p}\right] \cdot \ln\left[\frac{T_m - T_o}{T_c - T_o}\right] \tag{33}$$

which can be expressed

$$X_c = \frac{\mu}{H}, \text{ where } \mu \text{ is a material constant.}$$

According to Eq. (31)

$$T - T_o = (T_m - T_o)e^{-\left(\frac{VX\rho C_p}{K}\right)}$$

Therefore an examination of Fig. 11 shows that the amount of the heat energy Q_a which is added to a workpiece as a result of groove generation can be expressed:

$$Q_a = 1\,\lambda\,(T_m - T_o)\,\rho\,C_p \int_o^\infty e^{-\left(\frac{VX\rho C_p}{K}\right)} \cdot dx \qquad (34)$$

where 1 is the length of the cut.

Upon integrating Eq. (34) it can be shown that

$$Q_a = 1\,\lambda(T_m - T_o)\,\frac{K}{V} \qquad (35)$$

which can be combined with Eq. (32) to yield the following:

$$Q_a = \frac{\lambda\, X_c 1 (T_m - T_o) C_p \rho}{\ln\left[\frac{T_m - T_o}{T_c - T_o}\right]} \qquad (36)$$

Since the term λX_c is equal to the cross-sectional area of the heat affected zone A_h, the workpiece heat storage can be expressed:

$$Q_a = \frac{A_h 1 (T_m - T_o)\, C_p 1}{\ln\left[\frac{T_m - T_o}{T_c - T_o}\right]} \qquad (37)$$

The heat storage energy Q_a does not contribute to the removal of metal and is wasted energy. The melting inefficiency can be defined:

$$\eta_m = \frac{\text{Energy required for melting}}{\text{Energy received by workpiece}} = \frac{Q_m}{Q_m + Q_a}$$

and therefore:

$$\frac{1}{\eta_m} - 1 = \frac{Q_a}{Q_m} \qquad (38)$$

But,

$$Q_m = \rho\left[C_p(T_m - T_o) + L\right] A_m 1 \qquad (39)$$

Therefore, upon substituting Eq. (37) and (39) into Eq. (38) and simplifying, it can be shown that:

$$\frac{A_h}{A_m} = \left[1 + \frac{L}{(T_m - T_o)C_p}\right]\left[\ln\left(\frac{T_m - T_o}{T_c - T_o}\right)\right]\left[\frac{1}{\eta_m} - 1\right] \qquad (40)$$

which can be expressed:

$$\frac{A_n}{A_m} = \gamma\left[\frac{1}{\eta_m} - 1\right] \quad , \text{ where } \gamma \text{ is a material constant.}$$

REFERENCES

1. O'Brien, R.F. "Applications of the Plasma Arc in Fabriction". SAE National Aeronautic Meeting, 1961, Paper #340H.
2. "Metals Handbook," Volume 1, Eighth Edition, American Society for Metals, Novelty, Ohio, 1961.
3. Eckert, E.R.G., "Introduction to the Transfer of Heat and Mass," McGraw-Hill, New York, 1950.
4. Landau, H.G. "Heat Conduction in a Melting Solid," Quarterly Journal of Applied Mathematics, April 1950, PP 81-94.

POWER DENSITY EFFECTS IN LASER PRODUCED CRATERS

John D. Myers
Cornell Aeronautical Laboratory, Inc.
Buffalo, New York

ABSTRACT

The drilling capability of lasers is influenced by various parameters of the incident beam of radiation. Those parameters which have greatest influence upon the topography of the crater formed by a laser beam are peak power, pulse length, and power density. In the experiment reported here, two of these parameters were held constant and the third (power density) was varied in a series of irradiations of various metals of engineering interest. The resulting crater dimensions were then correlated with the respective power density used. In a second series of irradiations, higher peak powers and shorter pulse lengths were employed and the results noted. Finally, a crater formation mechanism is presented which explained the experimental results for the energy parameters used.

POWER DENSITY EFFECTS IN LASER PRODUCED CRATERS

INTRODUCTION

The exact mechanism by which craters are produced in metals by laser radiation is the subject of continuing speculation. Among the mechanisms cited as being responsible for the removal of material from the crater site are shock waves, trapped vapor explosions, evaporation recoil pressures, and simple evaporation. The experiments described in this paper were performed with the specific goal in mind of identifying the mechanism by which laser-produced craters are formed. It was hoped that such an identification could lead not only to a better understanding of laser cratering but also to other applications of the underlying principles.

The experimental program involved the irradiation of metals with a focused laser beam while holding all of the parameters but one constant at any given time. The changes in crater topography were then correlated with the varied parameter.

THEORETICAL CONSIDERATIONS

The case of a continuous point-source of heat located in an infinite solid, as treated by Carslaw[1] will be used as a basis for this analysis. The continuous point source model made five assumptions (all of which are of limited validity for this case) which are needed to prevent the mathematics from becoming unmanageable. The assumptions are:

1. Heat flows from a point source on the surface of the metal.
2. The metal is a semi-infinite homogeneous isotropic solid with temperature independent thermal properties.
3. No heat is lost from the surface of the metal.
4. No heat is lost due to changes in state.
5. No material is lost during heating.

This theoretical treatment has been supported experimentally by

C. J. Bahn and R. D. Engquist[2] with a laser using iron, copper, and aluminum samples. The heat transfer model alluded to is embodied in the following relationship:

$$T = \frac{1}{2\pi K_t r}\left(\frac{dQ}{dt}\right)\left[1 - \text{Erf}\left(\frac{r}{\sqrt{4\alpha t}}\right)\right]$$

where

$$\text{Erf}\left(\frac{r}{\sqrt{4\alpha t}}\right) = \frac{2}{\sqrt{\pi}}\int_0^{\frac{r}{\sqrt{4\alpha t}}} \exp(-x^2)\,dx$$

and:

T = temperature measured from ambient

α = thermal diffusivity

t = time from onset of laser emission

ρ = density of solid

C = specific heat of solid

r = radius of hemispherical isotherm of temperature, centered at point source incident at the surface

K_t = thermal conductivity

$\frac{dQ}{dt}$ = ratio of energy input to pulse duration

Two isotherms in the metal are of special interest; the boiling point isotherm (r_b) and the melting point isotherm (r_m). Let us assume that the material under consideration is stainless steel. Then, rearranging terms and inserting the appropriate physical constants[3] and a realistic value for $\frac{dQ}{dt}$, we have the following:

Density	=	7.9 gm/cc
Boiling Point	=	2740°C
Melting Point	=	1510°C
Specific Heat	=	0.5 J/gm - °C
Thermal Diffusivity	=	0.05 cm^2/sec
Thermal Conductivity	=	0.2 J/cm - °C - sec
$\frac{dQ}{dt}$	=	3.5 kw

$$r_b \cong \left[1 - \text{Erf}\left(\frac{r_b}{\sqrt{4\alpha t}}\right)\right]$$

$$r_m \cong 2\left[1 - \text{Erf}\left(\frac{r_m}{\sqrt{4\alpha t}}\right)\right]$$

And, for a given

$$r_m - r_t \cong r_b \cong \left[1 - \text{Erf}\left(\frac{r_b}{\sqrt{4\alpha t}}\right)\right]$$

Using published values[4] for Erf x we can now plot the position of the boiling point isotherm and the depth of the molten layer as a function of time during the laser pulse for different values of r_b (See Fig. 1).

As can be seen, increasing the power delivered merely shifts the curve upward. Furthermore, since $(r_m - r_b) = r_b$, this curve also implies that the boiling point isotherm can only be extended (at a given $\frac{dQ}{dt}$) to a point corresponding to a maximum surface area. When this point is reached, material will no longer be evaporated because of excessive heat loss through conduction.

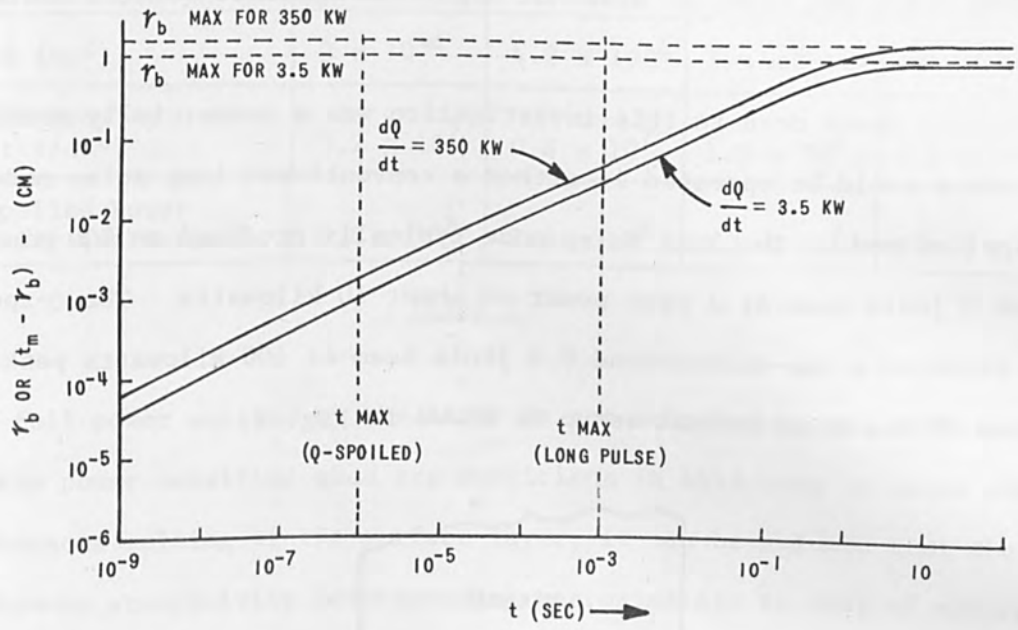

FIGURE 1 Depth of Boiling Isotherm vs Time

Since, ideally, the crater dimensions would be determined by this boiling point isotherm, the curve implies that an increase of the applied power will result in deeper craters. However, increasing the applied power incident on a surface is equivalent to increasing the power density. Therefore, one should be able to increase the depth of laser produced craters by simply increasing the power density while maintaining all other parameters at constant values.

It is recognized that the aforementioned thermal model leaves much to be desired. For example, the assumption that hemispherical isotherms will be formed is not justified in light of the fact that the real source is not a point. Also, the model ignores what happens to the material after it

reaches its boiling point. Nevertheless, the model does serve as a starting point and gives an order of magnitude estimate for the crater depths to be expected.

The ruby laser used in this investigation was a commercially available unit which could be operated in either a conventional long pulse mode or in a Q-spoiled mode. The long pulse mode typically produced an 800 microsecond 3 joule beam at a peak power of about 10 kilowatts. The Q-spoiled mode produced a one-microsecond 0.1 joule beam at 100 kilowatts peak. A diagram of the experimental setup is shown in Fig. 2.

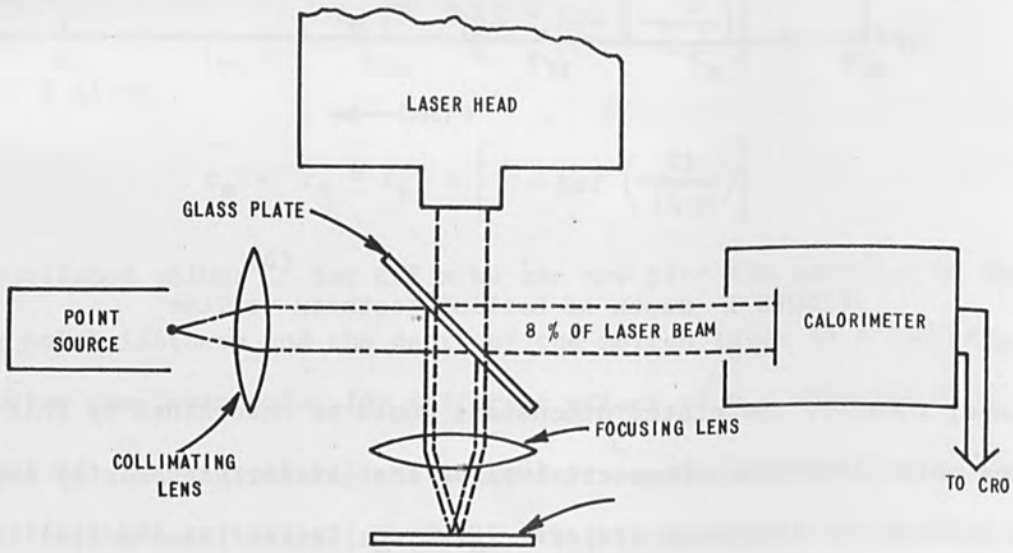

FIGURE 2 Experimental Set-Up

Different power densities were obtained by simply interchanging the focusing lens with one of a different focal length. Table I lists the various focusing lenses used together with the corresponding spot sizes and power densities obtained.

FOCUSING PARAMETERS

Focal Length	2 cm	2.5 cm	5.1 cm	7.6 cm
Spot Size (dia.)	.02 cm	.025 cm	.051 cm	.76 cm
Area (cm^2)	3×10^{-4}	4.2×10^{-4}	1.9×10^{-3}	4.3×10^{-3}
Power Density (watts/cm^2)	1.2×10^{7}	0.8×10^{7}	1.9×10^{6}	0.8×10^{6}
Q-spoiled Power Density (watts/cm^2)	9.4×10^{8}	2.6×10^{8}	5.8×10^{7}	1.4×10^{7}

TABLE I

The full power emitted by the laser is not absorbed by the workpiece. Since the power densities used are sufficient in this case to cause almost instantaneous melting of the surface layer, it can be assumed that the workpiece has an absorptivity corresponding approximately to that of molten material for the entire duration of the pulse. The absorptivity of molten iron is about 0.40[3]. Therefore, the workpiece will absorb only about 1.4 joules of a 3.5 joule laser pulse impinging upon it.

Samples of various engineering materials were polished and irradiated with 3 joule and 0.2 joule "Q-spoiled" laser pulses at varying power densities. The samples were imbedded in lucite, sectioned, and polished so as to reveal an accurate cross section of the crater at its centerline. Pictures were taken using a Leitz metallurgical microscope and calibrated against pictures taken of a 0.01 millimeter scale through the same lens system. A grid overlay was drawn according to the calibration pictures and used to perform graphical integration of the crater volumes. In performing the graphical integrations, cylindrical symmetry was assumed.

EXPERIMENTAL RESULTS

The results of the experiment will be presented in two sections. The first will be concerned with metals irradiated with the laser in the "long-pulse" mode of operation. The second will cover metals irradiated with the laser in the "Q-spoiled" operating mode (short pulse).

LONG PULSE RESULTS

The four photographs shown in Fig. 3 illustrate the cross sections of craters produced in 302 stainless steel by one millisecond, 3.5 joule laser pulses. The only parameter that was varied was the power density (by changing spot size) of the energy incident on the test specimen. As can be seen, the penetration varies directly with power density. The minimum thermal work (energy required to melt volume) done is approximately the same for each crater and agrees fairly well with the heat transfer model used.

Attempts to compute the thermal work accomplished in vaporizing the material were discarded because of the difficulty in (analytically) separating that material which was vaporized from that which was pushed or "blown" out. Titanium, Stellite - 21, and OFHC copper (Figs. 4, 5 and 6 respectively) also show the same relationship between power density and penetration depth. Copper was not damaged by the 0.84×10^6 w/cm^2 beam but cratered at 1.9×10^6 w/cm^2. Table II is a compilation of the long pulse results.

SHORT PULSE RESULTS

Those samples irradiated with the short pulse did not show the same clear correlation between crater topography and the varied pulse parameter as was

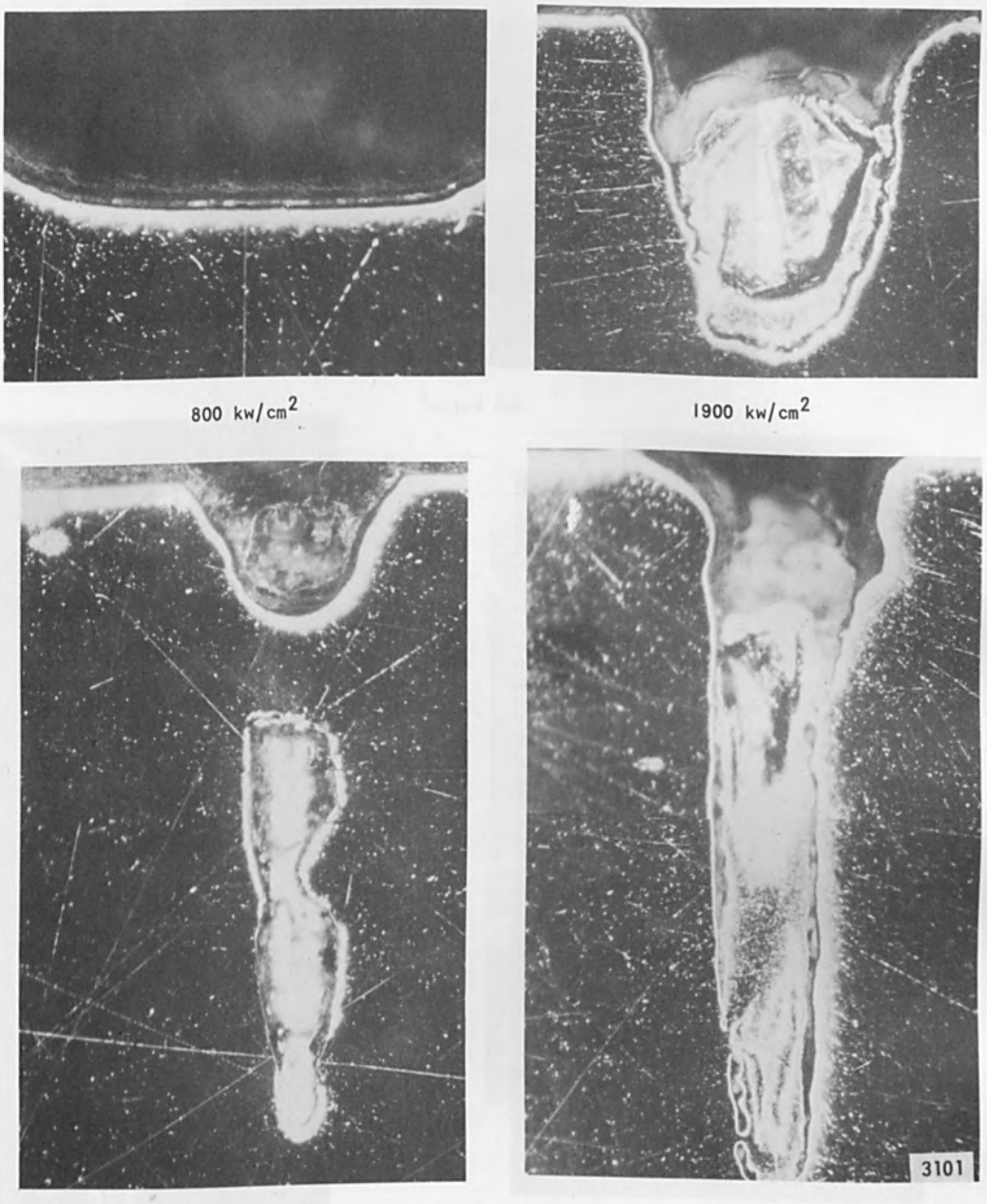

800 kw/cm^2

1900 kw/cm^2

8000 kw/cm^2

12,000 kw/cm^2

302 STAINLESS STEEL - LONG PULSE - 3.5 JOULES

Figure 3

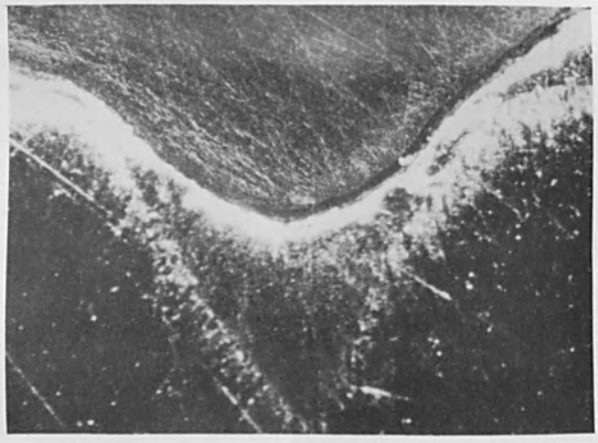

800 kw/cm^2

1900 kw/cm^2

8000 kw/cm^2

TITANIUM - LONG PULSE 3.5 JOULES

Figure 4

POWER DENSITY EFFECTS IN LASER PRODUCED CRATERS

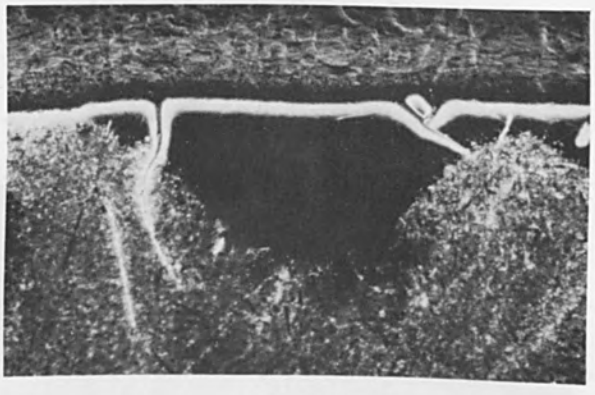

800 kw/cm^2

1900 kw/cm^2

12,000 kw/cm^2

STELLITE 21 - LONG PULSE - 3.5 JOULES

Figure 5

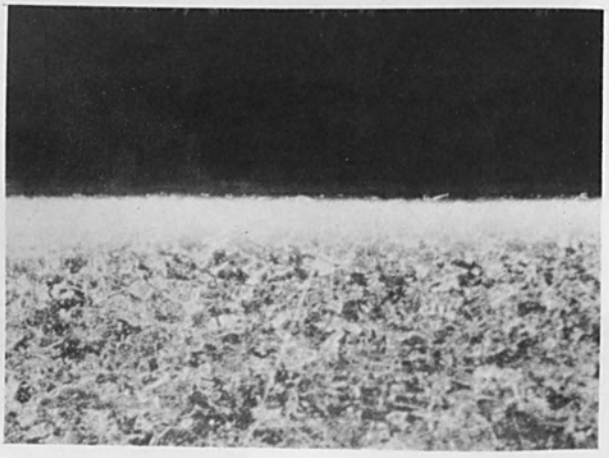

800 kw/cm^2

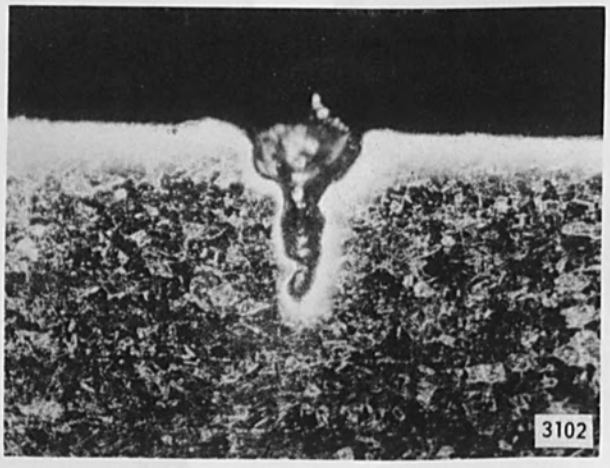

1900 kw/cm^2

OFHC COPPER - LONG PULSE - 3.5 JOULES

Figure 6

LONG PULSE RESULTS

Metal Specimen	Power Density (w/cm^2)	Melted Volume (mm^3)	Melted Depth (mm)	Min. Thermal Work Done (joules)
"Stellite 21"	8×10^6	0.066	1.05	0.31
"Stellite 21"	1.9×10^6	0.052	1.01	0.25
"Stellite 21"	8×10^5	0.032	0.23	0.15
302 Stainless Steel	1.2×10^7	0.032	1.15	0.26
302 Stainless Steel	8×10^6	0.025	1.02	0.20
302 Stainless Steel	1.9×10^6	0.046	0.53	0.37
302 Stainless Steel	8×10^5	0.025	0.07	0.20
Titanium*	8×10^6	0.059	1.01	0.27
Titanium*	1.9×10^6	0.060	1.00	0.27
Titanium*	8×10^5	0.055	0.20	0.26
Copper OFHC	1.9×10^6	0.002	0.25	0.01
Copper OFHC	8×10^5	None	None	None

*Commercially pure.

TABLE II

found with the long pulse samples. Fig. 7 shows the craters produced in the stainless steel sample by "Q-spoiled" laser pulses. As one can see, the differences between the crater cross sections are insignificant and do not indicate a clear trend with respect to the increasing power density. The other metals (tungsten, copper and "Stellite") irradiated with short pulses showed similar lack of dependence upon power density; in general, the craters formed in those three were shallower than the ones in steel. None of the samples examined gave indication of any significant melting of material beneath the crater floor. Copper produced the only measurable

POWER DENSITY EFFECTS IN LASER PRODUCED CRATERS

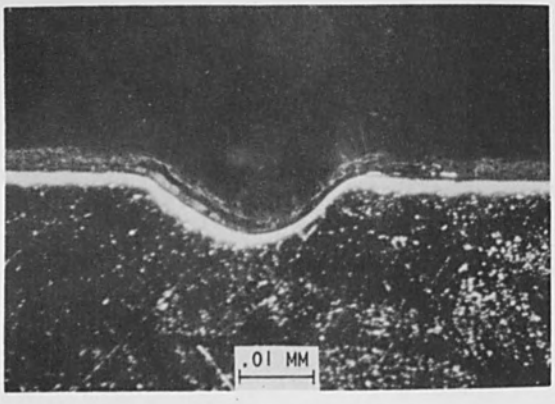

1.4×10^7 WATTS/cm^2

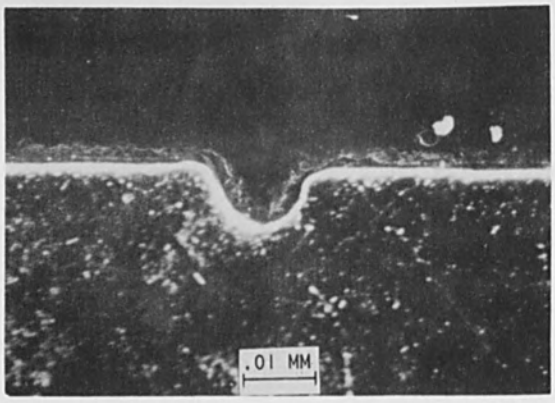

5.8×10^7 WATTS/cm^2

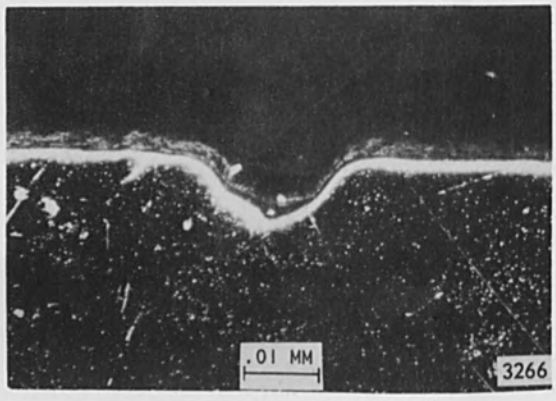

2.6×10^8 WATTS/cm^2

302 STAINLESS STEEL .18 JOULES "Q-SPOILED" LASER PULSE

Figure 7

amount, which was a rather uniform layer of about 0.01 mm in thickness. Evidence of molten material can be found, however, in the "splatter". Shown in Fig. 8 is a "Q-spoiled" laser burst on "Stellite". The short pulse crater cross-sections are in general, different from their long pulse counterparts. Instead of having a conical or cylindrical shape typical of the long pulse results, they are approximately hemispherical or at least spherical sections. A compilation of the short pulse results is given in Table III.

SHORT PULSE RESULTS

Metal Specimen	Power Density (w/cm^2)	Crater Depth (mm)	Thermal work done (joules)
Copper OFHC	2.6×10^8	0.03	0.016
Copper OFHC	5.8×10^7	0.015	0.012
Copper OFHC	1.4×10^7	0.01	0.015
302 Stainless Steel	2.6×10^8	0.08	0.027
302 Stainless Steel	5.8×10^7	0.08	0.028
302 Stainless Steel	1.4×10^7	0.07	0.025
"Stellite 21"	2.6×10^8	0.02	0.016
"Stellite 21"	5.8×10^7	0.02	0.016
"Stellite 21"	1.4×10^7	0.02	0.014
Tungsten*	2.6×10^8	0.01	0.019
Tungsten*	5.8×10^7	0.01	0.019
Tungsten*	1.4×10^7	0.01	0.019

*Commercially pure

TABLE III

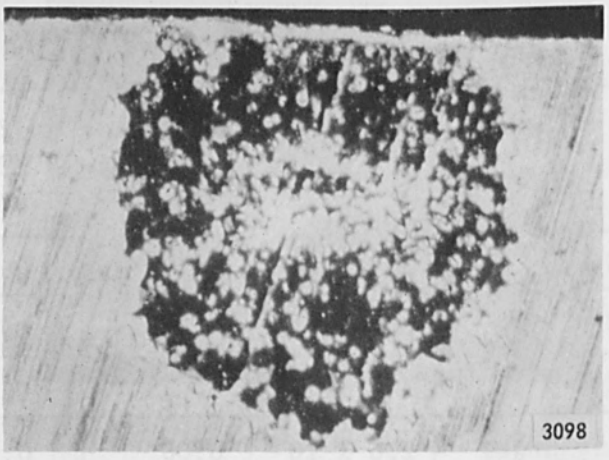

STELLITE 21
"Q-SPOILED" LASER BURST
0.16 JOULES

Figure 8

DISCUSSION

Using the photographs of the crater sections and with the aid of the thermal model, an attempt will be made to describe the manner in which the craters are formed.

In the case of the "Q-spoiled" craters, the thermal model, Fig. 1, indicated that the liquid layer between the vapor-liquid interface and the liquid-solid interface created during the laser pulse was vanishingly thin (10^{-3} cm). This fact implied that the majority of the material removed from the crater had been vaporized or boiled off, although some splatter was evident. Higher power densities, at higher total energy input, are needed to make the experiment sufficiently insensitive to material properties to remove ambiguities in interpretation.

The long pulse results give a somewhat clearer picture of what happens. When only the power density was varied, the total energy and pulse time remaining constant, it appeared that there was a direct relationship between power density and crater depth in the region under consideration. The relationship can be explained in the following manner:

There exists at the vapor-liquid interface a pressure directly proportional to the rate at which the atoms are boiled off and thus, also, proportional to the power input within the boiling area. Furthermore, since the volume beneath the boiling isotherm is liquid, that liquid will flow subject to the applied pressure. In accordance with this situation, the mechanism by which the craters are formed can be formulated (See Fig. 9). Envision within the material the existance of a boiling point isotherm preceded by a melting point isotherm. Vigorous agitation at the boiling point isotherm creates a sufficient pressure to force molten material behind the advancing melting point isotherm to flow up the sides, and out, of the

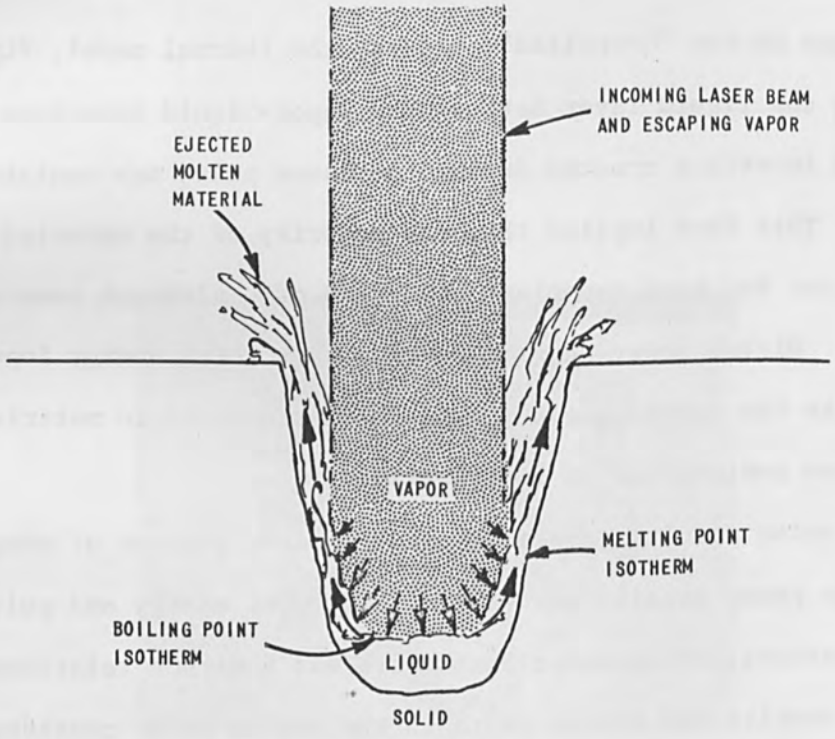

Figure 9

forming crater. In other words, a greater intensity of boiling at the surface will not only remove more material via vaporization but will also remove a much greater amount of the molten material trapped between the melting and boiling point isotherms. No doubt, there will be an optimum power density for the highest rate of removal for a given material. This will allow the melting point isotherm to precede the boiling point isotherm by a distance just sufficient to provide an optimum balance among molten material subject to ejection, thermal conduction losses, and evaporation

recoil pressure.

To lend support to the cratering mechanism proposed here, an estimate of the magnitude of the evaporation recoil pressures present during the event is in order. A value can be obtained using the following relationship[6]:

$$P \cong \alpha I \frac{v}{\lambda}$$

where

P = pressure

α = adsorptivity

I = power density in laser beam

v = velocity of vapor

λ = specific heat of evaporation

Using high speed photographs taken by Harris[5] of laser bursts on steel to estimate the velocity of the vapor, it is possible to calculate the evaporation recoil pressure. (The power densities used by Harris were comparable to those used in this experiment.)

The following parameters apply to a stainless steel target:

α = 0.40

I = 8000 kw/cm^2 or 8 x 10^{13} erg/cm^2 sec

v = 3 x 10^3 cm/sec

λ = 7.1 x 10^{10} erg/gm

thus:

$$P \cong \frac{0.4(8 \times 10^{13})\ (3 \times 10^3)}{7.1 \times 10^{10}}$$

$$P \cong 1344 \times 10^3 \text{ gm/cm}^2$$

Since 1 gm/cm^2 = 10^{-3} atmospheres,

$$P \cong 10^3 \text{ atmospheres}$$

(The 1000 atmosphere figure has been confirmed by us in two independent experiments.)

Recognizing that while this figure is an order-of-magnitude estimate, a pressure 10^3 atmospheres is more than sufficient to perform the material ejection role assigned to it. Since the workpiece sees only the energy and not the producing agent, the evaporation recoil pressures discussed here are also present in electron beam welding and machining. Equivalent power densities, using electron beams should produce comparable effects on materials.

ACKNOWLEDGMENT

Acknowledgement is due to Paul Rosenthal for his helpful suggestions and criticisms. The work was sponsored by the Air Force Systems Command under Contract AF 33(699)-42921, ASD Project NR 7-867

REFERENCES

1. Carslaw, S.S. and Jaeger, J.S., "Conduction of Heat in Solids", Oxford University Press, 1950, pp 216
2. Bahun, C.J. and Engquist, R.D., "Proceedings of the National Electronics Conference", Chicago, Illinois, 1962
3. Lyman, T., ed., Metals Handbook, 1948 Edition, American Society for Metal, Cleveland 3, Ohio, p. 185
4. Levy, H. and Roth, L, "Elements of Probability", Oxford, at the Clarendon Press, 1936, p. 197
5. Harris, T.J., IBM Journal, October 1963, p. 342.
6. Aikargan, G.A. and Moroz, E.M., Soviet Physics (JETP) 16 1638 (1963)

FORMATION OF THIN FILMS AND OTHER FORMS OF ISOTOPIC METAL BY ELECTRON BOMBARDMENT EVAPORATION*

H.L. Adair and E.H. Kobisk
Oak Ridge National Laboratory
Oak Ridge, Tennessee

ABSTRACT

A vapor source was developed, using electron bombardment heating, which will operate at temperatures up to 3000°C. This source could be used to evaporate milligram quantities of metals and metal oxides of isotopically enriched elements so that thin films or bulk forms of these materials could be obtained by condensation. Source design resulted in high efficiency of vaporization and simultaneous collimation of the vapor; condensation efficiency was enhanced as compared with other standard vapor sources. The reduction of several rare earth metal oxides to metal, and the preparation of self-supporting silicon films are described using this vaporization technique.

*Research sponsored by the U. S. Atomic Energy Commission under contract with the Union Carbide Corporation.

FORMATION OF THIN FILMS AND OTHER FORMS OF ISOTOPIC METAL BY ELECTRON BOMBARDMENT EVAPORATION

High efficiency vapor sources, which are capable of operation at 3000°C, have been developed at the Target Preparation Center of the Oak Ridge National Laboratory. High efficiency utilization of the evaporated material, very desirable in the case of certain rare, enriched, stable isotopes and radioisotopes, was achieved by collimation of the issuing vapors. To achieve the very high temperatures required to vaporize materials such as rare earth oxides, electron bombardment heating and tungsten crucibles were required.

The configuration of the vapor source employing electron bombardment heating is illustrated in Fig. 1. The two copper electrodes used to support the 0.020" diameter tungsten filaments and a water-cooled copper crucible holder were mounted on a glazed alumina insulator plate. The crucible was mounted vertically and co-axially with annulus formed by the circular filaments. A water-cooled copper heat shield directly above the crucible was used to reduce radiant heat transfer to the substrate. The top of the crucible extended slightly through the annulus of the shield.

The tungsten filaments were constructed so that the distance from the crucible wall to the wire was approximately 0.25". These filaments were heated with alternating current of about 50 amps at 10 V. Electrons were drawn from the hot filaments to the tungsten crucible under a potential variable from 100 to 1000 V. Commercially available power supplies could be obtained for both a.c. and d.c. functions, although those used in these experiments were custom fabricated. The d.c. supply consisted of a bridge-type full-wave mercury rectifier circuit capable of maximum output of 3 amp at 1000 V.

The tungsten crucible can be more clearly seen in Figs. 2 and 3. By using a design in which the tube length was much longer than the diameter,

FORMATION OF THIN FILMS AND OTHER FORMS OF ISOTOPIC METAL

BY ELECTRON BOMBARDMENT EVAPORATION

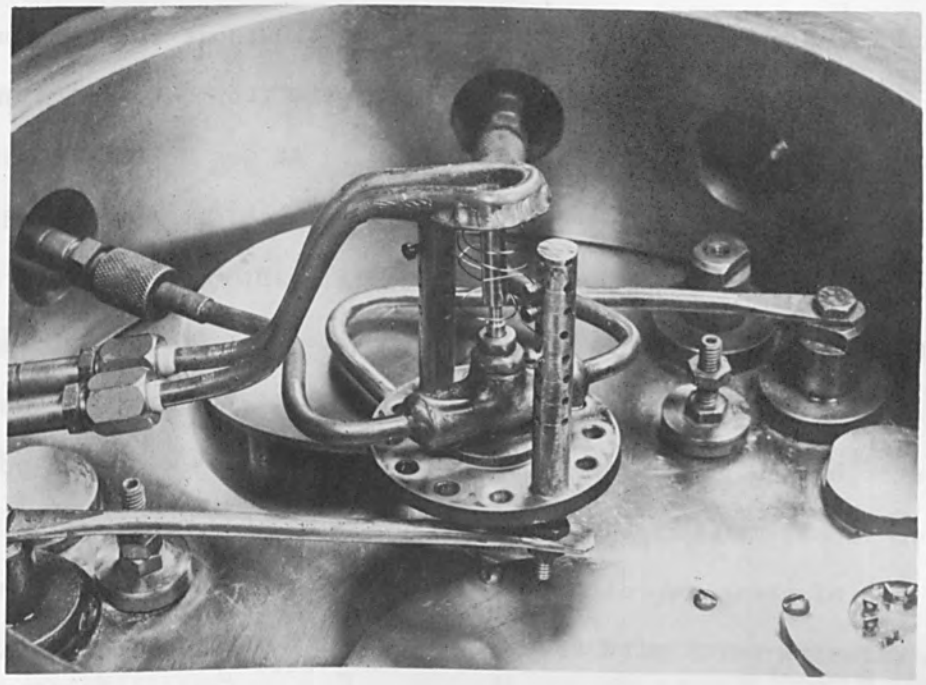

FIGURE 1 Electron Bombardment Vapor Source Assembly

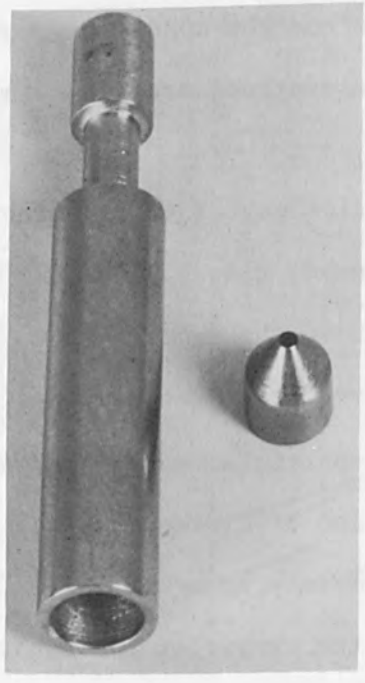

FIGURE 2 Tungsten Electron Bombardment Crucible with Effusion Port

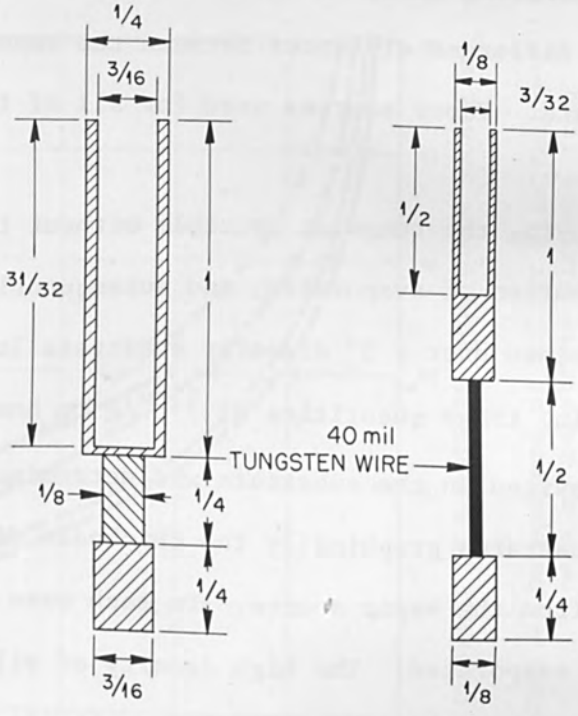

FIGURE 3 Tungsten Crucibles for Electron Bombardment Vapor Sources

Korsunsky and Vekshinsky[1] demonstrated that considerable collimation of the issuing vapors can be achieved. Crucibles were fabricated with an internal diameter of 0.1875" and a length of 1.0". It was hoped that significant collimation of the vapor would result through the associated decrease in solid angle as compared with a flat filament or a standard ceramic crucible vapor source. In Fig. 2, a tungsten plug is shown, tapered to form a tight press fit with the inside diameter of the crucible and having a center hole 0.04" diameter, which was used as an effusion port through which vapors were further collimated.

A comparison of these two electron bombardment vapor sources (with and without the effusion port) with several other sources of conventional design was made, and the results are shown in Fig. 4. Data were obtained by evaporating three charges of silver metal, each weighing 32 mg, at each of six different distances between the vapor source and the condensing substrate. Vapor sources used for all of these evaporations are shown in Fig. 6.

Using the tungsten crucible without the effusion port (Fig. 1), the distribution of evaporated, and subsequently condensed, silver metal was determined over a 3" diameter substrate located above the vapor source. By adding trace quantities of ^{110M}Ag to normal silver, the quantity of silver deposited on the substrate was determined by β-particle counting. Fig. 5 illustrates graphically the thickness distribution at distances of 4" and 5" from the vapor source. In each case approximately 25 mg of silver metal was evaporated. The high density of silver in the center of the substrates as compared with peripheral deposits is indicative of the collimation achieved using the tubular crucible. Since films used as targets in high energy particle accelerators require a high degree of uniformity in density,

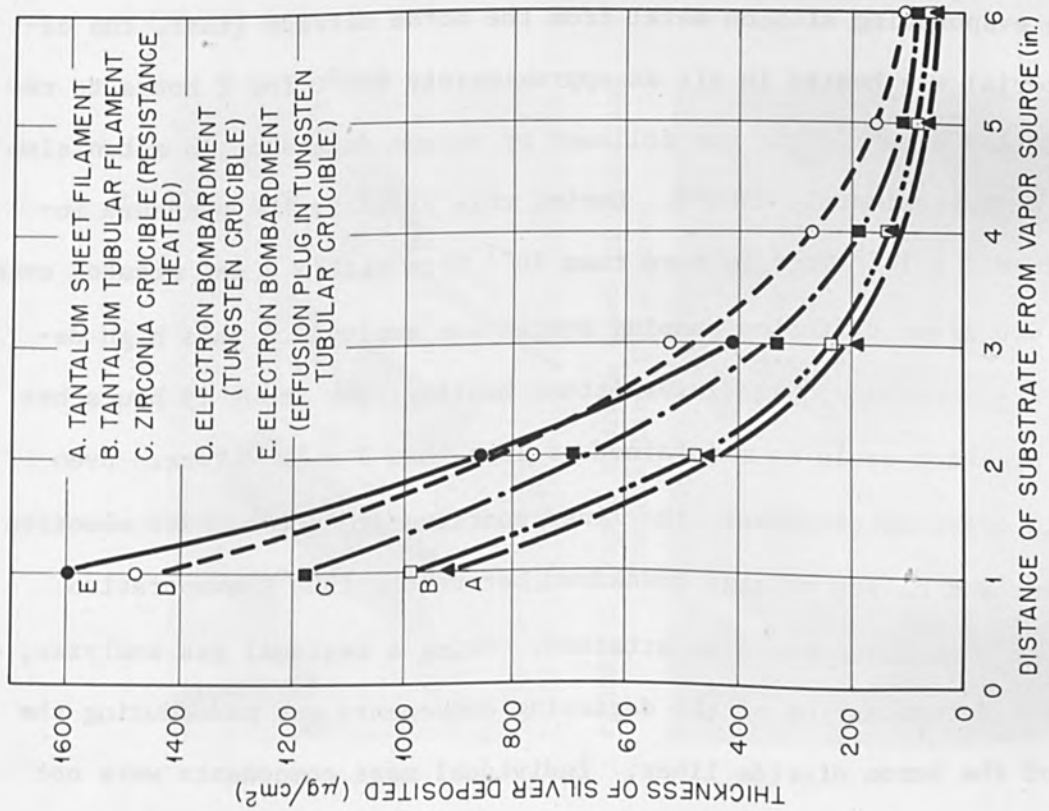

FIGURE 4 Dependence of Silver Film Thickness on Substrate Distance from Vapor Source

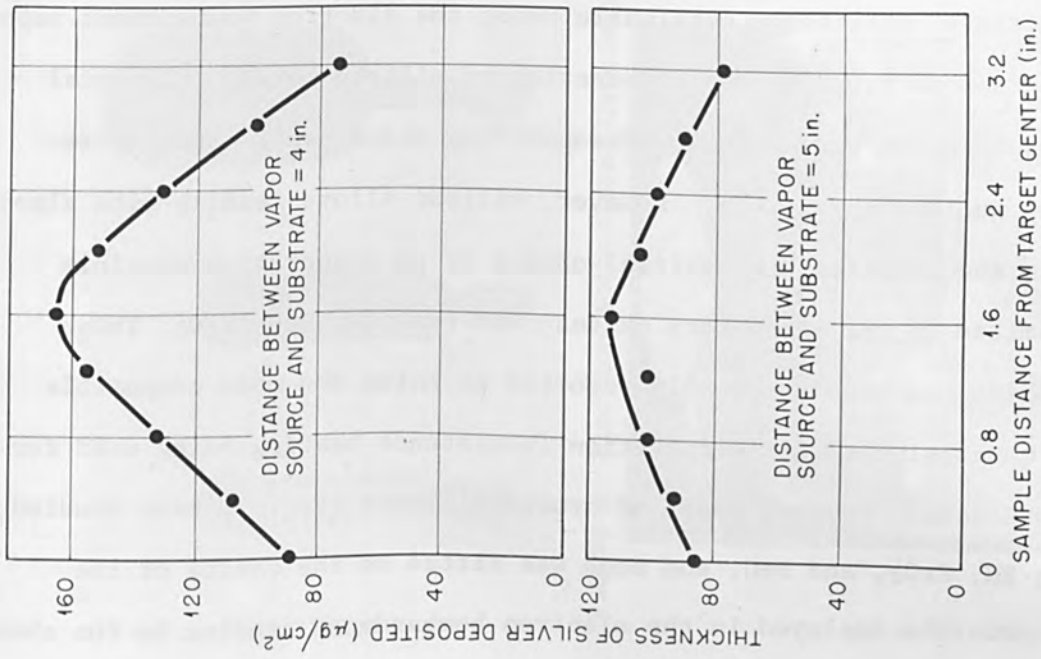

FIGURE 5 Distribution of Condensed Silver

rotation of the substrate over the vapor source is necessary.

The increased efficiency obtainable using the electron bombardment vapor source was demonstrated by the evaporation of silicon metal. Elemental silicon isotopes in very thin, self-supporting films are frequently requested by nuclear physicists. However, silicon alloys readily with almost any metal, and therefore the initial choice of an evaporation crucible seemed limited to the refractory oxides, for example, BeO, ZrO_2, ThO_2. Boron nitride has been frequently reported as being the most compatible crucible material for this evaporation (resistance heating being used for the evaporation). Several types of crucible liners (Fig. 7) were studied, including BN, ZrO_2, and BeO, and each was fitted to the cavity of the tungsten crucible employed in the electron bombardment studies in the above discussion (without the effusion port).

Before evaporating silicon metal from the boron nitride liner, the ceramic material was heated in air at approximately 600°C for 2 hours to remove contained water. This was followed by vacuum degassing in a tantalum crucible at approximately 1500°C. During this process, the pressure increased from 2×10^{-5} Torr to more than 10^{-1} Torr within a few minutes even though a 400 l/sec diffusion pumping system was employed. This high degassing rate continued, with intermittent heating, for about 15 hours before the pressure could be maintained at less than 7×10^{-5} Torr. Even after this vigorous treatment, the liner continued to degas under electron bombardment and caused voltage breakdown before the 1900°C evaporation temperature of silicon could be attained. Using a residual gas analyzer, a qualitative determination of the degassing components was made during the heating of the boron nitride liner. Individual mass components were not fully identified, but at temperatures greater than 1000°C, water vapor in-

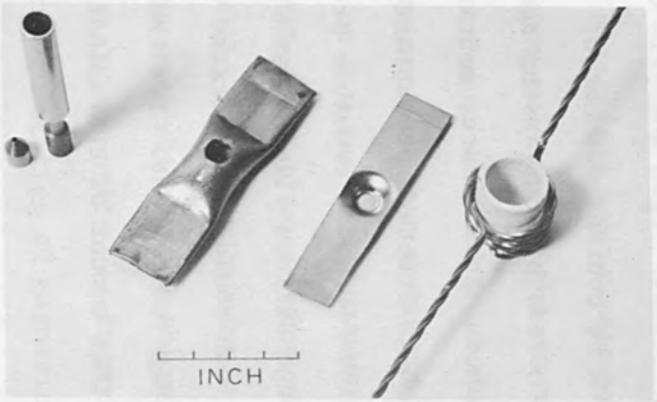

FIGURE 6 Vapor Sources Used in Comparing Condensation Efficiency

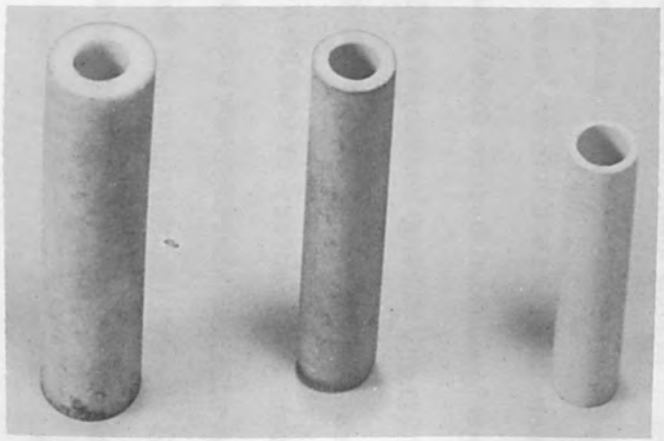

FIGURE 7 Refractory Crucible Liners

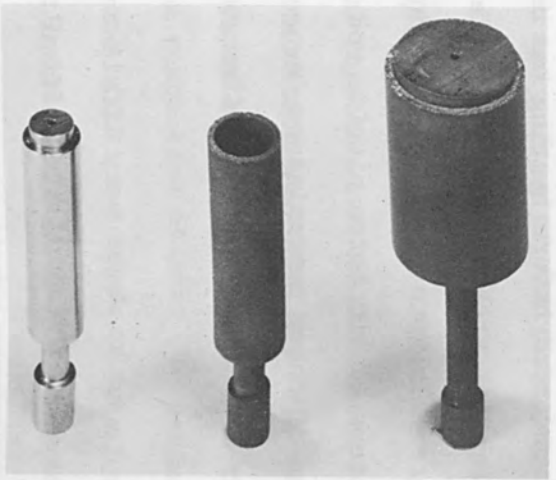

FIGURE 8 Electron Bombardment Crucibles

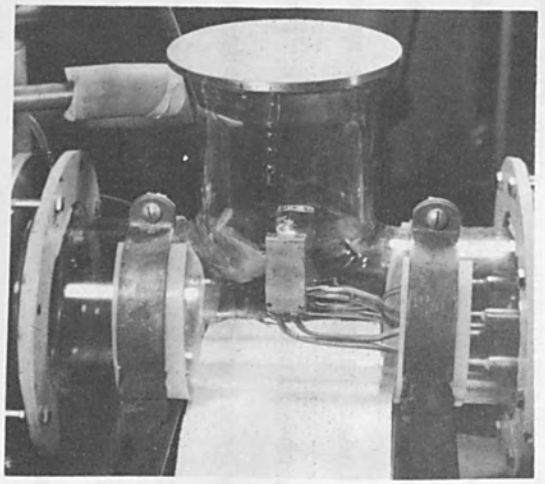

FIGURE 9 Vacuum Assembly and Electron Bombardment Vapor Source for Radioactive Materials

creased nearly 50-fold and hydrogen and nitrogen were evolved to levels nearly 100-fold greater than the levels recorded before heating was initiated. Furthermore, materials having masses greater than 36 were evolved in copious quantity. Possibly these materials were degradation products of the binder material used in the manufacture of the boron nitride rod from which the liner was fabricated. Because of these contaminants, especially those greater than mass 36, these liners were not used (other than experimentally) for silicon target fabrication.

Beryllium oxide crucible liners were found to degas very little and silicon was evaporated, using electron bombardment, with little difficulty. Condensed films of silicon were formed on quartz substrates using sodium chloride as the release agent and were easily stripped in water. With sodium chloride coatings of about 100 $\mu g/cm^2$ blistering and cracking of the silicon films were observed, but with heavier deposits, approximately 1 mg/cm^2, strong continuous films were obtained. Upon analysis of the condensed film, however, approximately a 10% Be content was noted.

Zirconia crucible liners were also studied, but outgassing again caused voltage breakdown before 1900°C was reached. Furthermore, embrittlement of these liners during heating resulted in high fracture probability. Direct evaporation of the silicon from the unlined tungsten crucible proved to be the most satisfactory procedure. Although silicon alloyed with the crucible upon prolonged heating, most of the silicon could be evaporated and condensed into films having less than 1% tungsten content. For the nuclear experiments using these silicon films, this amount of contamination was acceptable.

In previous experiments, silicon had been evaporated from a tantalum resistance filament. To obtain a film thickness of 150 $\mu g/cm^2$, 200 mg of

metallic silicon was required. However, using the electron bombardment method only 15 mg of starting material was required to produce the equivalent film thickness. Since isotopically enriched ^{30}Si has a monetary value of $16.50/mg, this new technique resulted in a saving of approximately $3,000 for each evaporation made.

In addition to preparing self-supporting films, these electron bombardment vapor sources have been used to convert MgO, Eu_2O_3, Sm_2O_3, and Yb_2O_3 to the respective metals. To perform these reductions, a tungsten crucible with the effusion port in place, has been most generally employed. However, other forms of this crucible have been used (Fig. 8), usually fabricated from spectrographic quality graphite rods.

Powdered aluminum metal was used to reduce MgO, and powdered lanthanum metal for the corresponding reductions of the rare earth oxides. In each case a small pellet of the reducing metal and oxide powder was prepared using a 100% stoichiometric excess of the reductant. The crucible temperature was maintained approximately 100°C above the temperature required to yield a vapor pressure of the desired metal of 10^{-2} Torr. Temperature measurements were made using an optical pyrometer. Upon reaching the prescribed temperature, the metal vapor jetted through the effusion port and condensed on a water-cooled tungsten substrate located 1/4" from the port. A small stalactite of metal condensate was formed and could be easily removed from the substrate by simply flexing the tungsten sheet. These metal beads were rolled to a thickness of 1 mg/cm^2 in an 8" Fenn mill. Less than 0.05% impurity was introduced into the metal by the reducing agent. Gram quantities of magnesium isotopes were prepared in this manner using the large graphite crucible illustrated in Fig. 8.

Because of the compact nature of the electron bombardment vapor source,

it could be adapted to very small vacuum systems such as that shown in Fig. 9. A 4" Pyrex glass "T" was used as the vacuum chamber; using a 2" oil diffusion pump with a mechanical backing pump, pressure levels of less than 3×10^{-6} Torr could be attained easily. Because of the minimal cost of this system, radioactive materials of high toxicity and/or biological hazard could be evaporated within a glove box enclosure. To dispose of residual radioactive deposits, the entire system could be buried with small monetary loss. Such systems have been used to evaporate plutonium and uranium oxides (above 2000°C) as well as fluorides of uranium, neptunium, americium, radium, and thorium.

REFERENCES

(1) Korsunsky, M. and Vekshinsky, S.; J. of Phys., IX, 399 (1945)

ELECTRON BEAM INITIATED REACTION DEPOSITION OF SILICON DIOXIDE

Rindge Shima, Arnold Miller and F.L. Morritz
Autonetics, A Division of North American Aviation, Inc.
Anaheim, California

ABSTRACT

The purpose of this investigation was to understand and control the processes pertaining to the electron beam initiated reaction deposition of SiO_2 in thin, continuous films by the activation and subsequent decomposition of ethyl silicate. This report describes the equipment used, some typical operating conditions, the results obtained, and the methods used for film evaluation. Three different modes of operation were used. The initial system utilized a differentially pumped apparatus operable to 20 microns pressure. The second system had a variable cathode-workpiece distance to operate within the mean free path up to 80 microns in pressure. The third system involved the use of a plasma cathode for pressures up to 180 microns pressure.

The decomposition of ethyl silicate was found to be due primarily to an electron beam activation rather than a thermal decomposition. The rate of electron beam induced deposition was in excess of 100 $\mathring{A}$/min under most conditions and went as high as 320 $\mathring{A}$/min in those cases where relatively thick films were desired. The rate of deposition was a function of the beam flux density and varied inversely with the impingement area.

Thin-film capacitors were fabricated readily, with a capacitance in the range of 0.01 $\mu F/in^2$ and with breakdown potentials in excess of 300 v. d.c.

ELECTRON BEAM INITIATED REACTION DEPOSITION OF SILICON DIOXIDE

INTRODUCTION

The pyrolysis of ethyl silicate vapor on heated surfaces is known to yield silicon dioxide[1]. Several years ago, Autonetics carried out such thermal decomposition at vapor pressures in the 300 micron range, and obtained continuous silicon dioxide films deposited at sensible rates on silicon, columbium, tantalum, and tungsten surfaces. It was desired to relate the results to a corresponding study of deposition brought about by the utilization of the dissipation energy of an electron beam[2]. Electron beam techniques were attempted, and thin, continuous dielectric films of silicon dioxide were obtained over a range of deposition parameters. This paper describes the equipment used, some typical operating conditions, the results obtained, and methods used for film evaluation.

EQUIPMENT

The vacuum apparatus consisted of a differentially pumped system as illustrated in Fig. 1. Two individual vacuum systems, each consisting of a 140 l/min mechanical pump, a 115 l/sec diffusion pump, and two liquid nitrogen cold traps, were connected at different locations to a pyrex reaction chamber. A minimum ID of 25 mm was maintained on all lines and stopcocks to provide adequate pumping conductance.

The reaction chamber was fitted with four removable 50 mm flanges to suit the mode of operation. Three different modes of operation were possible with this system. The initial system used was a differentially pumped apparatus with the electron gun entering from the top port. (See Fig. 1). The thermal cathode's life was increased by differential pumping, and the long tube length allowed the use of appropriate beam deflection coils. When maximum spot resolution and precise area scanning are necessary, this is an ideal method. A disadvantage is in having the small differential

FIGURE 1 Differentially Pumped Electron Beam System

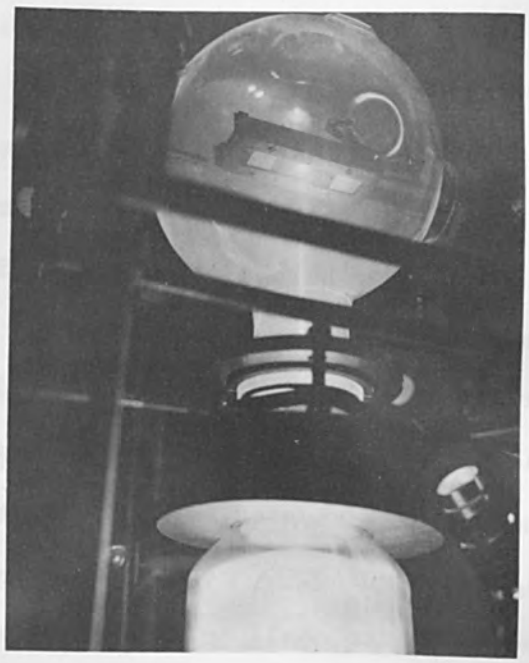

FIGURE 3 Plasma Cathode Electron Beam

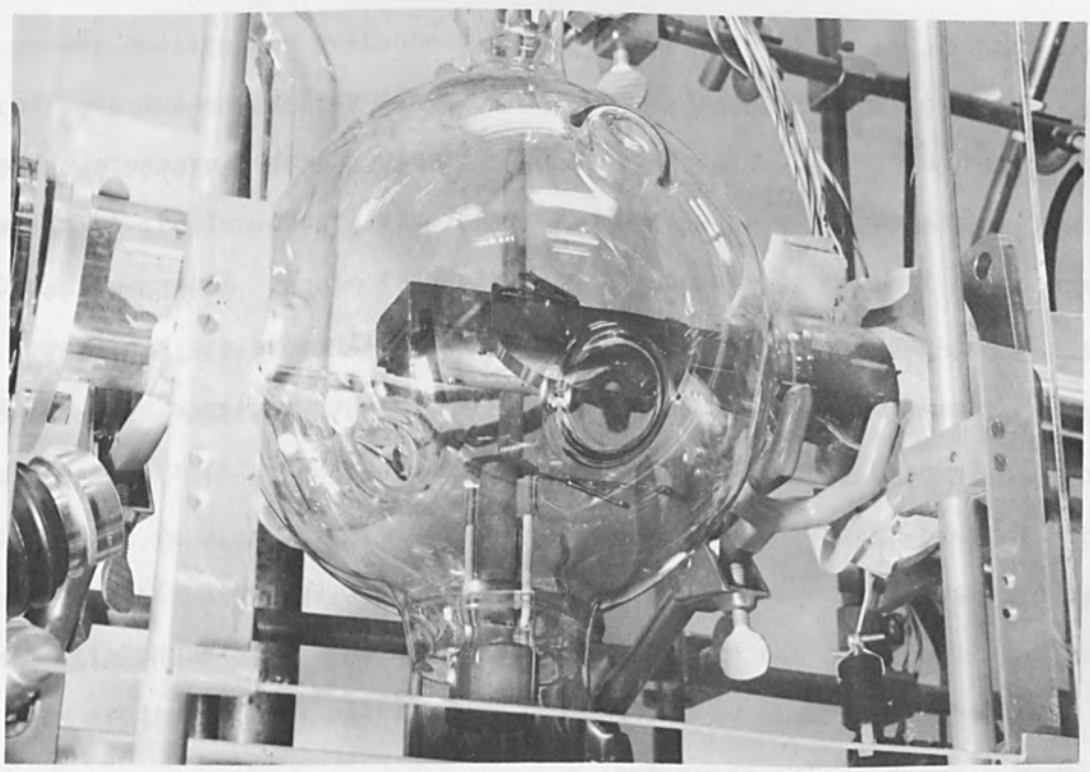

FIGURE 2 Direct Impingement Electron Beam

aperture which is less than 1.3 mm at 20 μ pressure. The power density of the final spot was limited because of the low voltages used, (300 to 500 v. d.c.)

The second system used had the electron gun entering from the bottom port and the cathode-workpiece distance could be varied to operate within the mean free path of the vapor. (See Fig. 2). The advantage of this equipment was in its ease of operation. Since the spot diameter was obtained by varying the anode voltage and the diameter of the aperture, the technique was effective for studying incident areas greater than 1.5 mm in diameter. The use of activated cathode structures resulted in a short life for the electron source. Once the operating parameters were established, the same spot diameter could be repeated readily. However, the gun had to be kept scrupulously clean. A third mode of operation involved the use of an adaptor flange to fit a plasma cathode from either port[3], and this is shown in Fig. 3.

The left port of the apparatus contained the vapor inlet valve and the thermocouple gauge tube for monitoring the reaction chamber pressure. The right port contained a movable lead screw, externally controlled, to allow two degrees of freedom of motion in the horizontal plane. An arm attached to a stainless steel bellows was used to mechanically move the substrate sideways. Thermocouple leads were also fed through this flange by a multi-header feed through. An auxiliary substrate bake out capability was not provided in this system.

Standard CRT components were used extensively for the thermal cathode mode of operation with the exception of the tungsten ribbon cathode. The grids and anode structures were identical. The following dimensions were maintained: aperture diameters for:

G_1 = 1.8 mm

G_2 = 2.0 mm

Anode = 3.2 mm

Spacing for G_1 - G_2 = 1.0 mm

G_2 - anode = 4 mm

Cathode - G_1 $\sim$ 0.05 mm.

The activated cathode was a standard tricarbonate coated CRT gun element as illustrated in Fig. 4. The tungsten cathode, cut from a 0.13 mm sheet, was etched down to approximately 0.02 mm at the point of emission and was mounted in a special holder as illustrated in Fig. 5. The plasma cathode was a 25 mm dia. stainless steel cage with a 6 mm dia. electron extraction hole. This is illustrated in Fig. 6.

The tricarbonate coated activated CRT cathode had the advantages of high current density and guaranteed alignment, but it disintegrated when exposed to the atmosphere after use and required frequent replacement. The tungsten cathode required a high filament current and was difficult to align but had a longer life. The plasma cathode had the advantage of operating at higher vapor pressures.

The spot size desired, the current density, and the resolution, all determine the choice of the electron gun, whether it be a diode, a triode, or a tetrode. Since the dielectric areas described in this report were greater than 3 mm in dia., a triode with enlarged apertures sufficed very well. Well-regulated power supplies with $\pm$ 2% ripple were necessary, except for the filament power.

A typical procedure will be described. With about 150 cc of ethyl silicate in the vapor chamber and the Dewar flasks cooled to about -5° to -15°C,

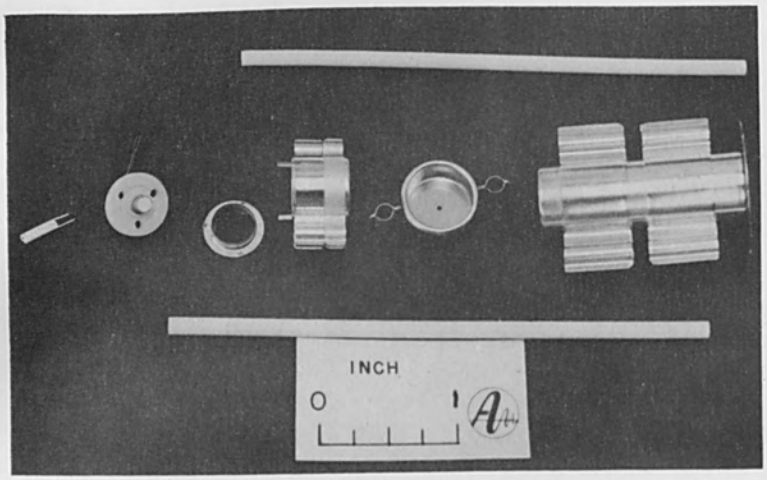

FIGURE 4 Tricarbonate Gun Element

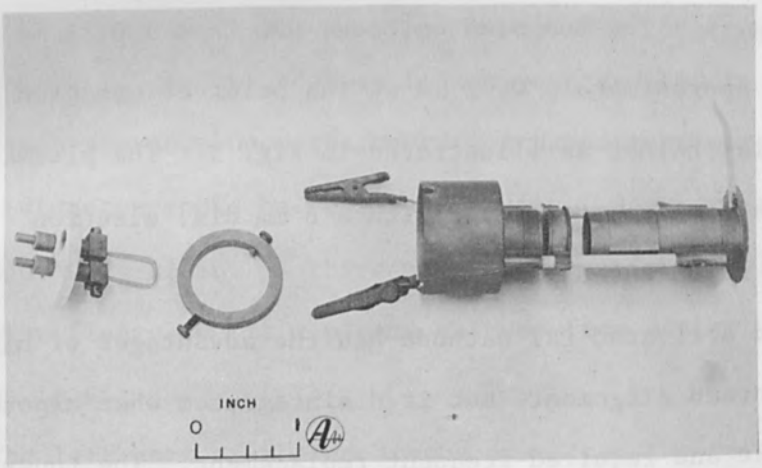

FIGURE 5 Tungsten Ribbon Cathode

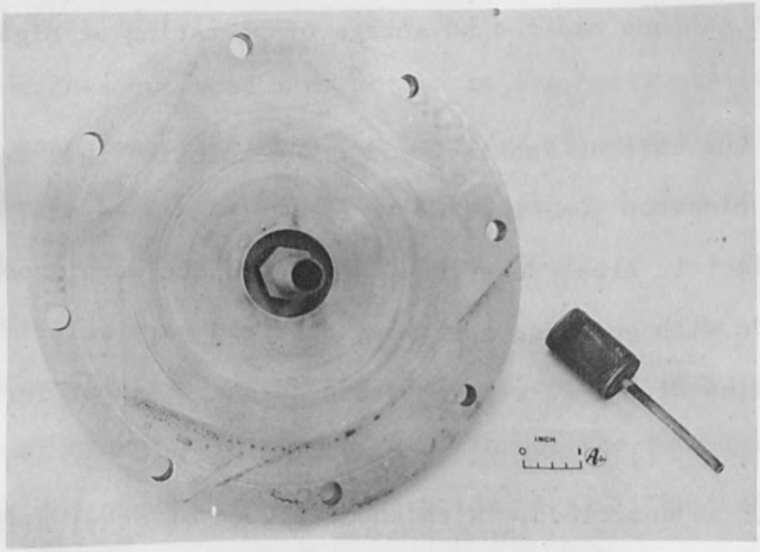

FIGURE 6 Plasma Cathode

both valves were slowly opened to a pressure of 5×10^{-5} Torr. The system was then pumped for three to four hours for removal of contaminants.

The electron gun was then started at a minimum high voltage setting, and increased gradually until the spot location and diameter were established. Once located, the electrical parameters were increased to the required values. There was no visible heat during the deposition, although silicon dioxide did fluoresce dependant upon its thickness. When adhesion was poor and questionable on certain substrate materials, the electron beam current density was increased to raise the substrate temperature to an effective level.

A typical set of operating parameters for the second mode of operation, which is a direct impingement of the electron beam, is shown in Table I.

TABLE I. OPERATIONAL DATA - THERMAL CATHODE

High Voltage	200-600	v
Target Current	0.02-4	ma
Vapor Pressure	10-80	microns
Effective Deposition Diameter	1.6-9	mm

Under these pressure conditions, high voltages and current densities, for example, 800 v at 4 ma, were deleterious to film properties. If the voltage or current density was excessive, a brownish to black film was formed. For example, at 200 v and 40 μ pressure, at a current density of 60 ma/cm^2, a dielectric film is formed. If the current density is increased to 120 ma/cm^2, a dark film forms and the dielectric properties disappear. The upper ethyl silicate pressure useable in the system is

limited by the type of electron emitter: oxide cathodes can be used to 20μ pressure, tungsten cathodes can be used to 80μ, and a plasma cathode can be used to 180μ.

The conditions of operation depend upon the specification of any two of the voltage, current, and pressure variables, thus automatically fixing the third. Most of the studies were accomplished within the ranges shown in Table I. Within these ranges, it was possible to fix a beam spot diameter by voltage adjustment. The distance of the gun from the substrate in this type of experiment was fixed at 20 mm.

To ascertain whether ethyl silicate decomposition was primarily thermal in nature or whether there was electron activation, a 1-mil tungsten sheet was placed in the reaction chamber and held rigidly in a frame so that both sides were exposed to the reactant vapor. A 10 kv, 3 mm diameter electron beam was impinged on one side of the sheet for 15 minutes in a pressure of 14μ of ethyl silicate. A temperature of 870°C was measured on both sides of the sheet. Upon examination, the side bombarded with the electron beam had a dielectric coating 1600 Å thick as measured by the monochromatic light fringe method, while the other side had no coating.

The rate of deposition was in excess of 100 Å per minute. In the direct, thermal experiments performed in earlier work, it was noted that at 750°C at pressures of 300 μ, the rate of deposition was about 1000 Å per minute. However, operation with the electron beam at substrate temperatures less than 400°C (no visible evidence of substrate heating) and 10-15 μ ethyl silicate pressure, gave films as thick as 35,000 Å in 110 minutes, a rate of 320 Å/min. The higher rates noted in the direct thermal reaction were not realized in the beam-activated depositions. Table II summarizes film formation with the various cathodes studied. In these examples, the beam spot

diameter was slightly larger in the case of the tungsten cathode (6 mm) than with the oxide and plasma cathodes (5 mm). The difference in deposition rate is probably due to the differing areas of impingement; although it is evident that the rates do not vary markedly.

TABLE II. SiO_2 DEPOSITION - GUN TYPE

Cathode	Anode Voltage (V)	Substrate to Gun (cm)	Target Current (ma)	Pressure (μ)	Time (min)	Film (Å)	Spot Diameter (mm)	Rate (Å/min)
Oxide	350	2	0.2	10-15	110	35,000	5	320
Tungsten	1000	2	0.02	15	90	18,000	6	200
Plasma	4200	28	3.6	32	20	6,000	5	300

Table III summarizes some data in which the beam diameter was varied. The rate varies inversely with the impingement area, as expected, and is a function of the beam flux density.

TABLE III. DEPOSITION OF SiO_2 - PLASMA CATHODE

Anode Voltage (v)	Target Current (ma)	Pressure (μ)	Time (min)	Film (Å)	Spot Diameter (mm)	Rate (Å/min)
5000	4.7	50	48	8000	5	170
5500	5.0	31	30	1700	6	57
5000	5.0	32	50	1700	10	34

The decomposition of vapor molecules between the substrate and the electron source was evidenced by an extremely thin residue on the chamber

walls, substrate, substrate holder, etc. The dielectric residue seemed to be due to the ionization or excitation energy being sufficiently high to decompose vapor molecules in the chamber with subsequent deposition at the walls.

The decomposition of an absorbed layer of vapor molecules on the surface of the substrate and the continuous replenishment of this layer results in film buildup. Since surface films as thick as 35,000 Å have been deposited at rates of 300 Å/min, it is evident that the main interaction occurs at the substrate surface. At higher voltages and current densities, brown deposits have indicated the possible presence of carbon. At higher pressures it has been found difficult to focus the beam because of scattering. Higher pressures required higher flux densities in order to maintain the original spot diameter.

Dielectric films were deposited in thin film capacitor arrays for study. The substrate used was a 25 mm x 50 mm x 0.6 mm Alsimag No. 614 with a normal finish. A base pattern of nickel was deposited by evaporation to a thickness of about 2000 Å. Representative data are summarized in Table 4. The beam diameter of 10 mm was sufficiently large to cover the capacitor pattern. After the silicon dioxide had been deposited, gold conductor electrodes were evaporated. Values of capacitance and breakdown characteristics compared well to SiO_2 capacitors made in our laboratories by the glow discharge initiated decomposition of ethyl silicate. The adhesion and strength of the films were satisfactory. It was feasible to carry out the breakdown tests with a sharp tungsten probe without problems.

TABLE IV. CAPACITORS

Voltage (v)	Target Current (ma)	Pressure (μ)	Time (min)	Capacitance ($\mu f/in^2$)	Breakdown (v dc)
300	3	80	60	0.013	350
200	4	50	60	0.009	300

CONCLUSIONS

The dissipation energies of electron beams have been utilized to deposit films of silicon dioxide by the decomposition of ethyl silicate - an example of an electron beam initiated reaction deposition. Three modes of operation have been used: a differentially pumped system allowing use of magnetic focusing and deflection, a direct impingement method in which the target to gun distance was within the mean free path, and a plasma cathode method. Deposition rates of 50 to 320 Å/min have been observed at pressures varying from 10 to 80 μ. Deposition occurs almost entirely at the substrate, but to a small extent some occurs on the chamber walls. The dielectric nature and the continuity of the film were evidenced by the fact that thin-film capacitors could be fabricated readily.

ACKNOWLEDGEMENT

The authors wish to thank E. Abrams and Robert Thomas for their able assistance in obtaining the technical data.

REFERENCES

(1) Law, H. B., Rev. Sci. Inst., 20, 12 (1949).

(2) a. Fotland, R. A., and Burkhard, W. J., J. Electrochem. Soc., 109 63C (1962).

b. Mann, H. T., ibid., 109, 63C (1962).

c. Christy, R. W.; J. Appl. Phys., 31, 1680 (1960); 33, 1884 (1962).

d. Baker, A. G., and Morris, W. C., Rev. Sci. Inst., 32, 458 (1961).

(3) Cocca, M. A., and Stauffer, L. H.; "Grid Controlled Plasma Electron Beam", Fifth Annual Electron Beam Symposium; Boston, Mass.; March 28-29, 1963, edited by J. R. Morley (Alloyd Electronics Corporation, Cambridge, Mass., 1963), p. 342.

IRRADIATION "FACTOR-DEPENDENCY" AS EVIDENCED BY STATISTICAL EVALUATION OF DATA FOR VINYL ACETATE

Ed. F. Degering, Gerald J. Caldarella and George H. Haines
U. S. Army Natick Laboratories
Natick, Massachusetts

ABSTRACT

The effects of various factors on the irradiation-induced polymerization of vinyl monomers have been investigated. Previous data from experiments which considered only single variables clearly indicate that the factors used have a variable effect on polymerization.

Statistical evaluations using data from experiments with multiple variables, confirm our conclusions that factors such as atmosphere, degassing of the monomer, dose increment, and flame-out of the reaction tubes, do affect the irradiation-induced polymerization of vinyl monomers and that, moreover, these effects are not independent of one another.

As an example, in the irradiation-induced polymerization of vinyl acetate the most efficient polymerization is obtained by an appropriate combination of atmosphere, degassing, and increment of dose.

IRRADIATION "FACTOR-DEPENDENCY" AS EVIDENCED BY STATISTICAL EVALUATION OF DATA FOR VINYL ACETATE

It has been shown previously that various parameters affect irradiation-induced polymerization of vinyl monomer systems[1]. The effects of the parameters were assumed to be independent. Replicated factorial experiments were performed, accordingly, to test the validity of this assumption. The results indicate that the experimental variables do not necessarily have independent effects but may be interdependent.

The fact that irradiation-induced polymerization of vinyl monomers is uniquely sensitive to experimental variables, enhances its potential applications for the syntheses of new polymers and the modification of conventional polymers. Irradiation-induced polymerization may be used for the production of polymers that are not available by conventional procedures such as irradiation-induced ionic polymerization at liquid nitrogen temperature, and for the production of modified polymers by appropriately varying the experimental procedure. The irradiation parameters predetermine the amount of polymer obtained, the molecular weight of the polymer, and even the molecular structure as indicated by infrared spectroscopy. This technique may be used advantageously also for the irradiation-induced graft-polymerization of materials such as teflon to enhance both their bonding properties and their dyeability. It should be recognized, however, that the useful applications of ionizing irradiation will most likely follow this more fundamental research.

EXPERIMENTAL DESIGN

One of the experimental designs used in this study was a 4-factor factorial[2] with three replications (Table I). Consideration was given to the spacing of factor levels in order to avoid "spurious" interaction terms, but the factor of 10 for increment of dose (Tables I and II) may represent too much spacing.

IRRADIATION "FACTOR-DEPENDENCY" AS EVIDENCED BY
STATISTICAL EVALUATION OF DATA FOR VINYL ACETATE

The advantages of using this statistical method are that it: (1) gives the maximum efficiency in the estimation of the effects, (2) is necessary to avoid misleading conclusions when interactions do occur, particularly if their nature is not known, (3) estimates the effect of a factor (or variable) at several levels of another variable, and (4) leads to valid conclusions over a wide range of conditions.

PROCEDURE

Forty-eight samples of vinyl acetate were prepared as follows: the monomer was distilled under reduced pressure, dried several days over anhydrous potassium carbonate at about 5°C, and siphoned as required into a 250 ml. glass-stoppered graduate, which was connected in turn to an automatic burette, through which a slow stream of argon flowed to exclude air and mositure. The burette was filled from the graduate by use of a slight argon pressure.

Twenty-four 1" x 12" borosilicate (Corning glass No. 9800) test tubes, equipped with 12/30 ground-glass male joints with a constriction for sealing, were placed on a vacuum manifold and flamed out three times, if programmed, at 5 microns. A 10 ml. sample of vinyl acetate was then transferred from the burette to each of the test tubes, which were then replaced on the manifold. Dewar flasks of liquid nitrogen were then slowly raised by the use of lab jacks to freeze the monomer. The manifold stopcocks were opened and the system evacuated with an auxiliary pump to about 300 microns, when a shift was made to the diffusion pump and the pressure in the system was reduced to 5 microns. Then the stopcocks to the tubes were closed, the Dewar flasks lowered, and the monomer allowed to melt and degas, if the degassing was programmed (samples which were not degassed were sealed after freezing). The monomer was refrozen, the stopcocks opened, and the system

IRRADIATION "FACTOR-DEPENDENCY" AS EVIDENCED BY

STATISTICAL EVALUATION OF DATA FOR VINYL ACETATE

Table I. Experimental Design and Data for Vinyl Acetate

Atms	DG	FO	16 P at 10,000 rads			1 P at 160,000 rads		
1. Air	0	0	0.032	0.094	0.008	0.291	0.401	0.357
2. "	0	3	0.027	0.021	0.024	0.501	0.470	0.389
3. "	2	0	0.021	0.027	0.019	0.493	0.526	0.469
4. "	2	3	0.019	0.014	0.018	0.525	0.520	0.500
5. Vacuum	0	0	3.69	3.81	3.95	0.958	1.01	0.356
6. "	0	3	4.65	3.64	4.75	1.17	1.10	1.22
7. "	2	0	4.93	5.13	5.16	1.35	1.21	1.28
8. "	2	3	5.34	5.35	5.37	1.37	1.23	1.36

Note: DG is for degassing, FO is for flame-out
Tabulated values are percent polymerization.

Table II. Vinyl Acetate, Significant Variables

Source and Combinations	Degrees of Freedom	Mean Squares		Variance Ratios
Atmosphere (A)	1	84.32	+	2381.9
Dose Increment (DI)	1	28.58	+	807.3
Degassing (D)	1	1.81	°	51.1
Flame-Out of Tubes (FO)	1	0.33		9.4
Atmosphere, Degassing	1	1.42	+	39.9
Atmosphere, Dose Increment	1	46.56	+	1315.3
Degassing, Dose Increment	1	0.35		9.8
Atmosphere, Degassing, Dose Increment	1	0.63	°	17.9
Residual	1	.000005		
Error (within)	32	0.0354		

F (1, 32 with α = 0.01 = 7.50
° Independently Significant
+ Dependently Significant

again evacuated in turn by the auxiliary pump and the diffusion pump. The tubes were sealed at 5 microns and then stored at -20°C until all the samples were ready for irradiation. Irradiation was carried out by use of an electron accelerator, operating at 2 Mev.

RESULTS

Two increments of dose per pass and one dose level were used to obtain the data in Table I. The computational techniques for the experimental results of the analysis of variance are given in Table II, and considered in the general discussion under design. A 1% Type I error was chosen because of the number of variables involved[4].

The data clearly indicate one second-order interaction (that is, the interdependency of atmosphere, degassing, and dose increment) and one single or main effect (flame-out). An interaction effect is a measure of the lack of the independence of the dependent variables. When an interaction is large and significant, the corresponding main effects (or single or lower interactions) cease to have independent meaning. A large interaction means that the effects of one factor are dependent on the level of the other, and when stating the effect of one factor it becomes necessary to specify the level of the other or others. If one factor has a qualitative connotation, the results must be examined separately for each level of any other given factor[3].

There was an obvious reversal of the effect of the atmosphere and degassing interaction as a function of increment of dose (Table I). At the lower increment of dose, on the average, there was an indication that more conversion was obtained in the presence of air with no degassing than with two degassings, but the effect appeared to be reversed at the higher increment of dose. In all instances a higher conversion was obtained under re-

duced pressure than in air, and with two degassings at 5 microns than with no degassing. At 5 microns, moreover, about four times as much polymer was obtained at the lower than at the higher dose increment, but in air a reversed effect was observed. This rather complex effect of the combinations of degassing, increment of dose, and reduced pressure was summarized statistically as a significant second-order reaction and is shown in Table III.

Table III. Vinyl Acetate; Air, Vacuum, Degassing and Increment of Dose (% Polymerization)

	16 Passes at 10,000 Rads		1 Pass at 160,000 Rads	
Degassing	Air	Vacuum	Air	Vacuum
0	0.03	4.1	0.4	1.0
2	0.02	5.2	0.5	1.3

Error Mean Square = 0.0354
Interaction Mean Square = 0.63
Each variable entry is the average of 6 observations.
Replications and Flame-Outs have been summed out.

The flame-out of the reaction tubes resulted in a significant main (or single) effect (Table IV). Regardless of the level of any other factor, more polymer was obtained from the use of three flame-outs than from no flame-out. This was attributed to the dual effect of flame-out, which removed both adsorbed moisture and oxygen.

The data from a one-factor design experiment supported the conclusion that, at a given dose level, more polymer was obtained from a lower instead of a higher increment of dose (Table V, Fig. 1). The results from the analysis of variance of these data are given in Table VI. The design of the experiment for the results of Table V might appear to simplify a com-

IRRADIATION "FACTOR-DEPENDENCY" AS EVIDENCED BY

STATISTICAL EVALUATION OF DATA FOR VINYL ACETATE

Table IV. Vinyl Acetate: Main Effect is Flame-Out

(% Polymerization)

No Flame-Out	3 Flame-Out
1.482	1.649

Error Mean Square = 0.0354
Mean Square (from sum of all variables) = 0.334
Square root of mean squares = 0.578
Each variable entry is the average of 24 determinations. Replications, increment of dose and degassing have been summed out.

plex problem, but it was observed that the results from the 48 samples of Table I provided much more useful information than did the results from the 94 samples of Table V.

DISCUSSION OF THE EXPERIMENTAL DESIGN

Consider a four factor experiment in which factor A is tested at c levels, 1,2,... i,... c: factor B at d levels, 1,2,... j,... d: factor C at e levels, 1,2,... k,... e: factor D at f levels, 1,2,... l,... f: and each treatment is tested n times, 1,2,... q,... n.

When the treatment combination $A_iB_jC_kD_l$ is tested for the qth time, the response is Y_{ijklq}; if the treatment were tested a large number of times the mean response would shift toward the true value of $E(Y_{ijklq}) = \mu ijkl$. The response Y_{ijkl} differs from $\mu ijkl$ because of experimental error, which has a standard deviation of σ.

The mathematical model used in the analysis of a factorial experiment postulates that: $\mu ijkl = \mu + A_i + B_j + C_k + D_l + E_{ij} + F_{ik} + G_{il} + H_{jk} + I_{jl} + J_{kl} + K_{ijk} + L_{ijl} + M_{jkl} + N_{ijkl}$. The true response, μ_{ijkl}, is built up, accordingly, from the overall mean μ plus a contribution characteristic

IRRADIATION "FACTOR-DEPENDENCY" AS EVIDENCED BY

STATISTICAL EVALUATION OF DATA FOR VINYL ACETATE

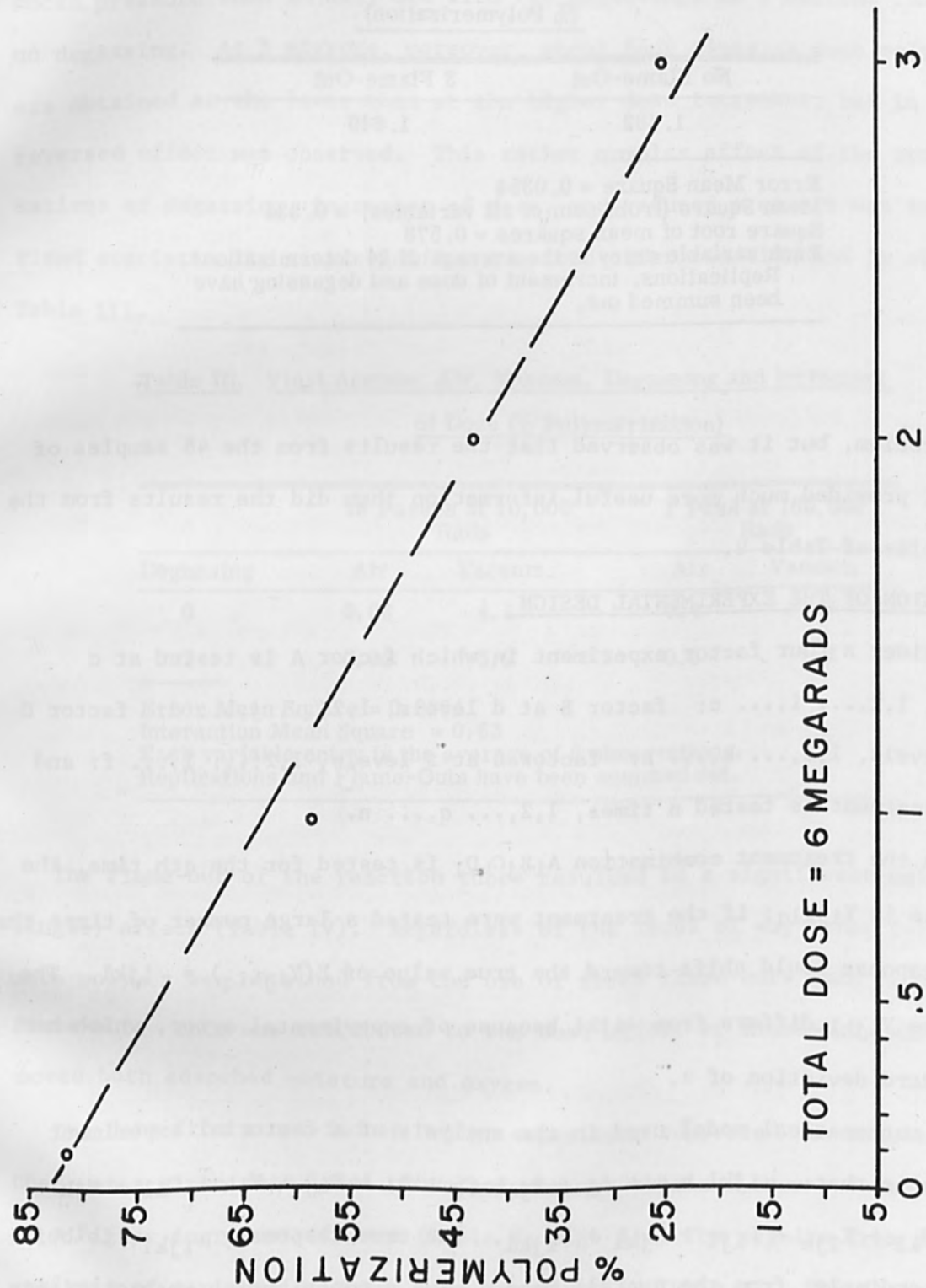

FIGURE 1 Irradiation of Vinyl Acetate

IRRADIATION "FACTOR-DEPENDENCY" AS EVIDENCED BY

STATISTICAL EVALUATION OF DATA FOR VINYL ACETATE

Table V. Vinyl Acetate and Dose Increment: Percent Polymerization

	60 Passes at 0.1 MR	6 Passes at 1 MR	3 Passes at 2 MR	2 Passes at 3 MR
1.	77.6	61.2	47.6	- -
2.	79.3	54.8	42.0	25.6
3.	78.6	57.2	39.4	24.1
4.	79.1	56.4	44.2	25.3
.	....	....	....	....
21.	81.1	59.7	42.0	24.8
22.	80.5	61.5	41.3	24.7
23.	82.0	58.3	41.5	25.7
24.	81.3	57.9	39.9	25.2
Av.	81.6	58.2	43.2	25.3

Note: The 24 samples at a given dose increment were irradiated at the same time with a 3 Mev electron accelerator.

Table VI. Vinyl Acetate: Analysis of Variance, Data of Table V

Source of Variation	Sum of Squares	Degrees of Freedom	Mean Square
Columns of Table V	39334	3	13111.5
Residuals	393	90	4.4
Totals	39727	93	13115.9

Imperical F Ratio (3, 90) = 13111.5/4.4 = 3002.06

of the i^{th} level of A, plus a contribution characteristic of the j^{th} level of B, ..., plus the term E_{ij}, etc.

If the effect of changing the level of A were always the same, irrespective of the level of B or C or D, and vice versa, the term E_{ij}, F_{ik}, ... N_{ijkl} would be zero. If, however, the effect of changing the level of A varies as the level of B changes (but not as the levels of C and D) then the value of E_{ij} is not zero. The value of E_{ij} becomes, consequently, a measure of the lack of independence of factors A and B or of their interaction or interdependency.

Inasmuch as μ is the mean of μ_{ijkl} and the same number of trials is made for each treatment, the results may be equated as: $\Sigma A_i = \Sigma B_j = \Sigma C_k = \Sigma D_l = \Sigma\Sigma F_{ij} = \ldots = 0$.

The expectation of a sum or difference of quantities (whether independent or not) is the sum or difference of the individual expectations, or $E(Y_{ijkl}) = \mu_{ijkl}$. It can be shown, moreover, that: $E(\bar{y}) = \mu$, $E(\bar{y}_i - \bar{y}) = B_j$, $E(\bar{y} - \bar{y}) = A_i$, and $E(\bar{y}_{ij} - \bar{y}_i - \bar{y}_j + \bar{y}) = E_{ij}$, where $\bar{y}$ is the average of all results, $\bar{y}_i$ is the average of all results at the i^{th} level of A, $\bar{y}_j$ is the average for the j^{th} level of B, and $\bar{y}_{ij}$ is the mean value of all results with the treatment A_iB_j, and so on.

Since the variation arising from changes in the levels of factors is systematic and not random, the mean squares vary between replications only because of random variations in the experimental error. In the systematic design of a factorial experiment, each mean square expectation contains only one term other than σ^2.

IRRADIATION "FACTOR-DEPENDENCY" AS EVIDENCED BY

STATISTICAL EVALUATION OF DATA FOR VINYL ACETATE

SUMMARY

From the data presented, one may conclude that: (1) experimental variables might be highly significant for the irradiation-induced polymerization of vinyl acetate; (2) variables may be interdependent as was the case for atmosphere, degassing, and increment of dose; and (3) flame-out resulted in a significant main effect, inasmuch as both adsorbed oxygen and moisture were removed.

NOTES AND REFERENCES

1. Degering, Ed. F., Merritt, Charles, Jr., Baxinet, M. and Caldarella, G. J., Irradiation Factor-Dependency, Exploratory Studies, Irradiation Cycle and Degassing, I and EC Product Research and Development, 2, No. 2, p. 114-8 (June 1963).
2. Davies, O. L., Design and Analysis of Industrial Experiments, pp. 247-493, Hafner Publishing Co., New York (1960).
3. Davies, O. L., Design and Analysis of Industrial Experiments, p. 255, Hafner Publishing Co., New York (1960).
4. A Type 1 error results from asserting that a real difference exists when there is no actual significant difference in the results. The type of experimental design used for the data of Table I gives 15 empirical variance ratios. One might expect, therefore, that one of these variance ratios might be larger by chance than the statistically accepted value of F (with α in this case equal to 0.05). The simplest way to avoid this problem is to use a value of 0.01 for α, which permits of about one chance in 100 of making a Type 1 error.
5. The data of Table II was obtained by Joseph A. Kay and that of Table V by Steven Gabelnick. The multiple replications were to test reproducibility and to accumulate polymer for evaluation.

THE EFFECT OF ULTRA-HIGH-VACUUM ELECTRON BEAM ZONE REFINING ON THE PURIFICATION OF METALS

I. Drangel, P. McMahon and S. Weinig
Materials Research Corporation
Orangeburg, New York

ABSTRACT

Previous work performed using electron beam zone melters at pressures between 10^{-5} to 10^{-7} Torr indicated that significantly greater purities might be achieved by zone melting materials at lower pressures. To investigate this effect on the purification of metals, an all stainless steel bakeable chamber containing an electron beam floating zone melter was constructed to operate at 10^{-9} Torr. The system included both external and internal bakeout units to facilitate achieving the desired operating pressure. Materials were evaluated using resistivity ratios as a measure of the impurity levels, and microhardness and fabricability at room temperatures as a measure of the mechanical properties. Preliminary results for tungsten and molybdenum are given. The effects of heat treatments on the measured resistivity ratios for molybdenum are discussed.

THE EFFECT OF ULTRA-HIGH-VACUUM ELECTRON BEAM ZONE REFINING ON THE PURIFICATION OF METALS

INTRODUCTION

The use of floating zone melting, the theory of which is described adequately by others,[1,2,3] provides a new experimental approach to the purification of many of the high melting point reactive metals. The electron beam as a heat source for the zone melting process was introduced by Calverly[4] and enabled high melting point materials to be processed by extremely low power inputs. These techniques were combined in an electron beam floating zone apparatus. In this process, purification takes place both by a zone refining action and by the vapor distillation of the impurities into the surrounding atmosphere. In many cases, particularly for high melting point solvents, preferential distillation of the impurity elements rather than purification by the zone refining process is the more prominent process. It is therefore of considerable importance that the greatest effort be made to understand the roll of the surrounding pressure on the ultimate purification.

Shadler[5] reported an electrical resistance ratio of 5600 for electron beam zone melted tungsten. Drangel and Murray[6] found resistance ratios for the bulk material greater than 20,000 after zone refining at a pressure of 10^{-6} Torr. They also noted differences in resistance ratios when the pressure varied by a factor of five. Seraphin[7] working with tantalum, found that the annealing of small wires at different pressure levels, in the range of 10^{-9} Torr, gave a higher resistance ratio or greater purity, at the lower pressures.

In order to study further this effect of pressure upon purity in floating zone melting, an electron beam unit was designed and constructed to operate at 10^{-8} to 10^{-9} Torr, or in what may be called the ultra-high vacuum range.

THE EFFECT OF ULTRA-HIGH-VACUUM ELECTRON BEAM ZONE REFINING ON THE PURIFICATION OF METALS

EQUIPMENT

A photograph of the ultra-high vacuum equipment used for this work is shown in Fig. 1 and a schematic drawing of the working chamber in Fig. 2.

The construction of an electron beam floating zone melter to operate at pressures of 10^{-9} Torr required that the new vacuum techniques and procedures be employed. Care was taken in the selection of the construction materials since bake out procedures were essential to effect system degassing.

An all stainless steel system capable of being heated to 450°C was built. The upper part of the vacuum chamber had three ports placed longitudinally down one side for the observation of the melting operation. The ports were sealed by Conflat flanges. Pyrex windows were connected to these flanges via housekeeper seals.

The vacuum chamber, which was sealed to a one piece stainless steel ring by a copper gasket, could be raised and lowered by a pneumatic hoist. The ring contained the electrical feed thrus for connection to the electron beam gun and also the rotary drives required to obtain the internal motions. The drive shafts were magnetically coupled to external motors and provided 6 lb-ft of torque to move the electron beam carriage assembly. The beam carriage was driven at speeds between 1 to 14"/hr by a variable speed motor. The lower specimen grip was manually operated for more effective control of the molten zone. A shutter device was used to shield and reduce the deposit of vapor onto the viewing ports.

The pumping system was a 4200 l/sec 10" oil diffusion pump filled with DC−705 silicone oil and fitted with an optically dense chevron baffle. A continuously operated liquid N_2 cold trap with an automatic feed controller reduced the amount of oil migration from the pump to the vacuum chamber.

THE EFFECT OF ULTRA-HIGH-VACUUM ELECTRON BEAM ZONE REFINING ON THE PURIFICATION OF METALS

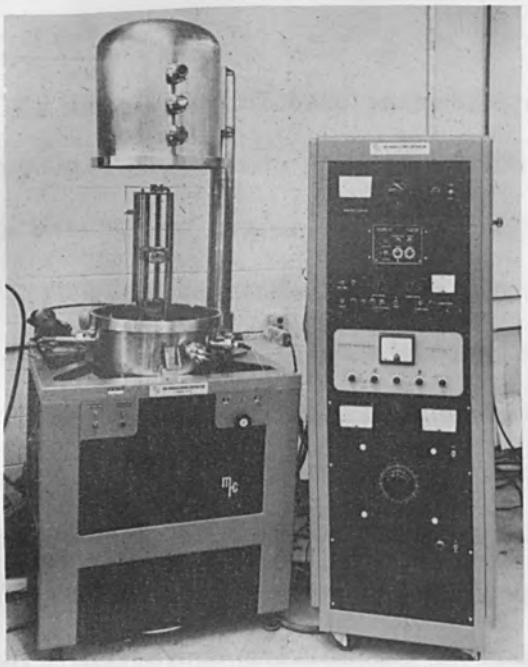

FIGURE 1 General View of Apparatus

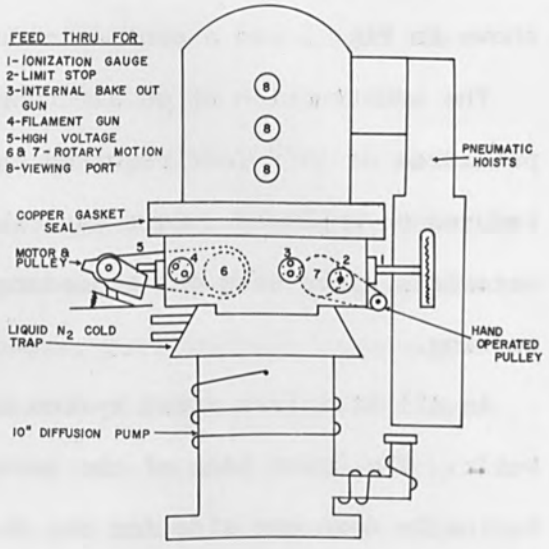

FIGURE 2 Schematic of Feed Thru Arrangement to Vacuum Work Chamber

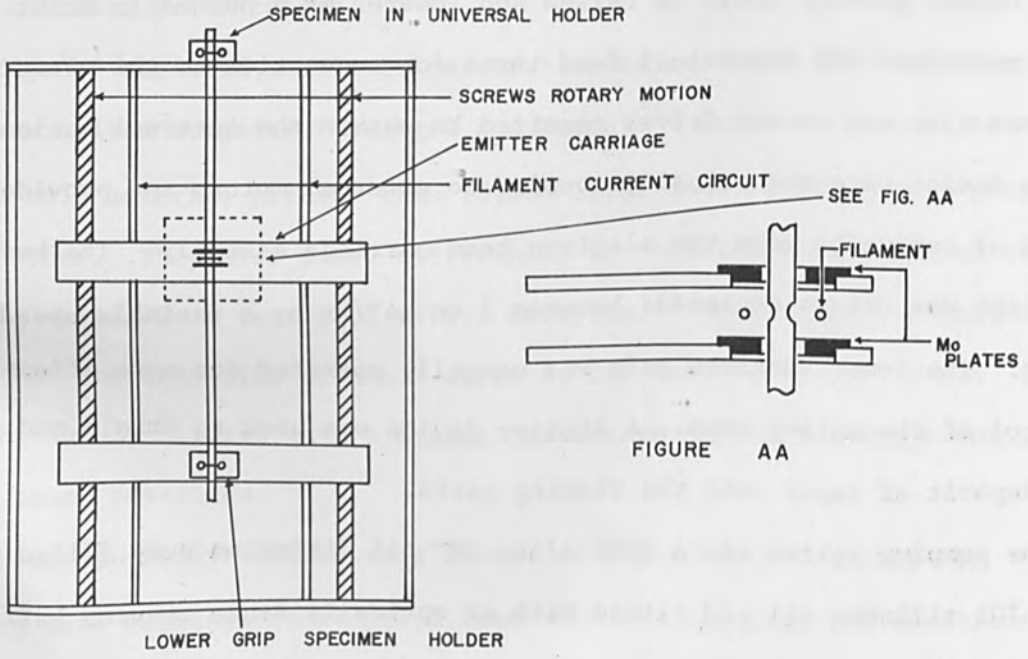

FIGURE AA

FIGURE 3 Electron Beam Carriage Assembly

An ionization gauge, capable of reading to 10^{-11} Torr, monitored the pressure in the chamber.

The electron beam scanner assembly is shown schematically in Fig. 3. It was fabricated from stainless steel to facilitate bake out. The vertical motion was supplied to the carriage and lower grip assemblies by ball bearing screws. This provided smoother motion and eliminated the sharp cuts and small crevices associated with common screw drive assemblies.

A 1% thoriated tungsten wire filament, 0.030" dia., surrounded the specimen and served as the electron emitter. Molybdenum focusing shields were placed above and below the filament to control the length of the melting zone. This arrangement also permitted the efficient removal of gaseous vapors from the vicinity of the specimen.

System bake out could be accomplished by the use of an outer heating blanket, which was very efficient for heating the outer metal chamber, but required an excessively long time to heat the mechanisms inside the chamber due to the poor thermal conductivity of stainless steel. An internally mounted electron gun* was designed to speed up the bake out process and is shown in Fig. 7. Three such guns can bake out the system by electron heating, and also provide a mild cathodic etching for the removal of surface contaminants.

The gun assembly provided a partially defocused electron beam. The filament was kept at a high negative potential with respect to the other components which were at ground potential. The ring which surrounds the emitting filament was moved to adjust the focus.

The power supply was a 10 kv, 500 ma d.c. unit with reversible polarity,

---

*Patents Pending

so that either the zone refining gun or the bake out guns could be operated from one supply. The filament power unit was equipped with a magnetic amplifier control which automatically regulated the power during pressure fluctuations caused by gas liberated from the melted zone.

It is interesting to note that with the use of the internal bake out guns, it was not necessary to use copper gasket bakeable components. In fact, after the substitution of a Freon-cooled Viton "O" ring for the main copper gasket there has been no difficulty in operating at 10^{-9} Torr.

EXPERIMENTAL PROCEDURES

1. Materials and Operational Procedures

The materials used for this investigation were tungsten and molybdenum rods produced by powder metallurgical techniques and supplied by the General Electric Co. Both materials were obtained as 0.125" dia. rods in 15" lengths.

To start the zone refining operation, the chamber was closed and sealed to the stainless steel ring by a copper gasket. After the mechanical pump had evacuated the system to below 5 microns, the diffusion pump was placed in operation. During pump down, which took 17 hours, the liquid N_2 cold trap was maintained at a full level to reduce the oil migration from the pump to the chamber. The apparatus was heated by the internal bake out guns to about 450°C for three to four hours. When this bake out procedure was not followed a vacuum of 10^{-8} Torr was achieved, but when the zone refining beam was operated the chamber walls degassed, on becoming heated, and the pressure rose by as much as two orders of magnitude.

After some initial operation the system was redesigned to further reduce backstreaming by backing the 10" pump with a 4" diffusion pump and a liquid nitrogen trap as shown in Fig. 6.

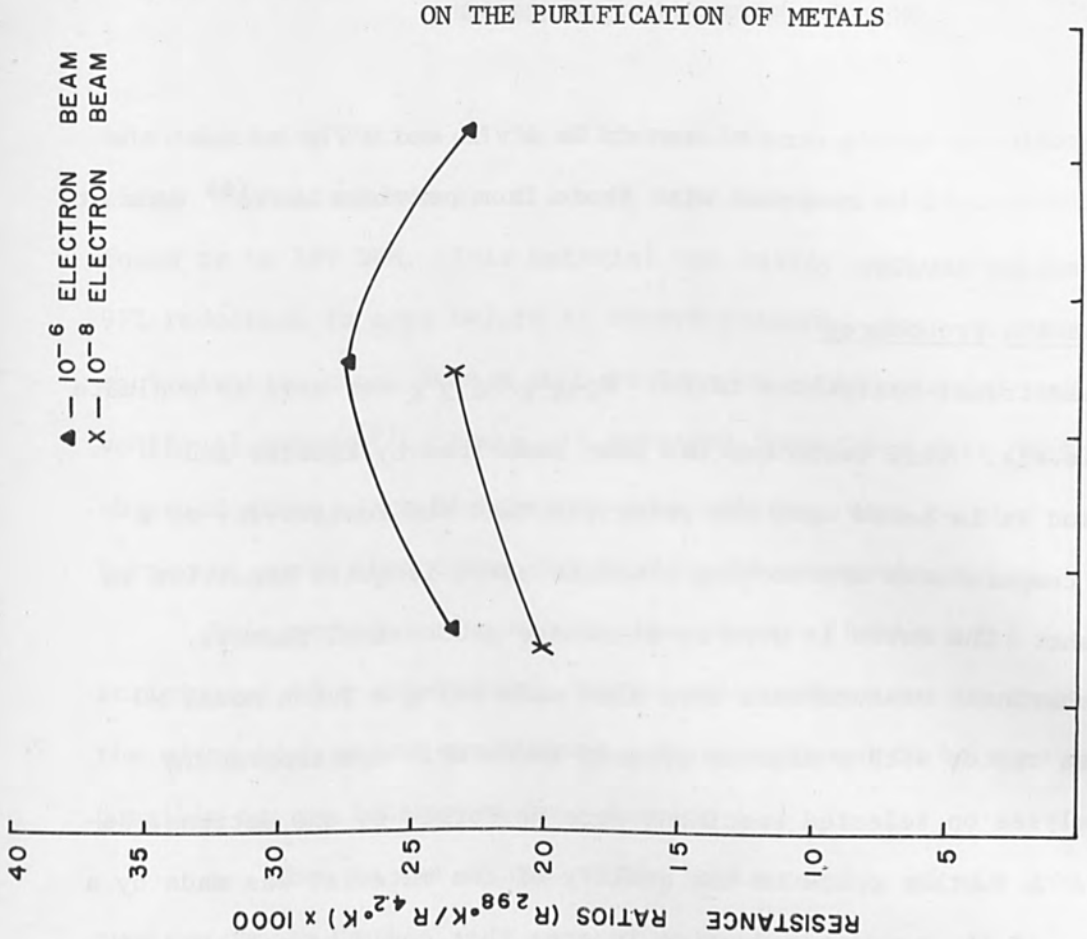

FIGURE 5 Resistance Ratios of 3 Pass W at 10^{-6} and 10^{-8} Torr., at 4"/hr Zone Speed

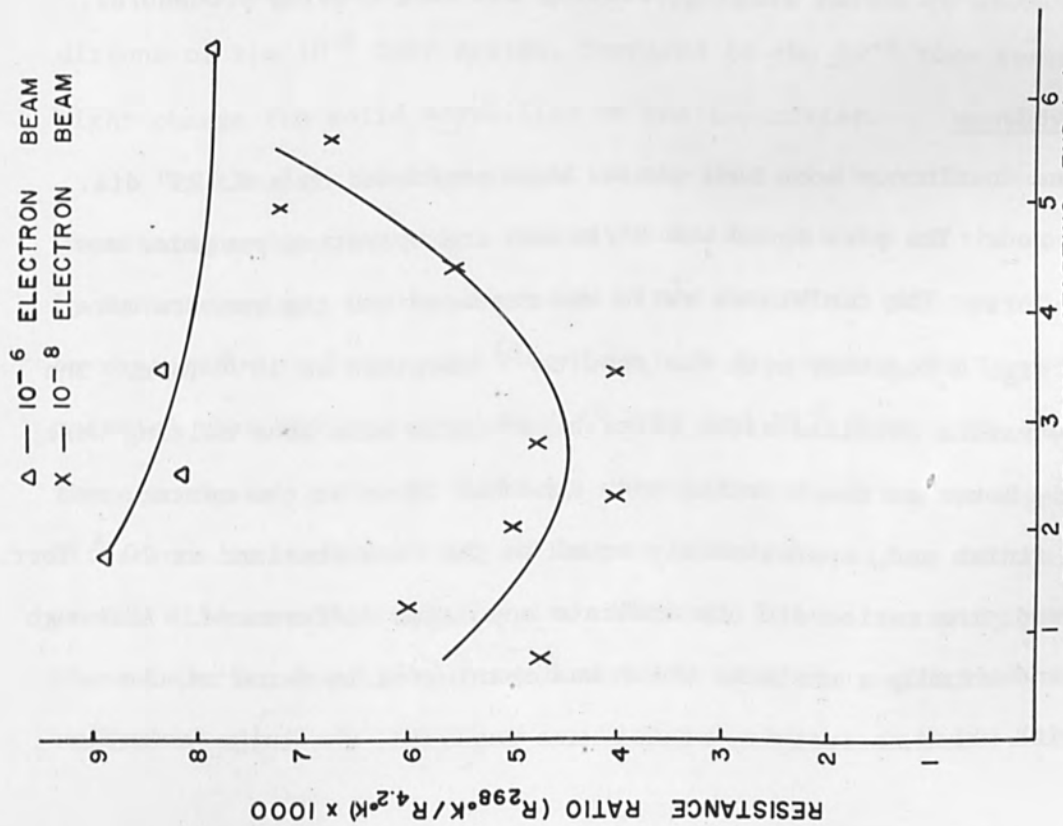

FIGURE 4 Resistance Ratios of 3 Pass Mo at 10^{-6} and 10^{-8} Torr, at 9"/hr

The zone refining speeds were chosen to be 4"/hr and 9"/hr so that the results obtained could be compared with those from previous work[6] done at different pressure levels.

2. Evaluation Procedures

The electrical resistance ratio: $R_{298^oK}/R_{4.2^oK}$ was used to evaluate the purity levels. This technique has been described by Knuzler and Wernick[8] and it is based upon the principle that the resistivity of a material at temperatures approaching absolute zero, is quite sensitive to solute content. The ratio is used to eliminate geometrical factors.

Microhardness measurements were also made using a Tukon Model M0 microhardness tester with a diamond pyramid indenter. Spectrographic chemical analyses on selected specimens were performed by the National Research Corp. A further check on the quality of the material was made by a determination of the percent reduction in area that could be achieved at room temperature by normal swaging, rolling and wire drawing procedures.

RESULTS

1. Molybdenum

Three continuous zone melt passes were performed on a 0.125" dia. molybdenum rod. The pass speed was 9"/hr and the operating pressure was 1.6×10^{-8} Torr. The resistance ratio was measured and the results were plotted in Fig. 4 together with the results[6] obtained at 10^{-6} Torr. The resistivity ratios obtained after ultra-high vacuum beam zone melting were considerably lower at the starting end, somewhat lower at the center, and toward the finish end, approximately equal to the data obtained at 10^{-6} Torr. When compared, the ratios did not indicate any major differences. Although there was undoubtedly a variance which was meaningful in terms of the accuracy with which resistivity ratios were measured, the large variation

of resistivity ratios of the different starting rods was far greater than this. The microhardness of a rod, with a resistance ratio of 6000, was found to be 197 DPH. This material was easily cold-worked by swaging to a 97% reduction in area before it showed failure. Both of these results were equivalent to those from a 6000 resistance ratio material made in the conventional manner[6]. Hence, it appeared from these data that the results obtained after ultra high vacuum zone melting, were neither significantly better or worse than those obtained in the conventional way.

This particular result was unexpected. Resistivity ratios were anticipated of a considerably higher value subsequent to processing under the ultra high vacuum conditions. There appeared to be some anomalies possible in the interpretation, namely:

a. What is the effect of the backstreaming of oil from the diffusion pump on purity, and

b. There is a drastic difference in the thermal equilibrium conditions of the 10^{-8} Torr system, compared to the 10^{-6} Torr system, which might change the solid solubility of the impurities.

If the lack of improvement in the resistivity ratio found after processing under ultra-high vacuum conditions was due to the contamination by backstreaming, then an increase in the amount of silicon or carbon would be expected. Analyses were therefore made to compare the impurity level in material that was processed at 10^{-6} Torr and 10^{-8} Torr. The results of these analyses, given in Table I, showed that there was no significant difference in the amount of silicon or carbon for either of the materials at the different pressure levels. Although it was certainly possible that these impurity levels were not detectable with the sensitivity of the analytical chemical techniques used, our experience indicated that the lack

THE EFFECT OF ULTRA-HIGH-VACUUM ELECTRON BEAM ZONE REFINING ON THE PURIFICATION OF METALS

RESULTS OF CHEMICAL ANALYSES TO DETERMINE Si AND C IN Mo AND W

Impurity	Material	10^{-6} Torr	10^{-8} Torr
Si	W	$<$10 ppm	$<$10 ppm
C	Mo	26-30 ppm	26 ppm

TABLE I

RESISTANCE RATIOS VERSUS THERMAL HISTORIES FOR MOLYBDENUM

Specimen		All Quenched From				
	As Beamed →	600°C 15 hrs →	400°C 64 hrs →	1000°C 15 hrs →	600°C 15 hrs →	200°C 240 hrs
67B (10^{-6} Torr)	6930	5000	6900	2640	4900	5000
90 (10^{-8} Torr)	1335	5000	5000	1520	5250	5000

TABLE II

of improvement in resistivity ratios could be attributed to the effects of oil backstreaming.

A second and more meaningful test was performed.

Since molybdenum is particularly susceptible to contamination by carbon, zone refining experiments were performed on a specimen with no liquid nitrogen in the cold trap. Upon opening the system, oil was found to be condensed in the vacuum chamber. The specimen had a resistivity ratio of 1335, and vacuum fusion analysis indicated a value of 26 ppm of carbon, which within the accuracy of the method, was about the same as the starting material.

Since a resistivity ratio only indicates the amount of impurity which is in solid solution, it was decided to investigate the stability of this ratio as a function of thermal treatment.

Two specimens were vacuum encapsulated and great care was taken to wrap them with a getter material. A succession of heat treatments were performed on both samples and measurements of the resistivity ratio were taken of each sample in the order shown in Table II.

It was interesting to note that the resistivity ratio could be changed either upward or downward, dependant upon the particular time and temperature used to obtain equilibrium. The resistivity ratio changes were found to be completely reversible and only in the "as-beamed" condition was there a marked difference between the two specimens. These results illustrate two significant points. Firstly, resistivity ratio data must be treated with extreme caution. Probably the correct way to make comparison of materials prepared under various conditions is to use identical heat treatments prior to the measurements. This treatment must be such that all impurities are placed in the solid solution state. If the solid solubility

limit of a particular impurity is considerably less than the total present, then the sensitivity is totally lost. The second significant point is that although one specimen showed no difference in the amount of carbon by a conventional analysis, there did appear to be some slight variation in resistance ratio due to zone refining in a chamber containing noticeable amounts of diffusion pump oil.

2. Tungsten

A tungsten rod was zone melted three times at a pressure of 1.2×10^{-8} Torr and with a pass speed of 4"/hr. The resistance ratio measurements gave the results shown in Fig. 5. A typical result for a rod similarly processed at 10^{-6} Torr is also included. The results for both are similar and within the experimental error of approximately 20%.

The microhardness of this specimen, in an area with a resistance ratio value of approximately 20,000, was 360 DPH. This results is the same as that obtained from material processed at 10^{-6} Torr[6]. At room temperature the reduction in area was 6% before failure, and is similar to the result obtained for material processed in the same manner at 10^{-6} Torr. Chemical analyses, of a tungsten specimen which had three zone refining passes at high vacuum, showed no elements above the detectable limits of emission spectroscopy.

Results for a section of this tungsten rod, given two more passes under the same conditions, show a decrease in resistivity ratio. This indicated that there may be two opposed processes, namely, purification by volatilization during zone refining and contamination by oil vapors.

After modification of the system to include a backing diffusion pump, another tungsten rod of the same starting material was given one pass. The resistivity ratio measurements of this were compared to a rod similarly

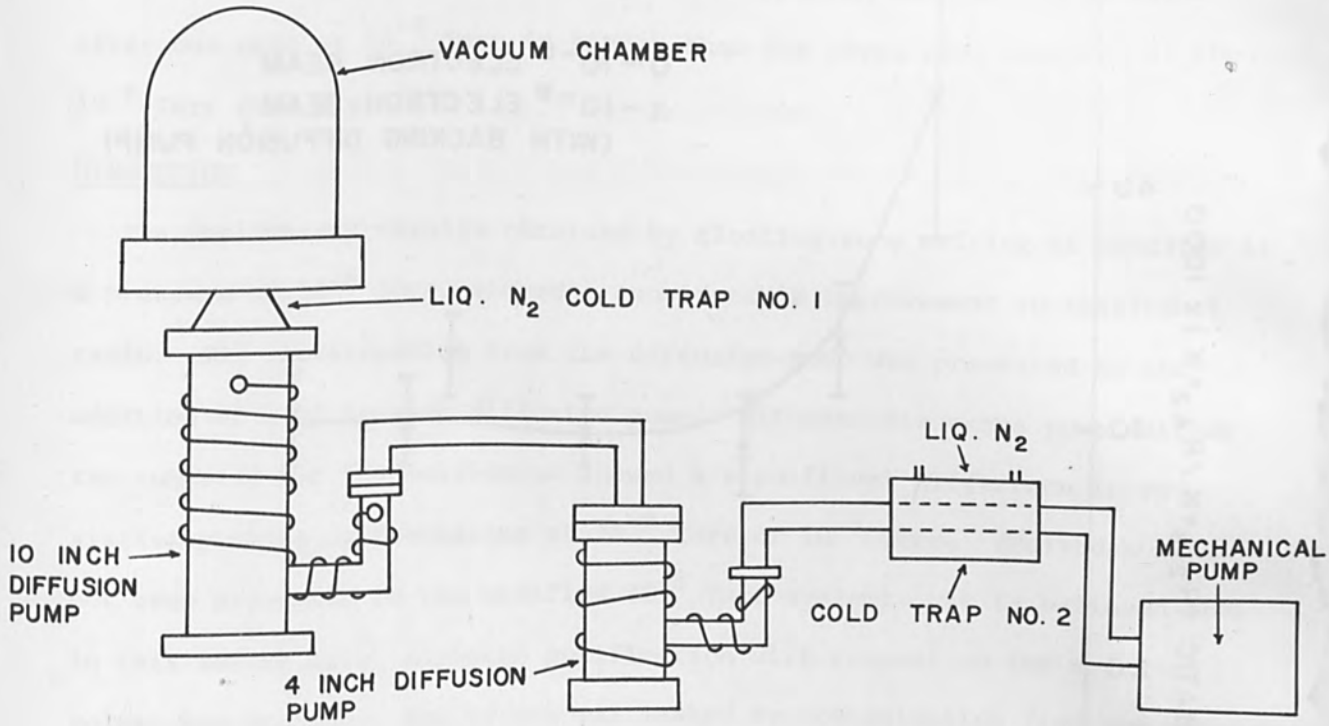

FIGURE 6 Present Vacuum System Arrangement

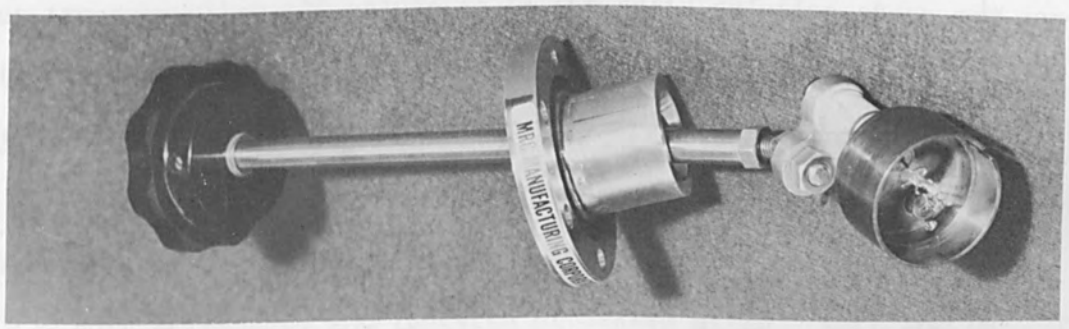

FIGURE 7 Internally Mounted Electron Gun

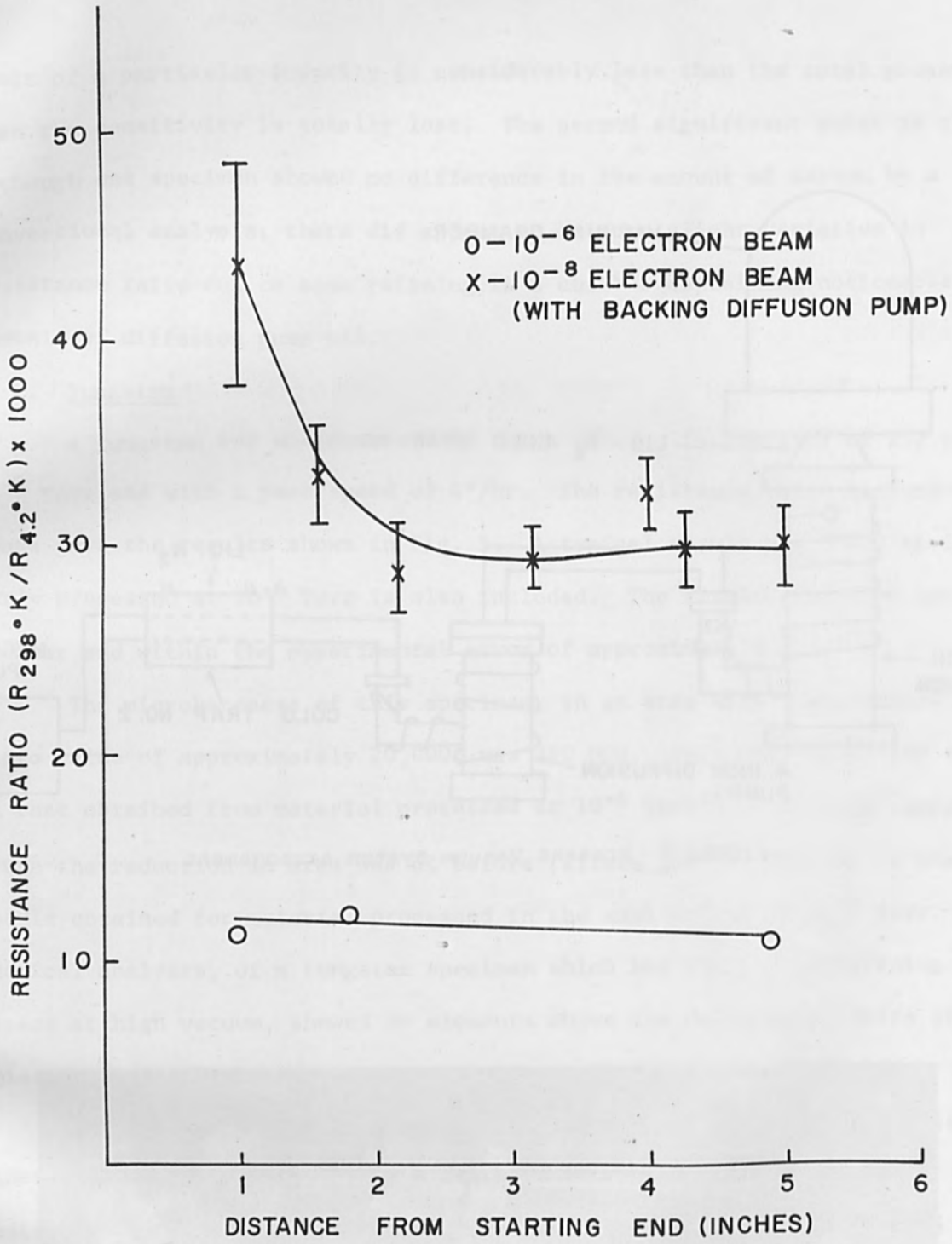

FIGURE 8 Resistance Ratios for One Pass Tungsten at 10^{-6} and 10^{-8} Torr., (modified system) at 4"/hr

treated at 10^{-6} Torr, and are shown in Fig. 8, and the effect is quite marked. The resistance ratio being three times higher than that of one pass material from the 10^{-6} Torr system. In fact, the resistance ratio after one pass at 10^{-8} Torr is higher than the three pass material at the 10^{-6} Torr (See Fig. 5).

DISCUSSION

The preliminary results obtained by floating-zone melting of tungsten at a pressure of 10^{-8} Torr, showed a considerable improvement in resistance ratio. Oil backstreaming from the diffusion pump was prevented by the addition of a 4" backing diffusion pump. Without this extra pump neither the tungsten nor the molybdenum showed a significant difference in resistivity ratio by processing at 10^{-6} Torr or 10^{-8} Torr. (Molybdenum has not been processed in the modified 10^{-8} Torr system). It is believed that in this latter case, although purification with respect to the original solute was obtained, the effect was masked by contamination from the diffusion pump vapors.

The experiments performed to affect the resistance ratio by heat treatments have shown that the ratio may not always reflect the purity of the material. When the ratio does not vary with precipitation or re-solution heat treatment then all solute is in the solid solution state and contributes to the measured resistance.

CONCLUSIONS

1. A 10^{-9} Torr system was constructed with a 5 ft^3 bakeable steel chamber, internal bakeout guns and a 10" diffusion pump.

2. Both molybdenum and tungsten processed at 10^{-6} Torr and 10^{-8} Torr, showed no difference in resistance ratio, unless an additional diffusion pump backing was utilized. With this modification, one pass tungsten showed

a markedly higher ratio after processing at 10^{-8} Torr.

3. Gage pressure is not always meaningful when working in the high vacuum range, as manifested by entirely different resistivity ratios on material processed under identical pressures.

4. The resistance ratio as a measure of purity must be used with caution for solvents with low solubilities of other elements.

ACKNOWLEDGEMENTS

The authors wish to acknowledge the experimental assistance of D. Mealer and R. Schwabik. Thanks are also due to G. T. Murphy for helpful comments and review of the manuscript, and to Virginia Boyce for preparation of the manuscript.

This work was sponsored by the Advanced Research Projects Agency and administered by the U.S.A.F. Office of Scientific Research.

REFERENCES

1. Pfann, W. A., "Zone Melting", John Wiley & Sons, New York (1958).
2. Wernick, J. H., "Ultra-High Purity Metals", American Soc. for Metals Seminar (1961).
3. Tiller, W. A., "The Art and Sciences of Growing Crystals", ed. Gilman, J. J., John Wiley & Sons, New York (1963).
4. Calverly, A., Davis, M. and Lever, R., J. Sci. Instr., 34 (1957) p. 142.
5. Shadler, H. W., AIME, 219, (1960), p. 649.
6. Drangel, I. and Murray, G. T., Proc. AIME Meeting, 1964, (to be published).
7. Seraphim, D. P., Budwick, J. I. and Ittner, W. B., AIME, 218, (1960), p. 527.
8. Kunzler, J. E. and Wernick, J. H., Trans. AIME 212 (1958), p. 868.
9. Power, B. D., Crawley, D. J., Vacuum, Vol. IV, October 1954, p. 415.

PRACTICAL APPLICATIONS OF THE ELECTRON BEAM MICROPROBE

Sheldon H. Moll
Advanced Metals Research Corporation
Burlington, Massachusetts

ABSTRACT

Since the microprobe can analyze a sample volume as small as 1-2 cubic microns, it is useful in solving problems concerned with compositional homogeneity, foreign inclusions, corrosion products, etc., for most solids. The essential components of the instrument are briefly described and typical applications are discussed. Recent advancements in technique, instrumentation and new applications are mentioned.

PRACTICAL APPLICATIONS OF THE ELECTRON BEAM MICROPROBE

INTRODUCTION

As a result of its ability to perform a point by point chemical analysis of a sample volume as small as 1-2 cubic microns, the microprobe has been useful in solving problems concerned with compositional homogeneity, concentration or diffusion gradients, foreign inclusions, unknown phases, corrosion products, etc., for most solid or semi-solid materials.

Applications of the electron probe to practical material studies has excited the imagination of scientists and engineers ever since the successful introduction of the first working instrument by R. Castaing in 1951. Today, the electron probe is rapidly being recognized as an investigative tool matching in importance the optical and electron microscopes.

The major applications and developments of analytical techniques have emerged from the metallurgical field where the investigation of precipitates, surface coatings, diffusion and corrosion phenomena, segregation, phase diagrams, inclusions, etc., is now routine. However, the instrument is also useful in other areas of research, development, quality and product control. Problems similar to those already mentioned have been studied in such non-metallics as; glass, minerals, semi-conductors, cermets, oxides, rubber, meteorites (stony), and plastics.

In the medical field; bones, teeth, stones and tissue have been successfully studied and the development of routine sample preparation procedures is a matter of much current interest.

The microprobe is also eminently suited as a tool for studying either the absolute or relative thickness and the chemistry of thin films, since the depth of penetration of the electron beam is quite limited in most materials of interest and can be readily adjusted by varying the acceleration potential of the electron gun.

PRACTICAL APPLICATIONS OF THE ELECTRON BEAM MICROPROBE

The purpose of this discussion is to present a few typical applications of the electron beam microanalyzer in order to illustrate its use as a routine problem solving, or basic research, tool and to briefly list the important components of the instrument.

COMPONENTS OF THE INSTRUMENT

The principles of operation of the microprobe are quite simple. A beam of electrons is accelerated with a high potential and focused by means of electro-magnetic lenses to a diameter of about 1-2 microns at the surface of the specimen to be investigated. As in an x-ray tube the specimen will act as a primary source of x-rays. A continuous or white spectrum is produced as well as fluorescent x-rays characteristic of the elements excited by the electron beam. A chemical analysis of the excited area is afforded by analysis of the characteristic x-ray lines by means of a single crystal x-ray spectrometer.

Fig. 1 is a schematic which illustrates the basic components of the instrument; the electron gun, magnetic lenses, x-ray spectrometer, including the curved monochromating crystal and a suitable detector, and x-ray readout. A light microscope concentric with the electron optical axis allows continuous visual observation of the specimen to be analyzed. The deflecting coils allow a mode of operation in which the electron beam is not held stationary but is traversed over the sample surface in a repeatable raster pattern. The cathode ray tubes then display a two dimensional x-ray or scattered electron pattern.

APPLICATIONS

Diffusion in Solids

The determination of the rate of atomic diffusion in solids is extremely important since this is often the rate controlling process for such

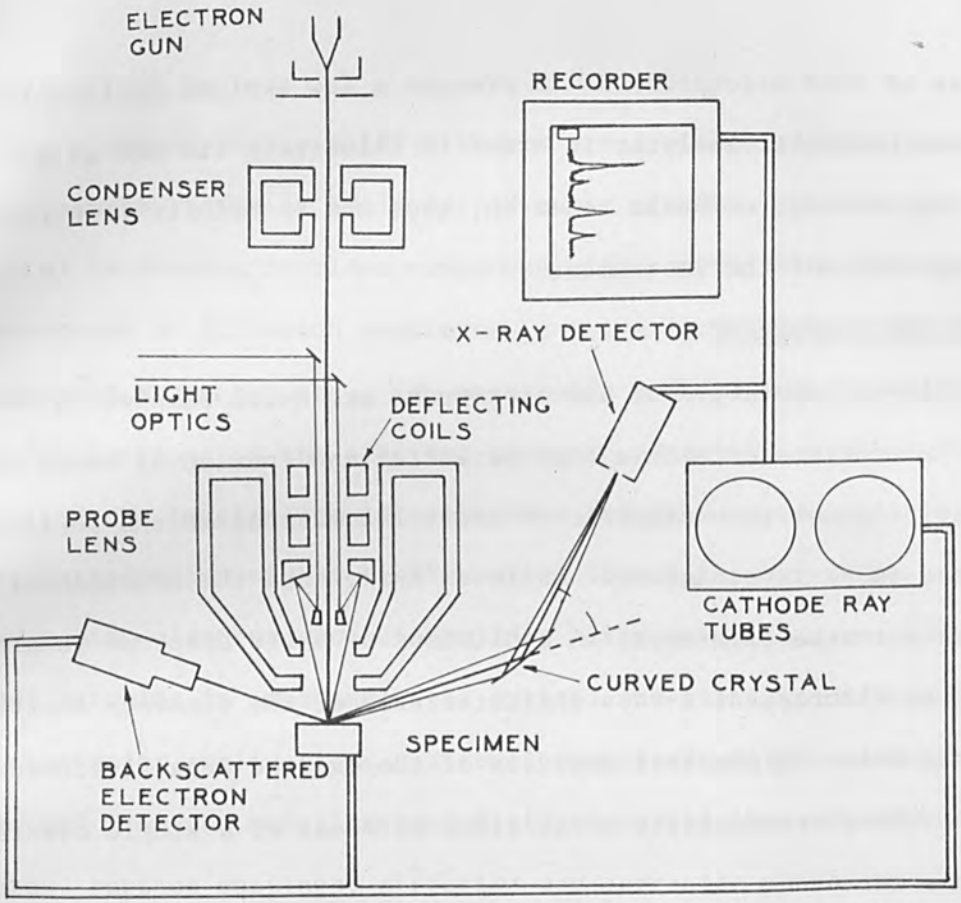

FIGURE 1 Schematic of AMR/3 Electron Beam Microanalyzer

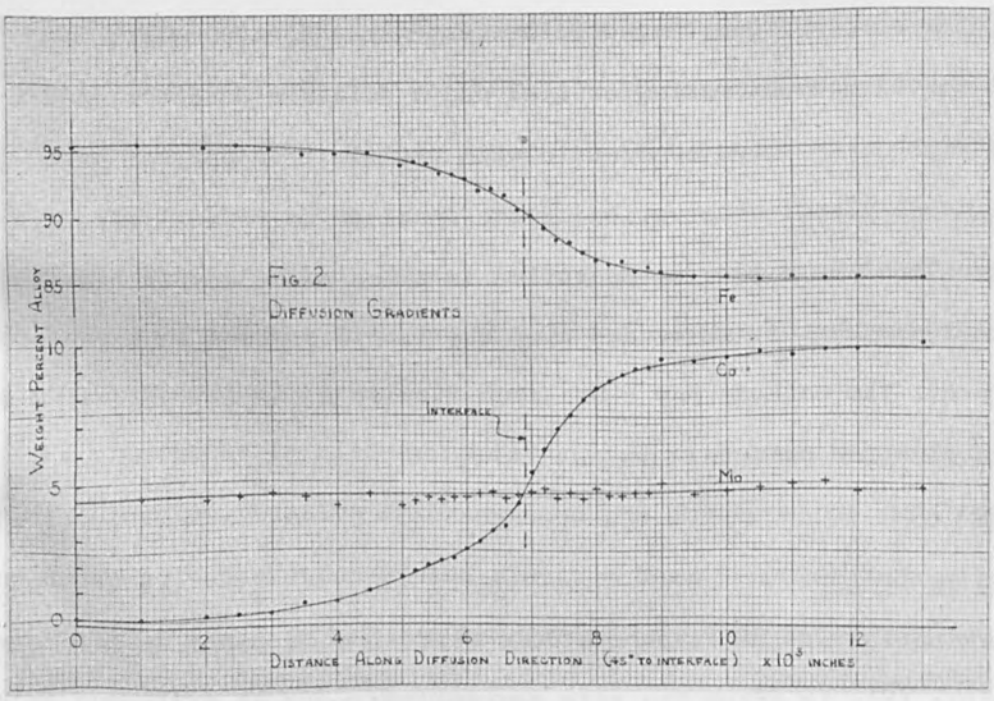

FIGURE 2 Fe, Co, Mo Concentration Gradients, Co, Mo Steel Diffusion Couple

phenomena as alloy homogenization, oxidation or corrosion, metallic bonding, etc. A usual technique for the determination of interdiffusion coefficients consists of bonding together two dissimilar materials of interest and subsequently heating these for a suitable time at temperature until a concentration gradient in the vicinity of the original interface has been established. If the diffusion couple is metallographically prepared along a mid-plane perpendicular to the original interface, the gradient can be determined.

A section of this type is inserted into the microanalyzer and one or more x-ray spectrometers are set up to simultaneously record the characteristic x-ray lines of the elements of interest. The specimen is then driven beneath the focused electron beam either continuously or in fixed steps and the x-ray intensity gradient recorded as a function of distance in the diffusion direction. The x-ray intensity gradient is converted to composition by means of calibration alloys or empirical calculations.

Fig. 2 shows a typical determination of the concentration gradients present in a diffusion couple formed between an alloy of 5 wt% Mo in Fe and an alloy of 5 wt% Mo and 10 wt% Co in Fe. A study of the gradient yielded the diffusion coefficients required to determine the homogenization rates of Co in a Co-Mo steel.

The analysis of concentration gradients with the microprobe is certainly not limited to the study of metals, as illustrated in Fig. 3. In this study, the concentration gradients of Pb, Zn and Si were determined across the bond between a solder glass, rich in Pb and Zn oxide, and a silica glass. The rapid relative movement of Si as evidenced by its relatively extensive interpenetration profile was quite clear. These data were the direct x-ray intensity gradients, chart recorded, from the sample when it

was continuously motor driven beneath the electron beam.

The gradients shown in Figs. 2 and 3 are simple and monotonic in nature. Very often, discrete discontinuities in concentration were noted in diffusion gradients. The concentration limits of these were identical to the concentration limits of multiphase fields present in the phase diagrams of the element systems of interest and the examination of these yielded a bonus for diffusion studies in general.

FOREIGN INCLUSIONS

The presence of inclusions foreign to the manufactured product is a serious problem in quality control. Inclusions very often directly affect surface finish, mechanical properties, chemical stability and general product appearance. In many cases inclusion sizes are quite small and a first step towards their elimination is often a determination of their chemistry as a means of identification.

During testing of a forged beryllium part for jet engine application, mechanical failure was traced directly to the presence of a number of dense inclusions exhibiting a metallic luster. After these were exposed by metallographic sectioning, the electron beam was positioned on a representative area and a complete spectral pattern, as shown in Fig. 4 was recorded. The characteristic lines of W, Ta and Co were found in the excited spectrum. It was fairly clear that this inclusion must have been a fragment of a WC-TaC-Co bonded hard metal, which could have been introduced during grinding or machining of the beryllium during processing.

Stainless steels are often stabilized against grain boundary attack by the addition of Ti. If the carbon content is excessive, or heat treatment abnormal, alloy carbide inclusions rich in Ti can be formed. Fig. 5 represents the data obtained in a study directed toward an identification of just

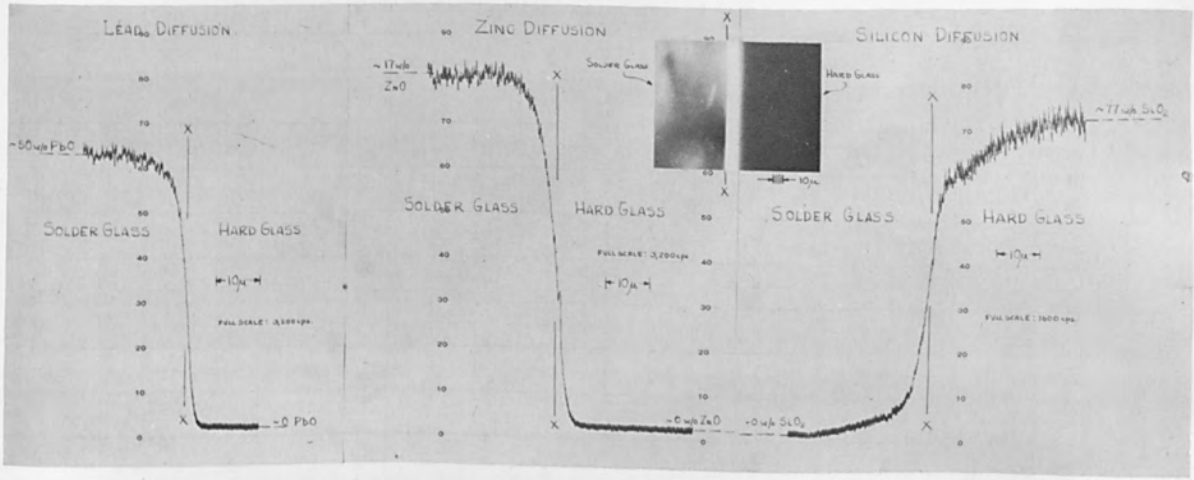

FIGURE 3 Pb, Zn, Si Concentration Gradients, Solder Glass to Silica Glass Bond

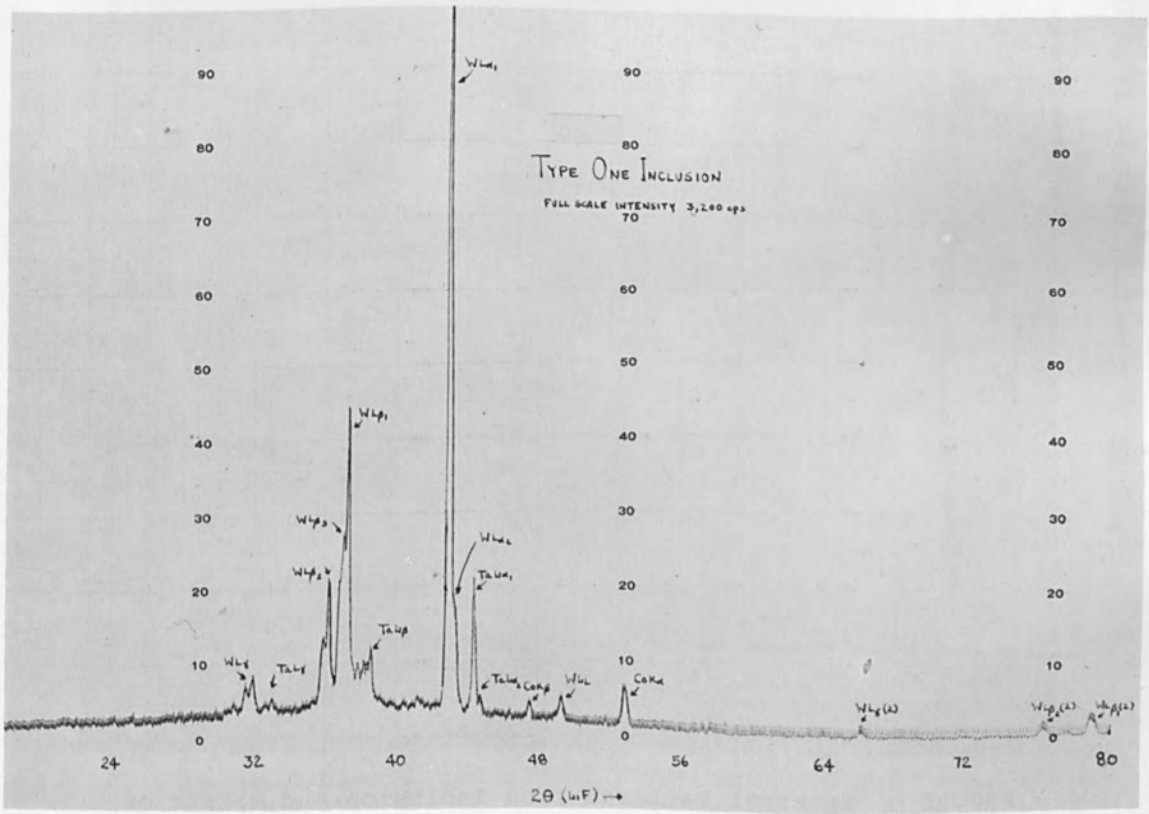

FIGURE 4 Spectral Pattern from Inclusion in Beryllium

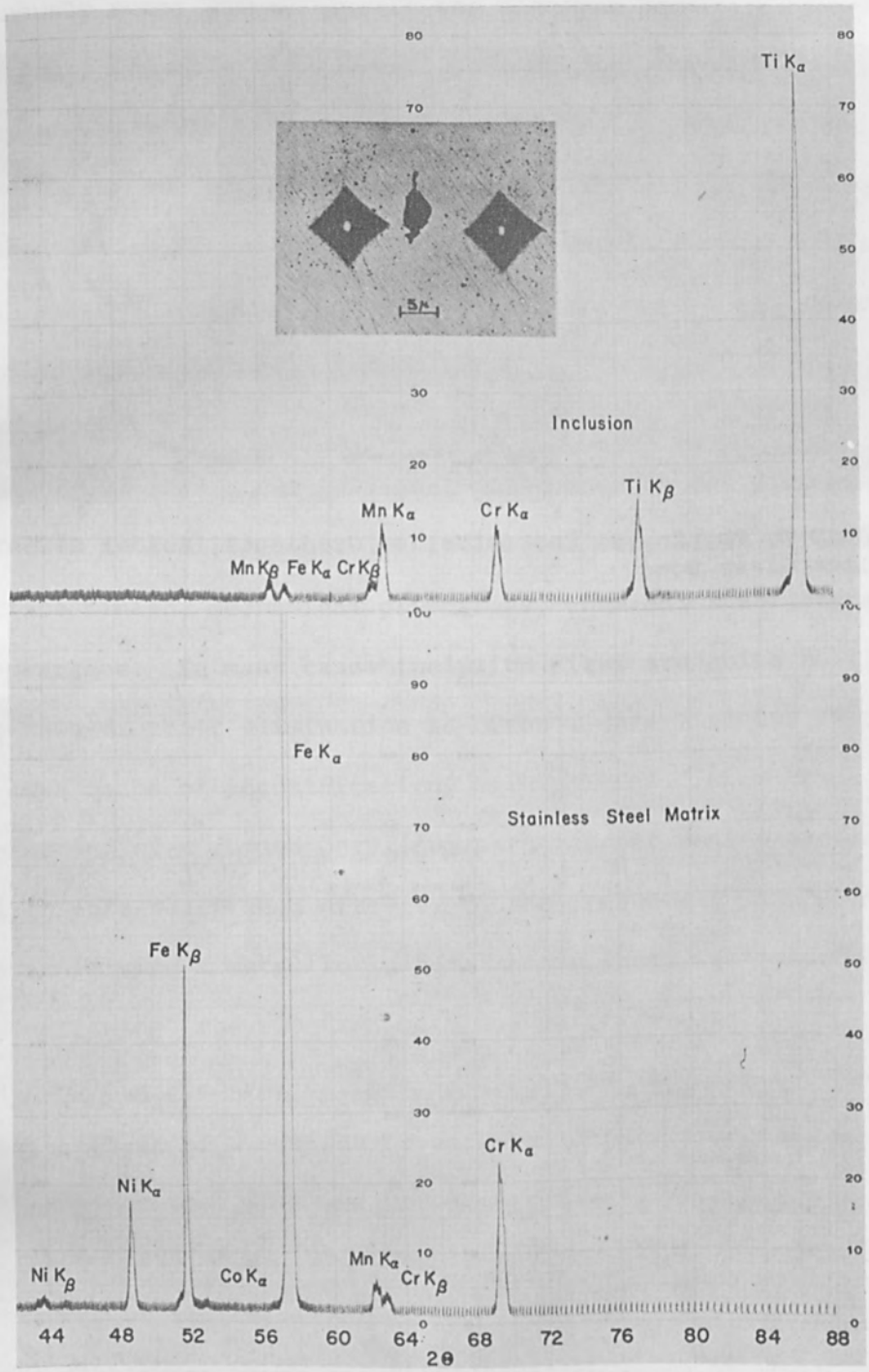

FIGURE 5 Spectral Patterns from Inclusion and Matrix of Stainless Steel

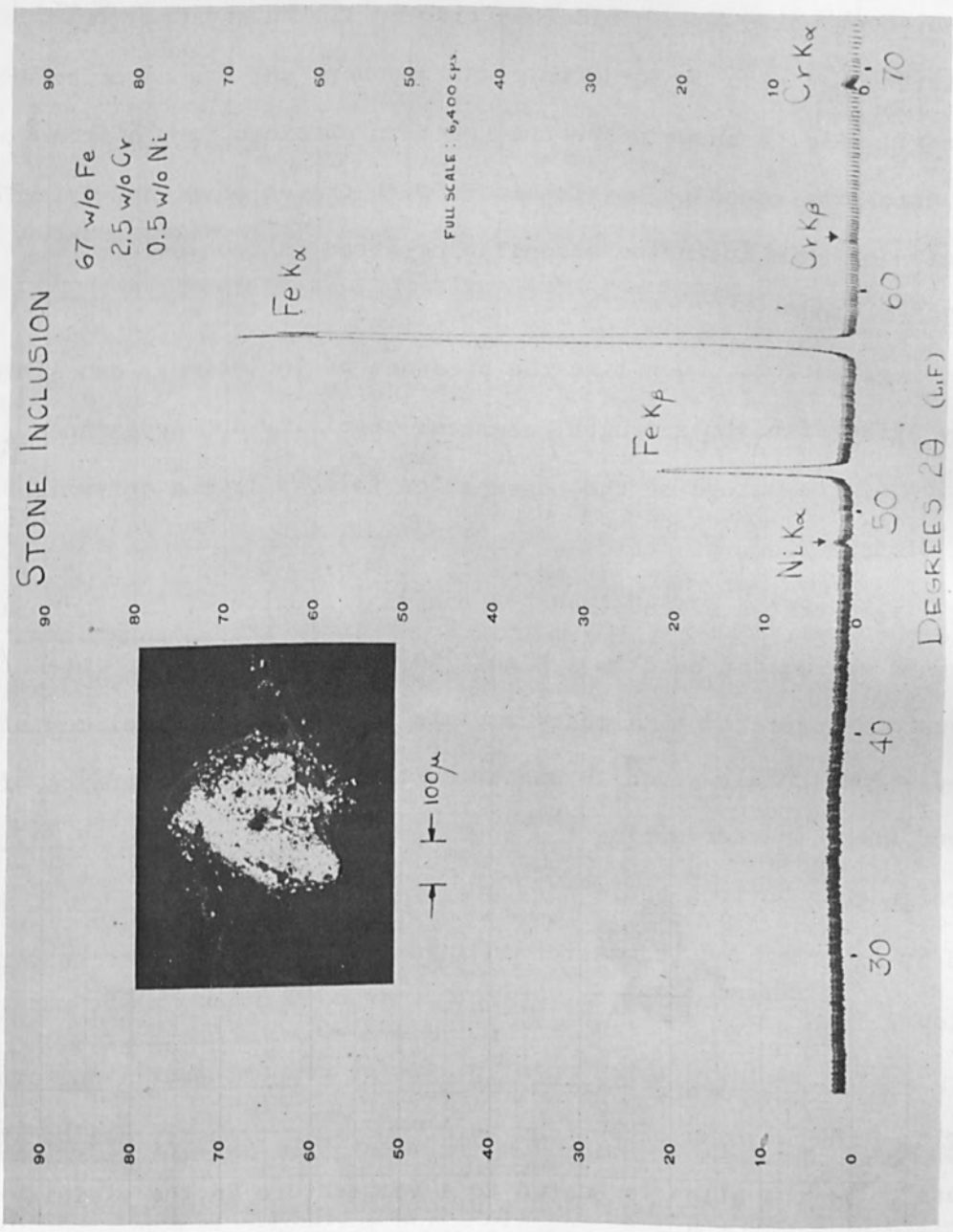

FIGURE 6 Spectral Pattern from Inclusion in Glass

such inclusions. The spectral patterns shown were obtained with the electron beam positioned on the matrix and on a 5 μ carbide inclusion. The matrix pattern exhibited strong Fe, Cr and Ni lines (traces of Mn and Co were also seen) while the carbide was rich in Ti, Mn and Cr.

Inclusions can also be found in glass products and are often referred to as "stones". Fig. 6 shows a spectral pattern obtained from a stone inclusion which was found to be rich in Fe with traces of Ni and Cr. The composition of this inclusion strongly suggested an iron oxide.

ALLOY SEGREGATION

Alloy segregations, much like the presence of inclusions, can often directly affect finish, strength, chemical stability and appearance. A definition of the nature of the segregation follows from a determination of element distribution.

Fig. 7 illustrates a study made of the distribution of Cr, W, Mn and Fe across a segregated band in a high alloy steel. The x-ray intensity distributions indicated an almost complete lack of alloying elements within the band. This result strongly suggested the accidental intrusion of an unalloyed steel spatter during the pouring or freezing of the steel ingot. The foreign chip obviously did not have time to dissipate before it was trapped by freezing and it was formed into a band during subsequent rolling operations.

The presence of low melting point phases or compositions along grain boundaries in metals can often lead to a condition commonly called "hot shortness". If the alloy is heated to a temperature in the vicinity of the melting point of the grain boundary lining phase, the material literally comes apart at the seams.

Fig. 8 illustrates a search for the presence of a Bi rich phase which

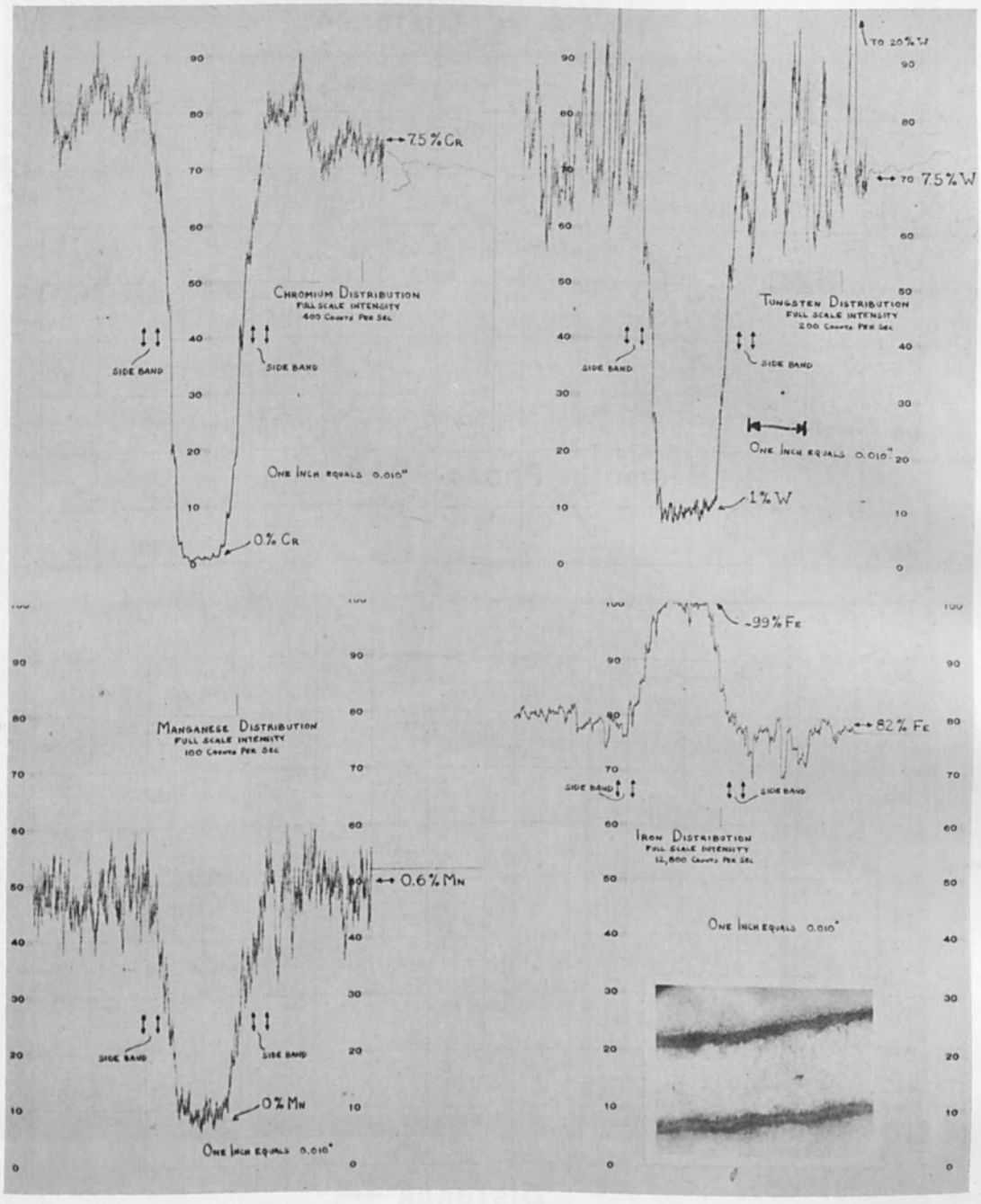

FIGURE 7 Cr, W, Mn and Fe Distribution Across a Segregated Band in a High Alloy Steel

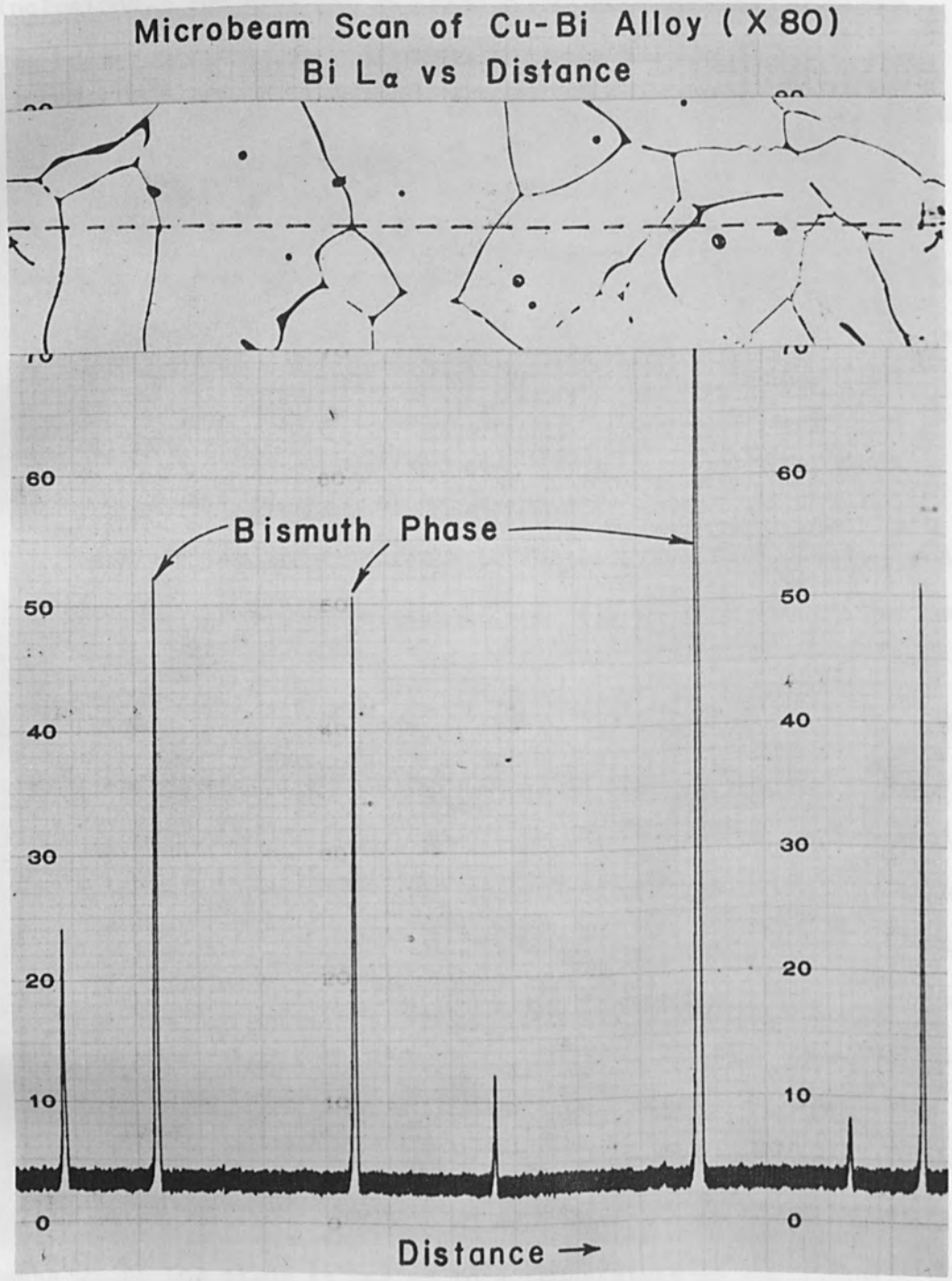

FIGURE 8 Bismuth Distribution in Cu-Bi Alloy

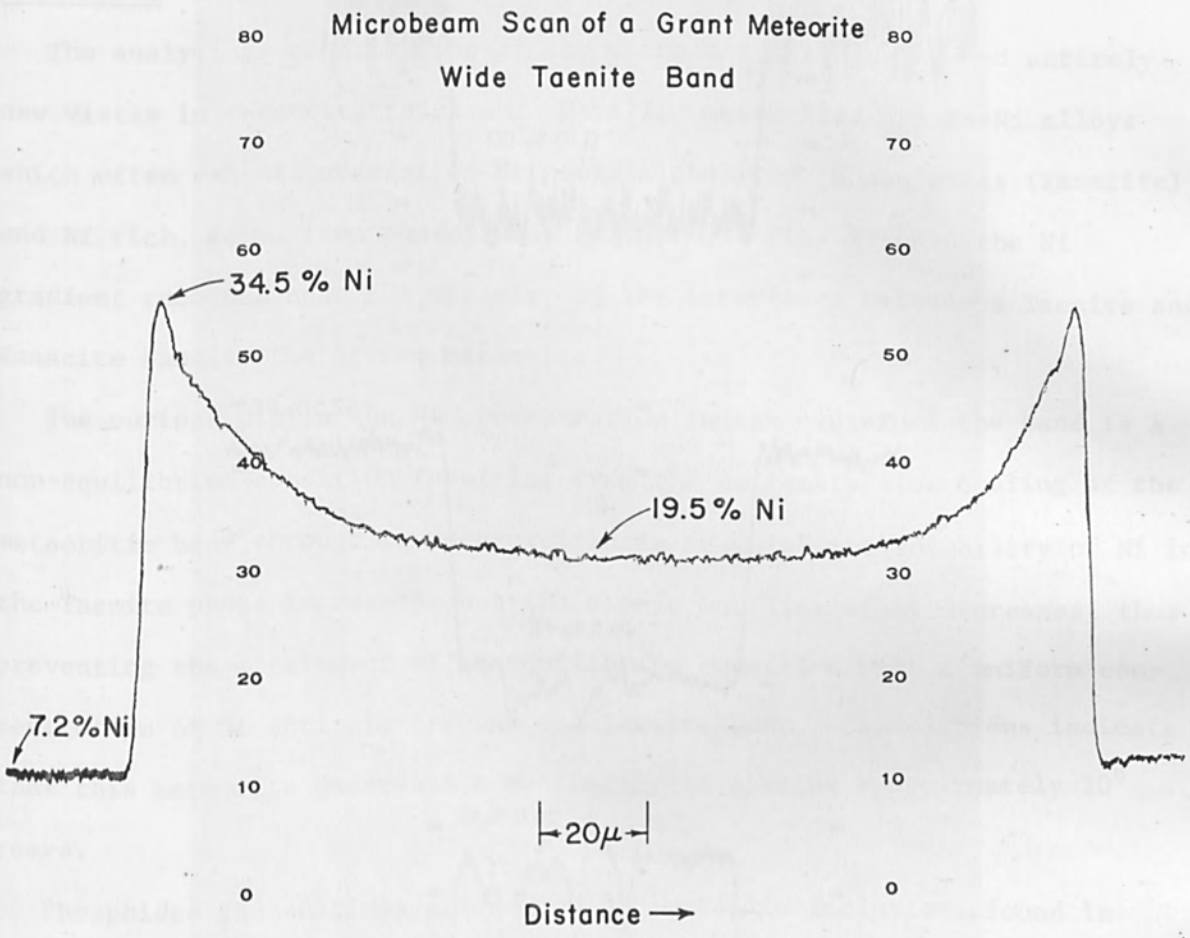

FIGURE 9 Ni Distribution Across Taenite Band (γ Fe-Ni) in Kamacite (α Fe-Ni) - Breece Meteorite

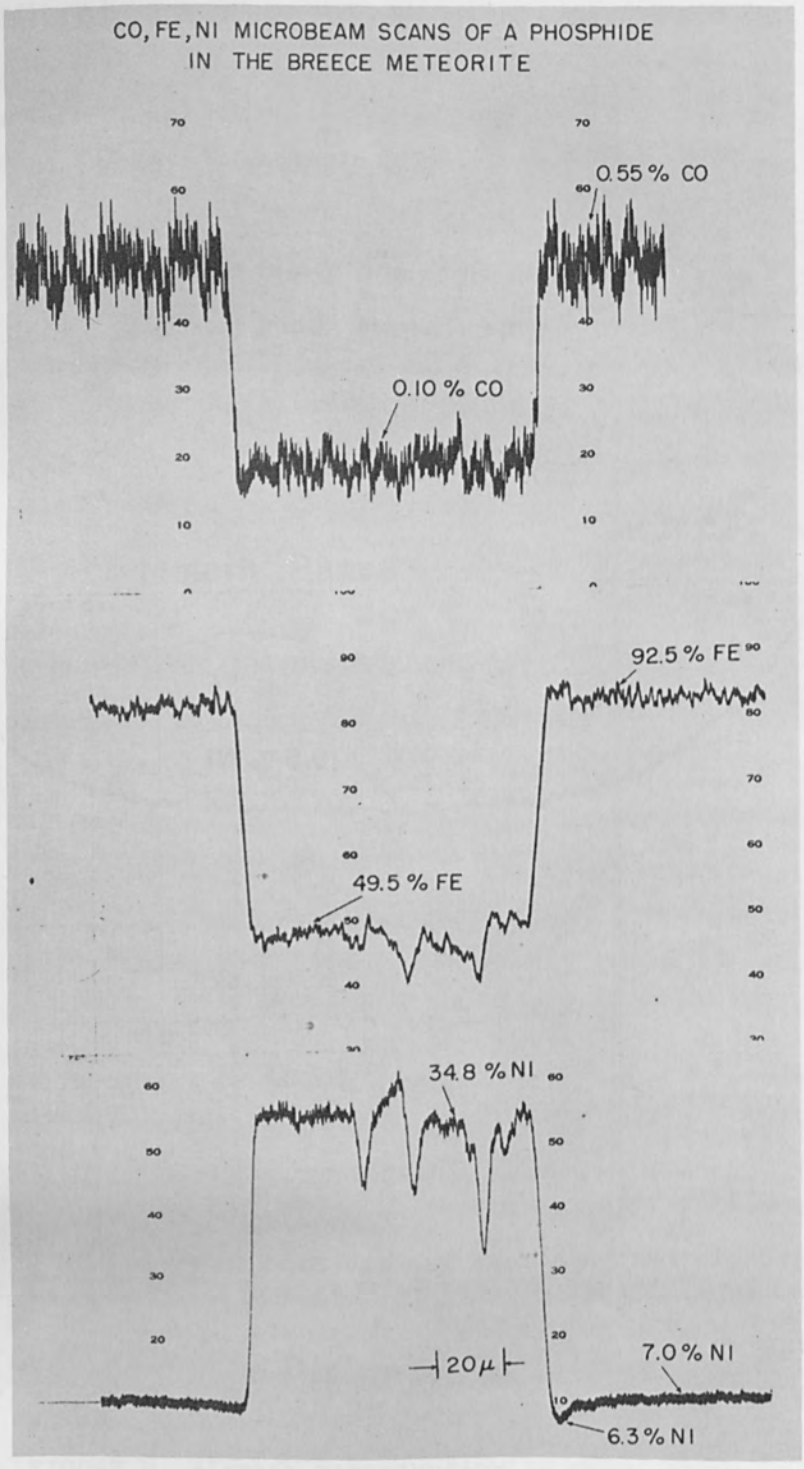

FIGURE 10 Co, Fe and Ni Distribution Across Phosphide - Breece Meteorite

often lines the grain boundaries of Cu-Bi alloys. The strong BiL_{α} intensity reaction occurred whenever the electron beam crossed a boundary on the traverse path shown, provided clear evidence of the susceptibility of this alloy to "hot shortness".

METEORITES

The analytical capabilities of the microanalyzer have opened entirely new vistas in meteorite research. Metallic meteorites are Fe-Ni alloys which often exhibit coexisting Ni poor, alpha iron, phase areas (Kamacite) and Ni rich, gamma iron phase areas (Taenite). Fig. 9 shows the Ni gradient recorded near the vicinity of the interfaces between a Taenite and Kamacite band in the Breece Meteorite.

The curious dip in the Ni concentration in the center of the band is a non-equilibrium condition resulting from the extremely slow cooling of the meteoritic body through temperature ranges in which the solubility of Ni in the Taenite phase increases, but the atomic mobility of Ni decreases, thus preventing the attainment of an equilibrium condition with a uniform concentration of Ni entirely through the Taenite band. Calculations indicate that this meteorite underwent a cooling cycle lasting approximately 10^6 years.

Phosphides and sulfides are common non-metallic inclusions found in metallic or non-metallic (stony) meteorites and their chemistry is often of interest. Fig. 10 revealed the distribution of Co, Fe and Ni across a phosphide found in Kamacite in the Breece meteorite. Calculations reveal that the phosphide was a complex $(Fe, Ni)_3P$.

SUMMARY

The examples presented above can, of course, only touch upon the wide variety of applications possible with the electron probe. The Advanced

PRACTICAL APPLICATIONS OF THE ELECTRON BEAM MICROPROBE

Metals Research Corporation instruments have been successfully applied to the determination of both the bulk and surface chemistry of individual detergent particles, the characterization of the chemistry and distribution of non-metallic inclusions in automobile tire rubber, the analysis of paint pigments from works of art, the study of minute corrosion products, powder residues and individual micro-meteorites, and many others of both fundamental and aesthetic interest.

Specimen preparation need only be as demanding as the required results, and polished sections are not always necessary or helpful. Actual fracture surfaces, snips of wire or thin sheet, chips of brittle samples, collections of powder, etc., have been directly examined.

Recent advancements in technique and instrumentation promise ever widening areas of application for the electron probe. Electron beam scanning, with which a two-dimensional mapping of chemistry or surface topography is achieved with cathode ray tube display, is already widely in use.

Interest has also been stimulated towards the study of Kossel lines which are essentially divergent beam x-ray diffraction patterns formed in the microprobe. This technique will allow lattice parameter and crystal orientation studies to be carried out on micron sized areas in specimens of interest. A number of successful applications can already be found in the literature.

Most recently, the first practical detection of the characteristic x-ray lines of B, C, N, O and F utilizing soap crystal monochromators and flow-proportional counters was demonstrated. This advancement alone enables the solution of many important problems heretofore unsolvable with modern instrumentation.

ELECTRON BEAM SCANNING SYSTEMS

R. S. Buritz and Rauf Argon
Alloyd General Corporation
Cambridge, Massachusetts

ABSTRACT

A system for magnetically sweeping an electron beam combined with an intensity modulation has been built for the uniform heating of test specimens to 6000°F. The system gives a uniform temperature over the entire piece, and end losses can be compensated for individually. Various specimen geometries are accommodated by means of a variable raster.

A variation of the basic system to provide a uniform flux density is described. Design and experimental data are presented.

ELECTRON BEAM SCANNING SYSTEMS

INTRODUCTION

The use of electron beams for high temperature melting and heating is well known[1,2]. It is convenient to be able to deflect the beam to heat specimens of various geometries, either to obtain uniform temperatures or for special effects. By providing two deflecting systems at right angles to each other it is possible to scan an area. The deflection may be electrostatic or magnetic. In addition, the intensity of the beam may be modulated which in conjunction with sweeping provides for operational versatility.

ELECTRON BEAM GUN

The electron gun used was a triode type with a focus coil. Two sets of deflecting coils at right angles are fitted externally over the drift tube, for simplicity and convenience in adjusting the direction of the deflection. The drift tube is 304 stainless steel 0.020" in thickness to minimize high frequency attenuation, which would result in a diminution of deflection. For frequencies less than 10 kc the effect of this wall thickness is negligible.

UNIFORM TEMPERATURE SYSTEM

Until recently the use of electron beams was restricted primarily to welding and evaporation. A need for mechanical data on structural materials at temperatures from 2000°F to 6000°F resulted in the development of a vacuum furnace[3] using electron beams for heating. The beams were swept the length of the specimen to obtain a uniform temperature distribution. Such a typical tensile test furnace is shown in Fig. 1. The vacuum system was portable for convenience and used an oil diffusion pump with a liquid nitrogen trap to minimize contamination from oil backstreaming. The furnace chamber was rectangular, 12" x 12" x 15", made from stainless steel

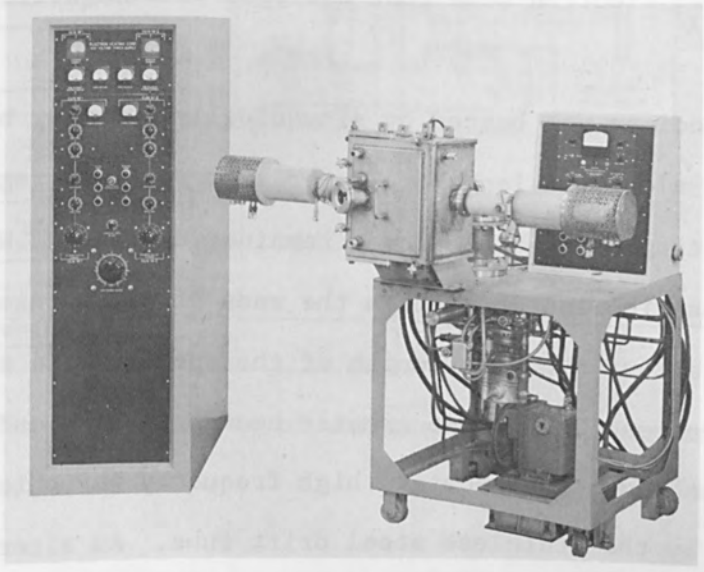

FIGURE 1a Electron Beam Tensile Furnace Shown Mounted on the Vacuum Pump Frame

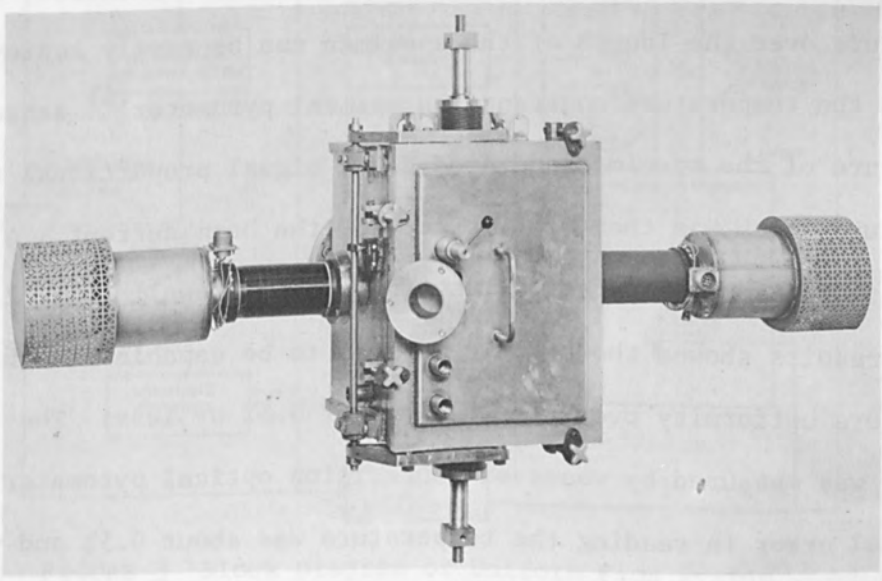

FIGURE 1b Close-up of Furnace

and water jacketed for cooling. The tensile pull rods are also stainless steel, internally water cooled and bellows sealed. There are two 5 kw self-accelerated electron beam guns equipped with magnetic deflection and focus coils.

The test specimen was heated by sinusoidally sweeping both of the electron beams along its length. The beam current was regulated so at a fixed accelerating voltage the power remained constant. With this arrangement, the conduction losses through the ends of the specimen produced a temperature gradient over the length of the specimen. A square wave sweep might have been used to provide greater heating at the ends of the specimen, except that such functions contain high frequency harmonics and these would be attenuated by the stainless steel drift tube. An alternative to this was the modulation of the beam at twice the sweep frequency, the beam current being increased at each end of the sweep. By adjusting the acceleration potential, sweep amplitude, beam current and modulation, a uniform temperature over the length of the specimen can be easily achieved. To maintain the temperature constant, an optical pyrometer[4] sensed the temperature of the specimen and produced a signal proportional to the temperature which was then used to control the beam current. A block diagram of the uniform temperature test furnace is shown in Fig. 2.

Test results showed the scanning system to be capable of achieving a temperature uniformity over the specimen of 0.5% or less. The temperature gradient was measured by means of a precision optical pyrometer. The experimental error in reading the temperature was about 0.5% and was a major difficulty in the achievement of a completely uniform temperature. Nevertheless, with reasonable care a 1% uniformity was easily obtained in practice. The automatic temperature control prevented drifting and

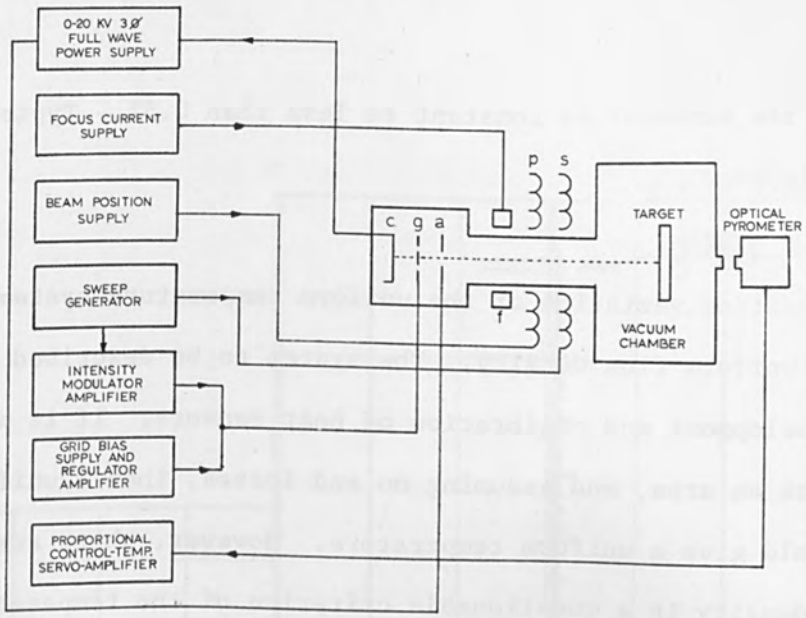

FIGURE 2 Block Diagram of Uniform Temperature Test Furnace

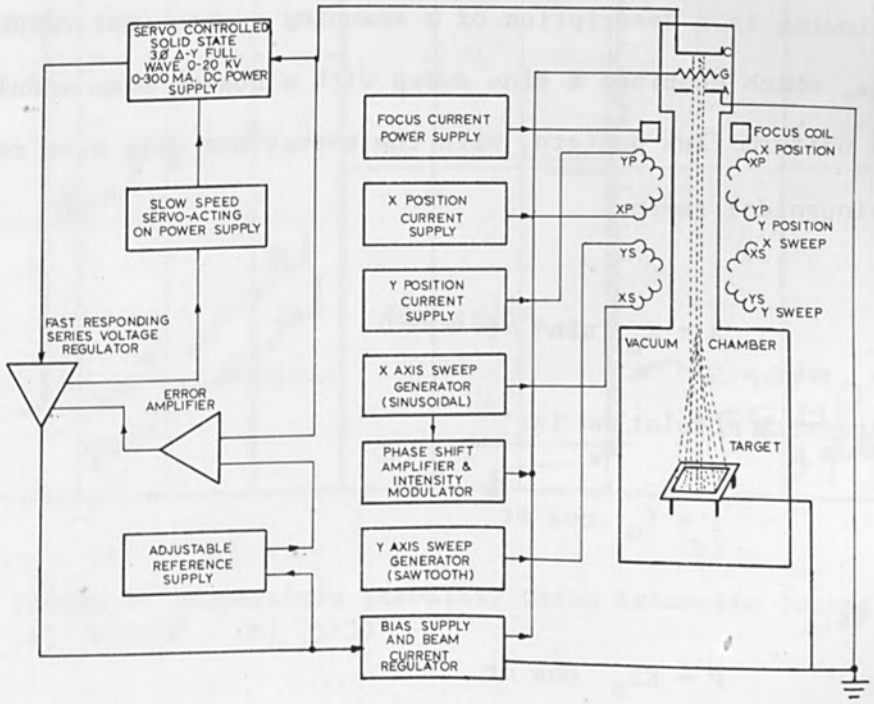

FIGURE 3 Block Diagram of Uniform Flux System

maintained the temperature constant to less than 0.5%. Typical data are presented in Fig. 4 .

UNIFORM FLUX SYSTEM

An interesting variation of the uniform temperature system is one which provides a uniform flux density. The system to be described will be used for the development and calibration of heat sensors. If it were desired to irradiate an area, and assuming no end losses, then a uniform flux density would give a uniform temperature. However, there are end losses so that flux density is a questionable criterion of the temperature uniformity. Except for the high frequency attenuation, uniform flux could be achieved in a straightforward manner with two saw-tooth sweeps at right angles and a constant beam current.

The following is a description of a scanning system, not requiring high frequencies, which combines a sine sweep with a cosine beam modulation to generate a uniform flux pattern, with the energy per unit area constant.

For a sinusoidal sweep,

$$x = x_m \sin \omega t$$

and the intensity modulation is:

$$i = I_m \cos \omega t$$

The power is:

$$P = EI_m \cos \omega t$$

Assuming a beam height or diameter of h, the area swept by the beam is:

$$A = x \cdot h = x_m \sin \omega t \cdot h$$

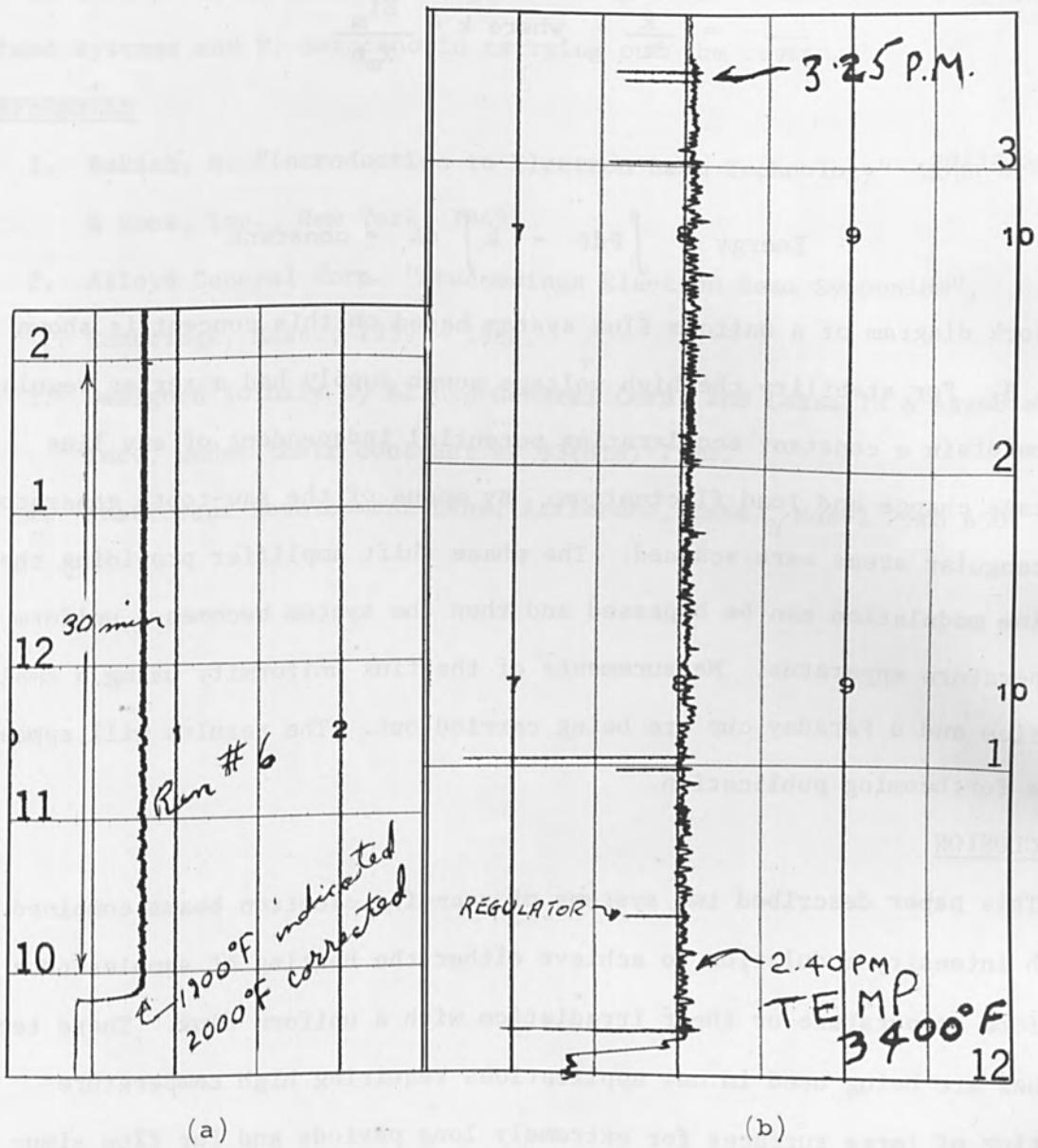

FIGURE 4 Temperature Stability Using Automatic Control
(a) 2000°F (b) 3400°F

Hence:

$$\frac{P}{dA} = \frac{k}{dt}, \quad \text{where } k = \frac{EI_m}{X_m h}$$

Integrating,

$$\text{Energy} = \int P dt = k \int dA = \text{constant}$$

A block diagram of a uniform flux system based on this concept is shown in Fig. 3. For stability the high voltage power supply had a series regulator to maintain a constant accelerating potential independent of any line voltage change and load fluctuation. By means of the saw-tooth generator, rectangular areas were scanned. The phase shift amplifier providing the cosine modulation can be bypassed and then the system becomes a uniform temperature apparatus. Measurements of the flux uniformity using a small orifice and a Faraday cup are being carried out. The results will appear in a forthcoming publication.

CONCLUSION

This paper described two systems of scanning electron beams combined with intensity modulation to achieve either the heating of samples to a uniform temperature or their irradiation with a uniform flux. These techniques are being used in new applications requiring high temperature heating of large surfaces for extremely long periods and for flux simulators for studying re-entry heating. With multiple gun systems it is possible to heat structures as large as desired. Furthermore, the heating cycle may be varied over a wide range, and programmed to meet most requirements.

ACKNOWLEDGEMENTS

It is a pleasure to acknowledge the help of J. O'Malley in designing these systems and F. Saraceno in carrying out the testing.

REFERENCES

1. Bakish, R. "Introduction to Electron Beam Technology" John Wiley & Sons, Inc., New York, 1962.
2. Alloyd General Corp. "Proceedings Electron Beam Symposium", Cambridge, Mass., 1959 - 1964.
3. Designed jointly by Alloyd General Corp. and Lessells & Associates, Inc., under their contract AF 33(616)-7554.
4. Instrument Development Labs, Attleboro, Mass., Model Pyro 650.

THERMOPLASTIC RECORDING MATERIAL SYSTEMS

Norman Kirk
Chemical Development Operation, General Electric Company
Pittsfield, Massachusetts

ABSTRACT

One form of thermoplastic recording employs a modulated electron beam to form a latent electrostatic image on the surface of a thermoplastic film. When the film was heated and subsequently cooled, the image developed as a form of diffraction grating. The thin, flexible, transparent composite tapes developed for this purpose are described. The unusual physical requirements of the tape materials are discussed and the new organic thermoplastics are disclosed.

THERMOPLASTIC RECORDING MATERIAL SYSTEMS

ELECTRON BEAM RECORDING

The high energy, high resolution, and low deflection inertia of electron beams have provided the basis for a number of information recording techniques. Electron guns can produce focused beams with energy densities greater than 100,000 w/cm^2 and with current densities of 10 A/cm^2[1]. Extremely short times were required to record measurable information elements with such beams.

The nature of these recording schemes depends upon the medium (material) which is on the receiving end of the modulated beam. In one approach, the electron bombardment produced a chemical change, such as polymerization, photochemical reaction, or polymer cross linking. Another method is to use the heat generated locally in the recording material by the focused beam spot to alter the properties of the medium. There are several recording variations in which an electrostatic charge pattern is formed by an electron beam on a dielectric surface. Electrical or xerographic readout can then be used.

Thermoplastic recording[2] is a variation of the electrostatic method which shows great promise. In this method the latent picture elements in the form of an electron charge pattern are laid down on the surface of a thermoplastic dielectric film. Subsequent heating of the film causes the surface to deform due to the electrostatic forces, to give a diffraction grating which is then frozen in place as the film cools. The information recorded in this manner is conveniently projected by means of a special optical system.

THERMOPLASTIC RECORDING PROCESS

The principle of thermoplastic recording is shown in Fig. 1. The most useful material system used to date consisted of a high melting point

transparent base tape coated with a transparent conductor, which in turn was coated with a thin film of a low melting point thermoplastic. In one possible application (television recording) the modulated electron beam scanned the thermoplastic surface horizontally while the tape motion past the recording zone provided the vertical scan. The tape was then heated to soften the thermoplastic. The thermoplastic was a good insulator and retained the charge pattern during this heating. This charge pattern was a latent image of the subject. Since a uniform ground potential was established by the conductive layer, the electrostatic forces between these charges and the conductive layer depressed the surface of the thermoplastic. The magnitude of these depressions at any point depended upon the magnitude of the charge at that location. The tape was then cooled, prior to spooling, to freeze the deformations in place and gave a permanent record. Cooling of the tape at a pressure below one micron was difficult, but gas conduction cooling at a pressure of several hundred microns in an auxiliary chamber was effective.

Conventional light optical systems which utilize differences in optical density of the transparent recording cannot be used to read out the information. The image is in the form of ripples, similar to a diffraction grating and hence the schlieren optical projection system was used and is shown in Fig. 2. In this system, a series of line light sources (slits) was imaged on a set of bars by the lens system. The recorded film was located between the condensing and projection lens. Where there were no ripples on the film, all light stopped at the bars and the screen was black. A ripple refracted light which then passed between the bars and appeared as a light spot on the screen. An extension of this system has been used to record and display color.

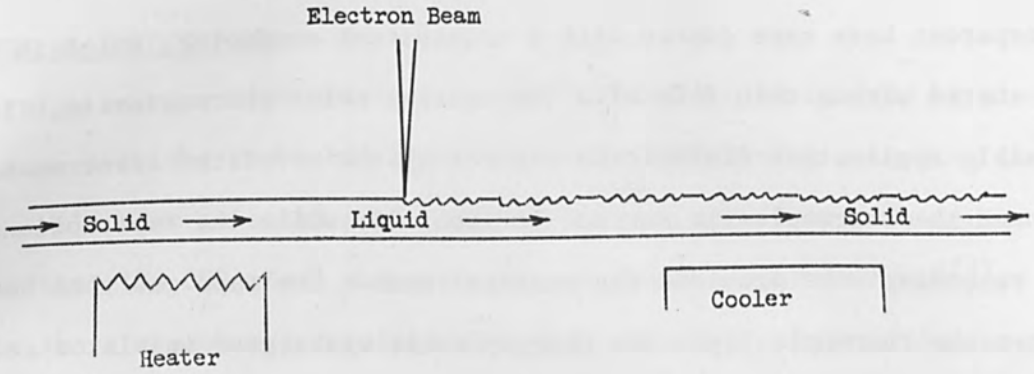

FIGURE 1 Section View of Thermoplastic Tape During Recording Process

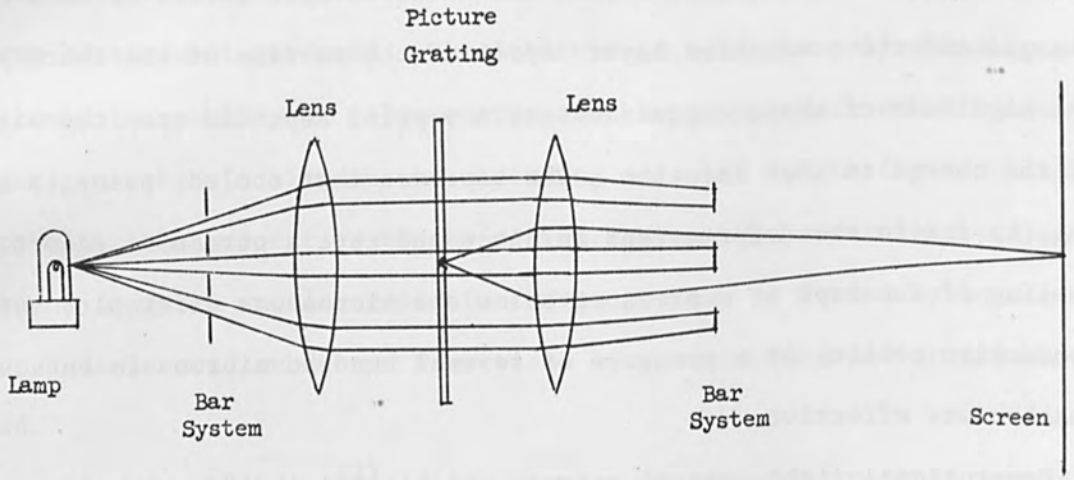

FIGURE 2 Schlieren Projection System

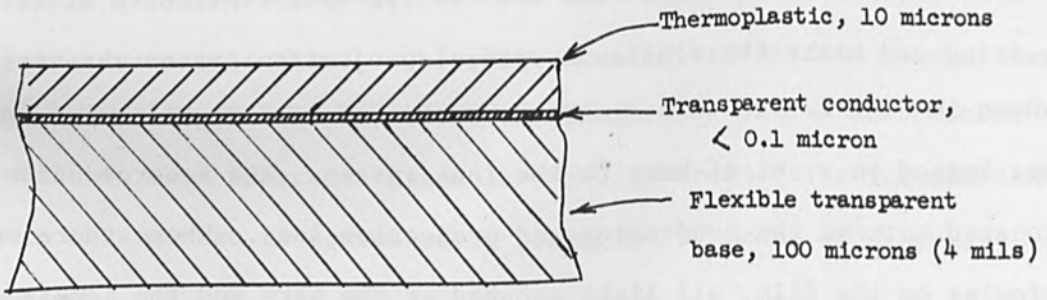

FIGURE 3 Section of 3-Layer Thermoplastic Recording Tape

The information pattern on the tape can be erased readily by heating the tape above the original development temperature for a short time. This will remove the residual electrostatic charge and permit the thermoplastic to flow and level the surface. Thus, the tape can be re-used a number of times.

LIMITING FACTORS

Three of the factors relating the electron beam to the recording medium established some important limits on the performance of the system. The first of these was resolution. This was limited by the depth of penetration of the electrons into the recording film. When penetration was a reasonable percentage of beam spot size, further spot size reduction gave no additional improvement in resolution; electron scattering prevented smaller recorded elements.

The second factor was sensitivity. This can be expressed in terms of the beam current required to produce a useful deformation of the dielectric thermoplastic surface, and is approximated by the following equation:

$$I = \frac{4 \times 10^{11} A \sqrt{N}}{Wt}$$

where:

I = beam current, amperes

A = raster area, cm^2

N = diffraction order accepted by the center of the slot in the schlieren bar system

W = wave length of charge pattern, for example, distance between raster grooves, cm

t = frame time, seconds.

Beam currents of about 1 μa. at 7.5 kv were typical. Useful deformations were obtained after exposure to such beams for about 10^{-8} seconds.

The third factor, which may establish an ultimate limit, was the effect of radiation dosage on the physical properties of the thermoplastic. At the outset, there was some concern over radiation-induced chemical changes which could impair the performance of the thermoplastic. The materials developed for the present work readily withstood the equivalent of 10 to 15 minutes of continuous exposure to the beam described above. This was equivalent to about 20,000 exposures at a rate of $1/30^{th}$ sec/frame, or a total does of 10^9 rads (1 rad = 100 ergs/gram).

THERMOPLASTIC RECORDING MATERIALS

The first thermoplastic recording experiments were done on stationary, 3-layer glass slides. The glass served solely as a support and had a transparent conductive coating of tin oxide beneath the thermoplastic layer. This system had a high optical quality, but its rigidity limited its usefulness to single frame applications. Flexible tape was the obvious need, and the structure shown in Fig. 3 was developed. The glass base was replaced by a flat, transparent, flexible, tough plastic tape so that continuous exposure and display was possible. The function of the conductive and thermoplastic layers remained the same, but each of these had to meet the flexibility requirements. The component layers developed for these flexible recording tapes will be described in the following sections.

THERMOPLASTIC WORKING FILM

The thermoplastic was the most important functional component in the tape system. A thin film, usually 5 to 15 microns thick, of the thermoplastic was the target of the electron beam. The behavior of this film to a large

extent established the performance capabilities of the entire recording system. Although early successful demonstration experiments were done using a mixture of polyethylene and paraffin, a much more sophisticated material was required for useful applications.

The physical property requirements for a good recording thermoplastic were formidable. Some of the more important factors are listed:

Transparency: - Optical clarity and transparency are essential. The film should be free of light-scattering haze and should be nearly water white.

Electrical Resistivity: - High electrical resistivity is required, preferably greater than 10^{11} ohm-cm while in the liquid state during the recording-developing process.

Radiation Stability: - The thermoplastic layer must be stable under moderate electron bombardment.

Melting Point: - A fairly sharp melting point is important for the proper development of the image. For example, the thermoplastic should be solid at a temperature of at least 65°C but should be convertible to the liquid or fused state at about 85°C. Higher temperature levels will depend upon the development of higher melting point backing tapes. The electrical resistivity of thermoplastics decreases at higher temperature which will ultimately determine the operational limits.

Sticking: - When incorporated into a tape rolled upon itself, the thermoplastic must be non-tacky. It should not stick to any other surface with which it may come in contact during use.

Adhesion: - On the other hand, the thermoplastic must adhere well to the supporting backing. Usually this means that it should adhere to

the conducting layer carried on the base tape.

Flexibility: - Thermoplastic tapes must be sufficiently flexible and strong to be wound around the 1/2" to 1" dia. sprockets and rollers encountered in recording and projection equipment. Crazing or spalling of brittle thermoplastic will introduce serious flaws into a recording.

Cold Flow: - To insure permanence of the recorded information, the thermoplastic layer must be free from any cold flow on storage. Since storage at temperatures up to 40°C or 50°C was foreseen , cold flow must not exist even at these temperatures. Cold flow is a slow form of erasure and its effects were accelerated when the tape was rolled upon itself.

Vapor Pressure: - The thermoplastic in the liquid state should have a vapor pressure below 10^{-5} Torr to be satisfactory for use in electron beam recording equipment.

This demanding list of requirements set off a thorough search for suitable thermoplastics already available on the market, but no completely satisfactory material was found. Hundreds of formulations were tested. Excessive cold flow was the most common deficiency in an otherwise satisfactory commercially available material. Also, some of the simplest and most available materials, such as polystyrene, gave excellent recordings but were brittle and would not adhere to flexible tape. One possible reason for the shortcomings of commercially available thermoplastics was that the properties needed for this application required polymers in a molecular weight range which had no use in other known polymer applications. The proper material was not available.

New materials were developed by original synthesis and formulation.

One successful formulation[3] was an alloy of a specially synthesized diphenyl silicone and a newly developed phenylene ether polymer.

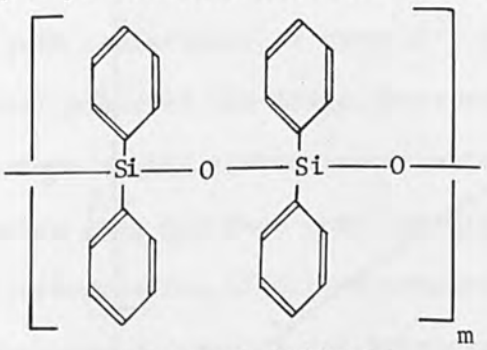

Diphenyl Silicone

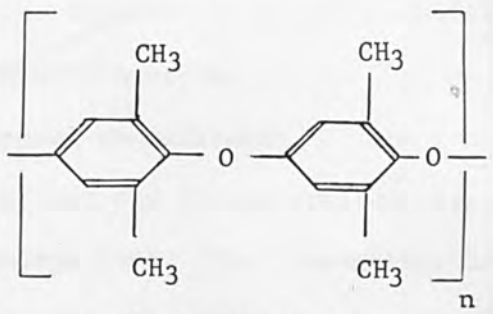

Polyphenylene Oxide

This combination was particularly resistant to cold flow. Recordings made on tape coated with about 10 microns of this formulation were tested for storage life of the image as a function of temperature. Two months storage at 50°C effected complete erasure, but at 30°C, the erasure time extrapolated to many years. Some recordings on this type of thermoplastic have now been stored at room temperature for four years without significant loss of image definition.

A typical viscosity-temperature curve for this new thermoplastic alloy is shown in Fig. 4. For this particular material the working range during the recording-developing process was between 5×10^5 and 5×10^7 centipoise. Other compositions having even higher viscosities have been used. Even with these viscous coatings, image development was easily achieved within one second. As mentioned previously, erasure was readily accomplished by heating to the development temperature or higher for a time which was at least 50 to 100 times longer than the time required for the initial development. This was a very approximate value, since the time-at-temperature for complete erasure depended upon the depth to which the pattern was indented.

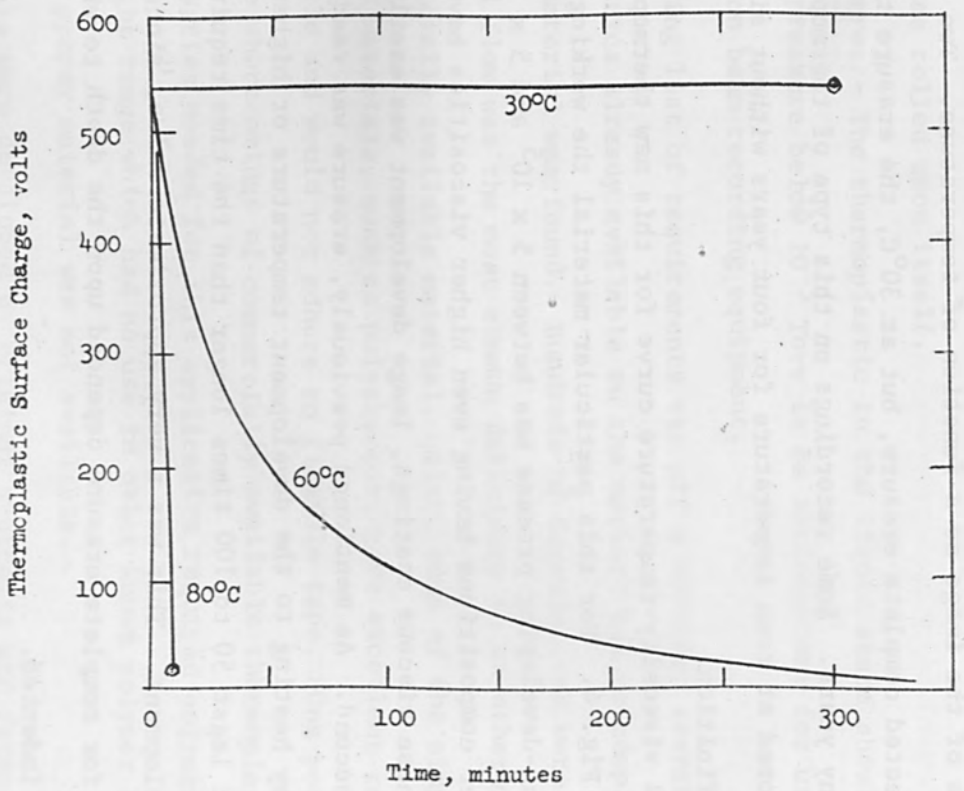

FIGURE 4 Melt Viscosity of Thermoplastic for Thermoplastic Recording

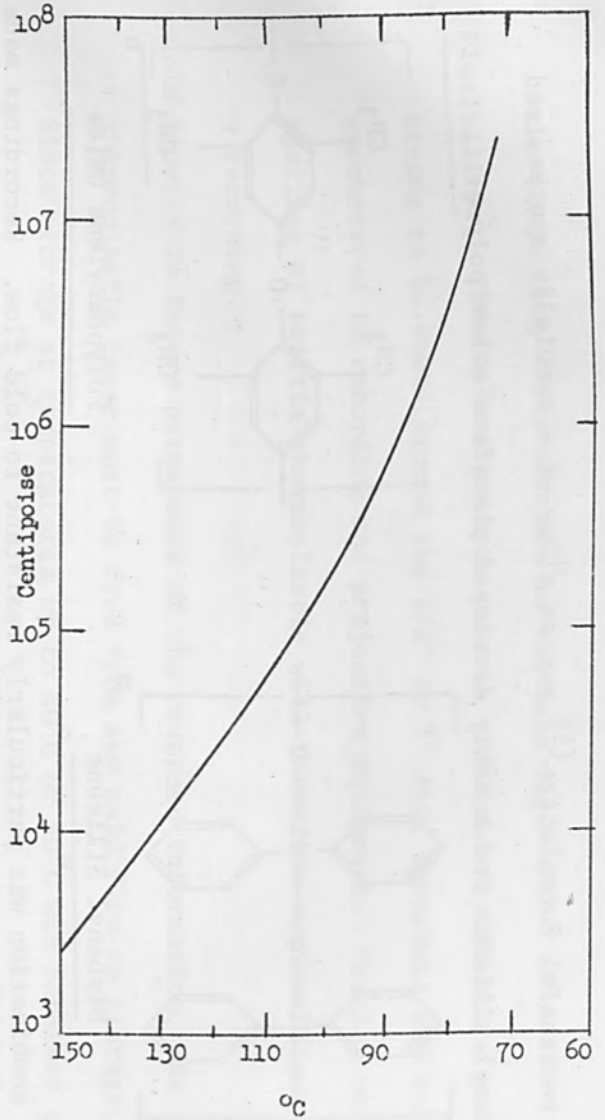

FIGURE 5 Charge Leakage from Thermoplastic Surface

The electrical resistance of the thermoplastic was an important factor in its ability to retain the charge pattern for a useful time interval. A bulk resistivity of over 10^{11} ohm-cm in the "liquid" state was required. Development of the image depended on the retention of the charge in the surface of the thermoplastic at the development temperature. If the charge leaked away too fast then the picture was either dim or was erased. Fig. 5 illustrates the effect of temperature on charge loss. The time-charge loss relationship imposes one potential upper limit on the melting point of useful thermoplastics; the other physical properties may be excellent, but poor electrical properties at a higher temperature will produce a poor recording.

The thermoplastic described above is a mechanical blend of two different but physically compatible materials. Other thermoplastics synthesized and used during this development program were copolymers or terpolymers, rather than blends. By adjusting the ratios of the reactants and the reaction conditions for these polymerizations, materials having the special properties required for recording were tailored. Examples of polymers found to be effective were styrene-butyl methacrylate copolymers, styrene-butadiene-methyl acrylate terpolymer, and bisphenol A-adipate polyester.

Conductive Coating

The transparent conductive coating provided primarily a uniform electrical ground plane permitting fidelity in the recording. To obtain high quality diffraction patterns with good contrast and gray scale capabilities required the use of this ground plane. This conductor was also used as a resistance heater and as a pick up for RF induction heating. Service as a heater imposed a much more severe requirement on the coating than did its use as a ground plane.

Vacuum-deposited films of chromium or nickel-chromium about 35 Å in thickness are about 65 to 70 percent transparent in the visible range and have resistances between 1000 and 10,000 ohms per square. The resistance level is not critical for recording, but it must be closely controlled if the chromium is to be used as a heater.

Cuprous iodide films made by vacuum depositing copper onto the tape base and then treating with iodine vapor under controlled conditions[4] resulted in a conductor which was over 90 percent transparent and had a resistivity above 1500 ohms per square. High quality recordings have been made on tapes using this conductor.

Tape Bases

Two different kinds of tape have been developed, the difference being in whether the readout system transmited light through the tape or reflected it from the tape surface. In either case, the functional thermoplastic film was supported by a strong, dimensionally stable base tape. In many respects this base was the limiting factor in picture quality.

The following criteria had to be met by base materials useful for transmissive tape:

High tensile strength at temperatures up to 130°C was required in order to permit signal development without distortion of the tape.

Dimensional stability during heating, or because of changes in moisture content was required. The tape should not shrink or swell.

Flexibility to travel over rollers and sprockets in equipment.

High optical quality was essential. Light scattering from physical imperfections on the surface or within the bulk of the tape was readily discernible by the schlieren optical system. These appeared on the screen as background spots, or "noise". This was a much more demanding service

than for ordinary photography.

Resistance to moisture and to solvents used in coating the thermoplastic on the base tape was necessary for the fabrication of useful 3-layer recording tapes.

The best transmissive tape base used to date was duPont's Cronar* polyester 4 mil thick photofilm base. Cronar showed essentially no adsorption in the visible spectrum. It adsorbed chiefly in the UV, 0.35 microns and below, and above 2.2 microns in the infrared. Mylar* can be used, but the optical quality was not as good as that of Cronar. The haze in Mylar was readily observed as a gray, rather than black, schlieren dark field. Cellulose acetate had fairly good optical quality, but its strength, dimensional stability, and moisture behavior were poor. All other transparent plastics were found to have such poor optical quality that they were unusable, regardless of their other properties.

Cronar was made into a high quality flexible mirror by vacuum metallizing with aluminum or silver. The thermoplastic working layer was then precision-coated by solvent casting directly onto the mirror surface. This gave a high quality reflective tape. Some advantage was obviously gained by using the mirror to hide blemishes in the base bulk and on the back of the base, thus decreasing the background noise.

The two disadvantages of Cronar were its 4 mil thickness and its 130°C working temperature limit. It was found possible to make useful reflective tapes with 1 mil stainless steel or phosphor bronze ribbon as the base. These had excellent dimensional stability, mechanical strength, and give a fourfold increase in storage density. However, careful topical coating was

---

*Trademark of E. I. duPont deNemours & Co., Inc.

required to prepare these metallic surfaces for service as high quality flexible mirrors.

PILOT TAPE PRODUCTION

These recording tapes are currently being developed and produced in a pilot plant using specially developed precision coating procedures. Continuous, long film runs are made to give tapes uniform in quality and performance. Particular care is taken to operate in a dust-free environment. Every effort is made to handle the tapes carefully at every stage in manufacture in order to prevent scratching and other mechanical marring of the surface. The pilot plant is capable of making finished tapes up to 70 mm in width.

REFERENCES

1. Glenn, W. E. and Wolfe, J. E., International Science and Technology, p. 28 (June, 1962)
2. Glenn, W. E., Journal of Applied Physics, Vol. 30, p. 1870 (December, 1959)
3. Boldebuck, E. M., U. S. Patent 3,063,872 (1962) (to General Electric Co.)
4. Herrick, C. S. and Tevebaugh, A. D., J. Electrochem. Soc., Vol. 110, p. 119 (Feb, 1963)

AN EVAPORATION FACILITY FOR THIN FILMS

T. R. S. Goel, E. G. Whitaker and D. W. McManaman
Delco Radio Division, General Motors Corporation
Kokomo, Indiana

ABSTRACT

A facility is described for the evaporation of thin films by electron beam and resistance heating. The facility incorporated most features necessary for controlled evaporation, and included for example, multiple evaporation, multiple sources, source to substrate distance variation, thickness and resistance monitors, rate of evaporation monitor, glow discharge cleaning, and shielding. A typical circuit is described for producing and evaluating the passive elements. A discussion is presented concerning the avoidance of pin holes in films.

AN EVAPORATION FACILITY FOR THIN FILMS

INTRODUCTION

An evaporation facility was developed to fabricate thin film circuits in a single pump down and contained both a self-accelerated electron beam gun and a resistively heated source for evaporation. The system was used in the mid 10^{-7} Torr range. The facility had the following features:

1. Independent or dual evaporation of six materials with electron beam and four locations for resistance heating.
2. Six 2" x 2" substrate locations and accommodation for all sizes smaller than this.
3. Six masks and six substrate locations with independent motion and accurate registration.
4. Variation of source to substrate distance from three to twelve inches.
5. A substrate heater with a temperature monitor.
6. A film thickness monitor.
7. A rate of evaporation monitor for use before or during evaporation.
8. A resistance monitor.
9. Glow discharge cleaning.
10. Sources for dielectric evaporation.
11. Complete shielding so that only one substrate was exposed at a time.
12. Flexibility to permit use as a pilot line for production.

Thus, the facility included most of the features of the evaporation jigs or facilities described in the literature[1,2,3,4,5], and allowed controlled evaporation of a much broader variety of thin films.

MECHANICAL CONSTRUCTION

The jig was designed to withstand the temperatures developed during electron beam evaporation; to be easily cleaned; and to provide adequate

shielding in order to keep contamination of the system to a minimum.

Essentially, it consisted of six stainless steel concentric plates. The framework and support of the structure was provided by the top and the bottom plates and three supporting rods (Fig 1). The rods were screwed through the bottom plate and provided legs which were seated in shallow holes in the vacuum system base plate. The source table rested on a brass plate and was chain driven. The brass plate was water cooled by a copper spiral welded to its underside. Indexing of the source to a position was provided by a spring loaded ball and notch arrangement, and sections of the source table were shielded from each other by radial fins which divided the source plate into six segments(6). The current contacts for the resistively heated filaments was provided by Inconel X spring loaded communtators. Above the source plate was a shield plate with an opening directly above the evaporation position. Two quartz crystals were mounted on its underside in the path of the evaporant stream which provided for the monitoring of the thickness and the rate of evaporation. The main shutter to close the opening in the shield plate, and the crystal shutter to close the opening in the crystal box were also mounted on this plate.

The mask and substrate plates were similar to those of Ref. 1 , but the mechanism was suspended entirely from the top plate thus leaving room for entry of the beam, the cooling lines and other accessories. In addition, such suspension permitted a variation in the source to substrate distance by simply raising or lowering the top plate.

The mask plate was located above the shield plate and was fastened to a large stainless steel nut. The drive screw passed through the nut and as it was turned the mask plate lowered away from the substrate plate. As the mask plate cleared the locating pins, a pick up arm at the end of the screw

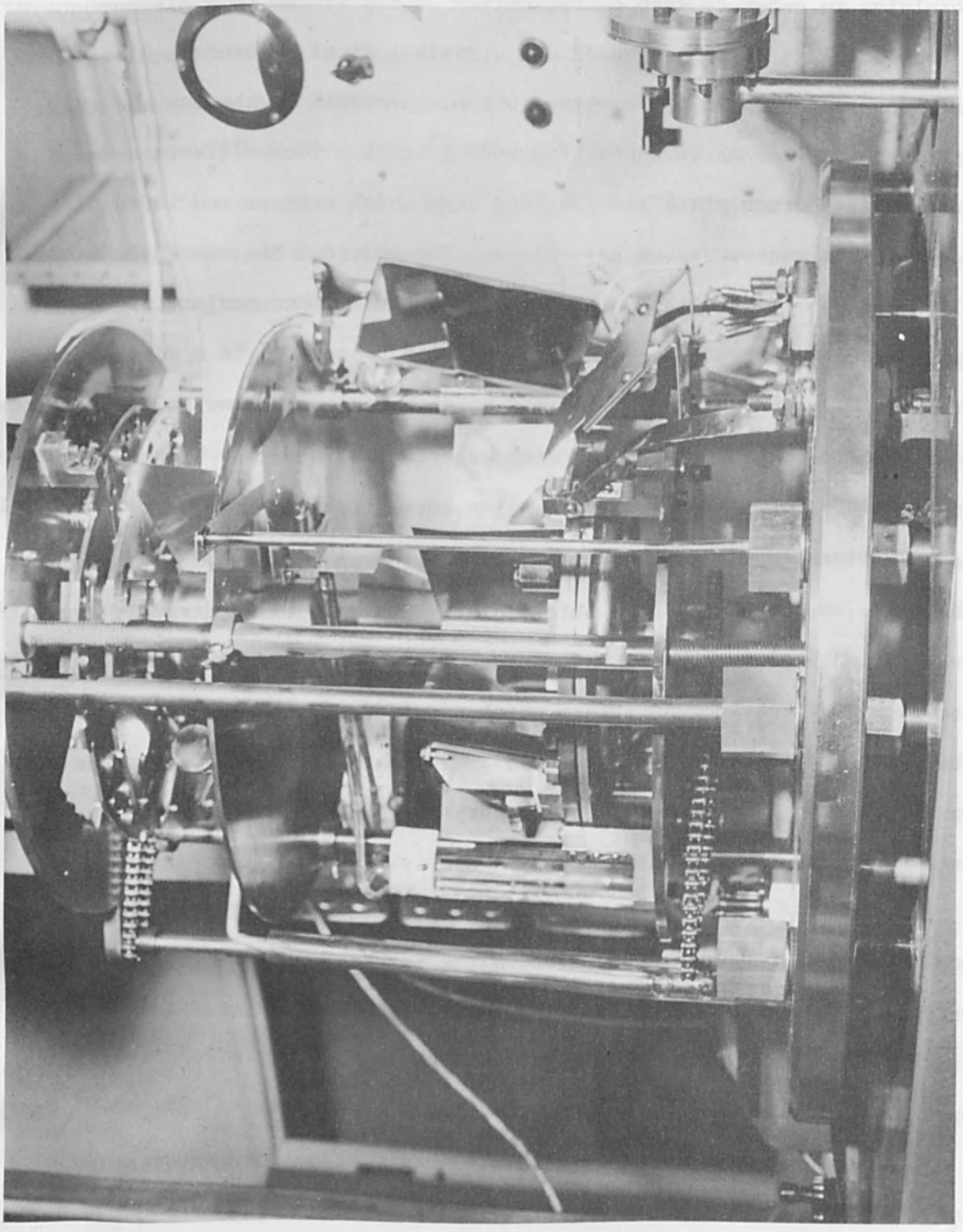

FIGURE 1 Evaporation Facility

engaged a pin in the nut and rotated the mask plate to the next position. The mask plate can be again raised to bring it in contact with the substrate plate. Preliminary registration was provided by a spring which engages in a notch cut in the substrate and mask plates. Accurate registration was provided by jig bored holes and two tapered pins.

Substrate Size

Location was provided for six two inch square substrates or half inch square substrates. The thickness and the material of the substrate was not a limiting factor.

Masks

Six mask positions were provided, and therefore, it was possible to make a six layer device on a single substrate. The masks were made from either metal or graphite. The thickness of the masks was not a limiting factor, and could be milled out or etched out by the conventional techniques. Etched molybdenum masks, 5 mil in. thickness, are used, and have been found to be quite free from the warpage. The registration of the successive masks has been found to be 0.0002".

Sources

The source plate had six segments (Fig. 2). Each segment had up to three sources to provide for triple evaporation. Of these two are evaporated by electron beam heating and third by resistive heating, from boron nitride crucibles. For the evaporation of materials in powder or sponge form, a special chimney was constructed, (Figs. 3 and 4), to avoid the evaporation of the macroscopic particles which cause pin holes. A comparison of this arrangement and a Drumheller Source will be discussed later. Vergara, et al[7] used similar sources with resistive heating. Essentially, this source provided a secondary evaporation from a heated

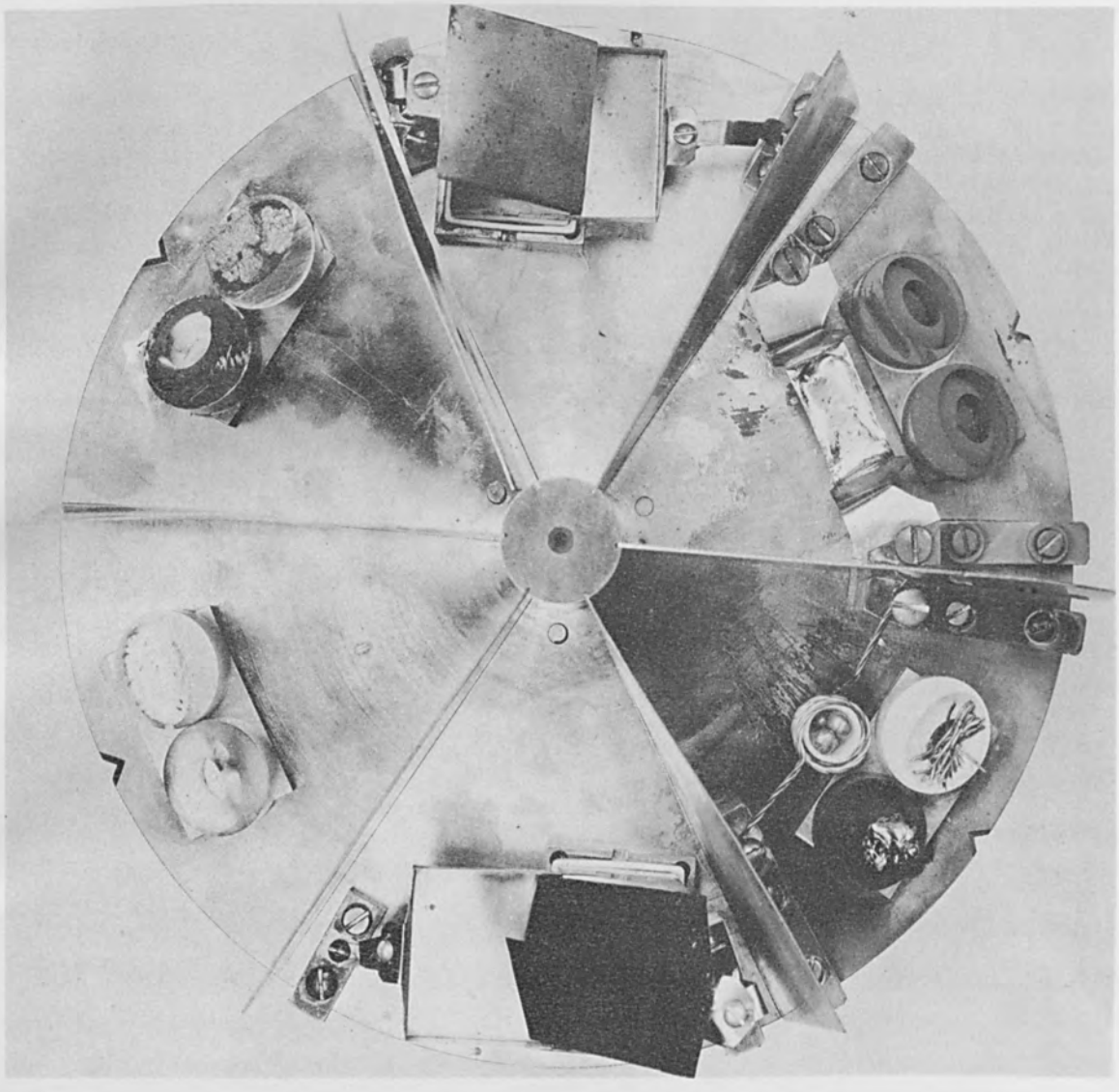

FIGURE 2 Source Plate

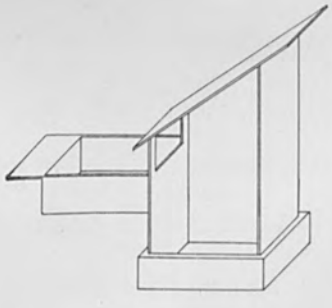

FIGURE 3 Dielectric Sources

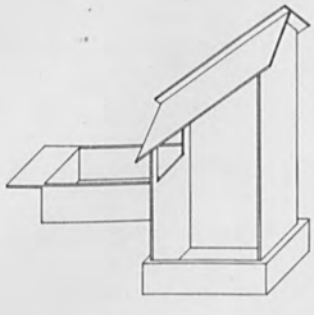

FIGURE 4

tantalum structure. The tantalum structure was welded, 5 mil thick tantalum sheet, and was approximately 1" x 1" x 2" in size. The input power to heat the structure was varied from 1 kw to 3 kw, to provide a structure temperature higher than that at which the evaporant vapor pressure was greater than 1 micron. Both types of structure are shown, and it was found that the evaporation rate using the chimney type was about 50% greater than for the first type for the same power input. This was due to the fact that the collimated evaporant stream was used more efficiently (Figs. 3 and 4).

SUBSTRATE HEATER

There were two 2.5" x 2.5" sandwich type substrate heaters (Fig. 5). Each heating element was a 5 mil thick, etched out, molybdenum spiral. The substrate temperature was measured by a Pt/Pt-Rd thermocouple situated in a shallow hole on the top plate of the heater assembly. The exact temperature of the substrate was then determined from a calibration curve between the temperature of the heater and that of the substrate. The temperature difference was less than $10^{o}C$. The temperature of the substrate was controlled by connecting the thermocouple to a Weston temperature controller.

GLOW DISCHARGE CLEANING

The final cleaning of the substrate was usually done by glow discharge just before evaporation. Holland[8] reported that if the substrates were placed in the positive column of a glow discharge, the best cleaning effects were obtained. This facility incorporated a hollow cathode[9]. The films obtained after cleaning the glass with glow discharge showed somewhat better characteristics than without it. However, the difference noticed was not very significant.

RESISTANCE MONITOR

The resistance of the deposited films were determined by monitoring test

slides, which were located next to the substrate holder so that temperature effects on the resistance were compensated. The resistance of the test slides formed one arm of a Wheatstone bridge and activated the main shutter when a preset value for the resistor was reached. The preset value was obtained from a ten turn helical potentiometer forming the opposite arm of the bridge (Fig. 6). The null indicator was a relay. As the deposition started the bridge was completely unbalanced and returned to the balanced condition as the deposition occurred. Once the bridge was balanced, the meter relay indicating contact returned to zero (the set point) and activated the second normally closed relay which closed the main shutter. Resistors have been deposited from 10 Ω to 100 k Ω with 1% accuracy. The bridge had a very low power dissipation. Figure 7 shows the current through the relay as a 500 ohm resistance was changed by $\pm$ 5 Ω. This indicates a 26 μv change per ohm, while only + 13 μv were necessary to keep the relay open. Therefore, in this resistance range the accuracy in the bridge was about 0.1%.

THICKNESS AND RATE MONITOR

The thickness of the films and the rate of evaporation was monitored by a pair of piezoelectric crystals. Similar techniques have been used by other investigators with different circuitry[10,11,12,13]. The beat or hetrodyne system was used to achieve a usable audio frequency range. The system consisted of three parts (Fig. 8).

Frequency Shift Monitor

This included two quartz crystal oscillators, both of which had a nomi-al radio frequency of 5 megacycles, a radio frequency mixer with an audio frequency output, a buffer amplifier stage, and a high pass LC filter. The two crystals (AT cut) were solidly mounted side by side in the evaporant

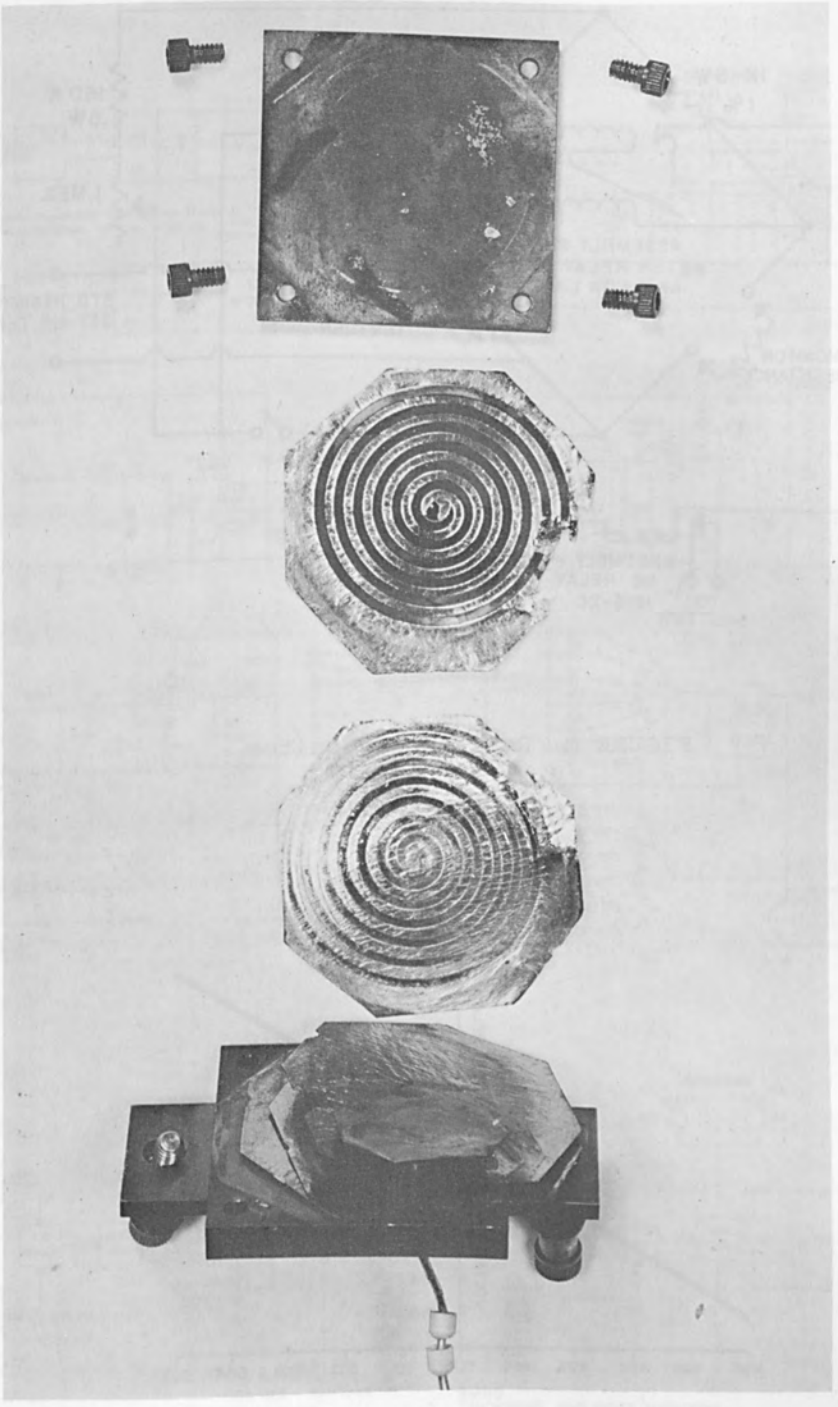

FIGURE 5 Substrate Heater

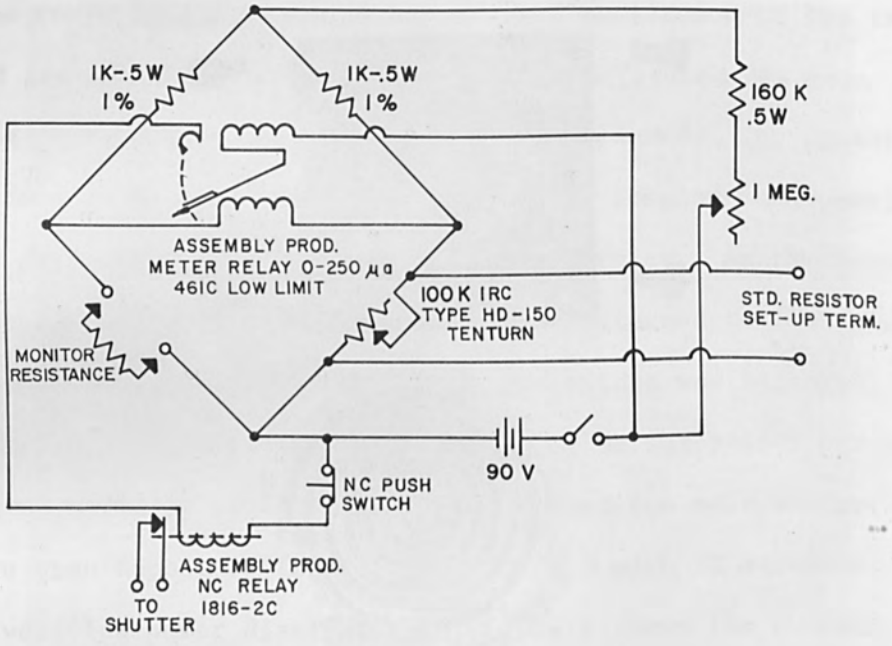

FIGURE 6 Resistance Monitor

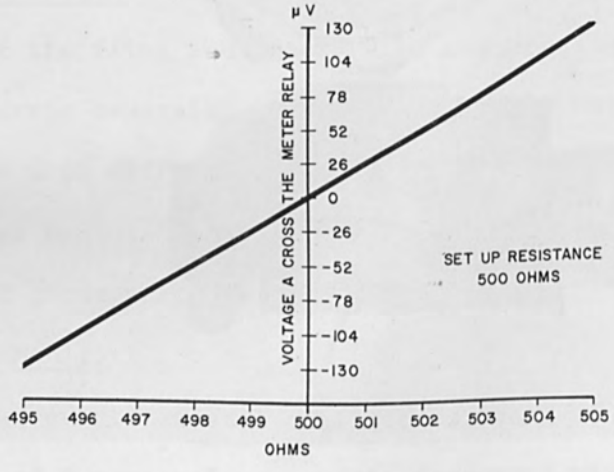

FIGURE 7 Sensitivity of the Resistance Monitor

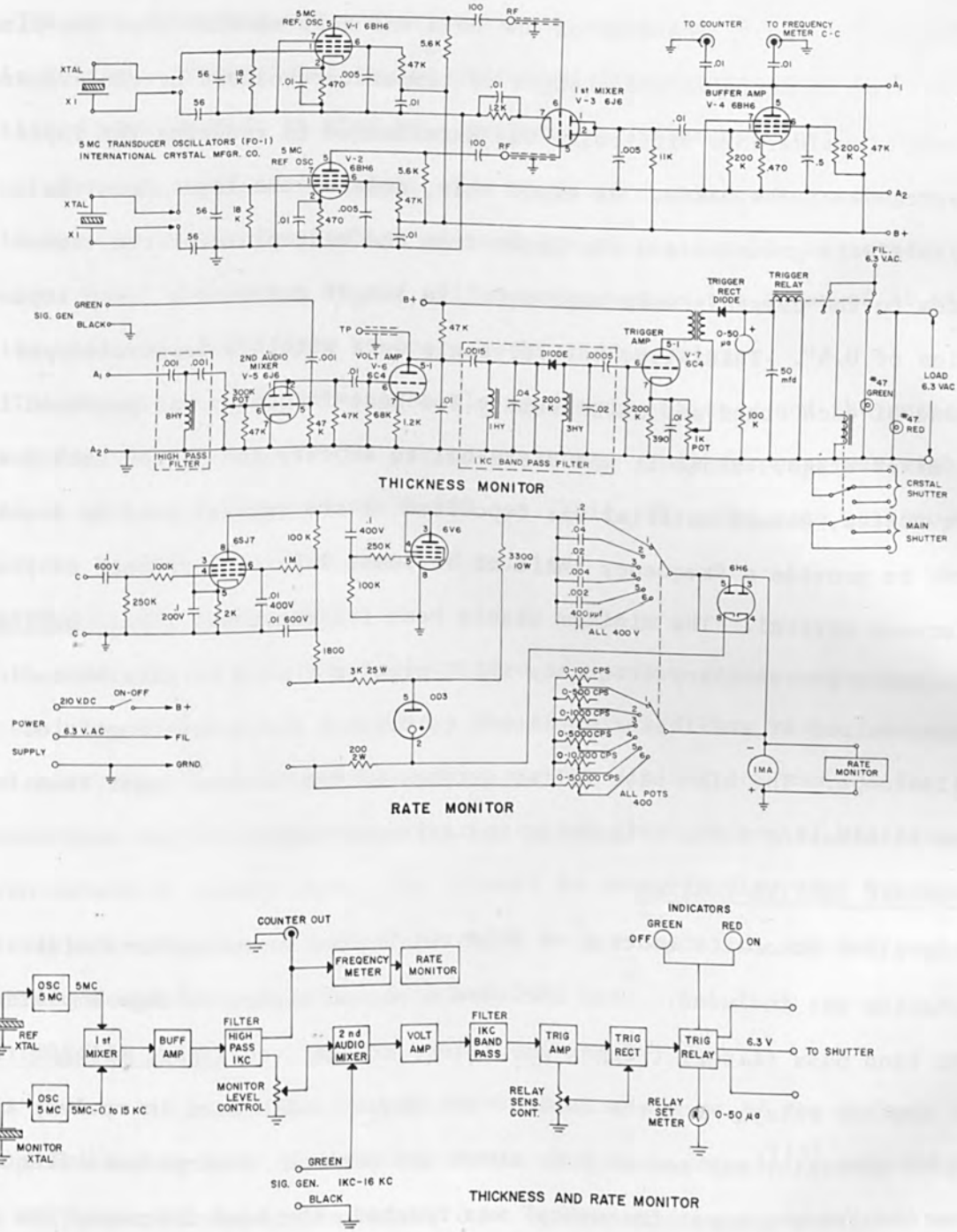

FIGURE 8 Circuit for Thickness and Rate of Evaporation Monitor

stream to eliminate temperature and pressure differences. One of the two crystals was completely enclosed while the other had a 1/8" hole at the center of its case. The size of the hole was kept smaller than the size of the crystal to minimize the changes of temperature caused by the evaporant stream. Considerable difficulty was experienced in reducing the input capacitance of the leads. To avoid this, none of the leads from the crystals were grounded and the leads from the base plate of the vacuum system to the crystals were kept equal in length and with a fixed separation of 0.5". Initially, both crystals were within a few cycles per second of each other and an extremely low beat frequency was produced in the mixer stage. Since it was difficult to amplify and filter such low frequencies, enough material was deposited on the crystal used as transducer to provide a frequency shift of at least 1 kc with respect to the reference crystal. The minimum usable beat frequency was 1 kc. During the deposition process, any frequency shift greater than 1 kc gave an audio frequency output of sufficient amplitude to drive a frequency counter or osilloscope. The high pass filter attenuated frequencies lower than 1 kc, thus eliminating false triggering and erroneous shift.

AUTOMATIC SHUTTER CONTROL

To allow automatic control of film thickness, an automatic shutter mechanism was included. This included a second mixer, voltage amplifier, 1 kc band pass filter, trigger amplifier, trigger rectifier, trigger relay and shutter relay. For the desired thickness (calibrated in cycles) the signal generator was set at 1 kc above the desired "stop-process frequency". When the "stop-process frequency" was reached, the beat frequency was 1 kc and was passed by the filter. This signal was amplified, activated a sensitive trigger relay, closed a direct current relay, and through an a.c.

power relay controlled the shutter in the bell jar.

Rate Monitor

The beat frequency was converted into a voltage by a frequency meter. This voltage, proportional to the deposited film thickness was then differentiated with respect to time by a mechanical differentiator[14] and so indicated the rate of evaporation. The range of the frequency meter was 0-50,000 cps in six steps which allowed for a considerable adjustment to the sensitivity. The output at the milliammeter was on the order of 50 millivolts which was sufficient to operate the differentiator.

The frequency readings were stable to within $\pm$ 5 cps, and the response was quite reproducible over a period of hours. This response was stable even at the beat frequency of 50,000 cps. (Fig. 9). The rate monitor was accurate to within $\pm$ 1% on repeated trials.

PERFORMANCE OF THE FACILITY

In order to evaluate the registration of various passive elements, a "School Boy Circuit" was designed. The circuit had four masks, one for resistors, one for bottom electrodes, one for dielectric, and one for interconnections and top electrode. This provided seven values of resistance and seven values of capacitance. The circuit is shown in Fig. 10. Various materials in single and dual evaporation were evaporated, and the registration was found to be accurate within 0.0002".

PIN HOLES IN FILMS

A systematic study was done to determine the causes of the defects in SiO films and methods of avoiding them. Jorgenson, et al[15] pointed out six different causes of pin holes; dust on the substrate, foreign materials on the substrates, volatile gases from the heated substrate, difference in thermal expansion coefficients of the film and the substrate, mechanical

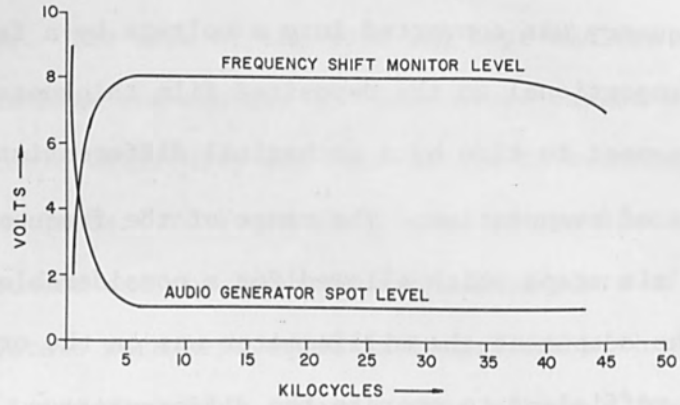

FIGURE 9 Sensitivity of the Thickness Monitor

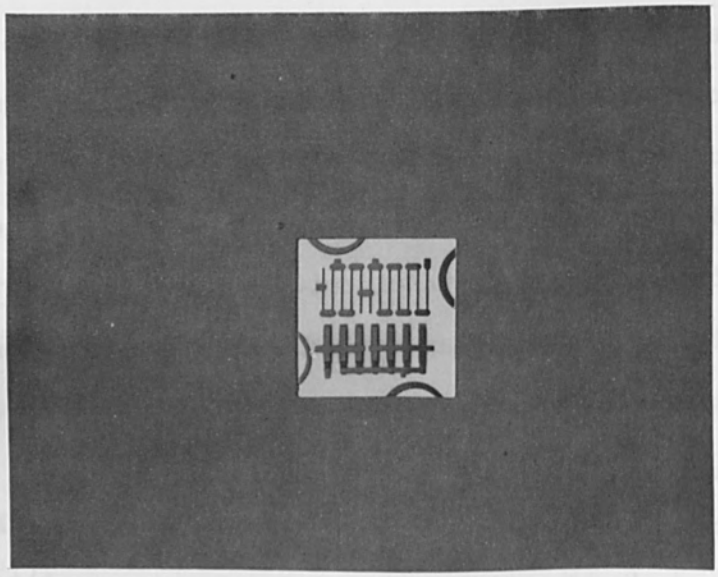

FIGURE 10 "School Boy Circuit"

stresses in the film, and macroscopic particles in the evaporation stream. Of these, three could possibly be eliminated by proper substrate and evaporant materials and one by proper design of a source. Jorgenson evaporated both hard and soft materials onto various types of substrate and showed that the thermal expansion coefficient difference, or the mechanical stresses in the films, do not make a major contribution to the cause of pin holes in films. Three cleaning procedures were tried on alumina substrates. There were:

1st Procedure:

10 minutes hot trichloroethylene, ultrasonically

10 minutes rinse, demineralized water, ultrasonically

10 minutes 50% HCl, 50% HNO_3

10 minutes rinse, demineralized water, ultrasonically

5 minutes rinse, methyl alcohol, ultrasonically

Dried in dust free box.

This procedure was intended to remove any foreign materials from the substrate.

2nd Procedure:

Same as 1st procedure except that it was preceded by a scrub with alconox and hot water. This procedure was intended to remove the dust and foreign material from the substrate.

3rd Procedure:

Same as 2nd procedure, but followed by glow discharge cleaning in the bell jar at an Argon pressure of 200 μ Hg for 15 minutes at 100 ma. This procedure was intended to remove all possible contamination from the surface of the substrate.

Capacitors deposited on substrates cleaned using the 2nd procedure had

breakdown voltages greater than those made on substrates cleaned by the 1st procedure. No significant difference was found between procedure 2 or 3. Therefore, dust seemed to be the major detrimental factor, while volatile gases from the surface of the substrate did not have any appreciable effect.

To establish the effect of macroscopic particles, SiO was evaporated from the sources described in this paper and also evaporated from a Drumheller source during the same pump down and under similar evaporation conditions. It was found that at the low evaporation rate of 1.5 $\mathring{A}$/sec, the breakdown voltages were similar; but, as the evaporation rate was increased to 100 $\mathring{A}$/sec, then a greater breakdown voltage was found for material evaporated with the sources described in this paper than with the Drumheller source. At this higher evaporation rate, the energy of the macroscopic particles is apparently enough to cause pin holes in the films.

CONCLUSION

An evaporation facility has been described that was a versatile tool for thin film evaporation research. The facility functions well and resistors and capacitors were made by controlled evaporations. A discussion was presented covering the possible causes and methods of removing pin holes in dielectric films.

ACKNOWLEDGEMENTS

The authors thank R. F. Miller and F. S. Stein for many helpful suggestions, R. Hendrix for making the thickness monitoring apparatus, H. Pefley for making the resistance bridge, Barbara Cassis for reading and typing the manuscript. Acknowledgements are also made to C. L. Meyer for consistent encouragement in the preparation of this paper, and to Delco Radio for the permission to publish this paper.

REFERENCES

1. Steckelmacher, W., et al., 10th National Vacuum Symposium, Macmillian Company, 1963, p. 415.
2. Riddle, G. C., 4th Electron Beam Symposium, Alloyd Electronics, Boston, 1962, p. 340.
3. Moore, D. W., 4th Electron Beam Symposium, Alloyd Electronics, Boston, 1962, p. 324.
4. Caswell, H. L., 10th National Vacuum Symposium, Macmillian Company, 1963, p. 393.
5. Caswell, H. L., et al., 9th National Vacuum Symposium, Macmillian Company, 1962, p. 138.
6. Simmons, J. G. and Moister, D. E., Reviews of Scientific Instr., 33 978 (1962).
7. Vergara, W. C., et al., Reviews of Scientific Instruments, 34 520 (1963).
8. Holland, L., British J. Appl. Physics, 9 410 (1958).
9. Van Passen, H., Reviews of Scientific Instruments, 32 871 (1961).
10. Behrndt, K. H., and Love, R. W., Seventh National Vacuum Symposium, October 12, 1960, Cleveland, Ohio
11. Thun, R. E., et al., Automatic Control, 26, February 1961.
12. Lins and Kukuk, Seventh National Vacuum Symposium, October 12, 1960, Cleveland, Ohio, p. 333, (Pergamon Press 1961).
13. Warner, A. W. and Stockbridge, C. D., Vacuum Microbalance Technique, Ed., K. H. Behrndt (Plenum Press Inc., New York).
14. Oberg, P. E., Reviews of Scientific Instruments, 34, 1055 (1963)
15. Jorgenson, G. V. and Wehner, G. F., 10th National Vacuum Symposium, MacMillian Company, 1963, p. 388.

A CONTROLLED RATE ELECTRON BEAM EVAPORATOR

Paul R. Payne, Jr.
Alloyd General Corporation
Cambridge, Massachusetts

ABSTRACT

A method to monitor and control the evaporation rate for the vacuum deposition of thin films is described. The detector incorporated an electron beam focussed through two ionization chambers and produced an ion current which was proportional to the evaporation rate but independent of residual gas pressure. Deposition rates of 1 to 300 Å/sec were measured with accuracies of $\pm$ 3% and regulated over background pressure variations up to 2×10^{-4} Torr. Results for silver and copper are presented and discussed.

A CONTROLLED RATE ELECTRON BEAM EVAPORATOR

INTRODUCTION

In recent years applications utilizing the unique properties of vacuum deposited thin films have rapidly increased. However, one of the most common problems encountered in the production of these films is the difficulty to reproduce a particular characteristic. Film properties such as mass, thickness, density, reflectivity resistivity, permittivity and permeability are all functions of the deposition parameters. These parameters include the evaporating material, evaporation rate, deposition geometry, background pressure, substrate temperature and surface conditions. With such a great number of variables, each with its own set of independently working variables, it is almost impossible to adequately control all of them. Fortunately, in many applications, it is not necessary to control more than one film property so that this problem is substantially reduced. However, in other cases it is necessary to control several film properties simultaneously to obtain reproducible films of optimum quality. Such cases would occur in the production of thin film resistors with low temperature coefficients, metallized capacitors with high dielectric strengths or optical filters with specific band width and transmission. The problem becomes more accentuated when alloy films are produced from several evaporating sources where the control of film composition is an additional factor.

There are two different approaches to obtain films with specific properties and in certain applications they may effectively compliment each other. In one, the desired film property can be directly monitored and the deposition variables suitably adjusted. In the other the deposition parameters can be controlled and the film properties measured and correlated indirectly.

There have been many direct methods and techniques developed to measure

thin film properties during the evaporation cycle. Film mass has been measured with a torsion micro-balance[1] for studying thin film densities. Although an instrument with a sensitivity on the order of 4 micrograms has been reported, it was extremely fragile for a production plant and was susceptible to the effects of electrostatic charge. A system to measure film thickness by noting the frequency shift of a resonating quartz crystal[2] placed in the evaporating stream has been developed. This technique was affected by heat radiation from the vapor source and was dependent on preknowledge of the film density. Schemes employing x-ray diffraction[3] and radio-active tracers[4] have also been used to measure the thickness and mass of a thin film, but have met with a limited success. Control of certain electrical properties such as resistance or permeability have been widely used to produce films having specific values of the property measured, but the results could not easily be correlated to other film parameters for optimization purposes. Film thickness has been measured optically by counting interference fringes[5] and has been used by many workers as a basic tool. This technique, however, is mainly limited to measurements after the film has been deposited.

The second approach was to control all of the deposition parameters with the subsequent correlation of these to the various film properties. One of the most evasive of the deposition variables was the measurement and control of the evaporation rate of the depositing material. Once this parameter was accurately regulated, the effects of substrate temperature and surface condition could then be effectively determined.

Several techniques have been recently developed to measure the depositing vapor stream density and control the evaporation rate during film production. A system for monitoring the ionization of a depositing vapor

stream from an electron beam evaporator was developed by Metzger[6]. Although the measurement was compensated by dividing the evaporator electron current into the collected ion current to provide an output signal proportional to evaporation rate, the ionization process was dependent on the geometry and the beam current of the work accelerated evaporator. An independent ionization current was employed by Giedd and Perkins[7] to ionize the vapor stream in a self-contained detector. The ion current which was collected could not be differentiated from the background and vapor stream particles. Berkerman and Thun[8] refined this method with an additional background pressure monitor in a system to control the simultaneous evaporation of an alloy film. One of the major problems, however, was the inability of the two gauges to accurately track each other when the background pressure fluctuated. Schwartz[9] reduced this tracking problem by producing an a.c. signal from a dual gauge[10] by electrically switching between the vapor and the background continuously. This eliminated the effect of stray ions and electrons in an electron beam evaporator.

The evaporation rate detector described in this paper was similar in many respects to the gauges outlined above. The detector incorporated an independently controlled electron gun which focused a single electron beam through two ionization chambers. The signal from the detector was proportional to the vapor stream density and was independent of background pressure fluctuations. Accurate tracking of the two output signals was ensured by careful regulation of the electron beam current and electrode potentials.

THEORETICAL DISCUSSION

There are several variables which define the deposition for a particular material that must be considered for measurement and control in the

preparation of thin films under vacuum.

A typical electron beam evaporator system is presented in Figure 1. Included is a heat source, which in this case is a self accelerated electron beam gun; an evaporating source, heated by the beam; and a substrate upon which the evaporant is deposited.

The power required to evaporate a particular material at a specific rate can be determined by considering the source temperature, T_o, the vapor pressure, P_v, and the particle density of the evaporating material, N_v. The power delivered to the evaporating source is dissipated by radiation, conduction, convection and the heat of vaporization. The quantity of heat which is radiated is a strong function of source temperature and results in the primary dissipation of power. Therefore, the minimum power which must be delivered to the vapor source by the electron beam gun is the power radiated from the evaporating surface.

$$Q = \varepsilon\sigma \; S \; T_o^{\,4} \quad \text{watts} \tag{1}$$

where ε is the emissivity of the material which is nearly a linear function of T_o, σ is the Stefan Boltzmann radiation constant and S is the effective surface area of the evaporating material at the source temperature T_o.

A practical figure of merit for an evaporator might be described as the ratio of the radiated power from the evaporating surface to the input power from the heat source. It can be increased by minimizing the heat loss by radiation from ineffective surfaces and by conduction through supporting members. In an electron beam evaporator this loss can be substantially reduced by using a vapor source of small surface area and supporting it with a structure of narrow cross section and low heat conductivity. The heat

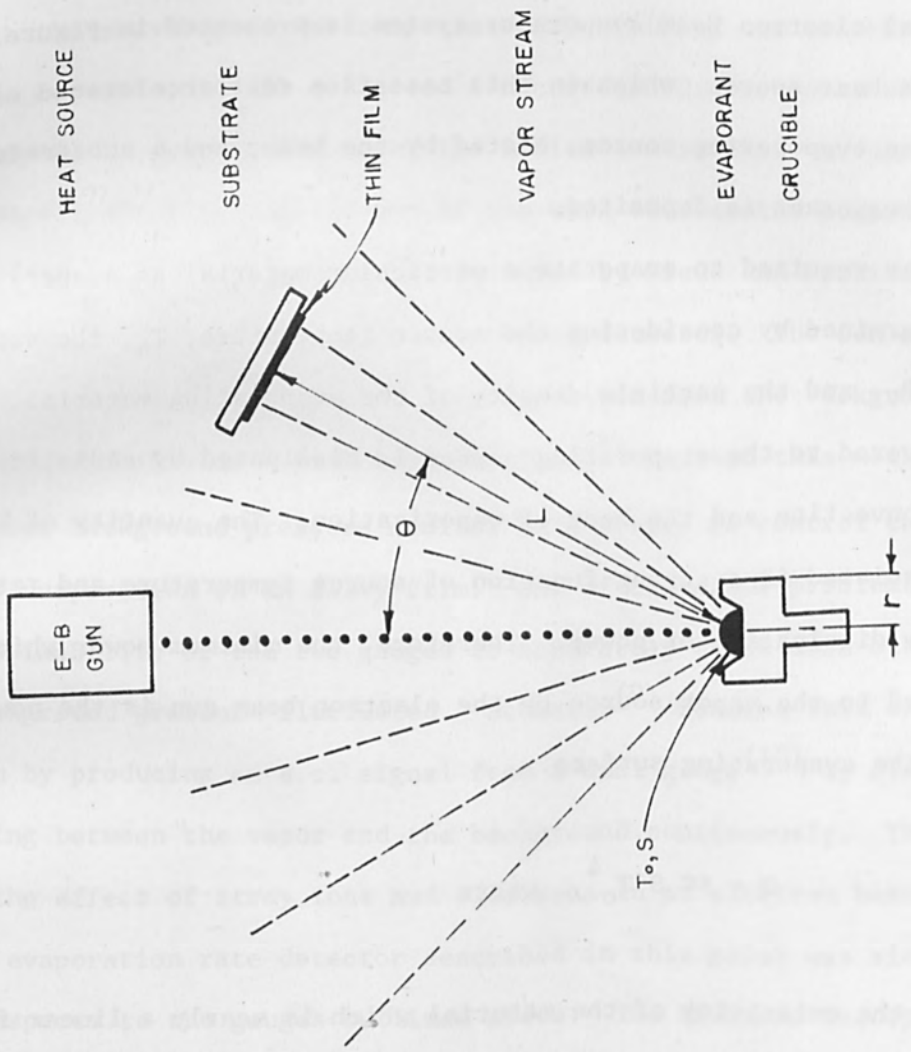

FIGURE 1 Typical Evaporator

lost by convection and vaporization are negligible in the production of vacuum deposited thin films.

The vapor pressure, P_V, can be expressed by a simplification of the Kirchoff and Clapeyron equation, since the vapor from the evaporating material can be treated as an ideal gas at pressures below 1000 microns.

$$P = 10\left(A - \frac{B}{T_o}\right) \text{ microns} \tag{2}$$

where A is a material constant in microns, and B is related to the latent heat of evaporation for a given material. Typical values of A and B for silver are 11.85 microns and 14.27×10^3 micron degrees, respectively. A series of vapor pressure curves are shown in Fig. 2 and have been plotted from data compiled by Dushman[11]. The vapor pressure which is in microns, is shown as a function of source temperature in degrees centigrade. The melting point for each material is denoted by a circle on the appropriate curve while those materials which are either liquid or solid throughout the range are indicated with an L or S, respectively. It is apparent from the curves that the vapor pressure is a strong function of temperature so that typically a change of only one hundred degrees in source temperature can produce a change of one order of magnitude in vapor pressure.

The evaporation rate, W_1, at the vapor source is a linear function of the vapor pressure but is also dependent upon the source temperature.

$$W_1 = \left(\frac{C_1 M}{T_o}\right)^{\frac{1}{2}} \cdot P_V \text{ gm/cm}^2\text{/sec} \tag{3}$$

where $C_1 = 5.82 \times 10^{-5}$, and M is the gram-molecular weight of the

evaporating material.

A series of evaporation rates are shown in Fig. 3 as a function of source temperature. The materials shown are indicative of the strong temperature dependence of the rate of evaporation. Again, the source temperature, ^{o}C, is plotted on the X axis while the rate, $gm/cm^2/sec$, is plotted on the Y axis.

In reference to Fig. 1. The deposition rate, W_2, at the substrate is a function of the evaporation rate at the source and is also dependent upon source and substrate geometry,

$$W_2 = W_1 \left(\frac{r_1^2}{L^2} \right) \cos \theta \quad gm/cm^2/sec \tag{4}$$

where r_1 is the radius of the evaporating source, L is the distance between the source and substrate and θ is the vertical angle between the axis of the substrate. The substrate is considered perpendicular to the vapor stream.

The condensation rate, D, of the vapor onto the substrate is a function of the deposition rate; the accomodation coefficient of the substrate, α and the density of the deposited film, δ .

$$D = \alpha \, \delta^{-1} \, W_2 \quad cm/sec \tag{5}$$

The accomodation coefficient is the ratio of the particles which adhere, to those which arrive at the substrate. It is generally an unknown function dependent upon surface temperature, contamination and smoothness, and is usually considered to be unity in most of the literature. The film

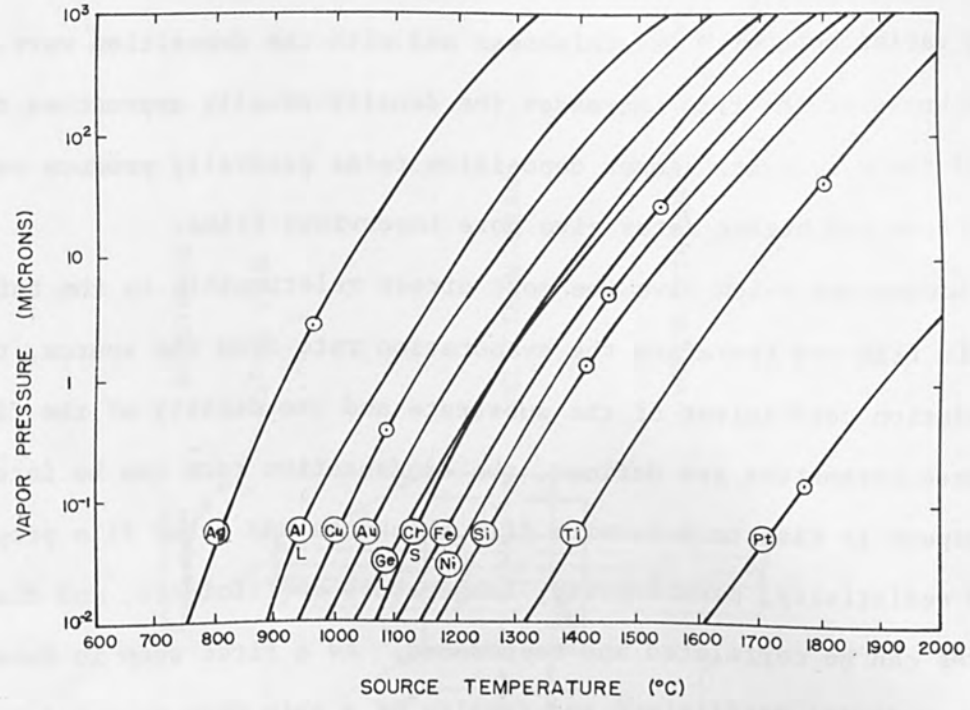

FIGURE 2 Typical Vapor Pressure of Several Materials

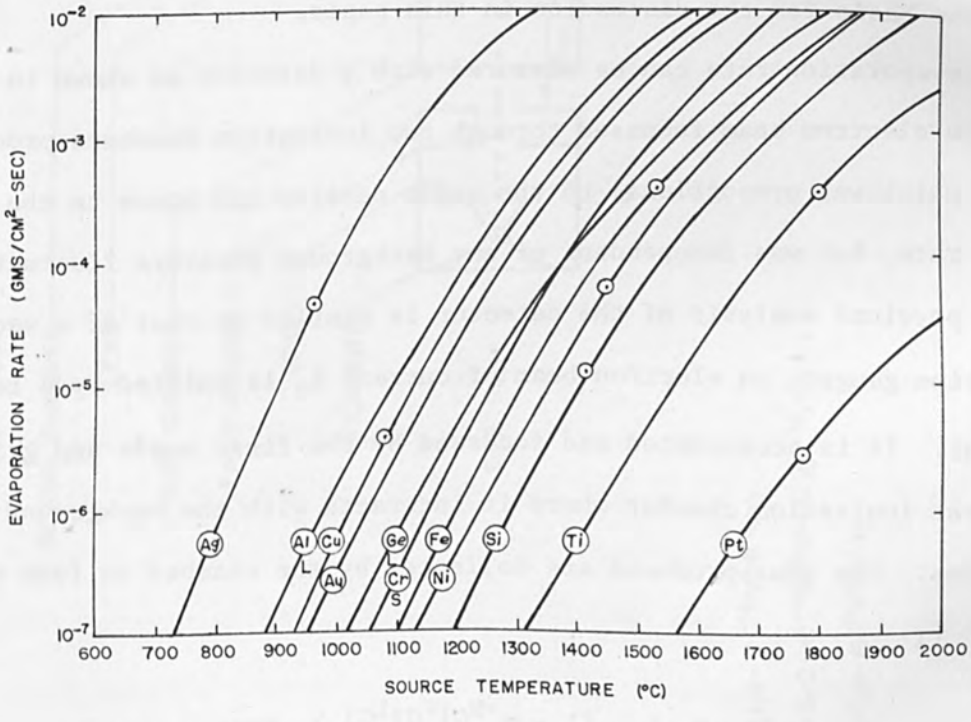

FIGURE 3 Evaporation Rates of Several Materials

density varies both with its thickness and with the deposition rate. As the thickness of the film increases the density usually approaches the bulk value of the evaporant. Lower deposition rates generally produce more porous films and higher rates give more impervious films.

The parameters which have the most direct relationship to the thickness of a thin film are therefore the evaporation rate from the source, the accommodation coefficient of the substrate and the density of the film. Once these parameters are defined, the condensation rate can be integrated with respect to time to determine film thickness and other film properties such as resistivity, permittivity, temperature coefficients, and dielectric strengths can be correlated and reproduced. As a first step in determining the accommodation coefficient and density of a thin film material, a detector has been developed to measure the evaporation rate. This device forms the basis for the discussion in this paper.

The evaporation rate can be measured with a detector as shown in Fig. 4. A single electron beam focussed through two ionization chambers produced a signal which was proportional to the vapor density and hence to the evaporation rate, but was independent of any background pressure fluctuations.

The physical analysis of the detector is similar to that of a vacuum ionization gauge. An electron beam of current I_o is emitted by a tantalum filament. It is accelerated and focussed by the first anode and grid into the first ionization chamber where it interacts with the background gas particles. The ions produced are collected by the chamber to form an ion current I_1.

$$I_1 = I_o \left(1 - e^{-N_{G1}\sigma_{G1}L_{G1}}\right) \text{ amps} \qquad (6)$$

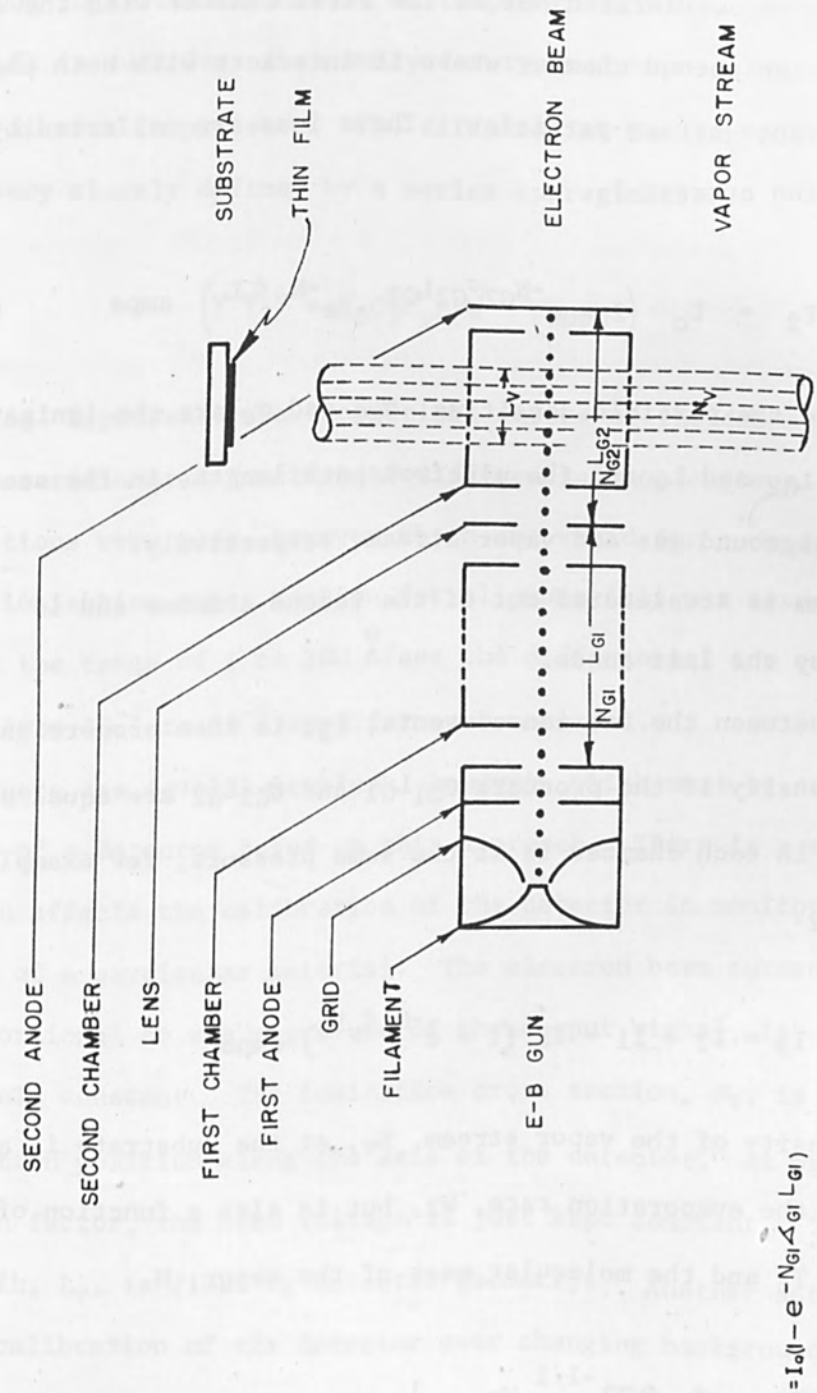

FIGURE 4 Evaporation Rate Detector

where N_{G1} is the particle density, $\sigma G1$, is the ionization cross section and L_{G1} is the electron path length for the background gas in the first chamber.

The electron beam is accelerated out of the first chamber with the lens and refocussed into the second chamber where it interacts with both the background gas and vapor stream particles. These ions are collected by this chamber to form an ion current I_2.

$$I_2 = I_o \left(2 - e^{-N_{G2}\sigma_{G2}L_{G2}} - e^{-N_v \sigma_v L_v}\right) \text{ amps} \qquad (7)$$

where N_{G2} and N_v are the particle densities, σ_{G2} and σ_v are the ionization cross sections and L_{G2} and L_v are the electron path lengths in the second chamber for the background gas and vapor stream, respectively.

The electron beam is accelerated out of the second chamber and is finally collected by the last anode.

The difference between the two ion currents, I_3, is then proportional to the vapor stream density if the products $\sigma_{G1}L_{G1}$ and $\sigma_{G2}L_{G2}$ are equal and the background gas in each chamber is at the same pressure, for example, N_{G1} is equal to N_{G2}.

$$I_3 = I_2 - I_1 = I_o \left(1 - e^{-N_v \sigma_v L_v}\right) \text{ amps} \qquad (8)$$

The particle density of the vapor stream, N_v, at the substrate is a linear function of the evaporation rate, W_2, but is also a function of source temperature T_o and the molecular mass of the vapor, M.

$$N_v = C_2 (MT)^{-1/2} \cdot W_2 \quad \frac{1}{CM^3} \qquad (9)$$

where $C_2 = 1.655 \times 10^{20}$. The value $C_2 (MT)^{-1/2}$ can be considered a material constant, C_3, over a wide range of evaporation rate for this is a strong logarithmic function of temperature. Furthermore, the product $N_v \sigma_v L_v$ is much less than unity for typical vapor stream densities less than 100 microns in pressure. The differential ion current, I_3, can therefore be very closely defined by a series approximation.

$$I_3 = I_o C_3 \sigma_v L_v W \quad \text{amps} \tag{10}$$

Fig. 5 presents the theoretical curves of the deposition rate for several materials as a function of differential ion current. Several assumptions were made, however which are valid for purposes of discussion. The ionization cross section for all materials was assumed to be $4 \times 10^{-16} cm^2$. Over the range of 1 to 200 $\mathring{A}$/sec the differential ion current varied linear-ly from 10^{-7} to 10^{-5} amps for each material.

There are several problems, however, which must be considered in the design of a detector based on this approach. There is a set of variables which affects the calibration of the detector in monitoring the evaporation rate of a particular material. The electron beam current, I_o, directly proportional to the magnitude of the output signal, I_3, must therefore be held constant. The ionization cross section, σ_v, is a function of electron position along the axis of the detector. At present this is an unknown factor, the beam voltage is just kept constant. The electron path length, L_v, is fixed by detector geometry. Another set of variables affect the calibration of the detector over changing background pressures. The ionization cross section and electron path length for background gas from each chamber must be equal to provide a differential signal that is

independent of pressure fluctuations.

SYSTEM DESCRIPTION

An evaporation rate detector was designed to fulfill the requirements necessary for accurate operation and was constructed from pre-fabricated parts which have a very close dimensional tolerance. A system was then developed employing this detector to both monitor and control the evaporation rate for the deposition of thin films. The essential elements for this system are shown in the block diagram in Fig. 6.

The material in the crucible was heated by electron bombardment from the annular work accelerated gun and was evaporated to form a stream of vapor. The stream consisted of both neutral and positively charged particles produced by particle interaction with the electron beam in the evaporator. An ion trap located directly above the evaporator consisted of a center electrode at the crucible potential to collect stray electrons, and a concentric tube at the filament potential to collect stray ions. The vapor stream, swept free charged particles, passed through the detector and onto the substrate to form a thin film.

The rate detector consisted of an independently controlled electron beam gun, two ionization chambers and an electron collector. The electron beam is emitted by a tantalum ribbon filament, accelerated by the anode and focussed by the grid. The beam enters the first chamber and ionizes a portion of the background gas. The ions produced are collected by the first chamber. The electron beam is then refocussed by the lens electrode and enters the second chamber. Ionization of a portion of the background gas and vapor stream occurs and these ions are collected by the second chamber. The electron beam is collected by the last anode. The electron beam current is regulated with a feedback control amplifier; this drives

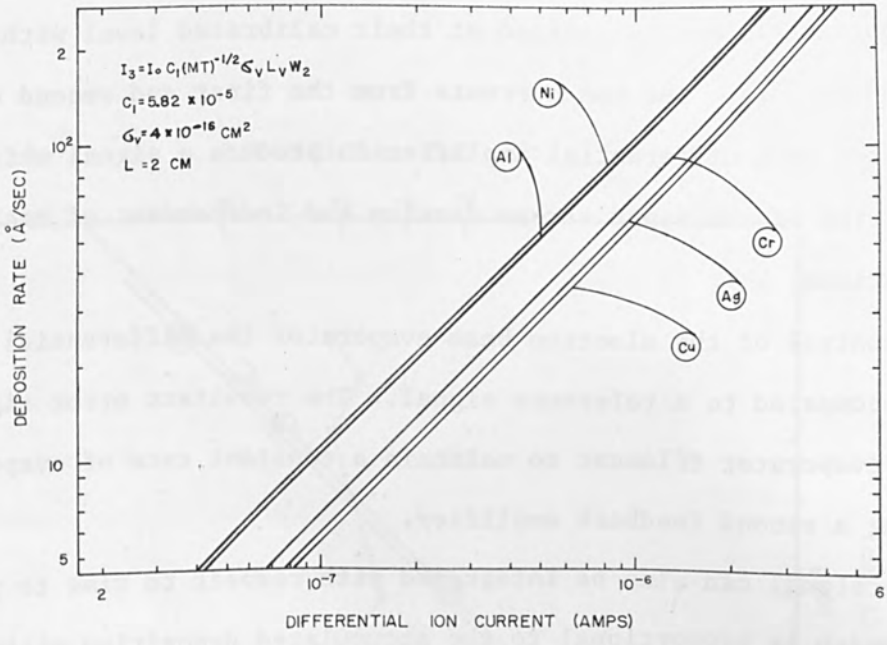

FIGURE 5 Theoretical Rate vs. Current

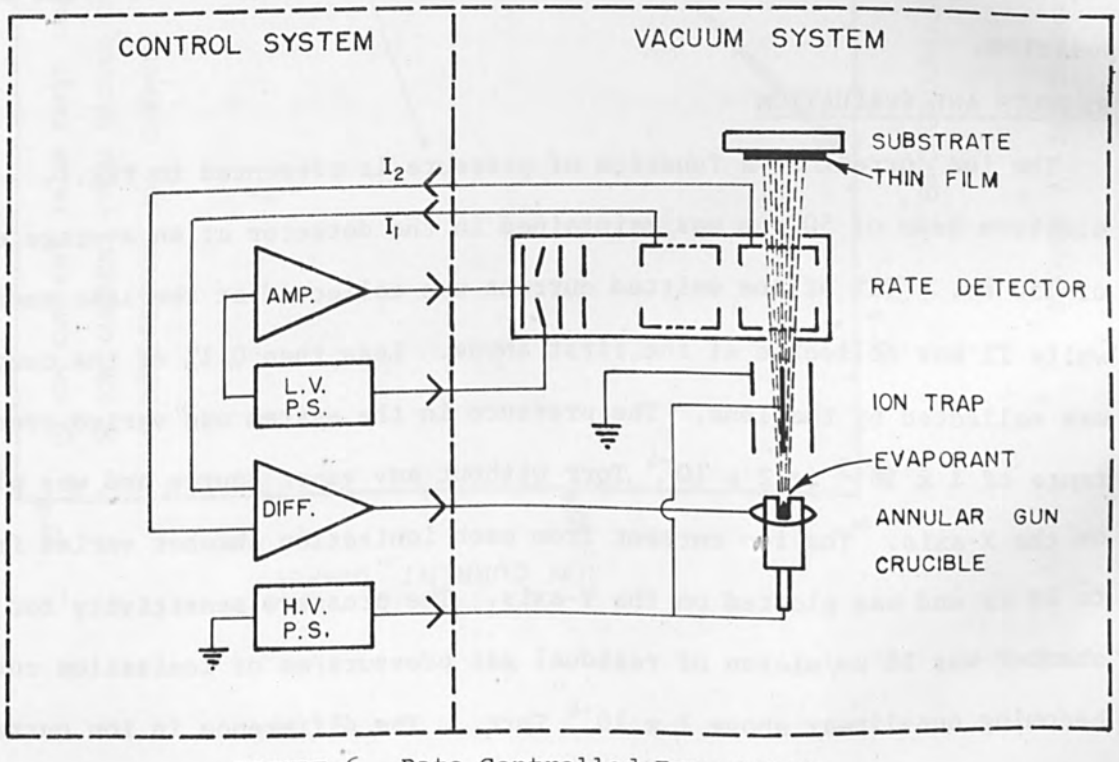

FIGURE 6 Rate Controlled Evaporator

the detector filament to maintain a constant emission current. All electrode potentials are maintained at their calibrated level with a series of regulated outputs. The ion currents from the first and second chambers are subtracted by a differential amplifier to produce a signal which is a linear function of the vapor stream density and independent of background gas fluctuations.

In the control of the electron beam evaporator the differential ion current is compared to a reference signal. The resultant error signal drives the evaporator filament to maintain a constant rate of evaporation by employing a second feedback amplifier.

The rate signal can also be integrated with respect to time to provide an output which is proportional to the accumulated deposition within the limits previously mentioned. A substrate shutter may also be automatically sequenced by electronic switching for a precise control of the total deposition.

RESULTS AND EVALUATION

The ion current as a function of pressure is presented in Fig.7. An electron beam of 500 μa was maintained in the detector at an average energy of 150 ev. 98% of the emitted current was collected at the last anode while 2% was collected at the first anode. Less than 0.1% of the current was collected by the lens. The pressure in the system was varied over a range of 1×10^{-5} to 2×10^{-4} Torr without any vapor source and was plotted on the X-axis. The ion current from each ionization chamber varied from 1 to 20 μa and was plotted on the Y-axis. The pressure sensitivity for each chamber was 16 μa/micron of residual gas pressure/ma of ionization current becoming non-linear above 1×10^{-4} Torr. The difference in ion current

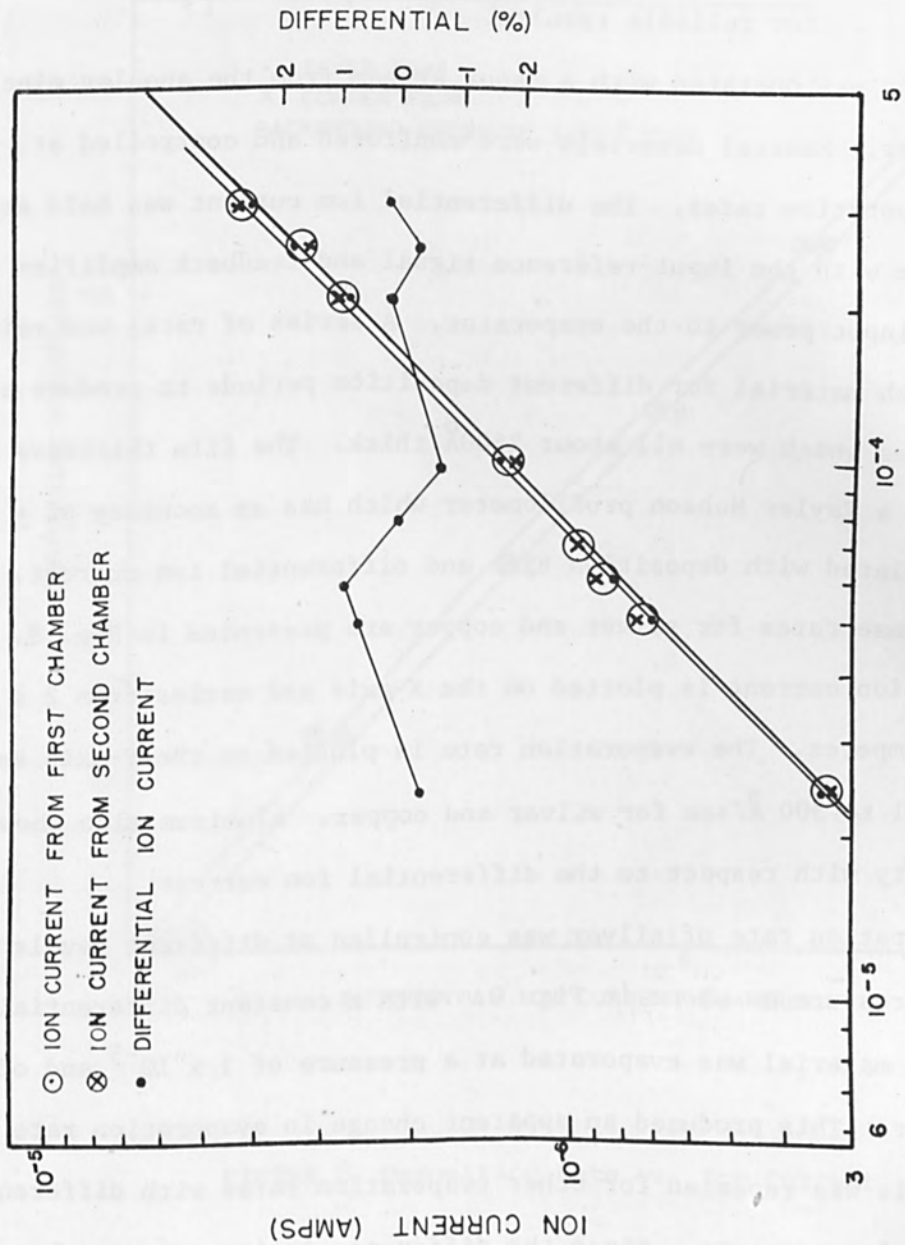

FIGURE 7 Ion Current vs. Pressure

between the first and second chamber was also plotted and was less than $\pm$ 2% over the range of pressure. The electrode potentials for a balanced conditon of ion current tracking were very critical and had to be maintained within $\pm$ 2% for reliable results.

The detector was operated with a vapor stream from the annular electron beam evaporator. Several materials were monitored and controlled at different evaporation rates. The differential ion current was held at a constant value with the input reference signal and feedback amplifier controlling the input power to the evaporator. A series of rates was maintained for each material for different deposition periods to produce a set of film samples which were all about 2500Å thick. The film thickness was measured with a Taylor Hobson profilometer which has an accuracy of $\pm$ 60Å and was correlated with deposition time and differential ion current. The results of these rates for silver and copper are presented in Fig. 8. Differential ion current is plotted on the X-axis and varies from 2×10^{-7} to 5×10^{-6} amperes. The evaporation rate is plotted on the Y-axis and varies from 1 to 300 Å/sec for silver and copper. Aluminum also showed good linearity with respect to the differential ion current.

The evaporation rate of silver was controlled at different levels of background pressure as shown in Fig. 9. With a constant differential ion current, the material was evaporated at a pressure of 1×10^{-5} and of 2×10^{-4} Torr. This produced an apparent change in evaporation rate of only 5%. This was repeated for other evaporation rates with different differential ion currents. Since the difference in ion currents has been previously shown to vary less than $\pm$ 2% with background pressure, it is possible that this is an indication that the rate of film formation on the

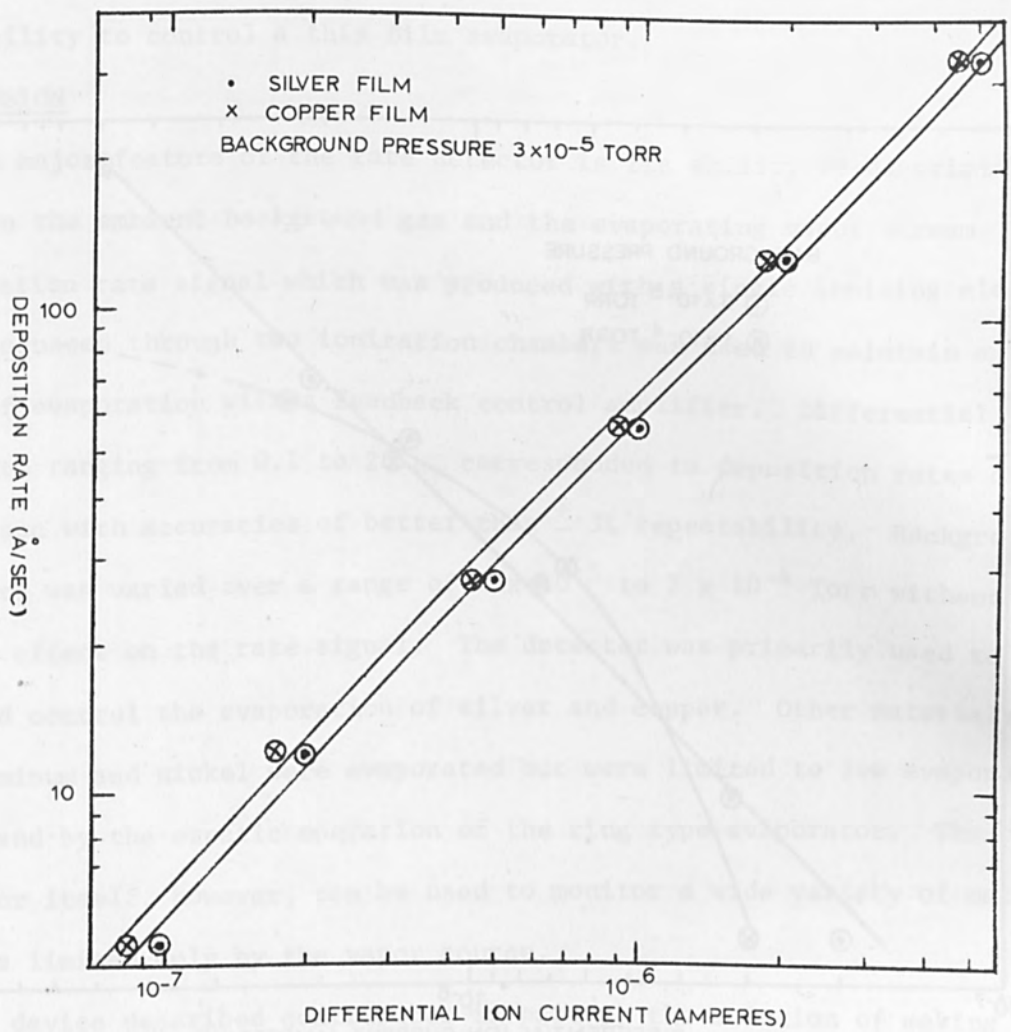

FIGURE 8 Deposition Rate vs. Ion Current

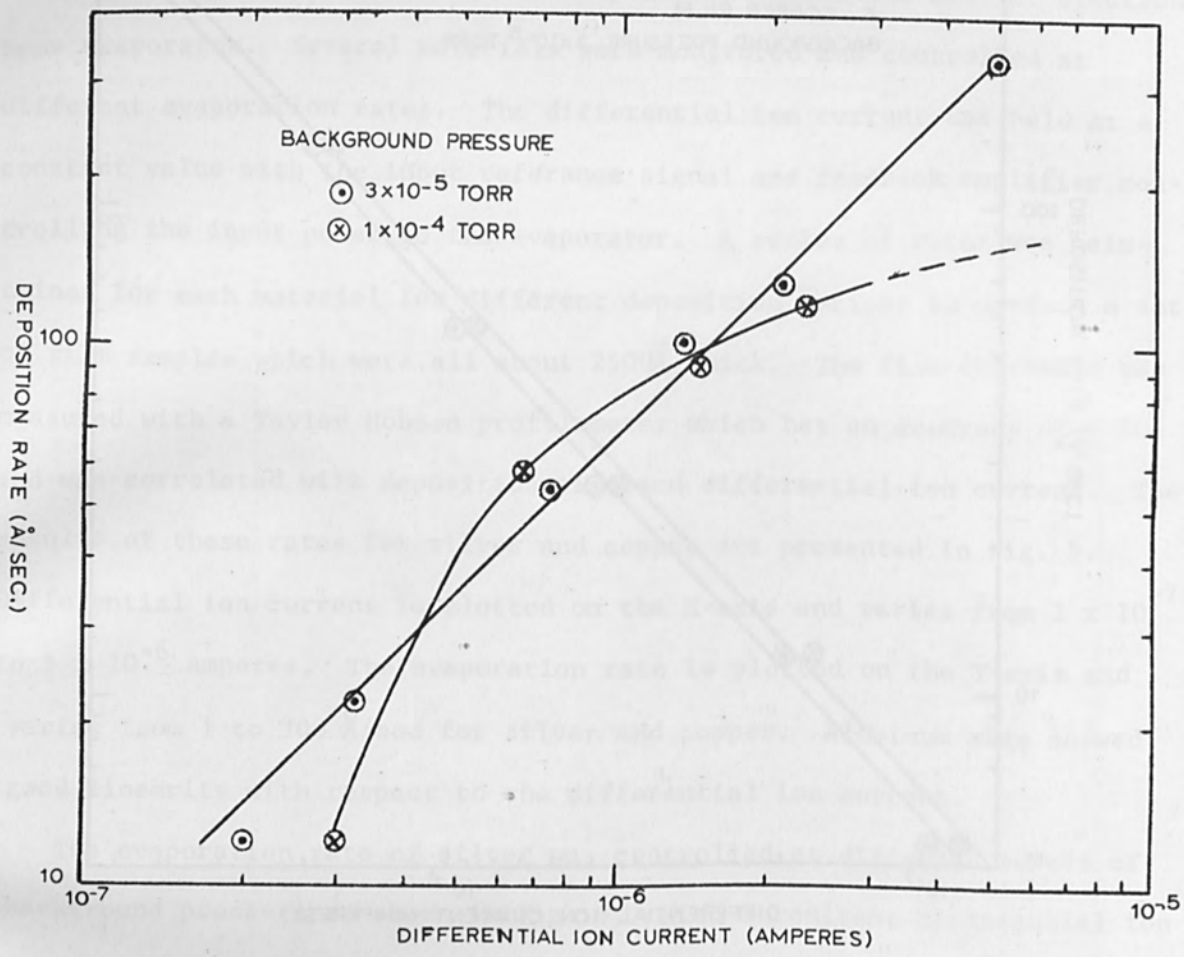

FIGURE 9 Deposition Rate at Different Pressures

substrate is a function of background pressure.

The merits of this technique are primarily the measurement of the evaporation rate of a material free of any dependence on background pressure and its ability to control a thin film evaporator.

CONCLUSION

The major feature of the rate detector is its ability to discriminate between the ambient background gas and the evaporating vapor stream. The evaporation rate signal which was produced with a single ionizing electron beam focussed through two ionization chambers was used to maintain a constant rate of evaporation with a feedback control amplifier. Differential ion currents ranging from 0.1 to 20μa corresponded to deposition rates of 3 to 300 Å/sec with accuracies of better than $\pm$ 3% repeatability. Background pressure was varied over a range of 1×10^{-5} to 2×10^{-4} Torr without significant effect on the rate signal. The detector was primarily used to monitor and control the evaporation of silver and copper. Other materials such as aluminum and nickel were evaporated but were limited to low evaporation rates and by the erratic operation of the ring type evaporator. The rate detector itself, however, can be used to monitor a wide variety of materials and was limited only by the vapor source.

The device described contributes in part to the solution of making reproducible thin films. Additional work in the study of the film properties and substrate characteristics is necessary to define the full deposition process. The measurement and control of the evaporation rate is an important function in attaining this goal.

REFERENCES

1. Clegg, P.L. and Crook, A.W., J. Sci. Instruments, 29 (1952), 201

2. Lins, S. "Resonence Frequency Shift Thin Film Thickness Monitor," Transactions of the Vac Symp. Pergamon Press, New York, 1960.

3. Friedman, H. and Birks, L. S., Rev. sci. Instruments, 17 (1946), 99.

4. Frauenfelder, H., Helv. phys. acta, 23 (1950), 347.

5. Holland, L., Vacuum Deposition of Thin Films, Chapman and Hall, London, 1956.

6. Metzger, D., "Process Control for Thin Films Vacuum Deposition" Memorandum 6M-5877, Lincoln Laboratory, 1958.

7. Giedd and Perkins Rev. Sci. Instruments, 31 (1960) 773.

8. Beckerman, and Thun "The Electrical and Structural Properties of Dielectric Metal Mixtures" Trans. of the Vac Symp, Pergamon Press, New York, 1961.

9. Schwartz H. "Method of Measuring and Controlling Evaporation Rates During the Production of Thin Films in Vacuum". Trans of the Vac Symp. Pergamon Press, New York, 1960.

10. Payne, P. R. "A System for the Control and Measurement of Thin Films" Thesis, M.I.T., Cambridge, Mass., June, 1961.

11. Dushman, S. Scientific Foundations of Vacuum Technology, John Wiley and Sons, New York, 1962.

A HALL MULTIPLIER CONTROLLED POWER SUPPLY

Dean S. Edmonds, Jr.
Nuclide Corporation
Allston, Massachusetts

Alexander Kusko
Alexander Kusko, Inc.
Cambridge, Massachusetts

ABSTRACT

This paper describes a five kilowatt power supply whose output voltage is controlled by means of a Hall multiplier circuit to maintain constant preset levels of power into a fluctuating load impedance.

The regulator was designed to control the power delivered by electron bombardment heating to a Knudsen effusion cell for use in high temperature mass spectroscopy. For this reason, the unit was provided with a separate filament heating supply. Radiation shields are generally used in high temperature applications; and at 1900^{o}C and above these shields become a separate source of bombarding electrons. The power regulator controls the total bombarding current.

Maximum ratings are: 1000 volts, and 5.0 amperes d.c. The filament supply is rated at 40 volts and 15 amperes a.c. Power regulation was better than 1% for a load change of 20%.

A HALL MULTIPLIER CONTROLLED POWER SUPPLY

INTRODUCTION

The device to be described in this paper is a power supply with a maximum d.c. power output of 5 kilowatts (1000 volts at 5 amperes). The output is regulated not on voltage or current, but on the product of the two, that is, on power. In operation, a certain power level may be set on a dial and the system will then maintain this level regardless of changes in load resistance, providing these do not require the maximum voltage or current ratings of the supply to be exceeded.

The reason for developing a supply which regulated on power by reducing the voltage when the current increased or vice versa, to maintain their product constant, was in connection with the operation of a high temperature molecular effusion, or Knudsen cell, ion source for mass spectrometers. The Knudsen cell is simply a crucible in which a sample is placed and heated to a temperature at which it has an appreciable vapor pressure. The crucible is closed by a close fitting cap with a small hole through which a molecular beam vapor effuses. The vapor beam is directed into an ionizer similar to a conventional gas sample ion source and ions are produced by interaction with an electron beam. A cutaway of the complete Knudsen cell source is shown in Fig. 1.

The Knudsen cell is used in various thermodynamic studies of compounds and alloy systems[1] and may be required to produce reasonably intense beams from materials having appropriate vapor pressures only at very elevated temperatures. To this end the crucible is arranged for heating to temperatures of the order of 3000°C, which represents a limit imposed by the softening of the most refractory metals available for the cell structure. For such temperatures, electron bombardment heating is the only practical method, and accordingly the crucible is run at a large positive

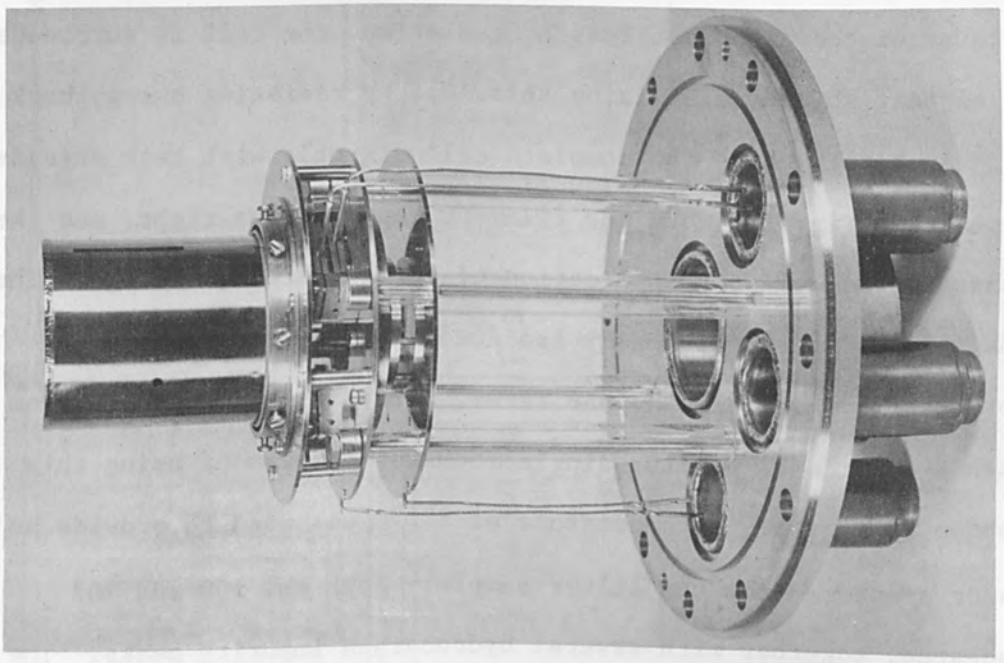

FIGURE 2 Knudsen Cell, Flange Mounted

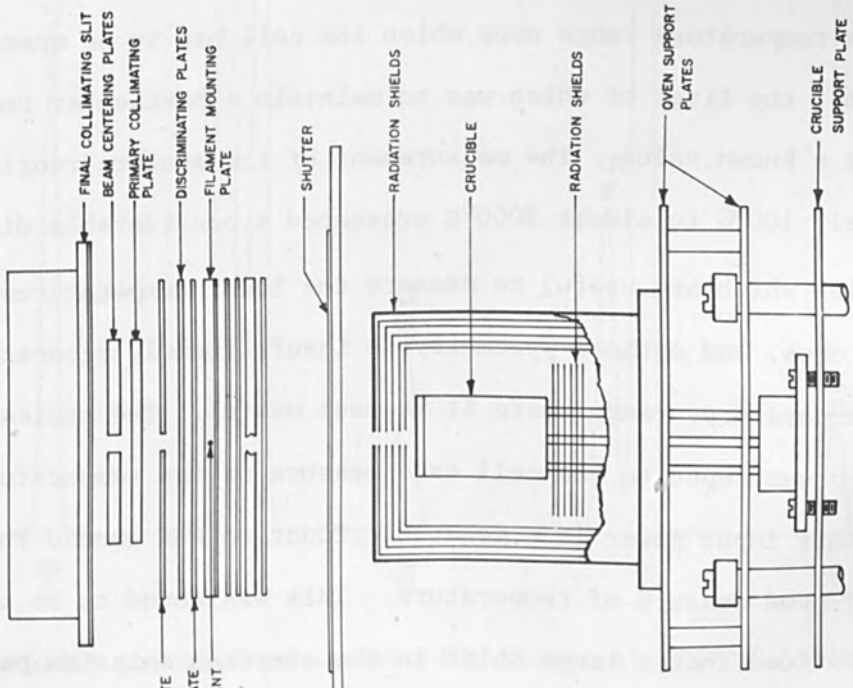

FIGURE 1 Diagram of Knudsen Cell

potential, as the anode of a thermionic diode. The electron-emitting filament is a loop of tungsten wire encircling the cell and does not appear in Fig. 1. Because of the high heat loss by radiation, the cell is surrounded by a series of heat shields minimizing this loss by radiating energy back to the cell. A photograph of the complete cell assembly with heat shields in place appears in Fig. 2. Note the filament leads on the right, and the separate leads to the cell for application of the bombarding voltage. The leads to the shields are electrically isolated from the remainder of the assembly for reasons which will appear later. A typical mass spectrogram obtained with a Nuclide 12" radius single focusing instrument using this source is shown in Fig. 3. A temperature of 875°C was used to provide an adequate vapor pressure from the silver sample. Both the 109 and 107 isotopes appeared, together with several hydrocarbon impurity peaks. The separation of the silver from the hydrocarbon peaks which occurred at the same mass numbers should be noted.

The wide temperature range over which the cell had to be operated posed two problems, the first of which was to maintain a particular temperature constant at a known value. The measurement of temperature ranging from approximately 100°C to almost 3000°C presented a considerable difficulty. Thermocouples which are useful to measure the lower temperatures, melt at the higher ones, and optical pyrometry is insufficiently accurate even for the high temperatures range where it is most useful. The choice made was to use the power input to the cell as a measure of its temperature. Theoretically this input power is a monatonic function and should thus provide a perfectly good measure of temperature. This was found to be true in practice provided that a large shift in the electron emission pattern did not take place. An average of the results obtained by careful measurements

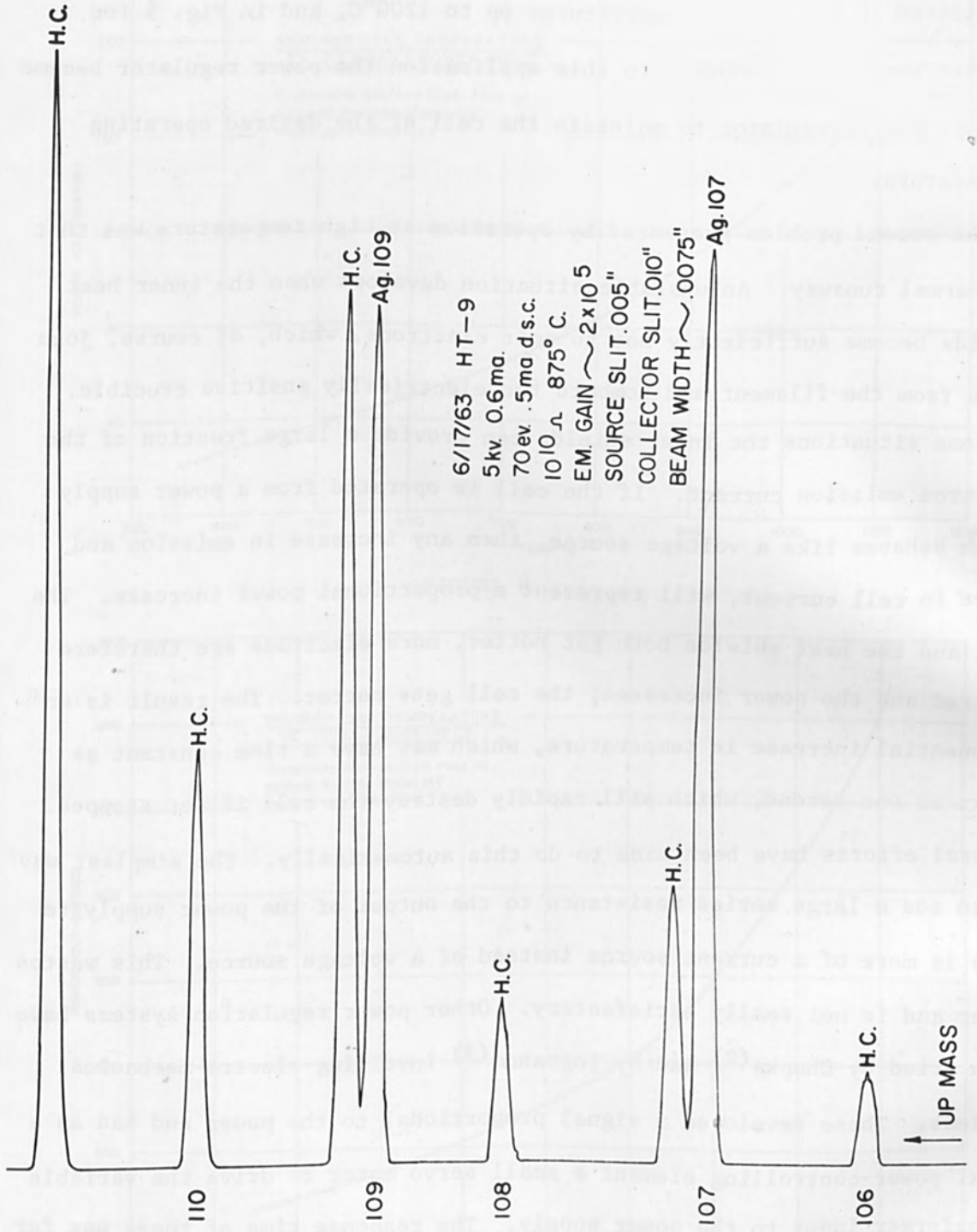

FIGURE 3 Mass Spectrogram for Silver at 875°c

of temperature as a function of power input to the cell for several sources is plotted in Fig. 4 for temperatures up to 1200°C, and in Fig. 5 for temperatures up to 2400°C. In this application the power regulator became a temperature regulator to maintain the cell at the desired operating temperature.

The second problem presented by operation at high temperature was that of thermal runaway. An unstable situation develops when the inner heat shields become sufficiently hot to emit electrons, which, of course, join those from the filament and bombard the electrically positive crucible. In some situations the inner shields can provide a large fraction of the electron emission current. If the cell is operated from a power supply which behaves like a voltage source, then any increase in emission and hence in cell current, will represent a proportional power increase. The cell and the heat shields both get hotter, more electrons are therefore emitted and the power increases; the cell gets hotter. The result is an exponential increase in temperature, which may have a time constant as short as one second, which will rapidly destroy the cell if not stopped. Several efforts have been made to do this automatically. The simplest way is to add a large series resistance to the output of the power supply to make it more of a current source instead of a voltage source. This wastes power and is not really satisfactory. Other power regulation systems have been tried by Chupka[2] and by Ingraham[3] involving electro-mechanical systems. These developed a signal proportional to the power and had as a final power-controlling element a small servo motor to drive the variable transformer input to the power supply. The response time of these was far too slow to stop a thermal runaway, although phased thyratron power control was later tried with more success.

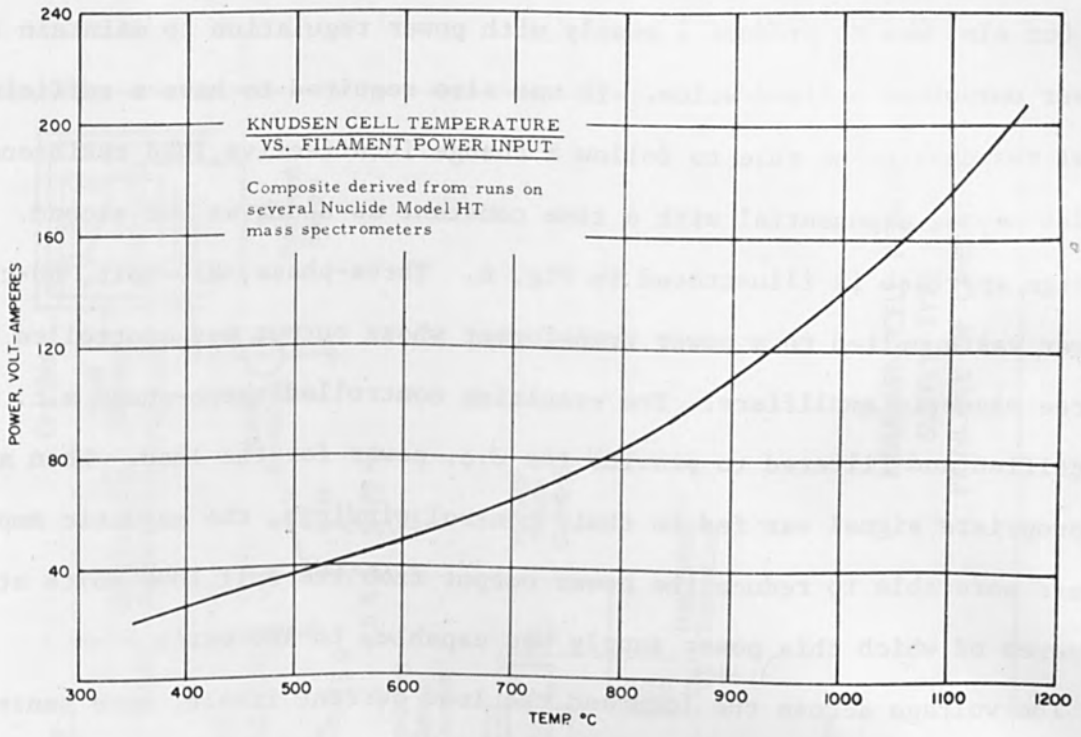

FIGURE 4

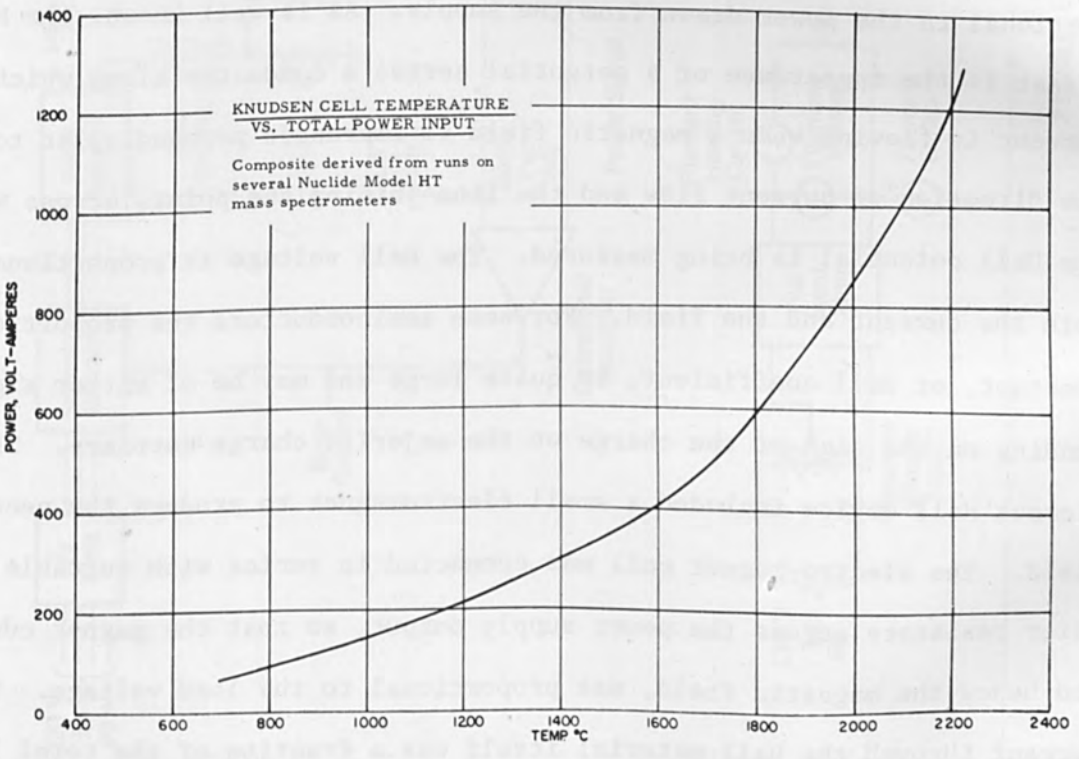

FIGURE 5

A HALL MULTIPLIER CONTROLLED POWER SUPPLY

Our aim was to produce a supply with power regulation to maintain the power output at a fixed value. It was also required to have a sufficiently fast response to be able to follow a change in effective load resistance which may be exponential with a time constant as short as one second. The design approach is illustrated in Fig. 6. Three-phase, 220-volt, 60-cycle power was supplied to a power transformer whose output was controlled by three magnetic amplifiers. The resulting controlled three-phase a.c. was rectified and filtered to provide the d.c. power for the load. When an appropriate signal was fed to their control windings, the magnetic amplifiers were able to reduce the power output from the full 1000 volts at 5 amperes of which this power supply was capable, to 100 watts.

The voltage across the load and the load current itself, were sensed as two currents by a Siemens Hall device to give an output voltage proportional to the power drawn from the supply. As is well known, the Hall effect is the appearance of a potential across a conductor along which a current is flowing when a magnetic field is impressed perpendicular to both the direction of current flow and the line joining the points across which the Hall potential is being measured. The Hall voltage is proportional to both the current and the field. For some semiconductors the proportionality constant, or Hall coefficient, is quite large and may be of either sign depending on the sign of the charge on the majority charge carriers. The Siemens Hall device included a small electromagnet to produce the necessary field. The electro-magnet coil was connected in series with suitable multiplier resistors across the power supply output, so that the magnet current, and hence the magnetic field, was proportional to the load voltage. The current through the Hall material itself was a fraction of the total load current and was determined by appropriate shunts. Hence, a d.c. voltage was

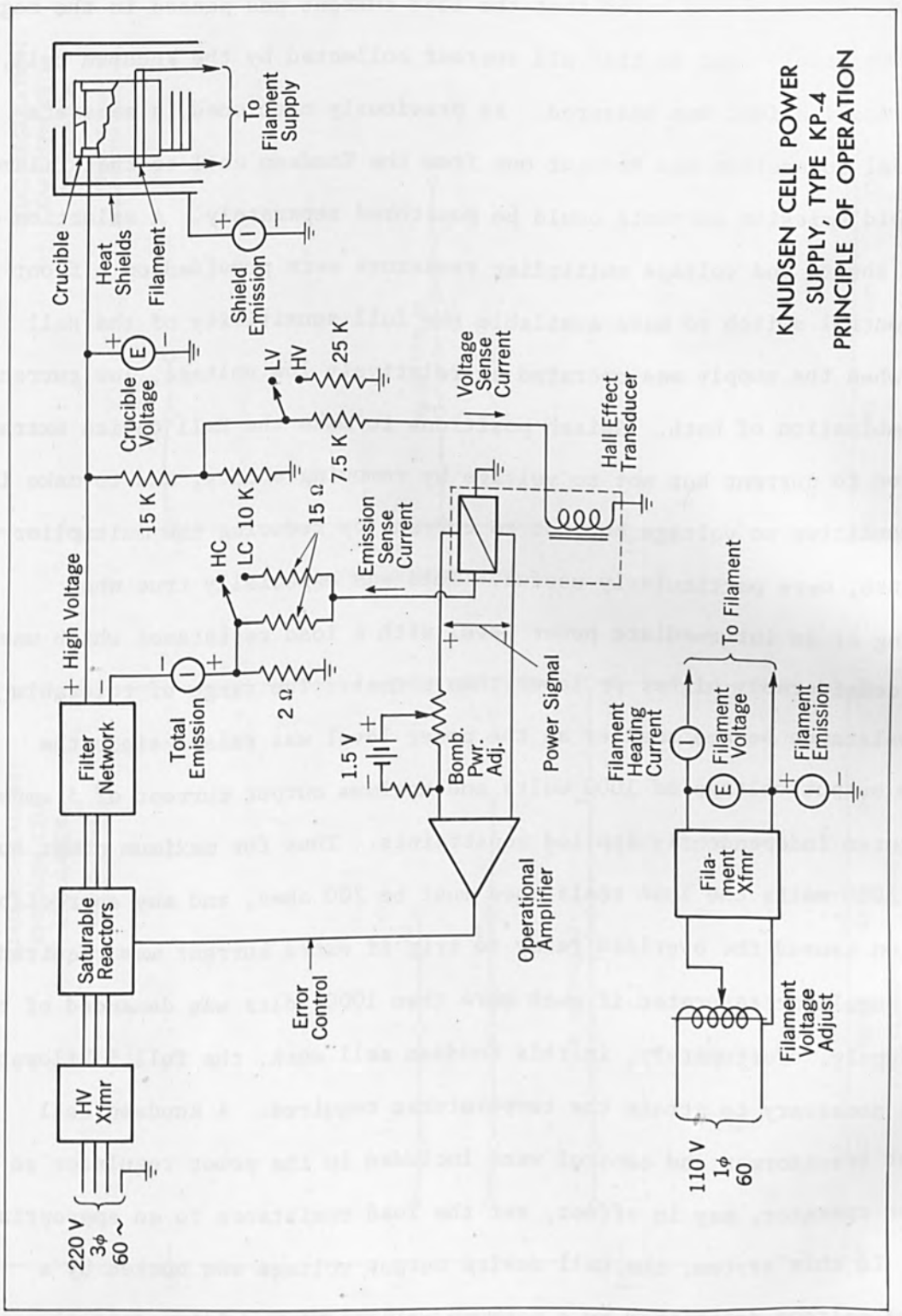
KNUDSEN CELL POWER SUPPLY, TYPE KP-4
PRINCIPLE OF OPERATION
220 V 3φ 60 ~
HV Xfmr
Saturable Reactors
Filter Network
+ High Voltage
Crucible
Heat Shields
Filament
To Filament Supply
Shield Emission
Crucible Voltage
LV
HV
25 K
7.5 K
15 K
10 K
15 Ω
HC
LC
2 Ω
Total Emission
Emission Sense Current
Voltage Sense Current
Hall Effect Transducer
1.5 V
Bomb. Pwr. Adj.
Power Signal
Operational Amplifier
Error Control
Filament Heating Current
Filament Voltage
Filament Emission
To Filament
Fila-ment Xfmr
Filament Voltage Adjust
110 V 1φ 60

FIGURE 6

developed by the Hall device proportional to the total power passing through the load. It should be noted that the load current was sensed in the negative power supply lead so that all current collected by the Knudsen cell, in this application, was measured. As previously mentioned, a separate electrical connection was brought out from the Knudsen cell so that filament and shield emission currents could be monitored separately. A selection of current shunts and voltage multiplier resistors were provided on a front panel control switch to make available the full sensitivity of the Hall device when the supply was operated at relatively low voltage, low currents, or a combination of both. Switch positions to make the Hall device extra sensitive to current but not to voltage by removing shunts, and to make it extra sensitive to voltage but not to current by reducing the multiplier resistance, were particularly useful. This was especially true when operating at an intermediate power level with a load resistance which was either considerably higher or lower than normal. The range of tolerable load resistance became smaller as the power level was raised since the maximum output voltage of 1000 volts and maximum output current of 5 amperes constituted independently applied constraints. Thus for maximum power output of 5000 watts the load resistance must be 200 ohms, and any appreciable deviation caused the overload relay to trip if extra current was required, or the regulator saturated if much more than 1000 volts was demanded of the power supply. Fortunately, in this Knudsen cell work, the full 5 kilowatts was not necessary to attain the temperatures required. A Knudsen cell filament transformer and control were included in the power regulator so that the operator, may in effect, set the load resistance to an appropriate value. In this system, the Hall device output voltage was bucked by a standard voltage determined by a mercury cell and a precision potentiometer

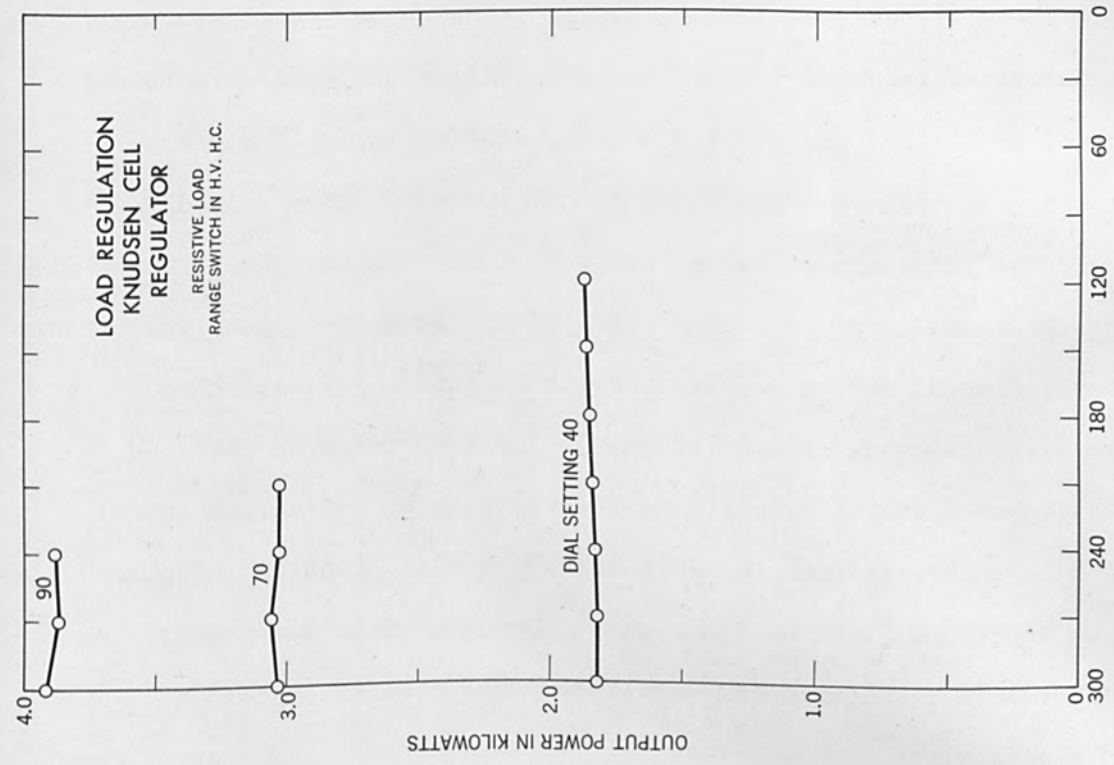

FIGURE 8

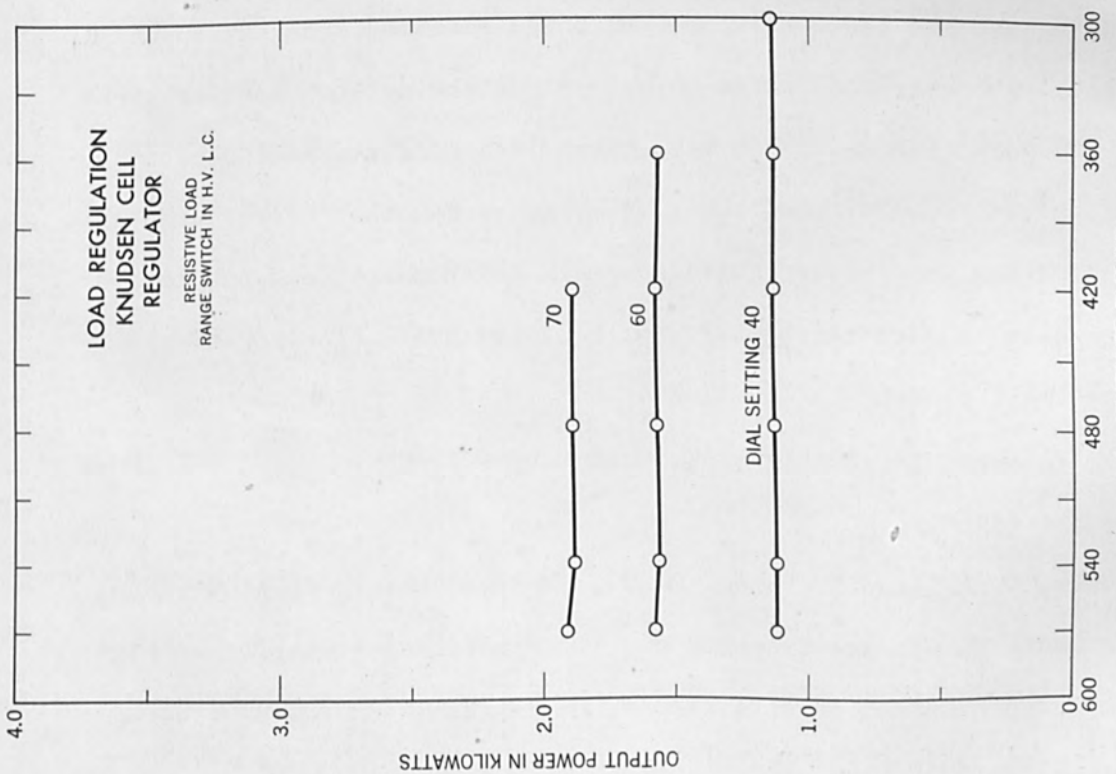

FIGURE 7

attached to the power control dial. The resulting error signal was amplified by a Philbrick type USA-3 operational amplifier followed by a Transistorized power amplifier, for driving the magnetic amplifiers' control windings. The results are illustrated by the curves of Figs. 7 and 8. Fig. 7 shows the situation with the load resistance somewhat higher than normal and the range switch set accordingly for high voltage and low current. In this way the shunt across the Hall device semiconductor wafer had a relatively large value so that a relatively large fraction of the load current passed through the material. A large value of multiplier resistance was used in series with the coil so that a high output voltage was required to produce a given Hall current. The plots show power output as a function of load resistance for different power dial settings. Fig. 8 is a similar plot for the high current, high voltage ranged used when it was desired to use high power with load resistance in the neighborhood of the normal 200 value. In the worst case the power remained constant to within 1% over the load resistance range shown. Since the meters used for these measurements gave readings which were themselves barely repeatable to 1%, the actual power regulation of the system may be somewhat better than this. Response time has also proved quite adequate to stop any tendency towards thermal runaway in electron bombardment heating applications.

REFERENCES

1. See, for example, Buchler, A., and Berkowitz-Mattuck, J. Chem.Phys., 39, 186 (1963)
2. Chupka, W. A., and Ingraham, M. G., J. Phys. Chem., 59 100 (1955)
3. Ingraham, M. G., and Drowert, J., International Symposium on High Temperature Chemistry at Asilomar, California, McGraw-Hill Book Co., N.Y., 1960

THE DESIGN OF A PROGRAMMED ELECTRON BEAM WELDER

J. P. Roos, P. R. Payne and J. R. Morley
Alloyd General Corporation
Cambridge, Massachusetts

ABSTRACT

A very large electron beam machine has been designed and constructed for the automatic welding of structures under vacuum. The system includes a 640 cubic foot chamber evacuated with a mechanical booster and a 20" diffusion pump. A 15 kw. electron beam welding gun is accurately driven along three axis of motion throughout the chamber. An analog point-to-point programmer provides circular or linear control of welding speed, and slope and level control of electron beam power. A closed circuit television system is used for remotely viewing the welding process. The basic design principles of several major components and their performance are presented and discussed.

THE DESIGN OF A PROGRAMMED ELECTRON BEAM WELDER

INTRODUCTION

The design of a large electron beam welder was prompted by the need to join together large parts made of aluminum, titanium and the refractory metals and alloys. The demand originated in the aerospace industry, where for many purposes conventional welding techniques are excluded. Electron beam welding within a large vacuum chamber was preferred to welding in air[1], or in a controlled atmosphere, because of its better performance in depth of penetration and its greater reliability.

The large sizes of workpiece, and the need for the electron gun to move freely in three-dimensional space, prevented the use of telescopes and other conventional fixed viewing systems, and instead a new approach was devised. A closed circuit television camera was mounted with the electron gun to view the welding process. Programming was also included in the design concepts, to accomodate production runs, as well as the one-of-a-kind jobs so typical of electron beam welding.

GENERAL DESCRIPTION

This electron beam welder has been designed and constructed to operate automatically from a pre-selected program, to accomodate the welding of materials having an infinite variety of shapes and sizes. It is shown in Fig. 1. The vacuum chamber is 11' long, 7'6" wide, and 7'6" high, and is evacuated to the welding pressure with a pumping system consisting of a diffusion pump, a blower, and a mechanical pump. All vacuum valves and pumpdown cycles are automatically sequenced and switched.

The electron gun is mounted inside the chamber on a moving carriage which can be driven in three dimensions by externally mounted printed circuit motors. In this way, the electron gun can be driven to any point within a volume of 8'6" long by 5' high by 6' wide. A pair of tachometers and one

encoder are coupled to each motor driven axis to accurately position the gun to any point within this volume. The velocity of the gun may be accurately controlled and its position is known at any instant in time from the encoder indications. An analog type of point-to-point programmer is used to control the beam power and the position and velocity of the electron gun. The program may be pre-set, and once set up, the electron gun will reproduce identical welds in three dimensions. Twelve such program points are provided.

Straightline paths in the X, Y, or Z directions can be performed by operating one motor alone or by the simultaneous operation of two or three motors at precisely controlled speeds; vector directions in any plane can be made. Circular welds are made by using a suitable function generator to control the motors so as to drive the gun in a circular path in a horizontal plane. If the function generator is energized only during a specific portion of the program, radiussed weld corners can be fabricated as well as full circular welds.

While large circular parts are made either with the circular function generator, or by use of the rotary table or lathe arrangement, electron beam deflection is also provided for the circular plugwelding of small parts.

The television camera is mounted on the carriage mechanism and moves with the electron gun, so that adjustments can be made to the beam, the gun position, and to speed during operation. A low contrast picture is obtained on the monitor screen by means of a system of narrow band pass optical filters, and an auxiliary light source. The liquid pool and the surrounding colder parts of the weld may be seen equally well.

SYSTEMS COMPONENTS

This section will discuss in some detail the design principles used in

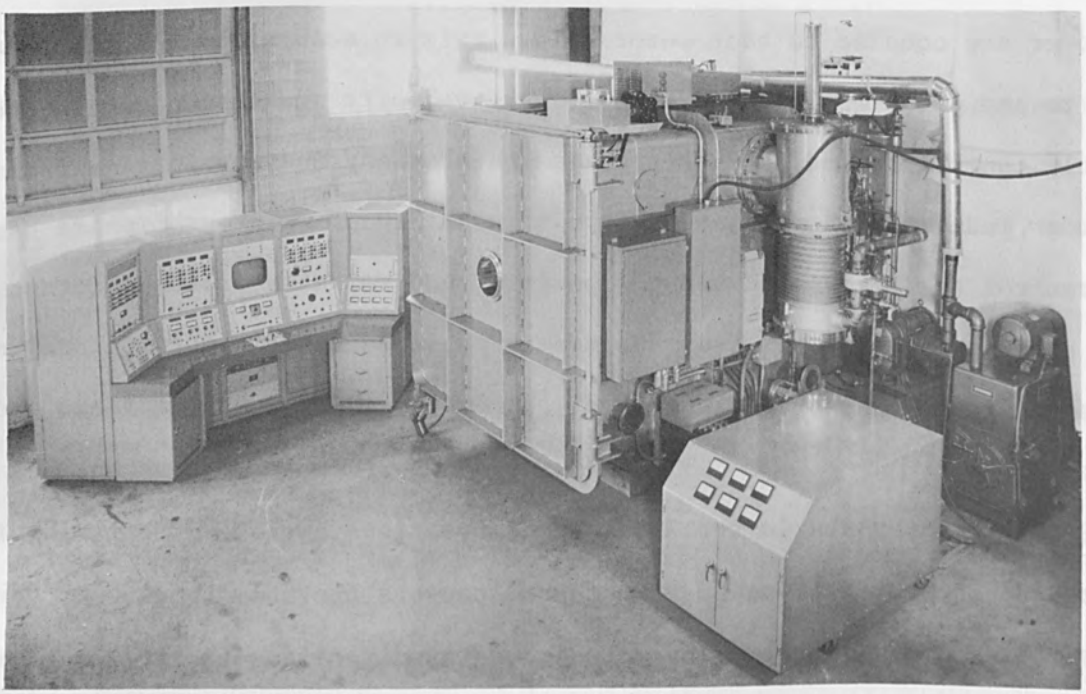

FIGURE 1 Electron Beam Welder

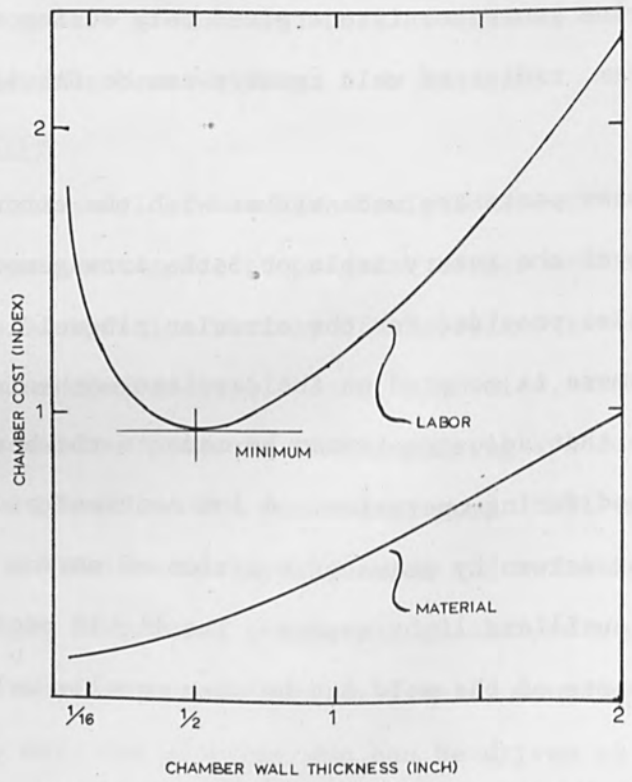

FIGURE 2 Cost vs Wall Thickness for a Welded Chamber

the equipment, the problems encountered and the reasons for decisions made. The better known sub-systems such as the vacuum chamber and pumps will only be summarized.

1. Vacuum Chamber

The design of a large rectangular vacuum chamber is a function of economics and utility. A wall thickness must be selected which is economically weldable, yet which is commensurate with a small number of supporting ribs. (See Fig. 2). Both of these being controlled by the permissable wall deflection of the chamber.

The chamber of this welder measured 7'6" x 7'6" x 11' internal size. Its walls were of 1/2" low carbon steel, and 3/4" x 6" ribs divided them into fields of 30" x 44". The wall deflections due to pumpdown were measured, and averaged 0.040" per field, and 0.080" for the ribs across the width of the wall. The doors were fabricated in a similar manner, and weighed 2,500 lbs. each. Needle bearings and needle thrust washers mounted in adjustable eccentric bushings were used to lower friction so that closing of the doors was done with a force of 3 lbs. Final closing was established by pneumatically operated toggle clamps which provided sufficient force to hold down the corners of the square doors during pumpdown of the chamber.

2. Pumping System

The volume of the chamber and pumping system was approximately 650 cubic feet. About fifteen minutes was required to obtain a pressure in the welding range of 10^{-4} to 10^{-5} torr. The pumping capability consisted of a 24,000 cfm diffusion pump, a 1200 cfm mechanical booster and a 300 cfm roughing pump. Use of the booster pump down to a pressure of 15 microns, before changing to the diffusion pump, reduced the large backstreaming of

oil which would occur during diffusion pumping down from 200 microns. As a consequence, the system required no cold trap to catch this oil; the regular cold cap supplied with the diffusion pump being sufficient. Because the machine was intended for production welding operations, a fully automatic system was necessary and was designed.

3. Motion Systems

For a given size of chamber, longer welds can be made by moving the gun within the chamber, than by moving the workpiece. The decision to use a moving gun and to program the welding sequence immediately raised the following design problems pertinent to a drive system.

(i) The electron gun must move freely in three dimensions in such a way as to take full advantage of the size of the chamber.

(ii) The electron gun must follow the weld joint with a maximum overall positional error of approximately one third of the beam diameter, or 0.010".

(iii) The position of the gun and of the workpiece must not be affected by deflection of the chamber walls during pumpdown.

(iv) The velocity range of the moving gun should be at least 100:1, to accommodate all types of welding.

(v) The carriage must respond rapidly to a program instruction, to avoid overshooting on weld runs or missing joints at a turn.

The solution of these design considerations will be discussed in some detail.

A. Motors and Shafts

In terms of mechanical response, the problem of selection of the drive motor was common to the design of all drive systems, and a review of motor characteristics was in order. Fig. 3 shows some

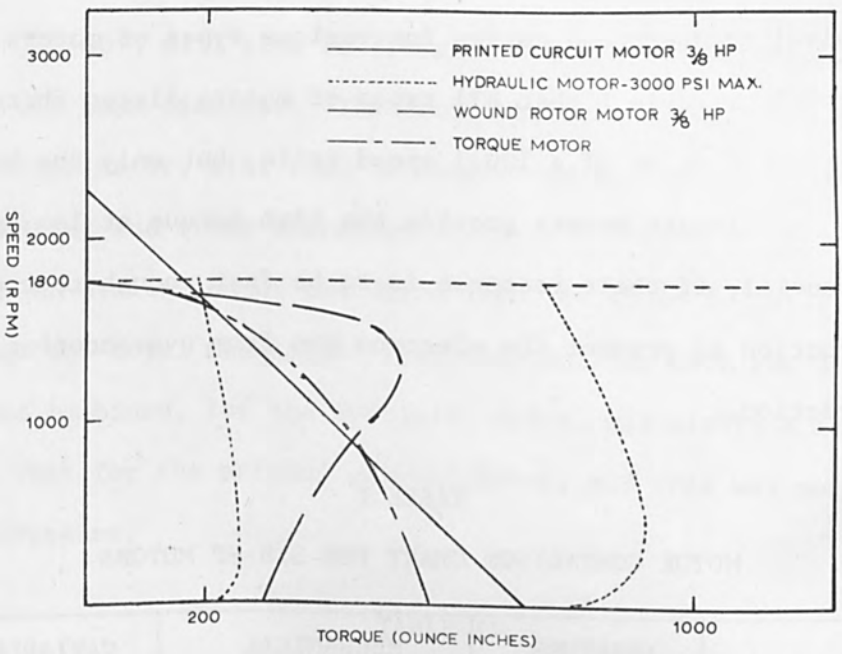

FIGURE 3 Motor Characteristics, Torque vs Speed

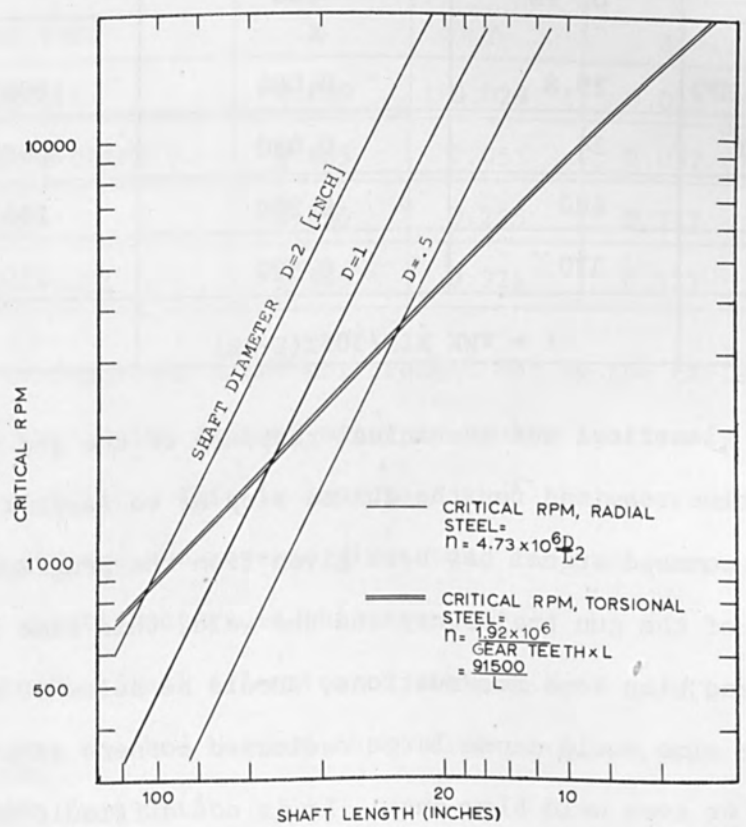

FIGURE 4 Critical R.P.M. for Shaft Drives

typical torque-speed curves for various types of motors. It will be noted from Table I that all types of motors listed there satisfy the design criterion of a 100:1 speed ratio, but only the hydraulic and printed circuit motors provide the high torque at low speed which is essential, if their response is to be fast enough to a program instruction to prevent the electron gun from overshooting on changing direction.

TABLE I

MOTOR COMPARISON CHART FOR 3/8 HP MOTORS

MOTOR TYPE	ARMATURE INERTIAL MASS	MECHANICAL TIME CONSTANT, t	VARIABLE SPEED RATIO	TOTAL SYSTEM COST
	OZ IN	SEC		$
HYDRAULIC (CAPABILITY 20 HP)	29.8	0.004	1000:1	2200.
PRINTED CIRCUIT	34	0.030	1000:1	500.
TORQUE	480	0.200	150:1	1200.
D. C. SHUNT	370	0.300	150:1	700.
	$t = \pi WK\ RIN/30fT(E-IR)$			

The electrical and mechanical response of the gun is a measure of the time required for the gun to stop or to reach a certain speed after a command signal has been given from the programmer. For good control of the gun trajectory and the weld, this time lapse must be short, and with some reservations, should be below 50 m.sec. A long response time would cause large radiussed corners at a turn, overshoots, or even weld blow-outs. It is not difficult to keep the electrical response below 25 m.sec. which, at a typical welding speed

of 30"-40", will give an error of 0.015", or approximately one half of the beam diameter. The choice between a hydraulic or printed circuit motor, will then be determined by the mechanical time constant and other characteristics.

An evaluation of the drive load, as shown in Table II, indicated that the total mechanical time constant for both the drive motor and load combined, for the hydraulic drive, was within a factor of two of that for the printed circuit motor, and this was not too great a difference.

TABLE II

TOTAL TIME CONSTANTS FOR DRIVES WITH MECHANISM LOAD (SEC)

MOTOR TYPE	X	Y	Z	ROT
HYDRAULIC	0.039	0.029	0.021	1.74
PRINTED CIRCUIT	0.065	0.055	0.037	1.77
TORQUE	0.235	0.225	0.317	1.94
D. C. SHUNT	0.335	0.325	0.417	2.04

An important point not brought out by the tables, is the ability of a particular type of motor to remain stationary at zero speed and not to drift. This is important when the motor has to be driven in both forward and reverse direction, and hydraulic motors are somewhat unsatisfactory in this respect.

In the final selection of the printed circuit motors, a compromise was reached between cost, time response, starting torque, and freedom from drift.

The small overall mechanical drive constants shown in Table II for the X, Y and Z drives (of which details are given later), were

obtained by a design which stressed a minimum of inertia for couplings, shafts and ballscrews. The small shaft diameters thus obtained, introduced problems such as critical rpm, (See Fig. 4) which could be of a radial as well as of a torsional character; and gun position lag, which could occur due to winding up of the shafts in torsion. The latter problem was less critical than the former. The usually high torsional critical rpm was lowered by a factor equalling the number of teeth in the bevel gear drive, and for the shaft lengths involved, came quite close to the maximum speed of 500 rpm for the X and Y shafts, and 400 rpm for the Z drive. The small diameters required to obtain low inertias introduced radial critical rpm which were lower than above maximum shaft rpm. Extra shaft supports were introduced to decrease the unsupported length of the shafts and ball screws to below their critical values.

B. Carriage Drive Mechanisms

A description of the carriage drive mechanisms is given to illustrate further design problems. The coordinate directions are referred to as X, Y and Z, which are the length, width and height coordinates respectively. The gun was mounted on a bridge which it can traverse in the Y direction, (As shown in Fig. 5). The bridge was supported at its ends by the long sides of a rectangular frame. The bridge can move in the X direction on rails supported by the frame. The whole frame, complete with the bridge and gun, can be driven in the Z (vertical) direction. The three coordinate motions are driven by printed circuit motor drives through a combination of spline shafts, regular shafts, ball screws and bevel gears. All moving components slide on split ball bushings along accurately

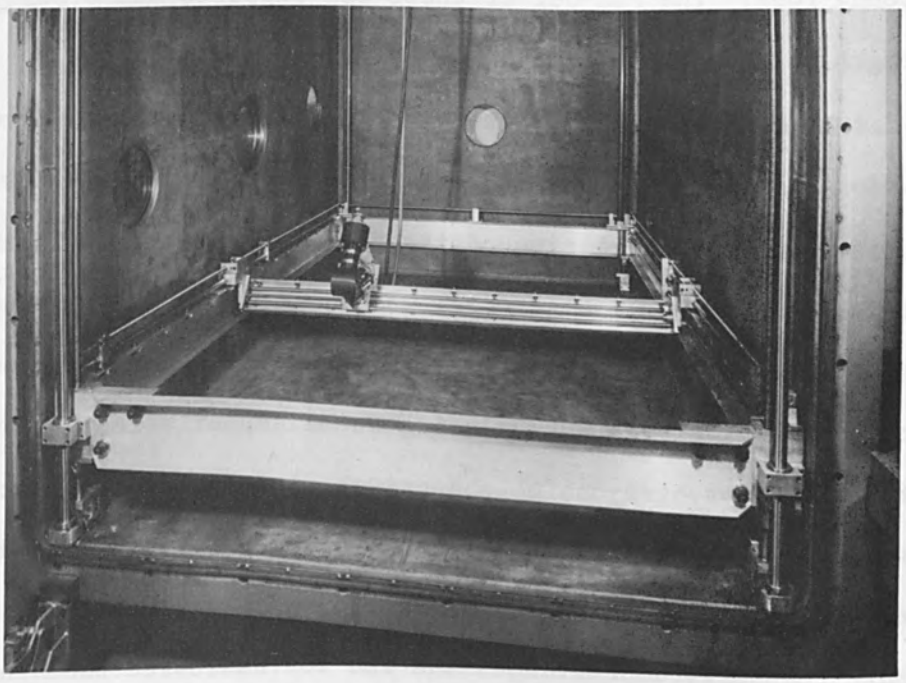

FIGURE 5a Gun Carriage

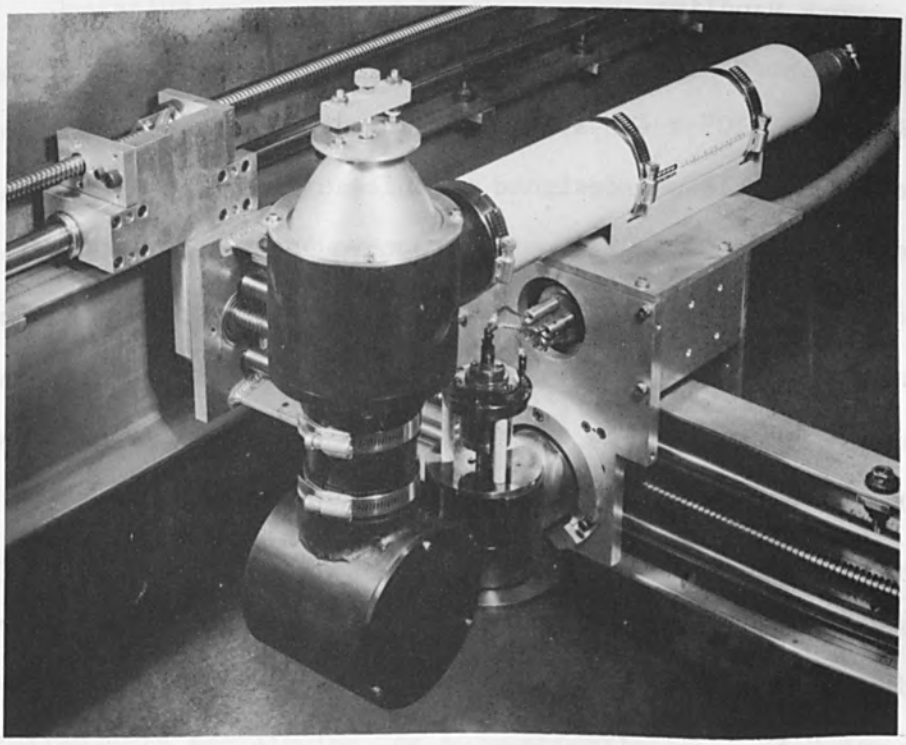

FIGURE 5b Close-Up of Gun Carriage

ground rods. The run-out of these rod supports was 0.005" over a length of 8'6".

In addition to the motor-driven motions, the gun had two manual motions. The first was the rotation of the whole Y bridge assembly; the second was the tilting of the gun at the carriage in the XY plane.

The X, Y and Z mechanisms were supported at both ends of the Z screw and guide rods. By placing these supports in the far corners of the chamber, two design objectives were fulfilled: maximum travel of the gun mechanisms; and minimum effect of wall deflection on the gun during pumpdown by positioning the supports at the corners where the heavy door flanges and the 90^{o} radiussed bend in the wall provided the most rigidity.

C. Work Handling

The work handling carriage was a trolley mounted on the chamber floor. A 120" x 78" x 8" heavy structural frame with six roller bearing wheels was designed to deflect less than 0.005" under a maximum load of 3000 lb. A cutout in the frame served to locate a 6' dia. rotary table, which could also be setup as a horizontal lathe in conjunction with a separate tail stock mechanism. Tee slots running along the length and width of the carriage provided accurate alignment of the head and tail stock assemblies.

The periphery of the rotary table was indexed in increments of 1/10 degree of arc. Accurate indexing with the rotary table was simplified by a large worm wheel drive.

4. Drive Control

A. Principles

Positionally controlled systems require a continuously changing reference voltage to maintain a particular velocity. Velocity controlled systems require a fixed voltage reference to maintain a particular velocity. It is far less difficult to obtain a fixed voltage reference than a continuously variable voltage reference which has sufficient accuracy to drive the gun carriage.

It was decided to drive the gun carriage along the three axes of motion by printed circuit motors as previously outlined. Each motor was controlled with a velocity servo-system including a feedback tachometer to regulate the speed of the driven element with the accuracy necessary for successful welding.

B. Operation

The motors for the X, Y and Z, and rotary drive mechanisms were controlled independently with separate electronics. These are represented diagramatically in Fig. 6. In use, the output reference voltage signal from the control panel is set for the desired speed and is added to the output signal from the tachometer. The difference is amplified by a transistorized feedback amplifier and triggers the gates of a silicon controlled rectifier to drive the motor in either direction at a controlled velocity. The actual velocity of the drive motor is measured on the control panel by the second tachometer. The motors can be driven either in a forward or reverse direction from 0 to 100"/min. They can be manually jogged for positioning, run continuously for slewing, or automatically controlled for welding. Diagonal welds can be made by driving two motors simultaneously.

Limit switches are used for X, Y and Z axis motors to prevent over-travel in any direction. The position of the gun carriage is continuously monitored with a decimal encoder mounted on the gear box and is presented as a decimal readout at the control panel. The X, Y and Z readouts have a range of 00.00 to 99.99" with an accuracy of $\pm$ 0.005 inch. The rotary readout operates from 000.0 to 359.9^{o} with an accuracy of $\pm$ 0.05^{o}.

5. Programmer

A. Principles

There are many different methods which could be used to provide automatic control of an electron beam welder. Digital systems have been shown to be unreliable when in an environment of high voltage transients, such as are generated when an electron gun sparks. Mechanical systems employing templates are useful for specific applications and can be very reliable, but are not versatile or accurate enough for a general purpose large size welder. Analog systems have certain features which make them a desirable method of control, and welding cycles can be programmed with nearly an infinite number of combinations. The accuracies which are attainable are generally sufficient for making large complex weldments. The technique also allows the operator to override the automatic control manually during a programmed weld cycle without disturbing the total program. Finally, analog circuits are not easily affected by the arcs and sparks generated in electron beam equipment. Since the time response of a system will be typically greater than 10 m.sec, it is not necessary for the control circuits to have a time response as fast as the high voltage discharges. The programmer developed for

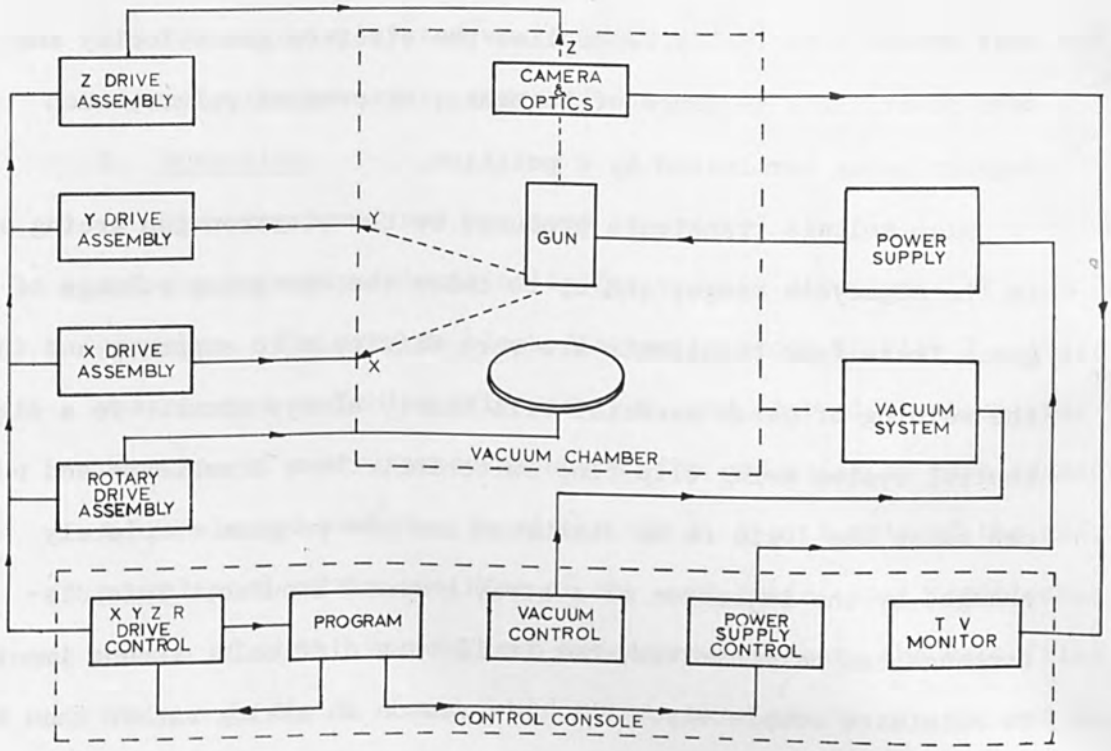

FIGURE 6 Block Diagram of Welder

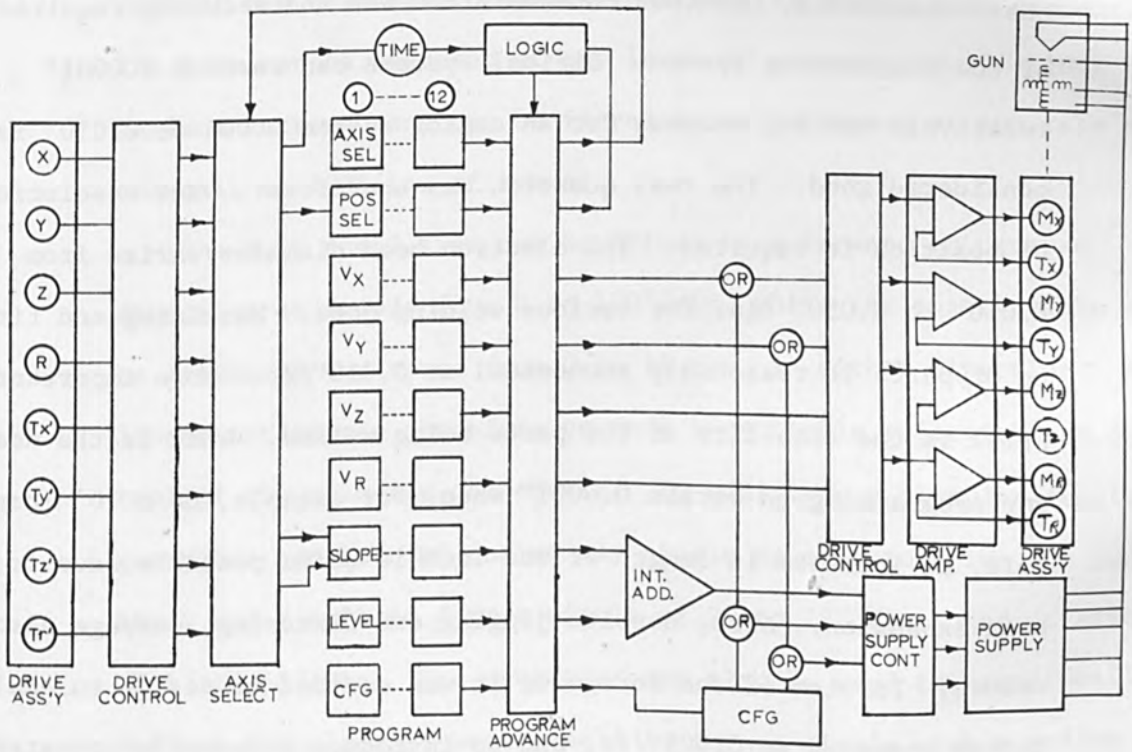

FIGURE 7 Block Diagram of Programmer

this system principally controlled the electron gun velocity and beam power for a sequence of segments, or program points, each segment being terminated by a position.

High voltage transients produced by the electron gun arcing are in the megacycle range, and up to twice the operating voltage of the gun. These fast transients are very difficult to suppress and in the welding of gassy material will nearly always occur. To a digital control system using flip-flop switching, these transients and pulses can cause the logic to be disturbed and the program completely changed by the injection of a stray command impulse. This disturbance can be minimized, but it is very difficult, if not impossible to eliminate completely. For this reason an analog rather than a digital approach was selected, for this is completely insensitive to these transients. Another consideration was the accuracy required of the programming system. Digital systems can resolve 0.0001" relatively easily, whereas for an analog system 0.005 or 0.010" is considered good. The real question was therefore: what resolution of position is required. The electron beam diameter varies from 0.010" to 0.050" dia. for various welding jobs. Machining and fit-up of parts is reasonably economical at 0.010"/ft. More important still is the stability of the parts being welded. What is the need for programming to within 0.0001" when, for example, on a 10' long weld, an increase in length of one inch is quite possible, due to heat expansion. Also, despite jigging and fixturing, warpage also occurs. In view of the foregoing it was decided to design an analog system accurate to 0.005"/ft, and to introduce a manually operated override or correction system. The only complication being that an

accurate viewing system would be required, to find out when and where to apply the necessary correction.

B. Operation

The programmer was designed to control the electron beam current and gun velocity automatically for welding structures of complicated geometry. The program block diagram is shown in Fig. 7. A set of preselected variables drive the gun, and control the beam, for the duration of a programmed request. The end point of each segment is a preselected position in either the X, Y or Z axis of the gun; a preselected rotary position of the work table; or a preselected length of time. During each programmed segment, the velocities of the gun in the X, Y and Z and rotary axes can be pre-set and operated simultaneously. The level and the slope of the electron beam current can also be programmed individually during each segment. The beam can be operated at any level of current from 0 - 100% of maximum current, and can be increased or decreased at any rate between 1% to 100%/in. of travel.

The X, Y and Z axes can be driven in a forward or reverse direction at speeds from 0 to 100"/min, while the rotary table can be driven at any speed from 0 to 16 rpm, in either direction. Any linear motion can therefore be made by suitable selection and control of the velocity components. In addition, a circular function generator can be used during any single segment to drive the gun in the X and Y axis to form a circle of 2" to 72" dia., and at speeds of 5" to 50"/min. The generator can also be used to magnetically deflect the electron beam itself to form a circle with a radius of 1/2 to 1 1/2", at the same speed. During this operation the gun

position can remain stationary or be driven as previously outlined.

The end point of each programmed position is executed by stepping a rotary switch which transfers the control of one set of variables to the next set. This occurs when the four digits of the programmed positions match the four digits of the selected axis, as seen on the decimal encoder. Any axis can be selected to define the end point, with a second stepping switch which transfers control to the selected axis.

The velocity and direction are preselected for each axis by producing a voltage proportional to the velocity with the correct polarity. The electron beam level is selected by producing a voltage proportional to the desired current and this is added to the beam current slope control signal. The slope of the beam current is produced by integrating a signal proportional to the velocity of the particular axis selected.

The circular function generator produces two signals which are sine and cosine functions. The amplitude is proportional to the velocity components in the X and Y axes. The radius of the generated circle is a function of this velocity and the rotational speed.

C. Manual Override Control

As was pointed out above, a manual override of the programmed drive was required, to correct the electron beam position for warpage of the work during welding.

The remote control panel comprised the controls necessary for operation of the system. It can be used at any point within a 20 foot radius of the console. Features included a "joystick" for proportional control of the X and Y velocities. Both the Z axis and

rotary table can be driven intermittently in either direction. All manual controls can be used to override signals from either the drive control, or the programmer. The current and voltage of the electron beam can be adjusted easily with manual controls, and the programmer can be started or stopped with this override at the convenience of the operator.

6. Viewing System

Override control by viewing from the chamber windows was not alone an adequate means of correcting beam trajectory. Many welds were too far away to be seen clearly, or at such an angle that accurate adjustment from a window was impossible. Therefore the closed circuit television viewing system was made an integral part of the electron beam welder.

A block diagram of the television system is shown in Fig. 8. The electron gun, which is mounted on the carriage, produces a high density beam of electrons which is focussed on the welding target by the focus coil. The beam passes through a small hole in a mirror which is placed at an angle of 45^{o}, between the anode and the focus coil. The television camera is mounted above the electron gun and is shielded from the heat radiation. Light from the molten target is directed to the television camera through a system of mirrors which optically align the axis of the camera with the axis of the electron beam. A light source producing a discrete band width of light is focussed on the target material to illuminate the background via the same set of mirrors. The light from both the welding zone and the base material returns to the camera through the system of mirrors, parallel to the incident electron beam.

Two major problems were encountered in the design of the television viewing system. Since a 30 kv electron beam has an inherently short

focal length for good weld penetration, it is necessary for the camera to view the target directly from above. This required the design of an optical system whose axis was parallel to the welding gun axis, but which would not interfere with the electron beam during the welding process. A second problem was the extremely high brilliance of the electron-bombarded spot. The contrast in intensities between the welding zone and base material is typically several million to one, at welding temperatures. Since a television system has a maximum contrast range of two or three hundred, a sophisticated filtering system was required if the welding zone and base material were to be viewed simultaneously.

A very narrow band width filter, about 60 Å wide, was placed between the lens and the vidicon tube in the camera, permitting only a specific wavelength of light from the weld zone to reach the camera. The filter was matched to the wavelength of one of the mercury vapor lines at 4358 Å. With a 200 watt mercury lamp illuminating the weld area, the contrast between the liquid weld zone at 3000°C, and the cold surrounding area was reduced to a factor of about 15. This was within the range of contrast response of the vidicon tube, and hence an adequate picture was obtained.

The cables for the television camera were carried to the outside of the chamber by the same mechanism that carried the high voltage cable to the electron beam gun. The television monitor was located in the center of the welding console for convenient inspection and control of the welding process and this is shown in Fig. 9. The picture displayed on the monitor has the fine resolution, high magnification and low contrast necessary to see the details of both the molten zone and the base material. The field of view enables the gun position to be accurately

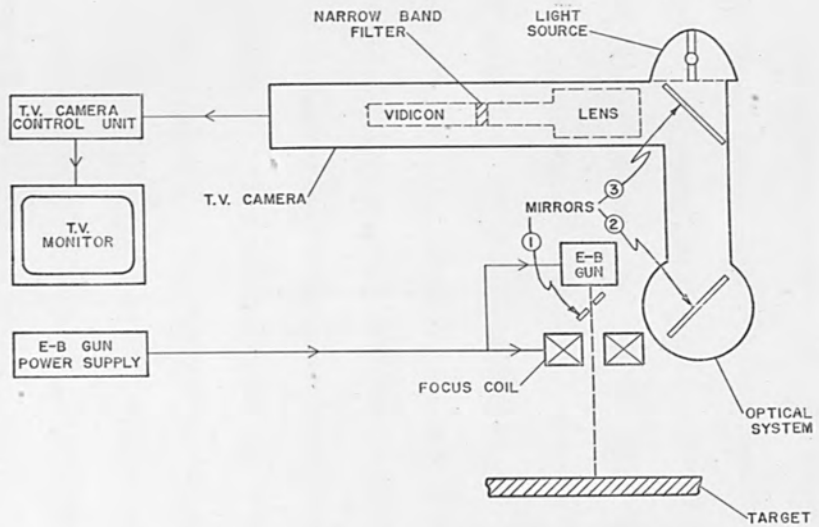

FIGURE 8 T. V. Viewing System

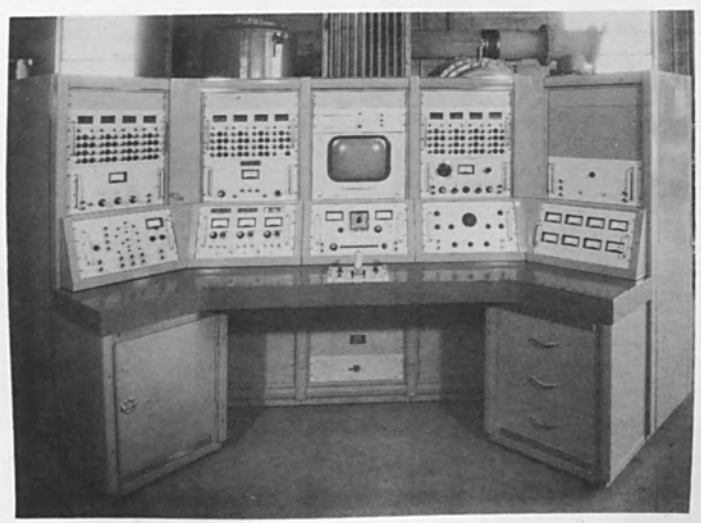

FIGURE 9 Console Arrangement

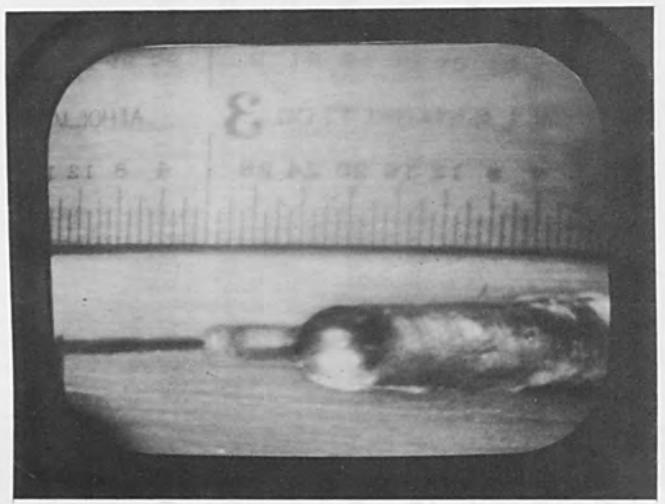

FIGURE 10 Welding of Aluminum

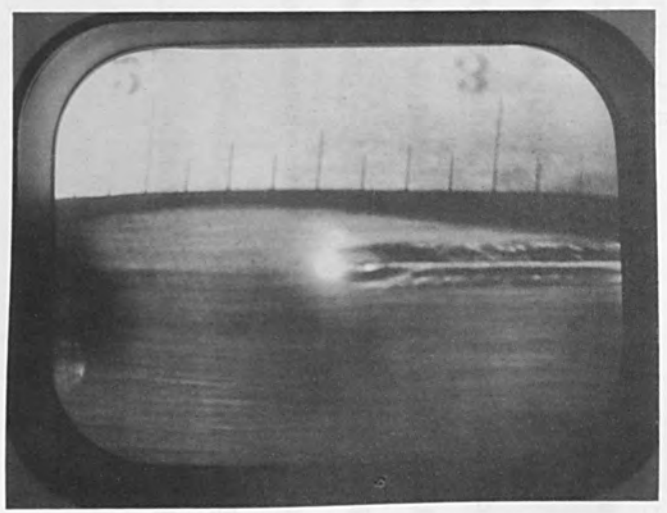

FIGURE 11 Welding of Tungsten

and smoothly controlled during the welding cycle.

Fig. 10 shows a weld in aluminum as it is monitored by the close circuit television. The low light contrast between the very hot bright beam spot and the surrounding cold area provides an excellent picture. Fig. 11 shows a photograph of the television screen taken during the monitoring of a weld in tungsten.

REFERENCES

1. Leonard, L. H., Morley, J. R. and Dunn, L. Air Force Technical Report, #63-7-962.

THE VACUUM ANALYZER

Roger P. Ellman
Aero Vac Corporation
Troy, New York

ABSTRACT

An instrument is described which is a total pressure vacuum gauge, and a residual gas analyzer. A new concept of vacuum system control employing the instrument is discussed as well as the design and development of the instrument.

THE VACUUM ANALYZER

INTRODUCTION

High and ultrahigh vacuum systems are tools, as are power supplies or voltmeters, and are only a means to an end. In the case of electron beam studies, the vacuum system generates the environment in which studies or processes take place. Hence, the vacuum system must be easily controlled and the environment generated must be well defined. Unfortunately these matters are not always so straightforward. The means of controlling a vacuum system, and defining the environment produced, are the vacuum system itself and its instrumentation. This paper describes an advance in vacuum instrumentation.

The total pressure gauge has been the principal vacuum measuring instrument for years. With such an ionization gauge the total pressure is known, and, with its use educated guesses can be made as to the nature of problems encountered within a vacuum system. For more information, a mass spectrometer, which can indicate the types of gas residuals and their relative partial pressures, can be used, but these have several disadvantages: they are expensive, frequently costing more than the vacuum system and experimental equipment that they are used on; they are difficult to operate; and frequently, they should not be used except in the ultrahigh vacuum range of 10^{-6} Torr or lower pressures.

The Vacuum Analyzer is an instrument without these disadvantages. It is an ionization gauge and a mass spectrometer combined in one instrument, and is simple to use, inexpensive, and will operate in the high and ultrahigh vacuum ranges. The development of such an instrument required a new approach to ion beam source design and the associated problems of x-ray shielding, optics, filaments, and power supplies. Each of these will be discussed, as will the application of the Vacuum Analyzer to system control.

MASS SPECTROSCOPY

As is well known, when charged particles are accelerated through an electric field, all particles receive energy proportional to their charge and emerge with velocities inversely proportional to the square root of the mass. In a magnetic field, charged particles are deflected into circular paths where the radius of curvature is directly proportional to the velocity. If singly charged positive ions are first accelerated in an electric field and then deflected in a magnetic field, the ions emerge on separate paths where all ions of the same mass are on the same path. Ions of a particular mass species can be selected by a suitably placed slit. (It is necessary that the electric and magnetic fields properly focus the ion beam). If either the electric or magnetic field is varied, ions of any desired mass species can be focused on a fixed collector slit. Such a device is a mass spectrometer.

Normally, in such instruments, the magnetic field is kept constant and the electric accelerating potential is varied over a selected range, and the ion current collected is plotted on an X-Y recorder against the accelerating potential. The result is a spectrum of the mass species present in the mass range scanned.

The sensitivity of a mass spectrometer depends on the efficiency with which ions are formed and on the accuracy of focusing. Resolution, or the ability to distinguish adjacent masses, depends on focus and on a variety of other factors such as space charge spreading of the beam, and the energy of the ions. The latter effect can be caused by power supply ripple and by ions being formed at different potentials. Since the incremental difference in mass of adjacent mass species becomes smaller for higher mass numbers, a mass spectrometer always has an upper limit in resolution.

THE VACUUM ANALYZER

At pressures in the high and ultrahigh vacuum range, the number of ions, formed by bombardment from a given electron current, varies linearly with pressure. This is the principle of operation of the ionization gauge. The cross sections for ionization of various mass species are different. Consequently a mass spectrometer will indicate approximate relative partial pressures only, and will require a different value of electron current to calibrate for the absolute partial pressure for each mass species. This same effect causes ionization gauges to read correctly only for the gas for which they have been calibrated and this is usually nitrogen. Generally, the relative information is sufficient.

DESCRIPTION

The Vacuum Analyzer consists of a spectrometer tube and a control unit. The spectrometer tube (Fig. 1) uses thermionic emission from a filament to provide an electron current to the cage where the ions are formed. The ions are then drawn out of the cage by the electric field, accelerated, and focused toward the exit slit. Some ions are collected by the exit slit and this current is amplified and displayed to provide the total pressure information in essentially the same way as in an ionization gauge. The remainder of the ion beam is focused down a tube, deflected by a magnet and collected. Ions with mass numbers, other than that to which the accelerating voltage is tuned, are collected on the walls of the tube enclosing the beam. The mass species selected passes through the collector slit, is amplified, and is read as the partial pressure of that particular mass species.

There are several significant features of the spectrometer tube which account for its simplicity of operation and construction. A conventional spectrometer tube employs an ion "gun", similar to the usual electron "gun",

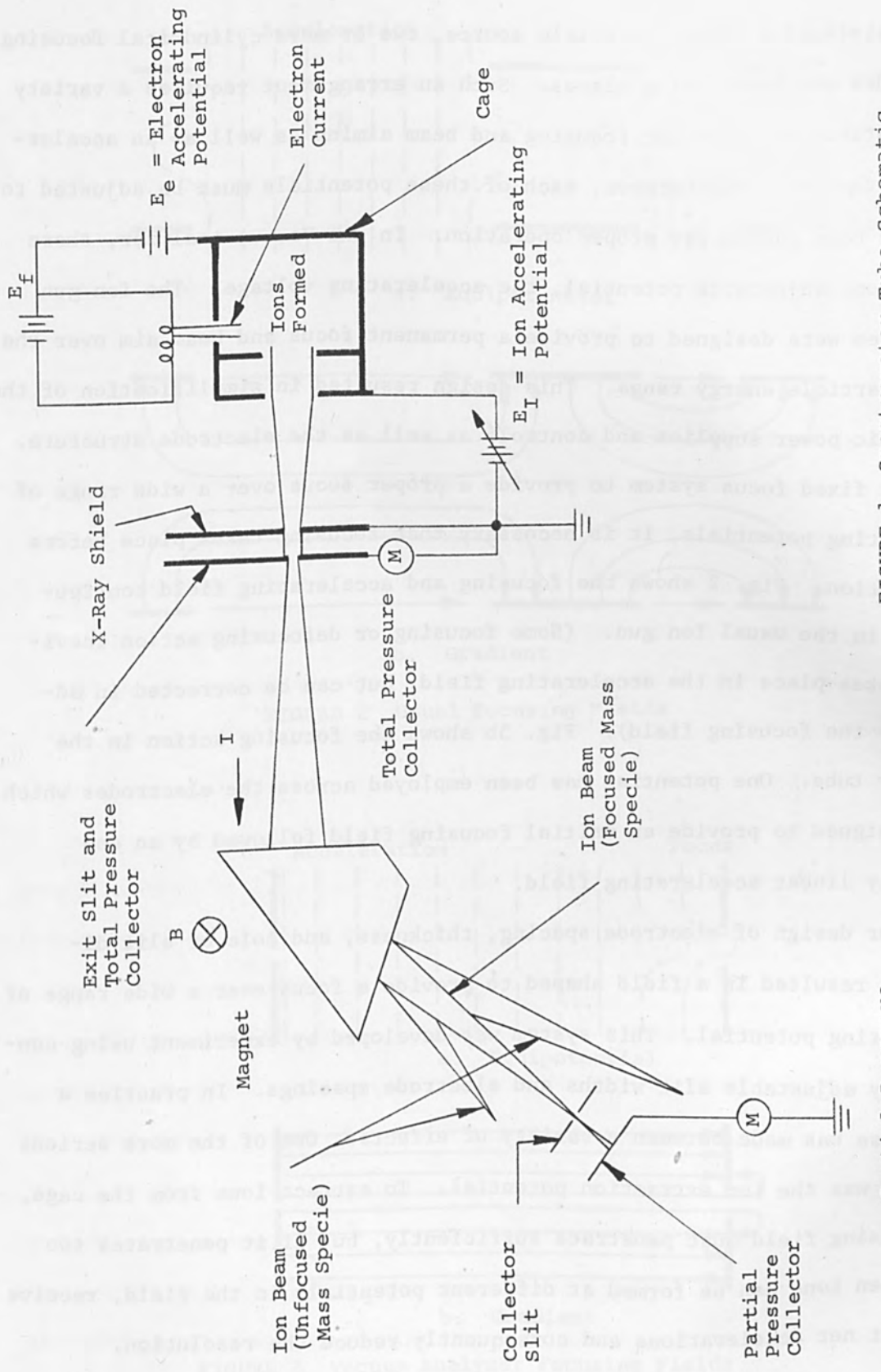

FIGURE 1 Spectrometer Tube Schematic

and consists of a charged particle source, two or more cylindrical focusing electrodes and beam aiming plates. Such an arrangement requires a variety of adjustable voltages for focusing and beam aiming as well as an accelerating potential. Furthermore, each of these potentials must be adjusted to tune the beam source for proper operation. In the Vacuum Analyzer, there is only one adjustable potential, the accelerating voltage. The ion gun electrodes were designed to provide a permanent focus and beam aim over the entire particle energy range. This design resulted in simplification of the electronic power supplies and controls as well as the electrode structure.

For a fixed focus system to provide a proper focus over a wide range of accelerating potentials, it is necessary that focusing takes place before acceleration. Fig. 2 shows the focusing and accelerating field configurations in the usual ion gun. (Some focusing or defocusing action inevitably takes place in the accelerating field, but can be corrected in advance by the focusing field). Fig. 3b shows the focusing action in the analyzer tube. One potential has been employed across the electrodes which were designed to provide an initial focusing field followed by an essentially linear accelerating field.

Proper design of electrode spacing, thickness, and hole or slit dimensions resulted in a field shaped to provide a focus over a wide range of accelerating potential. This system was developed by experiment using continuously adjustable slit widths and electrode spacings. In practice a compromise was made between a variety of effects. One of the more serious of these was the ion extraction potential. To extract ions from the cage, the focusing field must penetrate sufficiently, but if it penetrates too much, then ions can be formed at different potentials in the field, receive different net accelerations and consequently reduce the resolution.

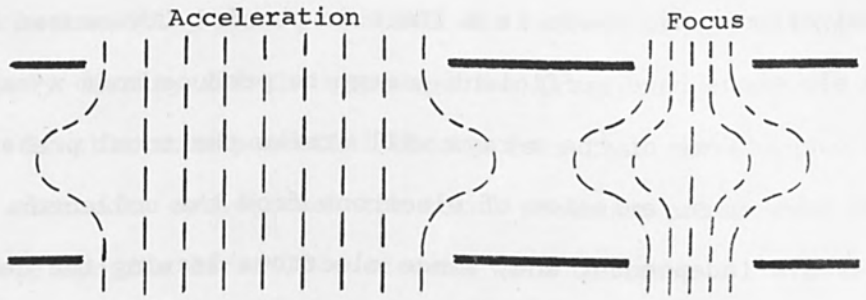

a. Equipotential

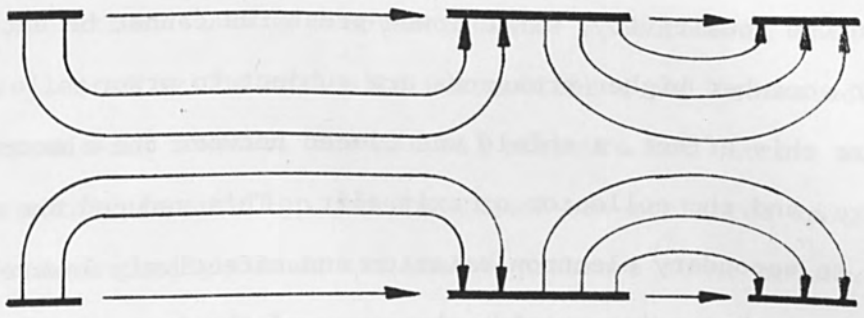

b. Gradient

FIGURE 2 Usual Focusing Fields

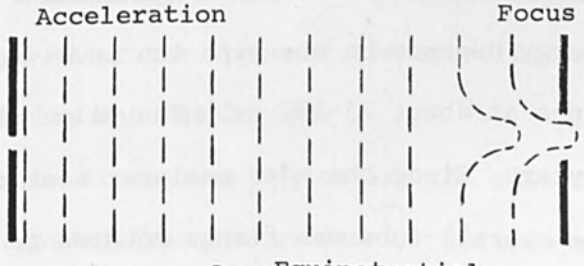

a. Equipotential

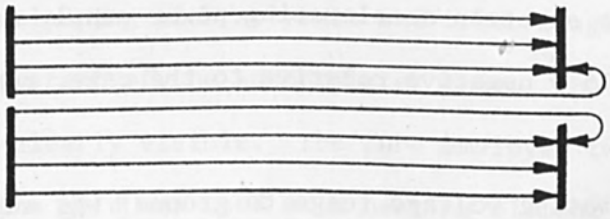

b. Gradient

FIGURE 3 Vacuum Analyzer Focusing Fields

In any ionization gauge there is a limit to sensitivity caused by x-ray action. The electrons have sufficient energy to produce soft x-rays upon striking the cage. Some of the x-rays will strike the total pressure collector and in turn cause emission of electrons from the collector. This action is pressure independent and, since electrons leaving the collector appear the same as ions arriving, there is a minimum current even in the total absence of ions. The pressure corresponding to this minimum current is a limit on the sensitivity, since lower pressures cannot be detected and equivalent or somewhat higher pressures are subject to error.

To minimize this effect, a shield was placed between the electron x-ray source or cage, and the collector or exit slit. This reduced the effective area subject to secondary electron emission and effectively lowered the limiting pressure to a point outside the range of the instrument. The ion beam was focused through the slit in the x-ray shield so that two-thirds of it was collected and read as total pressure, and one-third passed on to be mass analyzed.

There is a resonance effect for electron bombardment ionization. The optimum electron energy depends on the type ion involved. In general, most ions exhibit resonance at about 75-100 ev. The value of 75 v was selected for the Vacuum Analyzer. Since the mass analyzer section must be free from electric fields, the overall tube was flange mounted to the vacuum chamber. It was necessary to operate the collectors at ground potential and the cage above ground. The electron accelerating power supply was arranged so that the filament was 75 v negative relative to the cage, regardless of cage potential.

The ion accelerating voltage (cage to ground) was adjustable to select different mass species to be focused by the magnet on the partial pressure

collector. Normally, this potential was scanned over its range to successively display all the mass species (residual gases) which were present. If this scan potential became less than the electron accelerating voltage, electrons could reach the total pressure collector. This was undesirable and the first 75 v of scan were omitted.

Filament life time was considerably extended by providing automatic filament turn off when a pressure surge occurred, both for total or partial pressure operation. During a total pressure measurement, only the ion current collected by the exit slit was monitored and indicated. During a mass spectrum scan however, the partial pressure ion current was displayed while the total pressure ion current signal was monitored so that the filament was automatically turned off when a pressure surge occurred.

Ionization gauges and mass spectrometers are adversely affected by contamination of the electrodes. Such contamination can result from oxidation of the metal elements, adsorbed or "gettered" gases, and surface deposits such as hydrocarbons from pump oil. Contaminants cause an insulating layer to form on normally conducting surfaces. Consequently charge can accumulate on the electrodes and alter the shape of electric fields. This results in reduction of sensitivity and resolution.

Contamination can be cleaned up by heating the electrodes so that the contamination is outgassed from the surfaces. This is usually accomplished by either electron bombardment or direct resistance heating. Severe contamination requires cleaning with solvents and other reagents.

Fig. 4a is a photograph of the spectrometer tube. The exit slit, x-ray shield and cage are clearly visible. The tube employed two filaments, for use one at a time; the grid was used as a heating element to decontaminate the source. The magnet was fixed to the tube in the correct position by

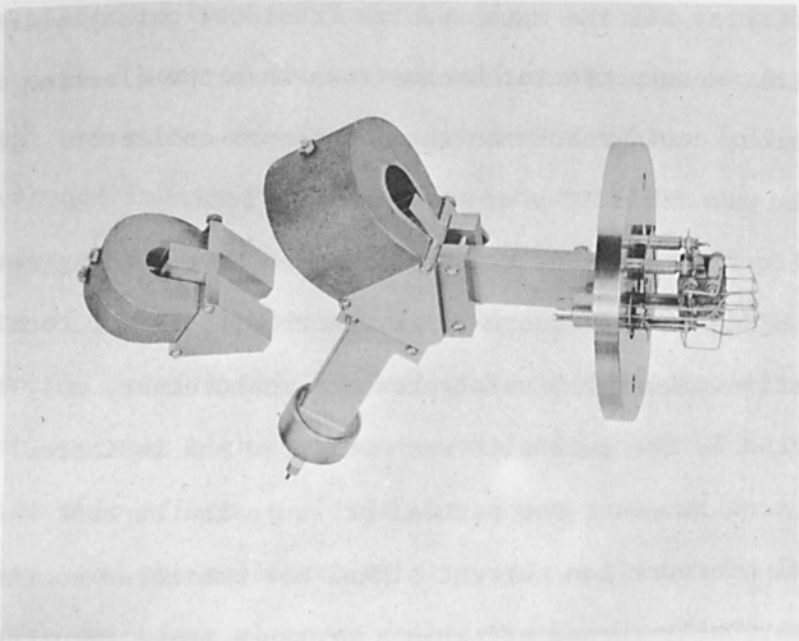

FIGURE 4a Spectrometer Tube

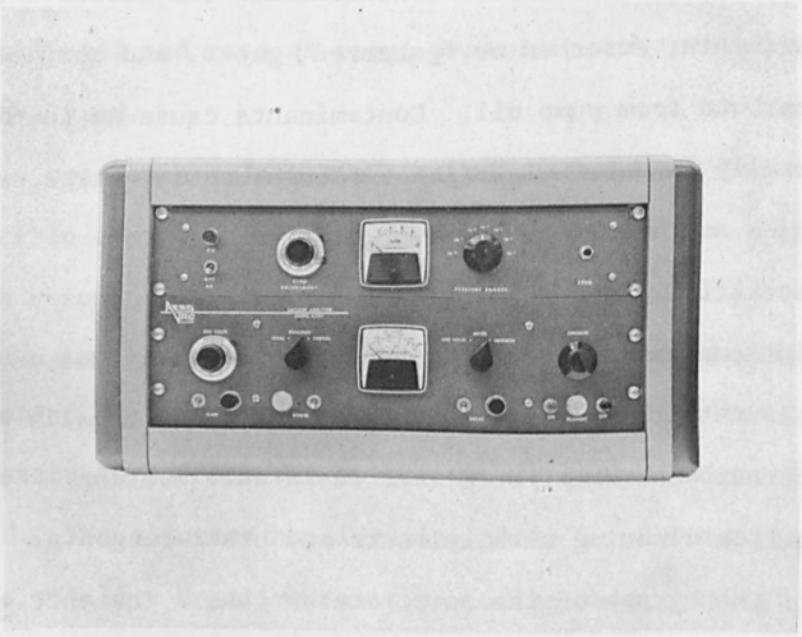

FIGURE 4b Control Unit

metal blocks and a strap.

The control unit (Fig. 4b) operated the filament and its automatic turn off, the degas grid, provided the electron and ion accelerating potentials, amplified the output ion current, and provided regulated direct current to heat the filament. Filament current was regulated for constant electron emission current as set by the emission control.

Normally, in scanning the mass spectrum, there will be a wide range of partial pressures of various mass species. If the amplifier was operated at sufficiently high gain to detect the small peaks, it saturated on large peaks and did not recover in time to prevent the loss of indication of some succeeding peaks. To prevent this, a circuit was developed which allowed the use of the most sensitive scale without saturation occurring while maintaining linear operation for on scale values.

APPLICATIONS

The following five examples of operating experience illustrate the application of a Vacuum Analyzer to vacuum system operation:

1. Water Vapor

Water is a factor which limits the ultimate pressure in vacuum systems. It is carried into the chamber by the atmosphere and by objects placed in the chamber. Water can also enter from the diffusion pump, the rate depending on the effectiveness of the water baffle. Water takes a relatively long time to pump out unless baking of the chamber is employed because a small amount of condensed or adsorbed water will outgas slowly at a vapor pressure much less than that of free liquid water.

During a test pump down of a 30" dia., 10^{-8} Torr, diffusion pumped chamber, the system stabilized at 2×10^{-6} Torr with an apparent leak. Normal procedure called for connecting a leak detector and searching for the

Water and Air

P = 2×10^{-5} Torr

CO_2 - Carbon Dioxide

A - Argon

O - Oxygen

N - Nitrogen

H_2O - Water

OH - Hydroxide Radical

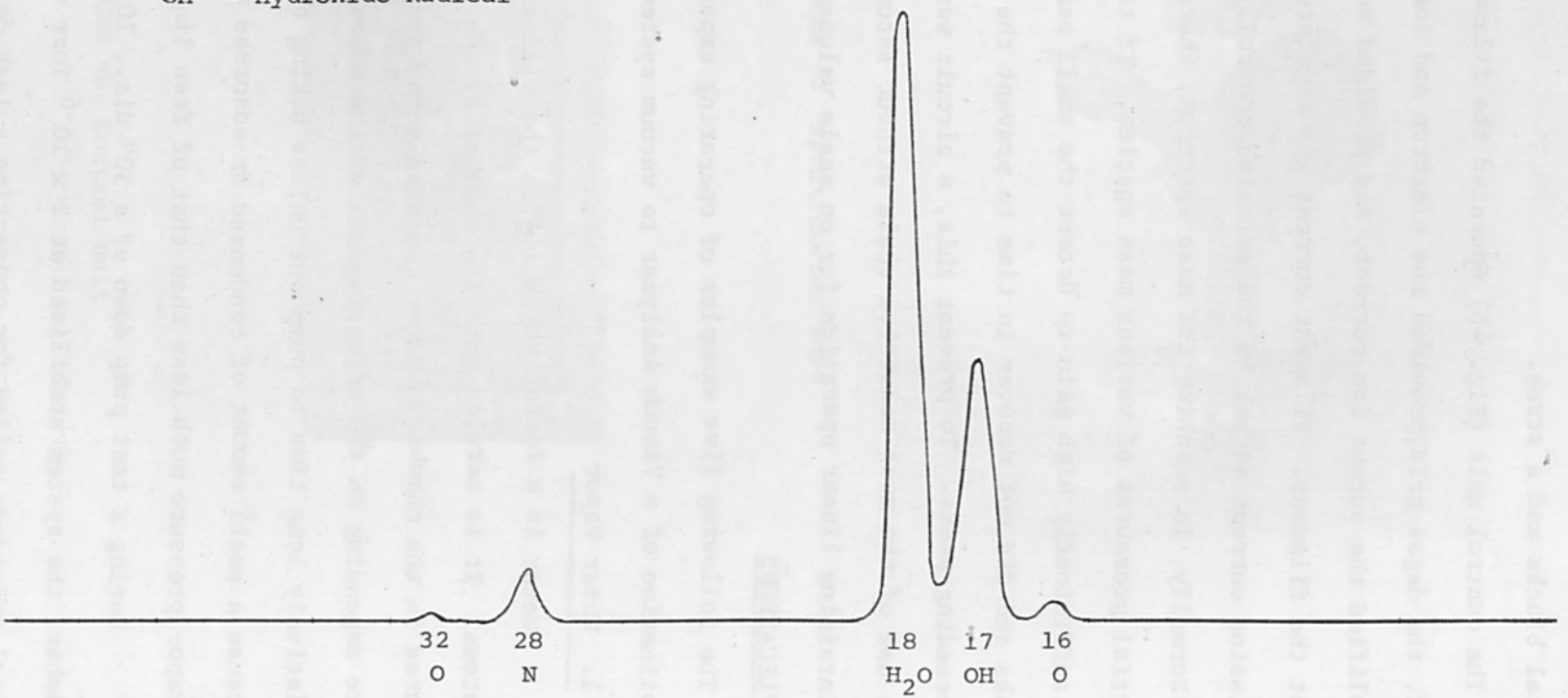

FIGURE 5

leak. Instead, a Vacuum Analyzer spectrum (Fig. 5) showed a large water vapor partial pressure in the chamber. Further pumping removed the water and the system performed as predicted.

Additional analysis disclosed that a paint which outgassed water vapor about ten times more than anticipated was the contaminating source. Considerable time would have been lost looking for a nonexistent leak with a leak detector.

2. Carbon Dioxide

Vacuum systems are baked to accelerate the outgassing rate of adsorbed gases to obtain lower ultimate pressures more quickly. Hydrogen and carbon dioxide are among the gases evolved. If a cold surface, such as a liquid nitrogen trap, is present during bakeout, then solid CO_2 may accumulate on the trap. After bakeout, the outgassing of the CO_2 can limit ultimate pressure.

For a routine test, a bakeable two-inch exhaust station was to be operated in the 10^{-9} Torr range. The system was pumped down to the low 10^{-6} Torr and baked for twelve hours. After cooling, the system stabilized at 6×10^{-8} Torr. Three different gases, air from a leak, hydrogen from insufficient bakeout, or carbon dioxide by sublimation from frozen CO_2 on liquid nitrogen trap, could have caused the system to stabilize. However, the corrective action for each of the three situation would be different: leak test for air, bake for hydrogen, clean trap for carbon dioxide. An analyzer spectrum (Fig. 6) disclosed a large CO_2 signal, negligible air and negligible hydrogen. Considerable time could have been lost using a trial and error approach.

One method of removing the CO_2 is to let the trap warm up so that it can be pumped out. Insufficient warming will not eliminate all of the CO_2,

CO_2 - Carbon Dioxide

CO - Carbon Monoxide

O - Oxygen

C - Carbon

CO_2 Sublimating Off LN_2 Trap

Total Pressure 9.0×10^{-5} Torr

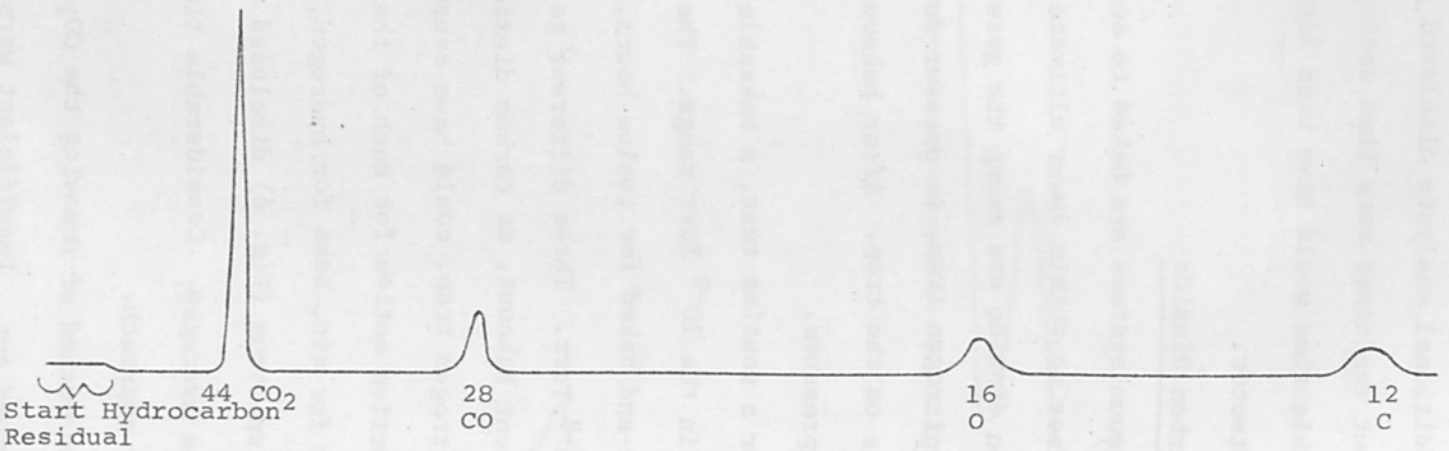

FIGURE 6

and too much heat can result in water or diffusion pump oil getting into the system. With the partial pressure information available, the process can be closely controlled.

By tuning to the CO_2 mass peak and removing the liquid nitrogen from the trap, an increase in the peak indicated trap warm up. Periodic scans of the mass spectrum monitored the other gas residuals, particularly for hydrocarbons in the mass 50 - 70 range, and water vapor. When the indication was that the CO_2 had been sufficiently eliminated, the trap was cooled with liquid nitrogen. The total pressure was found to be 5×10^{-9} Torr. Correction of this problem required only a slight variation in operating procedure.

3. Air

A pump down failed to achieve the desired low pressure on an exhaust station, and the indicated total pressure was 2×10^{-5} Torr. A mass spectrum (Fig. 7) indicated air, and one of the flange seals was suspect. The Vacuum Analyzer was set to mass 4 (helium) and the seals were successively sprayed with helium gas, until the leak was found.

4. Argon

A test required the introduction of argon at 1.5×10^{-5} Torr, into a chamber. The Vacuum Analyzer was tuned to Argon and used to monitor the Argon partial pressure. Periodic scans of the mass spectrum monitored other gas residuals (Fig. 8).

5. Pressure Oscillations

A developmental 10^{-11} Torr system using a 4" diffusion pump backing a 10" pump had an Analyzer connected in the foreline between the two pumps. The total pressure was approximately 5×10^{-6} Torr in the foreline with the gas residuals being mainly hydrocarbons and gases from cracked pump oil

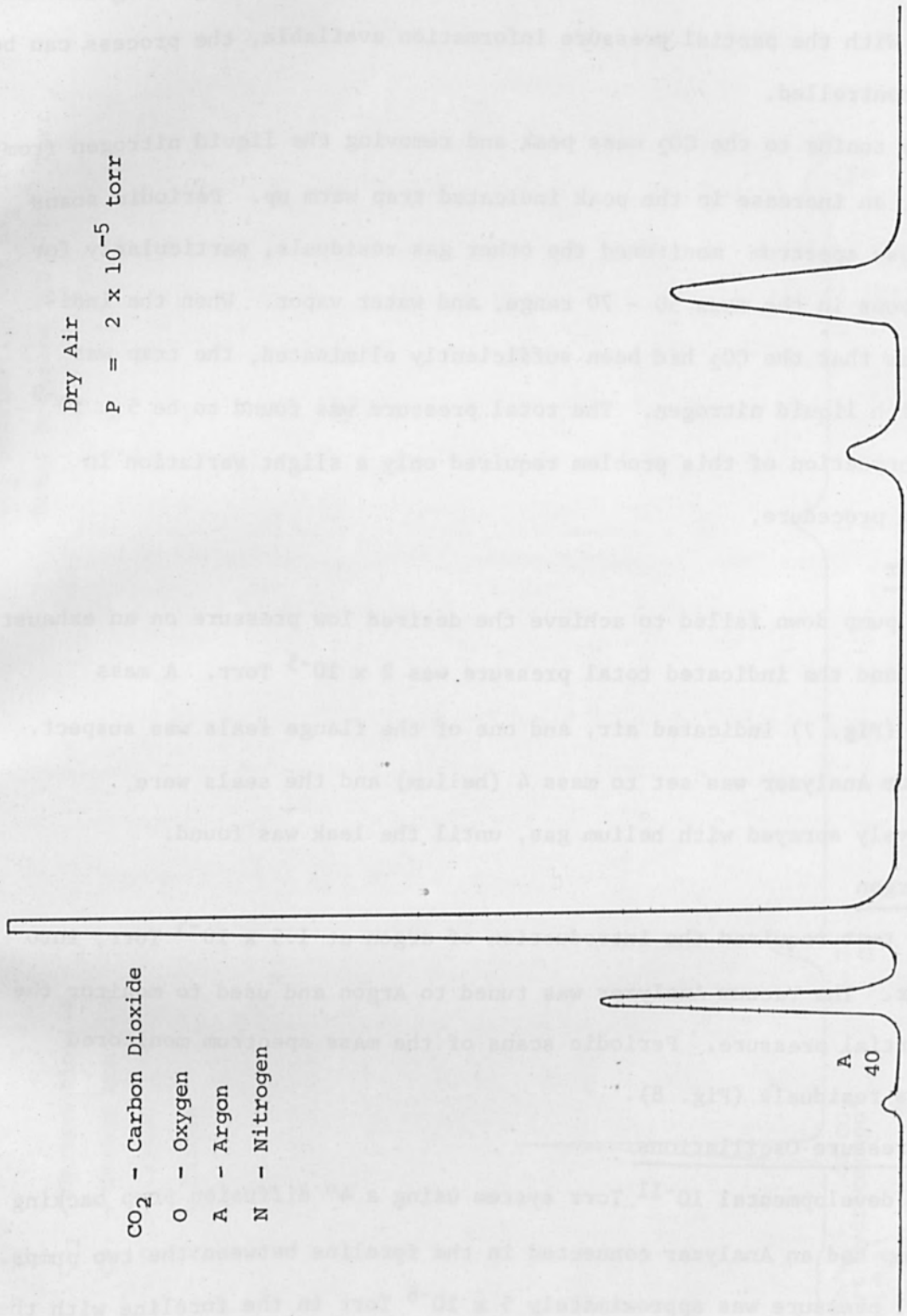
Dry Air
P = 2 x 10⁻⁵ torr
CO2 - Carbon Dioxide
O - Oxygen
A - Argon
N - Nitrogen
44 CO2
40 A
32 O
28 N
16 O
14 N

FIGURE 7

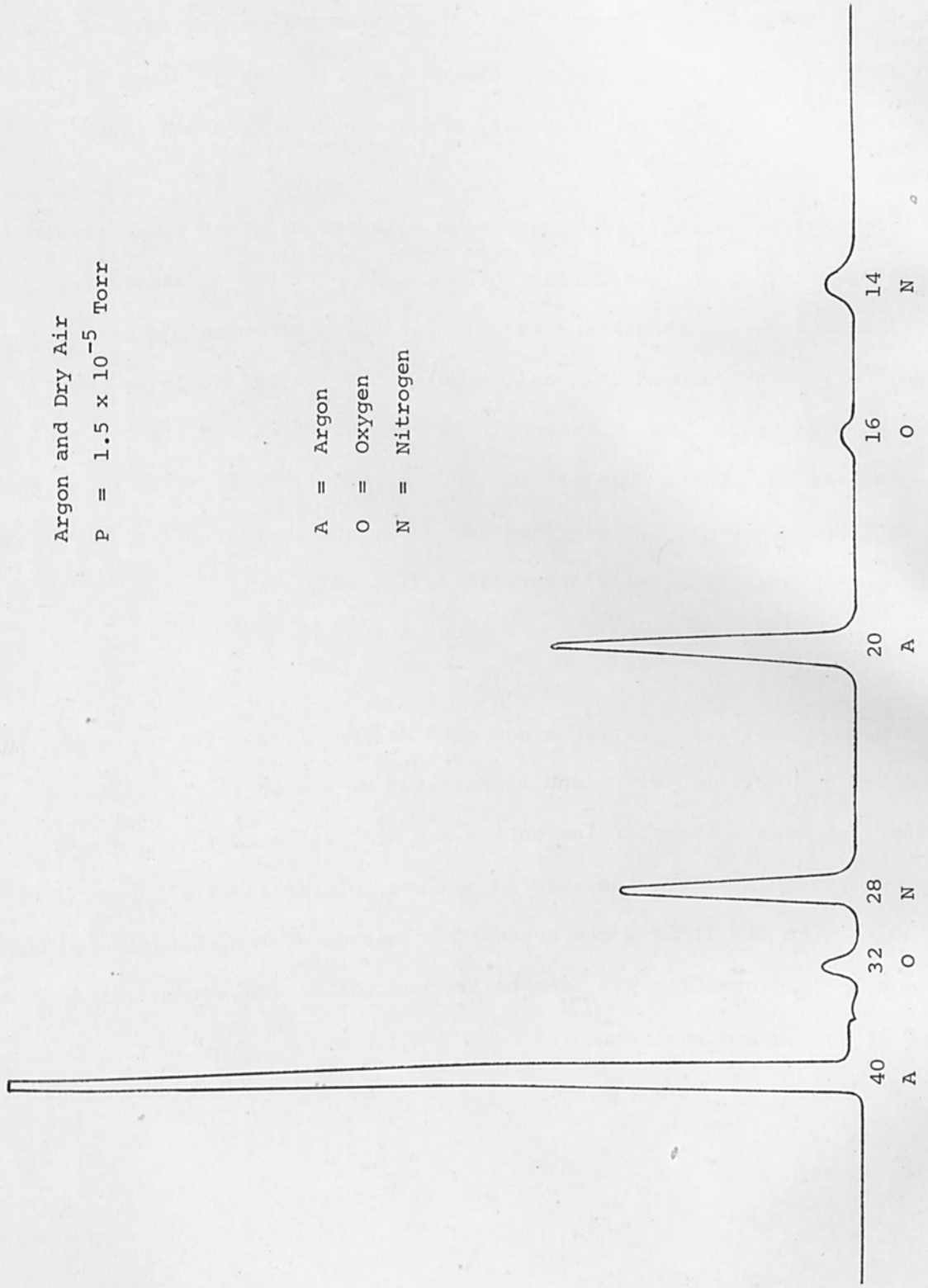
Argon and Dry Air
P = 1.5 x 10^{-5} Torr
A = Argon
O = Oxygen
N = Nitrogen
40
A
32
O
28
N
20
A
16
O
14
N

FIGURE 8

(CO_2, O, CO, H_2O, C, H). Resolution was somewhat reduced because of the heavy hydrocarbon contamination in the tube over the period of time. Useful information was obtained however, and the nude source was later easily cleaned.

During the initial pump down cycle with new oil, the total pressure in the foreline between the diffusion pumps was observed to oscillate approximately 10% of its average value. Diffusion pump trouble was suspected. A spectrum showed that only some of the gas residuals had oscillating partial pressures. These could be identified as the lighter radicals breaking out of the pump oil (C, H_2O, O, etc.). This established that the problem was one of remaining contaminants, not that of a defective pump. Spectrums taken at later time intervals indicated a steady reduction in the oscillating peaks, thus confirming the conclusion.

SUMMARY

The Vacuum Analyzer provides a new combination of existing types of vacuum system instrumentation and is packaged as one unit. It employed a new approach to spectrometer ion optics and was developed into a simple instrument which will provide more convenient information than previously available. The result is a new approach to vacuum system operation in which more complete information provides better control of the system and definition of the vacuum environment.

alloyd general corporation
MEDFORD, MASSACHUSETTS